UNIVERSITY OF CALIFORNIA SAN DIEGO

Guided surface acoustic wave device design and fabrication for the application of cell agglomeration

A dissertation submitted in partial satisfaction of the
requirements for the degree
Doctor of Philosophy

in

Materials Science and Engineering

by

Jiyang Mei

Committee in charge:

Professor James Friend, Chair
Professor Shengqiang Cai
Professor Vitali Nesterenko
Professor Lonnie Petersen
Professor Andrea Tao

2022

The dissertation of Jiyang Mei is approved, and it is acceptable in quality and form for publication on microfilm and electronically.

University of California San Diego

2022

DEDICATION

I dedicate this thesis to my parents for nursing me with affections and love, and their dedicated partnership for success in my life.

TABLE OF CONTENTS

LIST OF FIGURES

LIST OF TABLES

ACKNOWLEDGMENTS

First and foremost, I would like to thank my supervisor, Professor James Friend. He is such a nice guy who is always encouraging me to think, try, speak out, and practice my own ideas on the research. He is full of crazy ideas and inspiring suggestions that kept me on the right track of research throughout my entire Ph.D. years. The way he thinks about problems and how he handles them has deeply affected me and will be with me in the future. More importantly, his kindness to people, enthusiastic lifestyle, and passion for science will be exemplary throughout my future life and career. I hope he would be always happy and healthy, besides his remarkable success and contribution in research work.

I would like to thank my dissertation committees, Professor Vitali Nesterenko, Professor Lonnie Petersen, Professor Shengqiang Cai and Professor Andrea Tao for their insightful comments and constructive suggestions which gains my research experience and improve this dissertation. I would like to thank Dr. Sreekanth Chalasani from Salk Institute for guiding my experimental and especially knowledge concerning cell and biology. His profound knowledge largely helped the projects in my dissertation. I would also like to thank Professor Kenjiro Takemura from Keio University for helping me solve out experimental problems and accelerate the projects.

I would like to thank all the colleagues and collaborators I met and worked

with in the past five years. I would like to thank all my labmates in MADLAB, Dr. Jeremy Orosco, Dr. Amihai Horesh, Dr. C´ecile Floer, Dr. Gopesh Tilvawala, Dr. An Huang, Dr. Naiqing Zhang, Dr. Jiaying Wang, Shuai Zhang, William Connacher, Aditya Vasan, Edward Aminov, Dr. Yuta Kurashina, Antoine Pallois, Chikahiro Imashiro for their selfless guidance, effective discussions, and helpful insights in the research path. You all create a lovely, warm-hearted, and humorous lab that I could stay and forget about time and tiredness. I would like to thank all other collaborators, Uri Magaram, Minghao Li, Takumi Inui for helping me on the research projects.

I would like to thank all my friends I met in San Diego for helping me and bringing so much happy time and memories in such a long journey. And very special thanks to Tianhao Jiang, who is the first friend I made in San Diego, and his wife Ying Huang. I appreciate their accommodation and assist in my difficult times.

Finally, I would like to acknowledge the support and love from my family. I would like to thank my parents for absolute support to what I would like to do. They both kept learning and trying to do all the best in their life, which also drives me to keep moving forward.

Chapter 1, in part, is a reprint of materials appearing in Lab on Chip 2018. Connacher, William, Zhang, Naiqing; Huang, An; Mei, Jiyang; Zhang, Shuai; Gopesh, Tilvawala; Friend, James. “Micro/Nano Acoustofluidics: Materials, Phenomena,

Design, Devices, and Applications" Lab on a Chip 18.14 (2018): 1952-1996. The dissertation author was one of the investigators and authors of this paper.

Chapter 2, in full, is a reprint of material appearing in Mechanical Engineering Reviews 2020. Jiyang Mei, and James Friend. "A review: controlling the propagation of surface acoustic waves via waveguides for potential use in acoustofluidics." Mechanical Engineering Reviews 7, no. 1 (2020): 19-00402. The dissertation author was the primary investigator and author of this paper.

Chapter 3, in full, is a reprint of material appearing in Journal of Visualized Experiments 2020. Jiyang Mei, Naiqing Zhang, and James Friend. "Fabrication of surface acoustic wave devices on lithium niobate." JoVE (Journal of Visualized Experiments) 160 (2020): e61013. The dissertation author was the primary investigator and author of this paper.

Chapter 4, in full, is a reprint of material that is in review 2022. Jiyang Mei, Aditya Vasan, Uri Magaram, Kenjiro Takemura, Sreekanth Chalasani, and James Friend. "Non-contact three-dimensional cell cluster formation on demand in open dishware using focused surface acoustic waves through a couplant layer." The dissertation author was the primary investigator and author of this paper.

VITA

2007-2011	B. S in Applied Physics, University of Science and Technology of China
2011-2013	M. S. in Physics, Illinois Institute of Technology
2013-2015	M. S. in Materials Science and Engineering, University of California San Diego
2015-2022	Ph. D. in Materials Science and Engineering, University of California San Diego

PUBLICATIONS

Jiyang Mei, Aditya Vasan, Uri Magaram, Kenjiro Takemura, Sreekanth Chalasani, and James Friend. "Non-contact three-dimensional cell cluster formation on demand in open dishware using focused surface acoustic waves through a couplant layer." *Biomedical Microdevices* (Submitted)

Jiyang Mei, Minghao Li, James Friend and Jinhye Bae. "Surface acoustic waves adjustable anisotropic deformation of reduced graphene oxide hybrids embedded poly(N-isopropylacrylamide)." (In progress)

Jiyang Mei, Naiqing Zhang, and James Friend. "Fabrication of surface acoustic wave devices on lithium niobate." *JoVE (Journal of Visualized Experiments) 160 (2020): e61013.*

Jiyang Mei, and James Friend. "A review: controlling the propagation of surface acoustic waves via waveguides for potential use in acoustofluidics." *Mechanical Engineering Reviews 7, no. 1 (2020): 19-00402.*

Takumi Inui, **Jiyang Mei**, Chikahiro Imashiro, Yuta Kurashina, James Friend, and Kenjiro Takemura. "Focused surface acoustic wave locally removes cells from culture surface." *Lab on a Chip (2021).*

An Huang, William Connacher, Mark Stambaugh, Naiqing Zhang, Shuai Zhang, **Jiyang Mei**, Aditi Jain et al. "Practical microcircuits for handheld acoustofluidics." *Lab on a Chip (2021).*

Jiaying Wang, **Jiyang Mei**, James Friend, and Oscar Vazquez-Mena. "Frequency and damping effect of suspended silicon nitride membranes in water near the megahertz range." *Journal of Micromechanics and Microengineering 30, no. 12 (2020): 125006.*

Naiqing Zhang, **Jiyang Mei**, Tilvawala Gopesh, and James Friend. "Optimized, omnidirectional surface acoustic wave source: 152° Y-rotated cut of lithium niobate for acoustofluidics." *IEEE Transactions on Ultrasonics, Ferroelectrics, and Frequency Control (2020).*

William Connacher, Naiqing Zhang, An Huang, **Jiyang Mei**, Shuai Zhang, Tilvawala Gopesh, and James Friend. "Micro/nano acoustofluidics: materials, phenomena, design, devices, and applications." *Lab on a Chip 18, no. 14 (2018): 1952-1996.*

ABSTRACT OF THE DISSERTATION

Guided surface acoustic wave device design and fabrication for the application of cell agglomeration

by

Jiyang Mei

Doctor of Philosophy in Materials Science and Engineering

University of California San Diego, 2022

Professor James Friend, Chair

Acoustic actuation of fluids at small scales may finally enable a comprehensive lab-on-a-chip revolution in microfluidics, overcoming long-standing difficulties in fluid and particle manipulation on-chip. In the introductory chapter, we examine the fundamentals of piezoelectricity, piezoelectric materials, and transducers; revisit the

basics of acoustofluidics; and give the reader a detailed look at recent technological advances and current scientific discussions in the discipline. Recent achievements are placed in the context of classic reports for the actuation of fluid and particles via acoustic waves, both within sessile drops and closed channels. Other aspects of micro/nano acoustofluidics are examined: atomization, translation, mixing, jetting, and particle manipulation in the context of sessile drops and fluid mixing and pumping, particle manipulation, and formation of droplets in the context of closed channels, plus the most recent results at the nanoscale. These achievements will enable applications across the disciplines of chemistry, biology, medicine, energy, manufacturing, and we suspect a number of others yet unimagined. Basic design concepts and illustrative applications are highlighted in each section, with an emphasis on lab-on-a-chip applications.

This paper also presents a review of waveguides on lithium niobate for surface acoustic waves (SAW), including in particular the classic literature on the topic with the intent of renewing interest in them in the context of potential applications in the burgeoning discipline of micro to nano-scale acoustofluidics. From the fundamentals of the piezoelectric effect we describe interdigital electrodes and how they generate acoustic waves, consider focusing interdigital electrodes as a simple means of laterally confining the acoustic energy propagating across a substrate, and then quickly move

to waveguiding structures that provide confinement by defining either a region of slow wave velocity or a physically isolated structure. The ability to steer acoustic waves using these waveguides is considered. The many analytical, computational, and experimental tools devised by past investigators to design them are discussed in detail, as are the relative advantages and disadvantages of the waveguide designs considered over the years.

Two fabrication techniques, lift-off and wet etching, are described in producing interdigital electrode transducers upon a piezoelectric substrate, lithium niobate, widely used to generate SAW now finding broad utility in micro to nanoscale fluidics. We explicitly demonstrate the two methods of fabricating SAW devices on lithium niobate, step-by-step. Representative results for the electrode pattern deposited on the substrate as well as the performance of SAW generated on the surface are displayed in detail. Fabrication tricks and troubleshooting are covered as well. This procedure offers a practical protocol for high frequency SAW device fabrication and integration for future microfluidics applications.

Three-dimensional cell agglomerates are broadly useful in tissue engineering and drug testing. We report a well-free method to form large (1-mm) multicellular clusters using 100-MHz SAW without direct contact with the media or cells. A fluid couplant is used to transform the SAW into acoustic streaming in the cell-laden me-

dia held in a petri dish. The couplant transmits longitudinal sound waves, forming a Lamb wave in the petri dish that, in turn, produces longitudinal sound in the media. Due to recirculation, human embryonic kidney (HEK293) cells in the dish are carried to the center of the coupling location, forming a cluster in less than 10 min. A few minutes later, these clusters may then be translated and merged to form large agglomerations, and even repeatedly folded to produce a roughly spherical shape of over 1 mm in diameter for incubation—without damaging the existing intercellular bonds. Calcium ion signaling through these clusters and confocal images of multiprotein junctional complexes suggest a continuous tissue construct: intercellular communication. They may be formed at will, and the method is feasibly useful for formation of numerous agglomerates in a single petri dish.

Chapter 1

Introduction

1.1 Background

The problems and promise of microfluidics have served to motivate researchers for over twenty-five years. Small volumes, fast processing, dynamic control, low costs, and hand-held devices compete with numerous difficulties in actuation, manipulation, and eventual integration into practical devices [1]. The goal is to replace each step in a macro-scale process with a micro-scale counterpart and then to seamlessly integrate these parts without compromising the advantages, all embodied by integrated devices that can be used by non-experts. In 2014, Sackmann *et al.* [2] raised the question: *Why hasn't microfluidics seen widespread adoption?* Becker *et al.* [3] noted five years

prior to that, in 2009, that the success of any new discipline hinges upon a "killer application", and that microfluidics still lacked one. In the eight years since, much has been accomplished in the discipline, with Becker *et al.* [4] and others finally expressing a cautiously optimistic outlook.

However, an answer overlooked by many researchers is that much of the benefit of microfluidics is lost when actuation still must rely on an external bench-top pneumatic pump connected by a tangle of tubes—for example, the first figure in Whitesides' review. Such a system is difficult to operate by an expert in a laboratory, let alone a non-expert with a hand-held version. Biological assays represent one of the most important applications for lab-on-a-chip devices, yet requires mixing—difficult via traditional microfluidics where laminar flow is difficult to overcome and diffusion is glacially slow. Passive mixers [5] offer solutions in some cases, but require complex architectures. A good argument was put forth by Collins *et al.* [6]: relying on spatially and temporally distant means of pressure reduces the dynamic control one has over microfluidic processes. Finally, Sackmann *et al.* [2] point out that macro-scale technologies have likewise been advancing and, in order to compete, microfluidics must do better than simply matching the performance of larger technology for the same tasks, a sort of *red queen* [7] evolutionary problem in developing and applying microfluidics technology. In this review, we will show that the

actuation of fluids and particles via acoustic waves can overcome these hurdles and help fulfill the promise of microfluidics.

Vibration as a means to manipulate particles within fluids (and gases) has interested the scientific community since the work of Chladni*et al.* [8], Faraday *et al.* [9], and Kundt *et al.* [10]. Fluid actuation by acoustic waves is complex in analysis but simple in practice, with little hardware required to operate, and offers large actuation forces and force gradients. The seeds of acoustofluidics date from two centuries ago, and acoustics was considered a classic discipline as early as the 1960's. Few new areas of research had developed in acoustics until a recent and dramatic resurgence as a result of interesting results at small scales (*see* reviews on microscale acoustofluidics from Friend *et al.* [11], Ding *et al.* [12], Yeo *et al.* [13], and more recently Destgeer *et al.* [14]).

While some of the effects discussed in this review were known by Chladni, Faraday, Kundt, and their contemporaries, the acoustic devices available to them and fellow researchers until the 1960's were inadequate for small-scale applications. They were either underpowered, providing little more than laboratory curiosities like "quartz wind" [15], or generated ultrasound with wavelengths at centimeter to meter length scales from relatively large, inefficient, and strongly heating transducers. These devices brought with them a collection of side effects from cavitation to weak

acceleration unfortunately incompatible with micro/nano-scale fluidics.

Notably, the phenomenon of surface acoustic wave (SAW) propagation on a substrate was first reported by Lord Rayleigh in 1885 [16], but these were only properly produced with the maturation of microfabrication to form interdigital transducers (IDTs), thin finger-like electrodes formed upon a piezoelectric substrate as described by White and Voltmer in 1965 [17]. Many of the most recent reports in micro/nano acoustofluidics have relied on SAW generation at tens to hundreds of MHz, which was not possible prior to IDTs and reduces the acoustic wavelength to a scale compatible with microfluidics. There is an ancillary effect that is arguably far more significant. Because the particle velocity in typical acoustic devices is limited to around 1 m/s regardless of size or frequency due to the limitations in material integrity, selecting higher operating frequencies allows a concurrent increase in particle acceleration, to as much as 10^8 m/s^2. It is this very large acceleration that is responsible for many of the observed effects in acoustofluidics.

In this review, we first examine the piezoelectric materials that underpin this transformation in micro/nano-scale fluidics and then describe the basic device architecture used to generate acoustic waves before reviewing the most recent developments in the field. We explore mixing, manipulation of particles, translation, jetting, and atomization in sessile drops, and then consider mixing, pumping, and

particle and drop manipulation in closed channels. Nanoscale phenomena are examined as a new direction of work, and the review closes with coverage of an important observational technique, laser Doppler vibrometry.

1.2 Piezoelectric Materials and Electro-acoustic Waves

Microscale acoustofluidic actuation relies on the generation of acoustic waves in piezoelectric materials. The well-known *direct piezoelectric effect* generates electric charge upon the application of mechanical stress in certain materials; the generation of mechanical strain from the application of an electric field is the *inverse piezoelectric effect* [18]. Atoms or molecules present in the solid lattice structure of the material are either ions in the typical case [19, 20] or have strong polarization—a separation of dissimilar charges, forming an electric dipole—in the case of some piezoelectric polymers such as poly-vinylidene fluoride (PVDF) [21, 22]. In single crystal piezoelectric media formed from ions, the ions exhibit miniscule, thermodynamically favorable misalignment that forms dipoles over each unit cell of the crystal material. This misalignment tends to be identically oriented throughout the crystal, and so its effect accumulates for each repeated unit in the crystal as *polarization*, growing

to become physically significant and present in a natural state as *remanent polarization* [23]. Polycrystalline piezoelectric material exhibits similar behavior, though the orientation of the "misalignment" is unique to the *domains*, one or more of which are present in each crystal grain that forms the material [24]. An extremely large voltage is applied to polycrystalline piezoelectric material in the desired polarization direction for a few minutes to several hours while immersed in an inert fluid [25, 26] in order to reorient the polarization of each of these domains to generally lie along a particular direction. This step is necessary to form a useful piezoelectric coupling effect in any such media that lacks remnant polarization.

Piezoelectric materials have long been used to generate and detect acoustic waves. Rochelle salt and quartz were employed in the first large-scale application of piezoelectrics to acoustically detect submarines during World War I [27]. The earliest medical applications were for ultrasonic imaging of tissues in medicine [28, 29]. High-power ultrasound has been applied in industrial mixing and cleaning, applications familiar to most researchers [30, 31]. Other common uses include non-contact sensors and range-finders [32, 33]; more recently, local harvesting of energy from motion to eliminate or reduce the need for batteries have driven innovative use of piezoelectric materials [34]. The simplest of all these piezoelectric ultrasonic devices tend to be driven at resonance via planar electrodes on both faces of a flat and thin piezoelectric

element, itself polarized from one to the other planar electrode. These may be sandwiched into a rod to form a Langevin transducer [35], and rarely other modes of vibration are used, usually to generate more complex motion necessary for actuators or motors [36, 37]. Regardless of the application, the waves generated by piezoelectric media was generally limited to bulk acoustic waves (BAW) until the advent and broad acceptance of IDTs [17], which enabled high frequency SAW. The demonstration by White and Voltmer of spatially periodic thin-film metal electrodes on a piezoelectric quartz bar to produce a traveling SAW was broadly taken up by the electronics industry for use in signal processing at frequencies ranging from 10 MHz to 1 GHz. "True" SAW or Rayleigh waves are confined within three to four wavelengths of the surface of the material. Leaky SAW (LSAW) [38], Love waves [39], Bleustein-Gulyaev waves [39], surface skimming bulk waves (SSBW) [40], and surface transverse waves (STW) [41] are generally categorized as pseudo-SAW (PSAW), may have some limited applications in acoustofluidics, but mainly lie outside the scope of this review.

In order to generate high frequency acoustic waves, a panoply of piezoelectric materials have been used over the last 50 years. Polycrystalline piezoelectrics can be fabricated in more and simpler ways and have greater electromechanical coupling coefficients than single crystalline piezoelectrics, implying a greater ability to transform energy from one form to the other. However, single crystal materials have higher

quality factors, and lower damping than polycrystalline materials, and so the choice of material in a given application is not straightforward [42]. Single-crystal piezoelectric media are however generally compatible with microfabrication facilities whereas, for example, lead zirconate titanate (PZT) [43], the most common polycrystalline ceramic piezoelectric material, is not. Furthermore, PZT is toxic, with significant excess lead oxide present along the grain boundaries [44], and facing regulations that aim to eliminate it from use [45]. There have been some successes in eliminating lead while retaining good performance from polycrystalline ceramics, most notably those derived from potassium sodium niobate (KNN) [46]. The granular nature of polycrystalline piezoelectrics limits their use to relatively low frequencies ($\mathcal{O}$(1 kHz–1 MHz)) due to the finite size of the grains and domains within the material that strongly interact with the generation and propagation of acoustic waves at greater frequencies to generate heat [47]. Though some researchers over the years have synthesized polycrystalline ceramic piezoelectric materials with submicron grain size in an aim to increase the useful frequency range to 100 MHz or more [48], these materials have not been widely employed. The likely reason is the existence of single crystal materials that operate at high frequencies ($\mathcal{O}$(1 MHz–1 GHz)) with superior characteristics.

The materials most popularly used to make SAW devices include quartz,

lithium tantalate (LT, $LiTaO_3$) and lithium niobate (LN, $LiNbO_3$). Others include gallium arsenide (GaAs), cadmium sulfide (CdS), zinc oxide (ZnO), lithium tetraborate ($Li_2B_4O_7$), and langasite ($La_3Ga_5SiO_{12}$) [49]. All piezoelectric materials are anisotropic, and because these choices are especially so, the type of wave generated from them is strongly dependent on the material orientation. White and Voltmer [17] used a Y-cut, Z-propagating quartz plate. Shortly after, in the late 1960's Bell Laboratories were credited for the development of lithium tantalate (LT) and lithium niobate (LN) which exhibit significantly stronger electromechanical coupling coefficients than quartz [50, 51]. Due to its exceptionally high coupling coefficient relative to other single crystalline materials for SAW, LN has become ubiquitous for this application. Typically, wafers are obtained by growing a boule (*see* Fig. 1.1) of LN from a seed crystal with the desired orientation, which is cut into wafers of the required thickness.

Initially, SAW devices were designed so that waves propagated along the symmetric crystal axes. Later on, as enhanced properties along different rotated cuts were discovered, these cuts gained popularity in various applications. In particular, the Y-cut, Z-propagating orientation of LN (YZ LN) was extensively used for SAW filters requiring Rayleigh waves. Due to the dependence of wave velocity on the propagation direction in an anisotropic material like LN, waves in rotated cuts

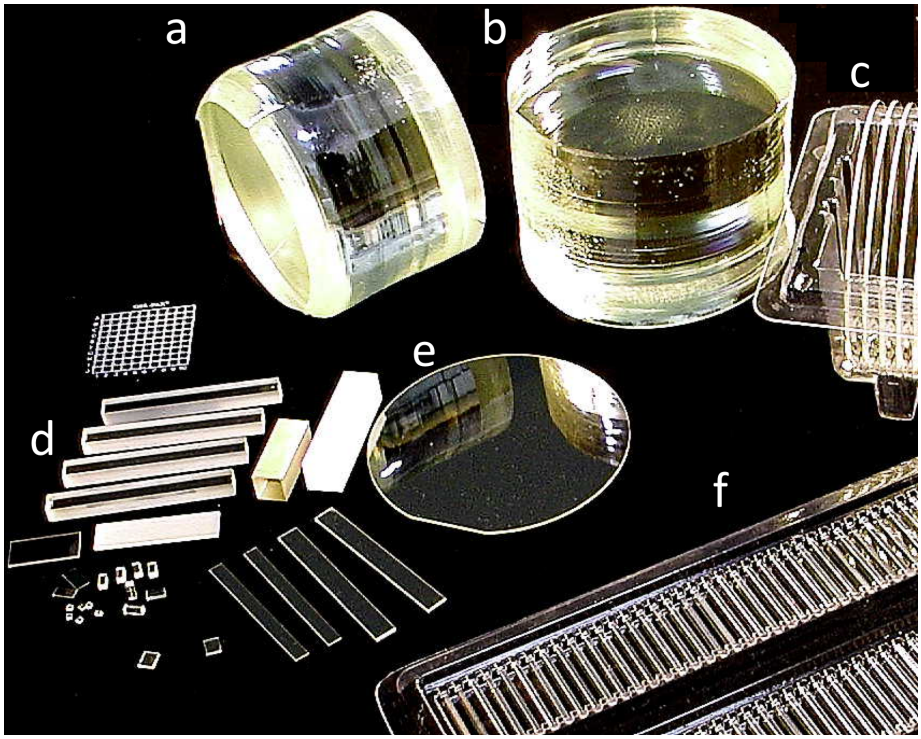

Figure 1.1: (a, b) A boule of LN, (c,e) with wafers and (d,f) other shapes cut for typical applications. *Image provided by Precision Micro-Optics, MA, USA.*

propagating in a direction not aligned with a principal axis in the material translate laterally in a phenomena known as *beam steering* [52]. With further studies, particularly the works of Takayanagi *et al.* [53] and Slobodnik *et al.* [54], the 131° Y-rotated cut of LN was found to have exceptional electromechanical coupling and low beam steering and became widely used. However, this cut exhibited spurious parasitic waves, and in 1976, Shibayama *et al.* determined that the 127.86° Y-rotated cut reduced the generation of these parasitic waves and consequently had the highest electromechanical coupling coefficient and lowest insertion loss [55]. The 127.86°

Y-rotated X-propagating cut of LN (128° YX LN) became the most popular and widely accepted orientation for applications requiring Rayleigh waves. Other cuts of LN have even higher electromechanical coupling coefficients, but these produce spurious modes and beam steering that preclude them from applications requiring "true" SAW. Among the other cuts, the 36°, 41°, and 64° Y-rotated cuts are the most popular. Table 1.1 lists some of the best-known cuts of LN and their electromechanical coupling constants, where $K^2 = 2\Delta v/v = 2\left(v_f - v_m\right)/v_f$. Here, v_f is the wave velocity in the free substrate and v_m is the wave velocity measured along a short-circuited plane.

Table 1.1: Commonly used cuts of LN and their corresponding electromechanical coupling coefficients and velocities. Reproduced with permission from Shibayama *et al.* [55], Campbell [56], Ciplys *et al.* [57], Soluch *et al.* [58] and Hickernell *et al* [59].

Cut	$2\Delta v/v$ (%)	Velocity (m/s)
YZ[57]	4.82	3488
ZX[57]	0.53	3798
ZY[57]	2.25	3903
XY[57]	3.58	3748
20° XY[58]	1.6	3727
120° XY[58]	4.1	3403
XZ[57]	5	3483
YX[57]	1.54	3769
36°[56] YX	16.7	4802
41° YX[59]	17.2	4752
64° YX[59]	10.8	4692
128° YX[55]	5.3	3992

Evidently, the 41° and 64° YX cuts of LN have higher electromechanical

coupling coefficients than the 128° YX, however, these generate PSAW and not "true" SAW/Rayleigh waves. Cuts that produce non-Rayleigh SAW have been used to make SAW resonator filters[60] (64° YX) and delay lines for liquid sensors[61] (41° YX) among other applications.

The majority of research conducted with SAW for microfluidics has utilized 128° YX LN. Recently, there have been some studies which demonstrate the use of X-cut LN [62]. Materials most commonly used in acoustofluidics are anisotropic in nature due to their crystal structure. The 128° YX and X-cut LN, for example, can generate SAW of the same frequency and amplitude only in one direction. Any veering from the primary propagation direction is affected by beam steering and changes in frequency and electromechanical coupling coefficients. Kurosawa *et al.* [63] demonstrated this for a two-axis motor made using the 128° YX LN wafer, showing that the vibration displacement and velocity were 200% higher in the X-axis propagation direction compared to the Y-axis propagation direction. In order to overcome the anisotropic nature of the substrate, Guo *et al.* [64] and Devendran *et al.* [65] demonstrated perpendicular IDT pairs at 45° to the X-axis to create an orthogonal standing wave of the same frequency. However, the issue of *beam steering* remains. The superior electromechanical coupling present along the X axis and the unmatched wave velocities along the X and Y axes contribute to wave propagation

with a lateral component. As a result, high frequency SAW devices made using LN substrates are limited to a single direction for acoustic wave propagation if optimal performance is desired.

1.2.1 Acoustic Wave Measurement

A laser Doppler vibrometer (LDV) is an interferometer that uses the Doppler effect to measure vibrations. When light encounters a moving surface, the reflected light incurs a frequency shift depending on the velocity of the surface and the wavelength of the light. In an LDV, the laser is split into a reference beam, directed straight to the photodetector; and a measurement beam, which reflects off the vibrating surface before being combined with the reference beam at the photodetector. This superposition creates a modulated signal, thus revealing the Doppler shift in frequency (*see* Fig.1.2). Signal processing and analysis provide the vibrational velocity and displacement of a point on the surface in the direction normal to the surface. The in-plane motion can be measured using a different configuration where two measurement beams impinge on a spot with an angle between them, thus yielding interference fringes, though other methods exist [66]. As well, the LDV can be operated in scanning mode so that sequential measurement at many points reveals the vibrational motion of a portion of the surface with desired resolution. These and

other advances are covered by Castellini *et al.* [67] and a more recent review was published by Rothberg *et al.* [68].

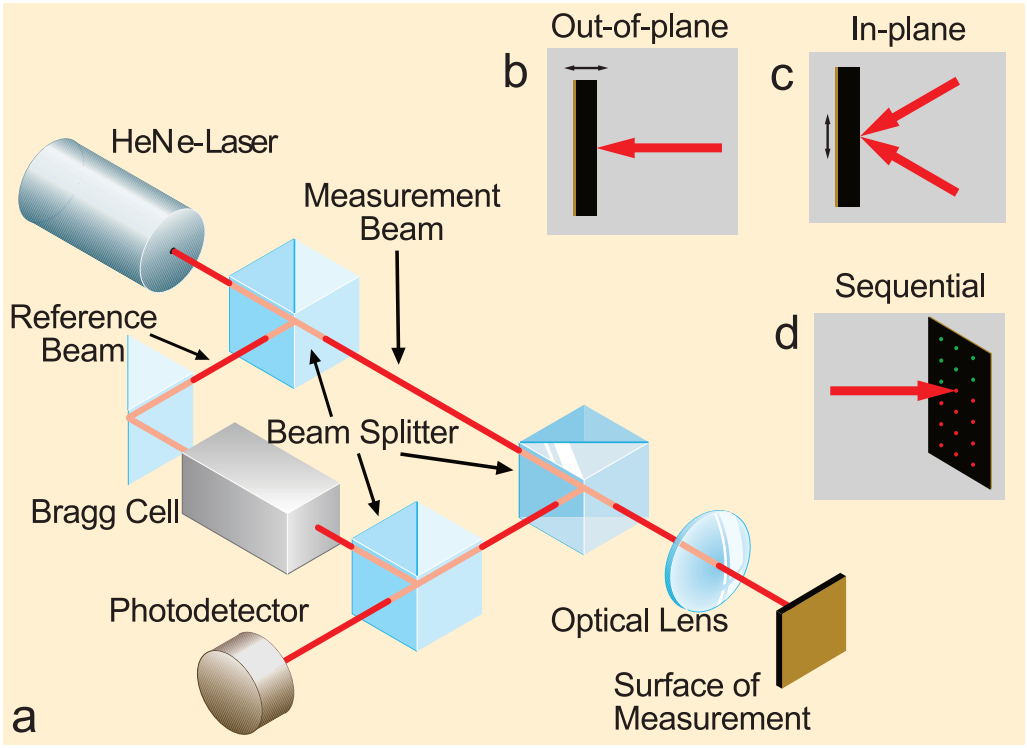

Figure 1.2: a) The interaction of the reference and measurement beams to produce a Doppler shift at the photodetector in this configuration of a Polytec laser Doppler vibrometer. b) Out-of-plane vibration measured by a single beam normal to the surface. c) In-plane vibration measured by two beams aimed at the same point with an angle between them. d) Sequential measurement, which is used to obtain the vibration of the surface in phase.

The LDV has been extensively used in aerospace [69], automotive [70], and hard disk drive [71] industries, and for land-mine detection [72]. The technology has also been broadly accepted for use in microelectromechanical systems (MEMS)

applications [73]. In the context of acoustofluidics, the LDV is well-suited to measure and characterize vibrational motion in the solid surfaces of devices. While the primary aim is usually the determination of the resonance frequencies and mode shapes of the devices (*see* Fig. 1.3, the LDV can also be used to identify the type of waveform obtained: Lamb, SAW, BAW, Love, etc. The piezoelectric coefficients (as discussed in Section 1.2) of materials used in acoustofluidics can also be measured with remarkable accuracy [74]. Due to the high frequencies and small amplitudes involved (especially in SAW), measurement of the vibration driven velocity has been vital for analytical validation which would otherwise be impossible at the micro/nano scale. This capability has been particularly useful for characterization of nanofluidic devices [75] and cantilevers for atomic-force microscopy (AFM) [76]. The technology can also be applied to identify vibrations on fluid surfaces [77] and even in air flow [78]. This capability has been helpful in studying fluid atomization and particularly in confirming the absence of the well-known Faraday wave response at half the excitation frequency [79].

The technology has some limitations and prevailing issues. The choice of interferometer design has important implications for the sensitivity and measurement range of the LDV, especially in scanning mode. For example, the Sagnac design is inherently more mechanically stable than others due its lack of moving parts (more

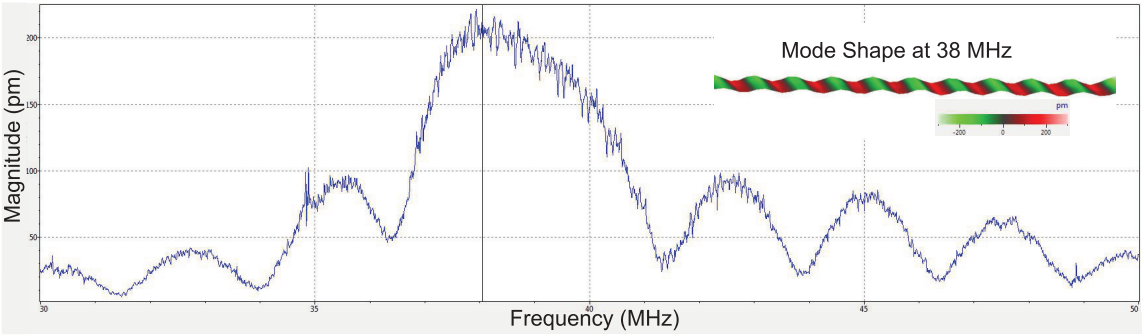

Figure 1.3: The resonance mode of a SAW device is revealed by this graph of amplitude vs frequency at a single point over an averaging period while the device is driven with a multi-frequency signal. Once this resonance is known, a sequential measurement over a region of the surface while the device is driven a the resonance frequency reveals the vibration mode, SAW in this case.

detail on this topic was provided by Tachizaki [80]). Non-ideal behavior of the interferometer has been known to lead to significant error when measuring small displacements. This and other sources of error, particularly alignment-based error, are covered by Siegmund [81]. Unwanted light waves can interfere with the desired interaction between the reference and measurement beams—known as three-wave interference—but the artifacts of this can be predicted [82]. The vibration of rotating objects and the in-plane motion can likewise be measured, but the setup is relatively complex [83].

Digital holographic (DH) microscopy has been investigated as an alternative to LDV. Data from a high density of points can be obtained simultaneously using DH but, so far it lacks the ability to provide continuous (non-stroboscopic) measurements

at frequencies greater than 1 MHz. Poittevin *et al.* [84] provide a good introduction to the interested reader. He highlight two new papers in this area as indications of what may follow in the future. Leclercq *et al.* [85] demonstrate the ability to measure three dimensions of displacement in acoustic waves traveling in a solid simultaneously using three-color DH. Typically, particle tracking is accomplished by optical videography and particle image velocimetry (PIV), but Cacace *et al.* [86] have applied DH to track particles in 3D that are moving under acoustophoresis. In the future, digital holography may enable new insights into previously well studied acoustofluidic phenomena.

1.2.2 Electronic Communication

The first widespread use of SAW was in wireless communication, playing a critical role in that industry to this day [87]. As filters and duplexers, they provide precise and sharp signal filtering and multiplexing [88, 89]. These aspects are relevant to the lab-on-a-chip community for two reasons. First, they demonstrate applications where, like lab-on-a-chip devices, space is at a premium in handheld devices. Second, they indicate potential future routes of research in acoustofluidics lab-on-a-chip applications in analogy to the development of the technology for communications.

The working principle of SAW filters for communication [90] is illustrated in

Fig. 1.4. An IDT (receiver) transfers the incoming electrical signal into SAW by the inverse piezoelectric effect [91], where approximately 90% of the energy is transmitted in mechanical form and the remainder is transmitted in electrical form to the output transducer (transmitter), where the SAW is converted back to an electrical signal via the direct piezoelectric effect. The IDT design determines the characteristics of the SAW receiver-transmitter combination: a *filter*. The same basic principle has been used for SAW based biosensors, to be discussed in Section 1.4.2. The typical frequency response of a SAW filter is shown in Fig. 1.4(b). The desired signal shows least attenuated while the rest of the signals are strongly attenuated. This sharp filtering and high selectivity is what makes SAW filters popular in the wireless communication industry [91, 88]. Fig. 1.4 shows the typical frequency response of a SAW duplexer, essentially a combination of two or more SAW filters [92] that provide one-way paths from the transmitter to the antenna to the receiver. The effort made in this discipline solved telecommunications problems at remarkably high frequencies, 1–100 GHz, and laid the groundwork for micro/nano acoustofluidics devices appearing today.

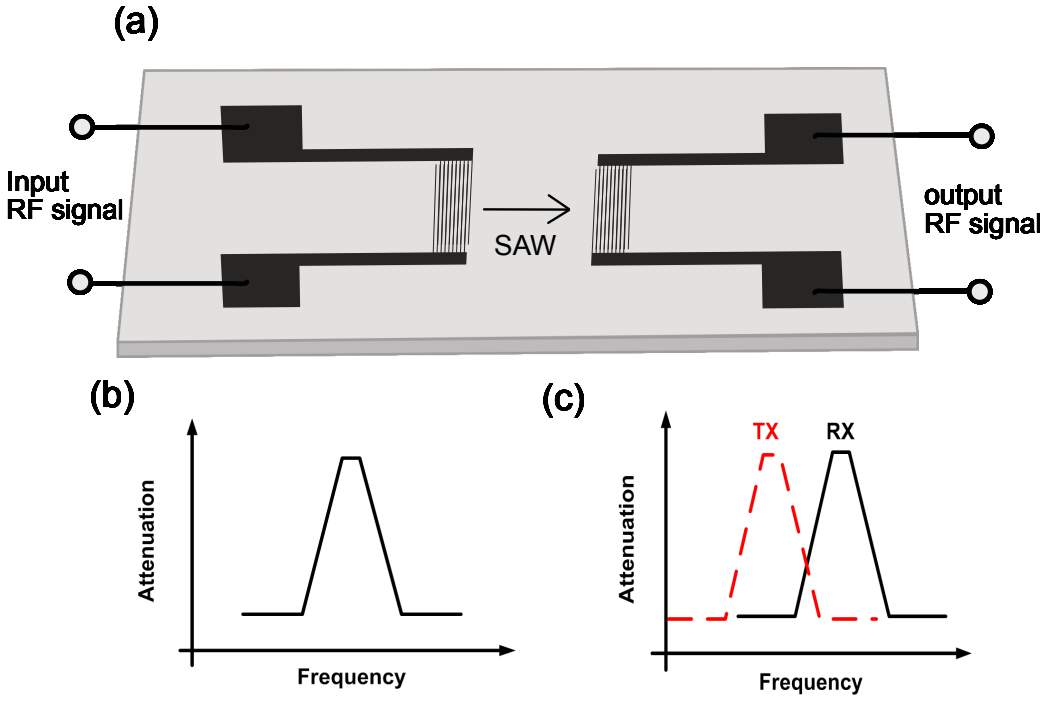

Figure 1.4: (a) The working principle of SAW devices in communication. A pair of IDTs are usually included, functioning as an input source (receiver, Rx) and output source (transmitter, Tx), respectively. Typical frequency characteristics of (b) Typical characteristics response of a SAW filters, and (c) SAW duplexers with similar characteristics as SAW filters shown to pass the signals at two different frequencies for cellular applications.

1.3 Electrode Design

Most acoustofluidic devices use either very simple thickness mode transducers are photolithographically patterned IDTs, which sometimes require complex microfabrication. Below we highlight two notable exceptions. Rezk *et al.* proposed a low cost alternative to photolithographic IDT fabrication. Aluminum foil electrodes

were simply cut with scissors and clamped in place on a LN substrate to produce a Lamb wave device capable of producing flow in a channel, mixing in a drop, and atomization from a drop [93]. It is likely that this type of electrode will significantly reduce performance due to poor electrical and mechanical contact, but may still be useful for some applications where cost and complexity are extremely limiting. Another alternative to expensive microfabrication was demonstrated by Nam *et al.* [94] in the form of patterned conductive liquid, but this method was able to produce IDTs for SAW rather than Lamb waves. Nam fabricated channels in PDMS taking the negative shape of the intended IDT design and these were then filled with eutectic gallium indium. Azimuthal flow was achieved at 162 mW and colored dye could be mixed with a viscous, 25% glycerin solution within 1 second using 578 mW of power.

The substrate thickness is an important factor in IDT design, as it determines the minimum frequency of the SAW. Most suppliers provide 500 μm thick wafers, and the Rayleigh SAW is known to extend 4–5 λ into the substrate. This places a lower limit on the frequency suitable to form true Rayleigh SAW of about 40 MHz. Using frequencies below this value cause the acoustic wave to penetrate all the way through the substrate to the other side forming, alongside Rayleigh SAW, spurious Lamb waves that can shed energy through the back side of the substrate into its mounting and affecting the wave propagation and device performance. This is not

merely a theoretical problem, as we have seen (in unpublished work) strong fluid transport in 20 MHz shear-horizontal SAW (SH-SAW) devices that should show no fluid transport at all. The 36° Y-rotated, X-propagating lithium tantalate cut used in this case also generated Lamb waves that appeared to be responsible for the confusing observations.

More importantly, much of the literature reports the generation of SAW at frequencies well below 40 MHz without noting or apparently being aware that this problem could arise. In our case, we were forced to use 20–30 MHz SAW for many years due to limitations of our laser Doppler metrology equipment, and fortunately this problem no longer exists.

In order to realize full miniaturization and widespread adoption, SAW microfluidics will require high power efficiency. Winkler *et al.* laid out the most important efficiency drains in these devices and proposed engineering solutions [95] (*see* Fig. 1.5). They covered optimal electrical impedance through IDT design, use of unidirectional IDTs, passive matching circuits, passivation and electrical shielding for submerged devices, and choice of wavelength based on geometry. Many of these solutions were utilized in a recent paper [96] demonstrating an atomization specific device, which will be discussed in section 1.4.2.

Heating occurs in acoustofluidics since energy must inherently be dissipated

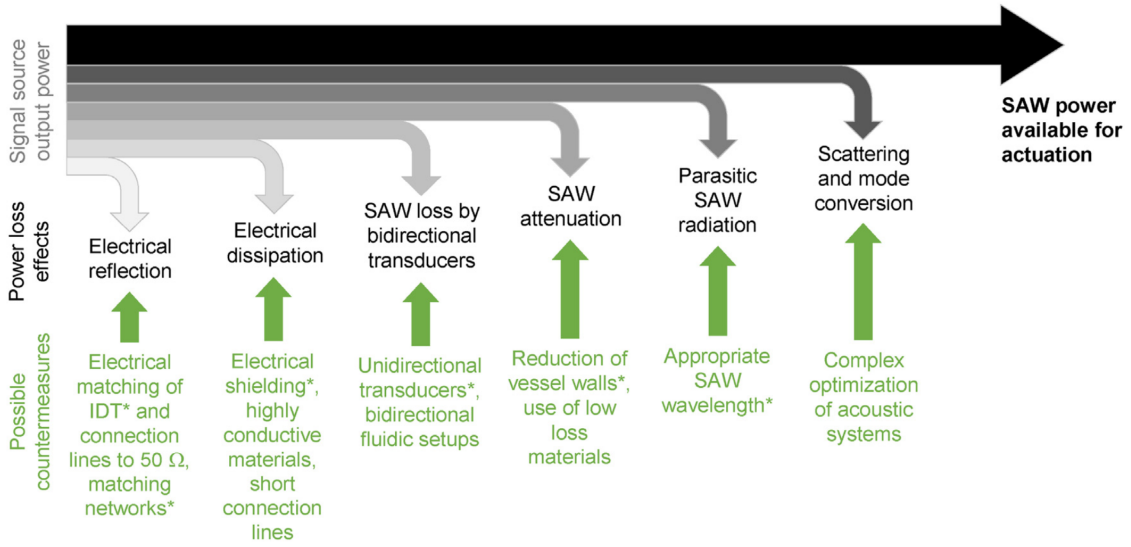

Figure 1.5: Power drains in typical SAW microfluidic devices along with proposed engineering solutions. Reprinted from Winkler *et al.* [95]

on chip in order to produce fluid and particle motion and resistive heating can be minimized or controlled but never eliminated. This is sometimes considered an issue (*e.g.,* evaporation in digital microfluidics), but can be controlled to support additional functionallity. Shilton *et al.* described the progress made in studying and using acoustofluidic heating, for example in PCR, in their paper on controlling and optimizing this phenomena [97]. Drops could be reliably heated to a stable temperature up to 12 degrees above room temperature within 3 seconds. The temperature increase was precisely controlled by the frequency and power. This heating was decoupled from the spurious resistive heating due to the IDT.

1.3.1 Straight IDTs

SAW are typically generated by applying an oscillating electrical signal matching the resonant frequency of the IDT. This signal translates into an acoustic wave via the inverse piezoelectric effect as described earlier. In the literature, frequencies in the range 1 MHz–1 GHz have been used in the study of acoustofluidics, which correspond to wavelengths between 200 and 4 μm for the case of 128° YX LN, implying a range of feature sizes of 50 to 1 μm. These feature sizes are typically microfabricated by photolithography and lift-off [98].

The first and simplest IDTs [17] consisted of straight rectangular metal bars—referred to as fingers—deposited onto the surface of a piezoelectric substrate and alternately connected on either end to contact pads or "bus bars" as pictured in Fig. 1.6. This structure creates an array of electric fields of alternating direction between the transducer finger pairs that in turn create, via the inverse piezoelectric effect, alternating regions of compressive and tensile strain in the substrate. Each finger pair thus produces displacement in the substrate that oscillates with the electric field and radiates a SAW [17]. The periodicity of the finger pairs defines the wavelength of the resulting SAW (λ_{SAW}) such that the distance from one finger to the next is $\lambda_{\mathrm{SAW}}/4$. The surface wave velocity (v_R) depends on the material properties of the substrate, the propagation direction, and the thickness of the IDT. Consequently,

the center frequency ($f_r = \omega/2\pi = v_R/\lambda_{\mathrm{SAW}}$) of a given device is determined by the choice of substrate, propagation direction, and IDT design [99, 17].

The thickness of the metal film that comprises the IDT, h, is typically chosen so that the film thickness ratio $h/\lambda_{\mathrm{SAW}} \approx 1\%$ so as to strike a balance between the efficient transmission of electric current in thicker films and the lower mass present upon the substrate for thinner films. Excessively thin films can cause premature finger failure and localized heating from ohmic losses [100], while excessively thick or heavy films can reduce the resonance frequency of SAW in the IDT region compared to the surrounding region that have no fingers, unintentionally producing an acoustic cavity. Slightly thicker films, $h/\lambda_{\mathrm{SAW}} \approx 1\%$, are optimal in most cases for reflectors, structures that appear similar to IDTs but act to reflect the SAW on the piezoelectric surface to form an acoustic cavity or improve the device's efficiency. The details of IDT finger design, and the closely related details of SAW reflector design, are provided in substantial detail in Morgan *et al.* [91] and references therein.

As the SAW propagates through subsequent finger pairs, the wave is diffracted, creating a near-field region of largely parallel wavefronts known as the Fresnel region. The far-field region, where the SAW is broadly diffracted along major and minor lobes, is known as the Fraunhofer region. To minimize diffraction losses, the aperture of the IDT must be contained within the Fresnel region. For design pur-

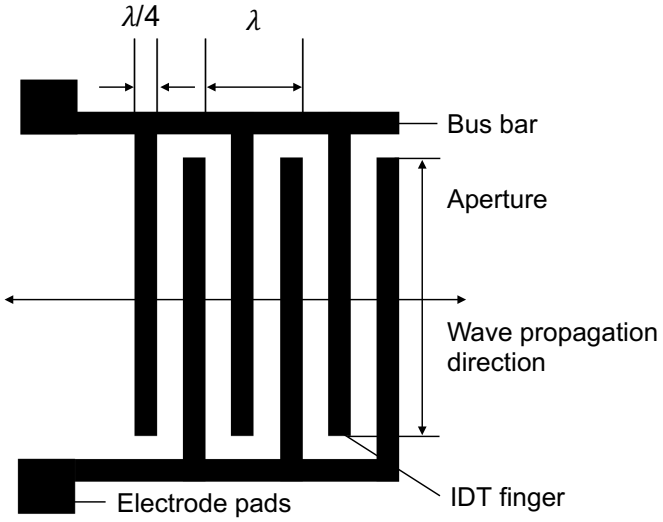

Figure 1.6: A SAW device consisting of comb-like interdigital transducers (IDT fingers), bus bars, and electrode pads on a piezoelectric substrate (*e.g.,* 128–YX LN). The resulting traveling wave propagates as shown (perpendicular to the fingers), which can be observed using a laser Doppler vibrometer (LDV). The periodicity of the finger pairs defines the wavelength of the resulting SAW, λ_{SAW}.

poses, a Fresnel parameter (F) is defined as $F = 4\lambda_{\mathrm{SAW}} D_F / a^2$ where a is the aperture width (shown in Fig. 1.6) and D_F is the distance from the IDT edge. To remain within the Fresnel region, the aperture should be selected such that $F < 1$.

The efficiency of a SAW device is commonly linked to its quality factor [101], $Q = f_r / \triangle f$, where $\triangle f$ is the width of the resonant peak in frequency space measured at one-half the peak's highest amplitude. The quality factor is influenced by dielectric losses of the piezoelectric materials, loading effects, ohmic losses, and acoustic leakage to the substrate. The number of finger pairs (N_p) of a SAW IDT is an important

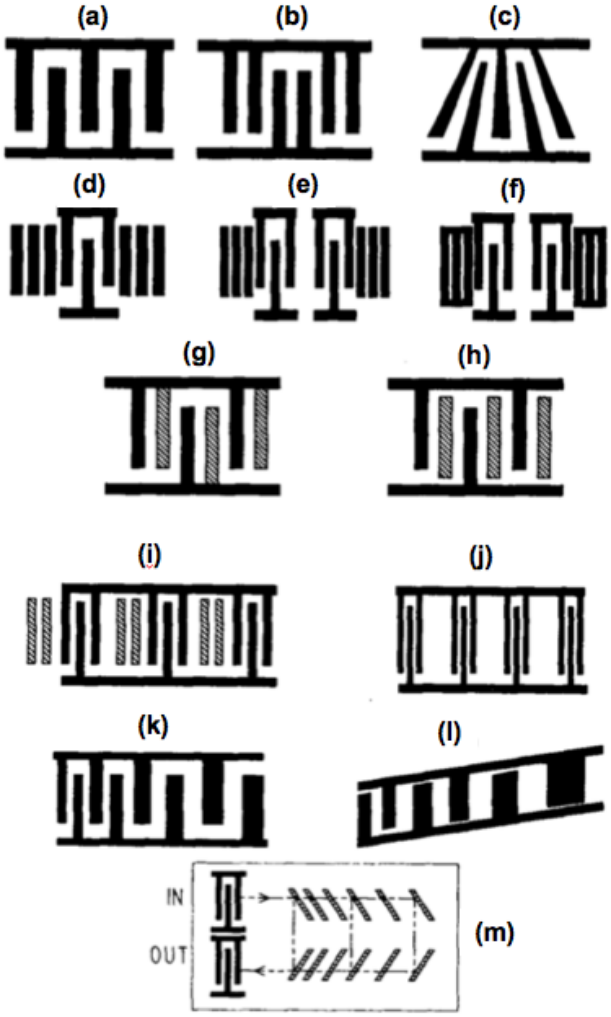

Figure 1.7: Common IDT designs for SAW devices: (a) single electrode IDT, (b) double electrode IDT, (c) slanted-finger IDT (SFIT) on collimating substrate shown with exaggerated tilt, (d) one-port resonator, (e) two-port resonator with open-circuited reflection-grating elements, (f) two-port resonator with short-circuited reflection-grating elements, (g) double-metalization single- phase unidirectional transducer (SPUDT), (h) floating-electrode SPUDT,(i) Lewis-type SPUDT,(j) "conventional" comb-filter, (k) chirped IDT, (i) chirped IDT for slanted-array compressor (SAC), and (m) geometry of a reflective array compressor using etched-groove reflectors. Reprint permis. Campbell (1989) [88].

parameter partially due to its effect on the quality factor [91]. The other aspect that drives the choice of the number of finger pairs in a SAW IDT is the effective piezoelectric coupling coefficient of the substrate, which can be defined in terms of the change of SAW velocity from an open-circuit configuration to a short-circuit configuration, divided by one-half of the average of that velocity, $2\Delta v/v$. The greater the coupling, the greater the amount of energy that can be transduced in the IDT to mechanical output as a SAW. The amplitude of the SAW increases with N_p up to a material dependent limit, but the bandwidth is likewise reduced. In signal processing applications, optimizing N_p is a complex procedure [91]. However, when the primary concern is transduction power alone, typical in acoustofluidics, the constraints are simpler. For example, the bandwidth must only be sufficent to allow the device to be driven by signal generation and frequency response analysis equipment.

Optimization begins by defining the electrical admittance ($Y_t(\omega)$) of the IDT, which is dominated by capacitance (C_t), conductance ($G_a(\omega)$), and susceptance ($B(\omega)$), as in $Y_t(\omega) = G_a(\omega) + j(\omega)B(\omega) + j(\omega)C_t$. The equivalent circuit therefore consists of three components in parallel. When a voltage (V) is applied to the transducer, the power that is absorbed and produced are respectively defined as

$$P_a = \frac{1}{2} G_a V^2 \tag{1.1}$$

and

$$P_s = \frac{1}{4}\omega\epsilon_\infty a N_p^2 \left(\frac{\triangle v}{v}\right)\left(\frac{\sin(x)}{x}\right)^2, \tag{1.2}$$

where ϵ_∞ is the capacitance per period of a unit-aperture, single electrode transducer, which depends on the substrate. At a certain frequency, the susceptance becomes negative and begins to counteract the capacitive term. When these terms cancel out, the admittance becomes real and directly corresponds to a resistive load, and also corresponds to the most efficient operation of the IDT. This occurs when the following equations are satisfied: $N_p = v\pi Q_t/2\triangle v$ and $\triangle f/f_r = 1/N_p$. Therefore, N_p=21 for a single electrode IDT, as in Fig. 1.7(a), with a bandwidth of 0.05, while $N_p = 26$ for the double electrode IDT with a bandwidth of 0.038 on 128° YX LN (*see* Fig. 1.7 (b)).

Figure 1.7 depicts other commonly used IDT designs to fit different design requirements. The double electrode IDT (*see* Fig. 1.7(b)) eliminates the in-phase reflections produced by standard, single electrode IDTs by producing 180° phase shifted reflections that cancel out. The electrode sampling frequency changes from $2f_r$ to $4f_r$. Ma *et al.* [102] presented a self-aligned method to fabricate double electrode IDTs. The slanted-finger IDT (SFIT) (*see* Fig. 1.7(c)) is used to generate a wide-band response filter. The maximum angle that can be achieved depends on the coupling coefficient of the substrate. For example, the limit for a YZ LN substrate

is 7° due to beam steering losses. The chirped IDT (*see* Fig. 1.7(k)) has a linear gradient in finger spacing that allows it to resonate at a wide range of frequencies, allowing the excitation of SAW at different wavelengths by tuning the input signal. Another common method of reducing SAW efficiency loss due to in-phase reflection is by adding reflectors, as shown in Fig. 1.7 (d), (e), and (f). The reflectors are typically the same size as the fingers and are offset by one wavelength from the fingers. Finally, to decrease the reflection loss from a source or finite impedance, a single-phase unidirectional transducer (SPUDT) design is used to cancel out those reflections (Fig. 1.7(g)-(i)) [103, 56]. Normally waves radiate in both directions from an IDT, but SPUDTs radiate in only one desired direction, towards the right in Fig. 1.7.

1.3.2 Focused IDTs

Compared to the designs described in Fig. 1.7, focused IDTs (FIDTs) can generate SAW with higher intensity by laterally focusing the SAW energy towards the main axis of the IDT, producing what is called a higher beamwidth compression ratio, $\eta_c = W_b/w$, where W_b is the -3 dB transverse bandwidth and w is the equivalent aperture of the FIDT. They have been utilized in many applications, such as signal processing convolvers [104, 105, 106], storage correlators [107], and time-

Fourier transformers [108]. High intensity acoustic fields can also be generated, and thus enhance the acoustic-electric effect in order to manipulate electron-hole pairs in GaAs quantum wells [109]. Later in this review we will see examples of their use in acoustofluidic devices.

The FIDTs were first introduced by Kharusi *et al.* in 1972 [110]. They proposed a structure that consisted of a series of identical curved fingers, so-called conventional circular-arc-shaped FIDTs (*see* Fig. 1.8(a)), which focus the waves into a narrow rectangular region along the X propagation axis. They discovered that the degree to which the waves were focused and the focal length depended on the anisotropy of the substrate. Their results matched Cohen *et al.*'s finding [111] that the focal length is given by $R_f/(1-2b)$, where R_f is the finger curvature and b represents the anisotropy of the substrate material ($b = 0$ for an isotropic substrate). In addition, they emphasized that the focusing properties of conventional circular-arc-shaped FIDTs do not improve as N_p is increased. Therefore, this type of FIDT was suggested to not be used on a highly anisotropic material, such as LN. In the 1980s, Fang *et al.* [112] calculated the amplitude field of circular-arc-shaped FIDTs on YZ LN and confirmed that the acoustic energy could be focused into a long, narrow region about the propagation axis on a substrate with high anisotropy (*see* Fang *et al.* [112], Fig. 1.8). Their results showed the beam compression ratio to be

about 3% at a distance farther than R_f, which coincided with their experimental data. An important discovery in their work was that the actual focal point for SAW generated from a given set of fingers in the FIDT did not correspond with the geometric focal point. The anisotropy of the substrate typically causes the actual focal point for the SAW to lie up to two times farther away from the IDT than the geometric focal point.

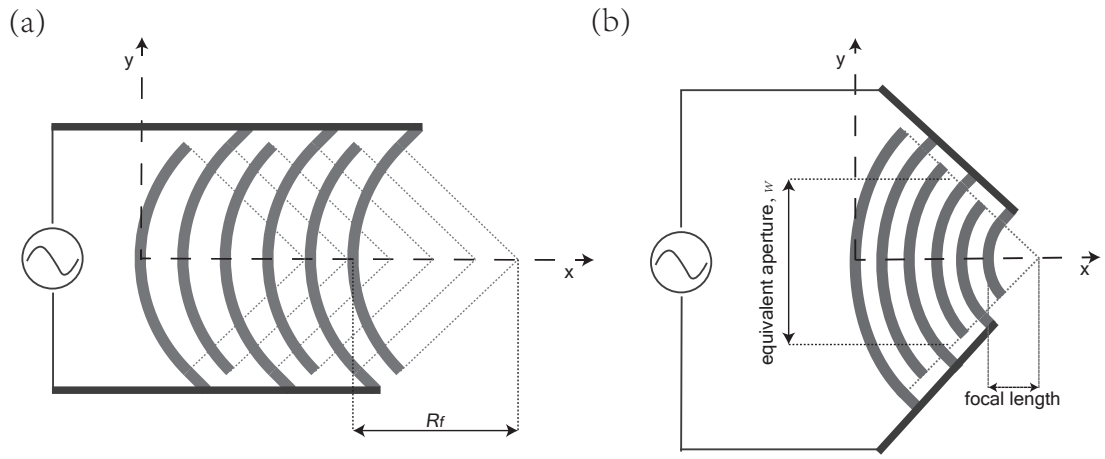

Figure 1.8: Commonly used FIDTs designs: (a) conventional circular-arc structure (characterized by R_f as curvature of transducer finger) and (b) concentric circular-arc structure (characterized by w as equivalent aperture). It shows clearly that the concentric design focuses to a point instead of a narrow region, resulting in better focusing property.

More recently, an alternative FIDT design was investigated by Wu *et al.* [113, 114] consisting of a series of concentric fingers (*see* Fig. 1.8(b)) that focus the waves to a single spot. These concentric-arc-shaped FIDTs produce higher SAW in-

tensity and beamwidth compression ratios than the conventional circular-arc-shaped FIDTs. The intensity of the SAW is proportional to N_p^2—much stronger than the N_p dependence of a straight IDT with an equivalent aperture. So as N_p increases, concentric-arc FIDTs display a stable amplitude field and better focusing characteristics while the conventional circular-arc FIDTs become unsteady. Moreover, increasing the curvature of the arc does not increase the amplitude, but it does increase the compression ratio, according to Wu *et al.*'s data.

Like the traditional FIDT design, modified circular-arc FIDTs exhibit an actual focal point farther away than the geometric focal point due to the anisotropy of the material, as was discussed earlier in the section. Positive values of b in $R_f/(1-2b)$ tend to defocus the transducer, while negative values of b bring the focal plane closer toward the transducer. Shilton *et al.* [115] experimentally showed that a concentric-circular FIDT focused to a point $\sim$1.7 times farther than the geometric center (*see* Fig. 1.9 (d)). This agreed with earlier work in which Wu *et al.* [114] measured the amplitude vs propagation distance of various configurations of concentric FIDTs and concluded that the actual focal length was $\sim$1.5–1.8 times greater than the geometric focal length. Work done earlier by Kharusi *et al.* [110] recognized this phenomena and suggested another type of FIDT design, the group-velocity surface shape. This type of shape, as its name indicates, consists of points tracked by the

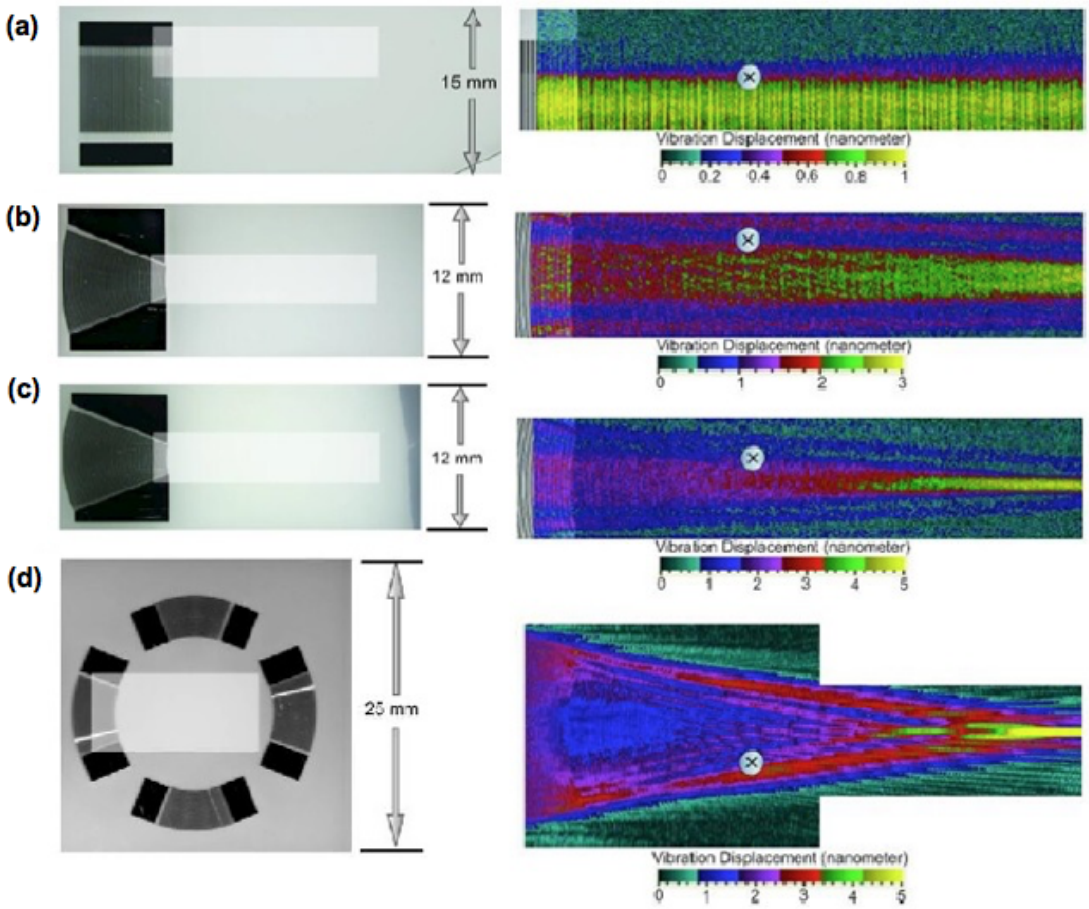

Figure 1.9: The distribution of SAW displacement on a LN substrate of different IDT designs at a center frequency of 30 MHz: (a) straight SPUDT, (b)&(c) focusing elliptical SPUDTs with approximate eccentricities of 0.616 & 0.831 respectively, and a (d) focusing circular SPUDT. It shows that the displacement of the SAW produced by straight SPUDT is uniform on the substrate, a line parallel to the propagation direction for the elliptical SPUDTs, and a single point with a circular SPUDT. Reprint permis. Shilton (2008) [115].

end of the energy velocity vector and ensures that waves are focused to a single point despite the dependence of wave velocity on propagation direction in an anisotropic material. The group-velocity surface pattern would become identical to the circular-arc pattern in the case of an isotropic surface. Further investigation by Wu *et al.* [113, 114] revealed that this shape is indeed a superior focusing structure, producing a higher intensity and beam compression ratio than the concentric circular-arc shape. An efficient application of this group velocity design was reported by Laude *et al.* [116], as they constructed the IDTs in an fully annular shape following the wave surfaces for Y cut and Z cut LN. The generated SAWs were experimentally proven to greatly overcome the anisotropy of the piezoelectric substrates and converge to an intense spot at the center.

Besides curved and annular shape of FIDTs, there are more advanced designs worth mentioning. Riaud *et al.* [117] proposed an IDTs array (IDTA), which consisted of 32 unidirectional slightly curved IDTs placed along the wave surface of the substrate to compensate for beam steering. By tuning the input signal of each IDT using the inverse filter method [118], the IDTA was reported to be able to not only focus the waves at an arbitrary position, but also generate swirling SAWs, with an even higher intensity at the center. Later on, an alternative design, called the single spiraling IDTs, was introduced by the same group [119], *see* Fig. 1.10, which

encoded the SAWs like a hologram and induced acoustical vortices when there was fluid on the surface. Applications of these SAW devices will be further discussed in subsection 1.4.2.

Efforts have been made to visualize the amplitude field generated by FIDTs. Tan *et al.* [120] were able to directly visualize SAW using smoke particles with a mean diameter of 250 nm. The large transverse surface accelerations generated by SAW carry these particles aloft to relatively low vibration regions (*see* Fig. 1.11). Furthermore, Shilton *et al.* [115] showed SAW propagation patterns generated on a 128° YX LN surface for a straight SPUDT, concentric-elliptic SPUDTs with various eccentricities, and a concentric circular SPUDT by scanning the surface with an LDV (*see* section 1.2.1). Their results (*see* Fig. 1.9) offer clear visual evidence that curved IDT fingers focus SAW while straight SPUDTs do not. However, the smoke particle method allows measurement in larger frequency and amplitude ranges and does so in a shorter time compared to LDV visualization. Rambach *et al.* [121] recently introduced another rapid and simple method of visualization using a wetting fluid film on the piezoelectric substrate, where film deformation was induced by acoustic radiation pressure causing a visible contrast between excited and non-excited areas. This method not only makes visualization of the sound path possible, but also possibly exposes the crystal anisotropy and SAW velocity.

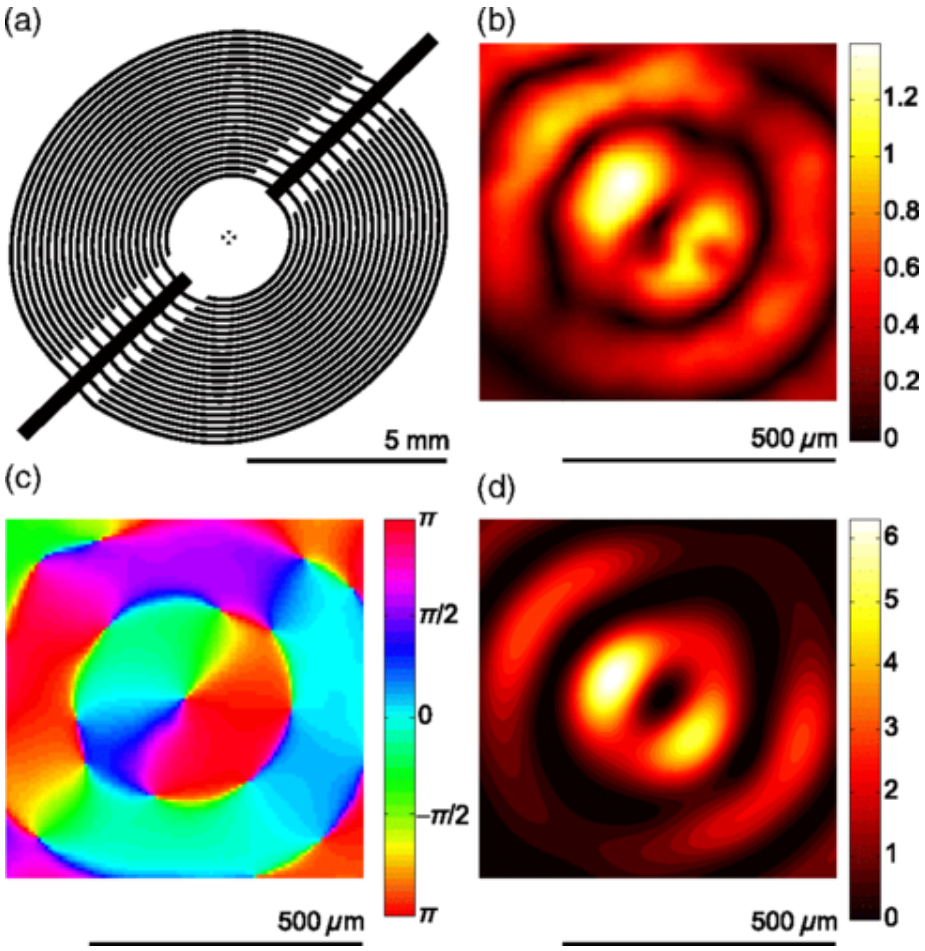

Figure 1.10: (a) Single spiraling IDTs design. (b) Experimental substrate vertical vibration amplitude (max amplitude 1.4 nm_{pp} at 7 V_{rms}). (c) Experimental substrate vertical vibration phase. (d) Calculated potential well from experimental data (max height 6.3 fJ). Figures are reprinted with permission from Riaud (2017) [119]. Copyright (2017) American Physics Society.

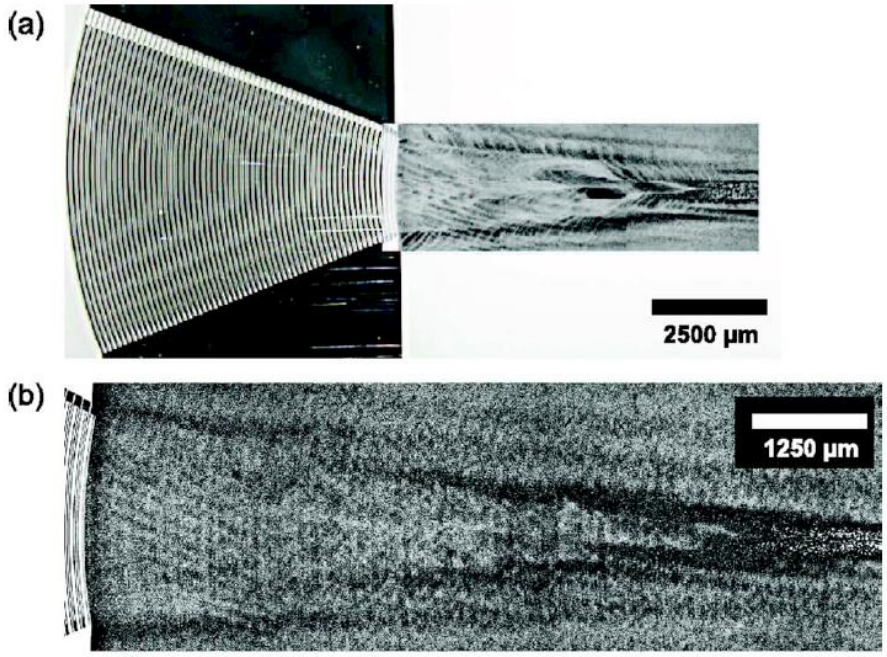

Figure 1.11: Visualization of SAW generated by FIDT with 250 nm sized smoke particles placed on the substrate after (a) 15 s exposure, and (b) after 30 s exposure. The distribution of pattern is achieved by the large transverse surface acceleration that carries the particles aloft to relatively quiescent regions nearby via acoustic streaming. Figures are reprinted with permission from Tan (2007) [122].

The above contributions have allowed FIDTs to be widely employed in acoustofluidic applications where their high intensity and greater bandwidth compression ratio can be utilized. Sessile drop translation and merging, particle concentration and mixing, and cell sorting have all benefited from the use of FIDTs due to their ability to maximize the proportion of acoustic energy that results in efficient acoustic force gradients and acoustic streaming. These advances will be covered in Sections 1.4.2, 1.4.3, and 1.4.4.

1.4 Microscale Acoustofluidics

1.4.1 Principles of Operation

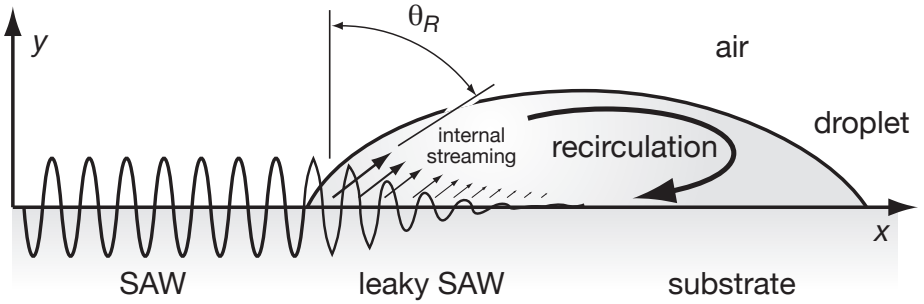

Figure 1.12: Sketch of a SAW acting on a small sessile drop. The acoustic energy is diffracted into the fluid at the Rayleigh angle, θ_R, leading to internal streaming in the small fluid volume, which drives recirculation. Adapted from Li *et al.* [123].

Surface acoustic waves propagate upon single crystal piezoelectric substrates with weak attenuation. Upon encountering a fluid on the surface (*see* Fig. 1.12),

SAW "leaks" into the fluid, forming sound that propagates in the fluid and acting to quickly attenuate the SAW in the substrate. The mechanism of the acoustic energy attenuation is balanced by viscous attenuation and dialative dissipation. This can be described as: $\frac{\partial W}{\partial t} + \nabla \cdot J = \rho_0 v_o[bu_0 \cdot \nabla u_0 - u_0 \cdot \nabla \times \nabla \times u_0]$, where W is the acoustic energy density, J is the energy flow, $\nabla \times \nabla \times u_0$ describe the viscous attenuation, and $u_0 \cdot \nabla u_0$ describe the dialative dissipation. The sound, a progressive longitudinal acoustic wave, travels through the liquid at a Rayleigh angle $\theta_R = sin^{-1}(v_l/v_R)$ [124], where v_l and v_R represent the speed of sound in the liquid and the speed of the Rayleigh SAW upon the solid substrate, respectively. For example, for the case of SAW traveling from 128° YX LN into water, v_l =1485 m/s and v_R = 3965 m/s, results in $\theta_R = 22°$.

Generally, the acoustic wave will turn into the media with a slower acoustic velocity, analogous to Snell's law. It is important to remember, however, that modal conversion can occur, allowing acoustic waves to travel across interfaces even when the Snell's law prediction suggests total internal reflection would occur, as explained by Hodgson *et al.* [125] where modal conversion from longitudinal acoustic waves (sound) in a fluid to Lamb waves in a superstrate are found. Furthermore, SAW likewise will leak into viscoelastic solids, particularly those typically used in microfluidics like polydimethylsiloxane (PDMS). While SAW devices can be used in

enclosed microfluidics devices that employ PDMS, it is best to minimize the area of PDMS bonding to the piezoelectric substrate over the region carrying the SAW. Inexpensive alternatives to PDMS are possible to mitigate this problem, especially via the use of ultraviolet-sensitive, low-viscosity epoxies for layer bonding [126].

The length along the surface of the piezoelectric substrate over which a Rayleigh wave decays by a factor of e due to the leakage of SAW into the fluid to transmit sound is the attenuation length $\alpha^{-1} \propto 1/f$: [124]

$$\alpha^{-1} = \frac{\rho_s v_R \lambda_{\mathrm{SAW}}}{\rho_f v_l}, \tag{1.3}$$

where ρ_f and ρ_s are the densities of the fluid and the solid respectively, v_l is the speed of sound in the fluid media and $v_R = f\lambda_{\mathrm{SAW}}$ is the Rayleigh wave phase velocity. The sound wave in the fluid, on the other hand, propagates uniaxially at the Rayleigh angle [127] and has a distinctly different attenuation length, $\beta^{-1} \propto 1/f^2$:

$$\beta^{-1} = \frac{\rho_0 {v_l}^3}{4\pi^2 f_{\mathrm{SAW}}^2 \left(\frac{4}{3}\mu + \mu'\right)}, \tag{1.4}$$

where f_{SAW} is the SAW frequency and μ and μ' are the shear and bulk viscosities of the fluid, respectively. Values of the solid and fluid attenuation lengths in the LN-water system were measured by Dentry *et al.* [99] and are listed in Table 1.2.

Table 1.2: Attenuation length of the SAW surface displacement at the LN and water interface, expressed as α^{-1} (*see* Eqn. 1.3) and attenuation length of the sound in water, expressed as β^{-1} (*see* Eqn. 1.4). Reproduced with permission from Dentry (2014) [99].

f_{SAW}(MHz)	α^{-1}(mm)	β^{-1} (mm)
19.7	2.4	120
54.2	0.87	16
122	0.39	3.1
240	0.19	0.80
490	0.097	0.19
936	0.046	0.052

Attenuation of the sound in the fluid induces a momentum flux responsible for the formation of steady state fluid flow: acoustic streaming [128, 127]. Acoustic streaming can be crudely classified depending on the acoustic path length permitted in the fluid and the location of viscous attenuation. Schlichting streaming is the result of viscous shear attenuation near the solid-fluid boundary [129] and Eckart streaming is the result of sound attenuation in the bulk of the fluid [15]. Rayleigh streaming arises from Schlichting streaming [16]. Further details on the types of streaming, their respective characteristics, and previous studies are summarized in Table 1 of the review by Friend *et al.* [11]. In cases where a free fluid surface is present, the nature of streaming and how it causes fluid transport is slightly more complex [130]. In later sections, we will explore how streaming produces fluid and particle motion.

Particle behavior in acoustofluidic systems is typically controlled by the fol-

lowing forces: direct and indirect (Bjerknes) acoustic radiation forces, viscous Stokes drag, van der Waals forces, and electrostatics and electrodynamics. The latter two, van der Waals and electrically-driven forces, tend to be negligible in acoustofluidics, though there have been reports of combining these phenomena to achieve results not possible with acoustics alone. The direct SAW radiation force under a traveling wave was derived by King [131] and is expressed as:

$$F_{rt} = 2\pi\rho_0 A^2 \left(\frac{kr}{2}\right)^6 \left[\frac{1 + \frac{2}{9}\left(1 - \left(\frac{\rho_0}{\rho_p}\right)^2\right)}{2 + \left(\frac{\rho_0}{\rho_p}\right)^2}\right] \tag{1.5}$$

where r is the particle radius, $k = \omega/v_R$ is the wavenumber of SAW, A is the amplitude of the incident wave, ρ_0 is the liquid density, and ρ_p is the particle density. On the other hand, the radiation force under a standing wave is expressed as [132]

$$F_{rs} = \left(\frac{\pi p_0^2 r^3 \beta_w}{2\lambda_{\mathrm{SAW}}}\right)\left(\frac{5\rho_p - 2\rho_0}{2\rho_p + \rho_0} - \frac{\beta_c}{\beta_w}\right)(\sin(2kx)) \tag{1.6}$$

where p_0 is the acoustic pressure, x is the position of the particle, λ_{SAW} is the wavelength of SAW, and β_c and β_w are the compressibility of the particle and the surrounding fluid, respectively. Notice that the radiation force is proportional to r^6 for a traveling wave, but only proportional to r^3 for a standing wave. However, the reader

should consult more recent literature by Bruus [133], Lauga [134], and Marston [135] to properly take into account fluid and particle compressibility and other important effects. We finally note that acoustic radiation interacts with surfaces in a more complicated way, demanding care in its treatment [136].

The stream-wise drag experienced by a particle of radius r can be approximated by the Stokes drag equation, $F_D = 6\pi\mu r v_D$, where v_D is the velocity difference between the surrounding fluid and the particle. Finally, the Bjerknes force, an interparticle force arising from the scattering of the incident acoustic wave can be used to describe the interparticle interactions between bubbles [137] or compressible particles [138, 139, 140, 141]. The Bjerknes force is defined as:

$$F_B = 4\pi r^6 \left[\frac{(\rho_p - \rho_0)^2 (3\cos^2\theta - 1)}{6\rho_0 r^4} U^2 - \frac{\omega^2 \rho_0 (\beta_c - \beta_w)^2}{9L^2} {p_0}^2 \right] \tag{1.7}$$

where U is the particle velocity amplitude, L is the distance between two particles, θ is the contact angle between the fluid and particle, and p_0 is the acoustic pressure amplitude.

1.4.2 Fluid Manipulation in Sessile Drops

Sessile drops rest on top of a surface and have been successfully actuated by electrowetting, SAW, and even light using special photoresponsive surfaces [142],

forming virtual walls using optical illumination of photoelectric layers [143, 144]. The dominant application of these technologies is in biological assays. The reader is referred to the review by Haeberle *et al.* for a comparison of these and other methods for microfluidic lab-on-a-chip platforms [145]. However, none of the other methods are capable of all the types of actuation described in this section.

Both acoustic streaming within the drop and acoustic radiation force on the free surface of the drop can be induced using SAW. Traveling SAW (TSAW) and standing SAW (SSAW) dominate the literature, but other acoustic modes are also useful in select situations. However, we note that acoustic waves in solids are not easily isolated so that unintended modes are often present. These waves, whether SAW or not, deliver sound into a sessile drop at the Rayleigh angle as described in Section 1.4.1, as long as the wave propagates from a region without the fluid to a region where the fluid is present. In general, the effect of the acoustic wave in the drop depends on the properties of the original wave in the substrate, the properties of the fluid, and the geometry of the drop. We break down manipulation into four regimes: mixing, translation, jetting, and atomization. For each regime, we highlight recent work regarding the basic understanding of the phenomena as well as recent advances in the associated applications. After mixing we pause to consider particles in sessile drops.

Mixing

Acoustic streaming at the Rayleigh angle produces recirculation in a stationary sessile drop (*see* Fig. 1.12). Almost fifteen years ago, Wixforth *et al.* [146] described the idea of an acoustically-actuated, miniaturized digital droplet lab on a chip, including sessile drop transport and internal mixing with recirculation. The primary internal flow promotes mixing in the drop, but is not generally helpful for other applications such as particle concentration as will be explained in Section 1.4.2. Li *et al.* [123] demonstrated that an azimuthal flow with a vertical component can be induced in a sessile drop from asymmetric SAW exposure on a LN substrate, driving vortical flow about a tilted axis [147]. Li *et al.* [123] provided several designs for generating asymmetric SAW as illustrated in Fig. 1.13.

Improvements have been made in producing internal flow in drops by exploring other types of acoustic waves. Shilton *et al.* [115] explored circular and elliptical FIDTs in a similar asymmetric exposure arrangement. Elliptically focused SAW produced more intense streaming and thus stronger primary internal flow while circularly focused SAW produced stronger azimuthal flow, concentrating the SAW power to a single small region of size comparable to the SAW wavelength, accentuating the effects of the asymmetric droplet placement.

Theoretical work on acoustic streaming, which induces mixing in sessile drops,

was undertaken by Nyborg in the 1960s who suggested that the nonlinear hydrodynamic term due to the Navier-Stokes momentum equation could be neglected [148]. He argued that streaming and the resulting fluid velocity were both second order phenomena and thus the above term was fourth order and negligible. In the 1970s, Lighthill argued that the nonlinear term was only negligible for slow streaming [127]. Shiokawa followed Nyborg's use of an effective body force for calculating streaming velocity in the theory following his experimental work on manipulation of sessile drops using acoustic streaming [149]. Both authors neglect viscosity and argue that the attenuation, which is fundamental to streaming, comes mostly from refraction of the wave at the solid/fluid interface rather than from viscous attenuation.

Most modern numerical work on streaming has closely followed Shiokawa's procedure including a 3D simulation of low power mixing performed in 2010 by Alghane *et al.* [150]. They include the nonlinear hydrodynamic term, but continue to neglect viscosity. They experimentally measured the SAW amplitude as a function of input power and separately measured the streaming velocity as a function of input power. Then, in their numerical calculation, they determined streaming velocity in three spatial dimensions as a function of SAW amplitude and correlated these results to their experiments using a fitting relationship between the two measured quantities. The numerical and experimental results illustrate some simple flows in relatively large

drops (30 μL) under relatively low power (up to 0.025 W).

In contrast, Vanneste *et al.* [151] contributed a numerical formulation of acoustic streaming that incorporates viscous attenuation. They derive three contributions to the resulting mean flow: internal Eulerian, boundary Eulerian, and Stokes drift. They point out that without viscous dissipation (as formulated above) Reynolds stress and the pressure gradient are balanced and there can be no mean flow generated in the interior. Instead of using the effective body force in the averaged momentum equation, they use an averaged vorticity equation due to Eckart [15]. The authors are able to apply their results to a variety of geometries, but their solutions are only in two dimensions. Importantly, neither of these two numerical simulations accounts for acoustic radiation force and the reflections that result from a finite boundary.

In 2014, Rezk *et al.* [152] were able to produce *poloidal* flow using a simplified transducer, a pair of L-shaped electrodes that generate Lamb waves. Poloidal flow only occurred above a critical frequency that was found to be dependent on the diameter of the drop. Lamb waves occur in the bulk of the substrate so their attenuation is different from that of SAW, but the concept is the same. The acoustic streaming-driven primary internal flow from the Lamb wave becomes poloidal flow only when both the acoustic energy impinges radially from all sides and the attenu-

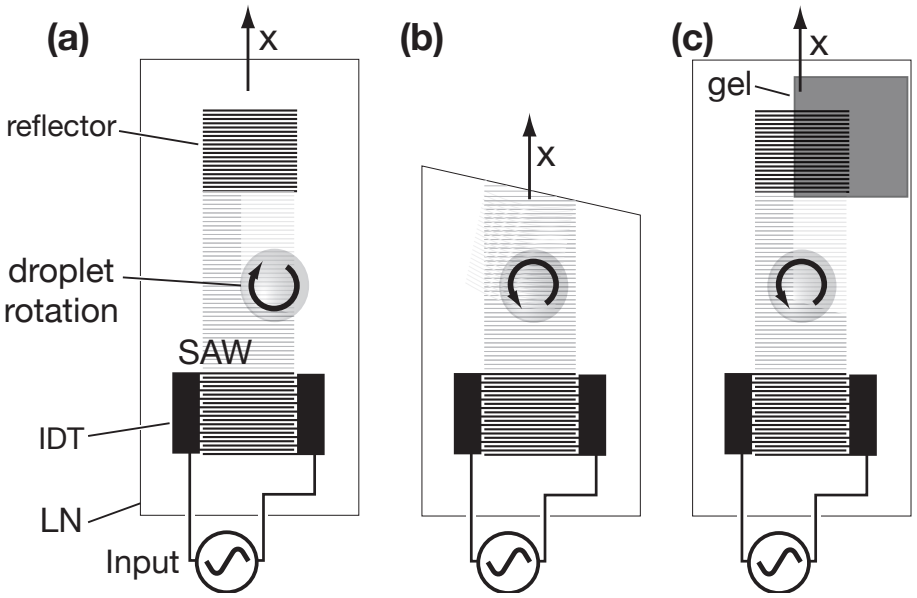

Figure 1.13: Three methods used to produce azimuthal flow via asymmetric SAW actuation. (a) Symmetry is broken offsetting the drop from the center line, (b) Asymmetry is generated from the angled edge of the LN substrate, and (c) Asymmetry is generated by absorbing SAW in one region, while reflecting them in another.

ation length of the Lamb wave in the substrate is less than the radius of the drop as in Fig. 1.14. Since the attenuation length is dependent on frequency, the existence of a critical frequency is due to the necessity of this attenuation length being less than the drop radius for the poloidal flow to exist.

At the same time, Riaud *et al.* [153] described a more complicated acoustic wave that they claim allows greater control over the internal flow. They suggested the use of helical waves (Bessel beams) to generate cyclone-like flow with both poloidal and toroidal streamlines. Theoretically, the shape of vortices in the fluid can be

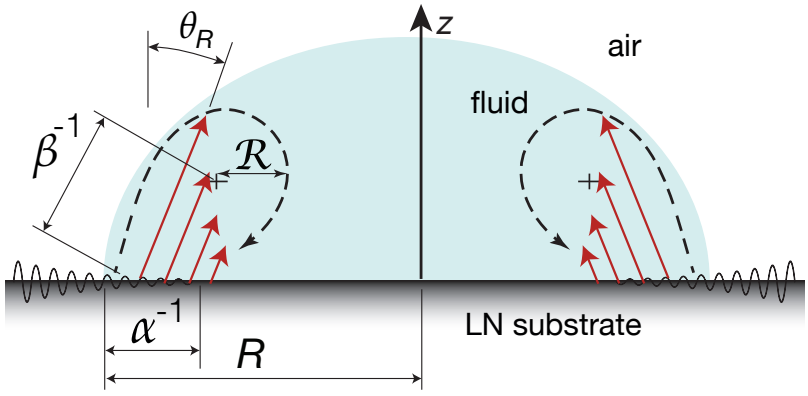

Figure 1.14: Poloidal flow is set up in a sessile drop due to the chosen ratio of drop radius, R, to recirculation length, $\mathcal{R}$, which depends on β, α, and θ_R. Corrected and adapted with permission from Riaud *et al.* (2014) [93] Copyright (2014) American Chemical Society.

controlled by the boundary conditions of the fluid and the properties of the helical acoustic waves. Specifically, the axial vorticity is controlled by the acoustic field while the azimuthal vorticity is controlled by the boundary conditions. This result is analogous to the conclusions drawn above regarding internal flow produced by asymmetry and different wave-forms [154]. Riaud *et al.* argue mathematically that these effects are decoupled. This implies that the variables can be independently chosen to produce desired internal flows. They also observed a curious phenomena: fluid flowed *away* from the acoustic energy source when the acoustic beam-width was small compared with the width of the fluid boundary, but flowed *toward* the source when the beam was confined. The authors call these repeller and attractor vortices respectively. The helical acoustic waves used to produce these flow effects can be

generated using inverse filtering techniques. In fact, in another paper Riaud *et al.* [62] demonstrate the production of "swirling SAW" by an array of IDTs; in a more recent paper, Riaud *et al.* [155] also use these waves for particle manipulation.

Riaud *et al.* [156] also investigated the effects of viscosity on acoustic streaming flow, showing that it strongly affects the Eckart streaming in the bulk of the sessile drop and therefore should be considered even though it is absent from the velocity expression obtained by a balance of acoustic attenuation and fluid shear. This is an important improvement upon the traditional perspective perhaps best espoused by Lighthill *et al.* [127]: viscosity is crucial to acoustic streaming, yet its specific value is said to not affect the streaming characteristics. This work expands on the simulations by Vanneste *et al.* described earlier. They reproduced experimentally observed flow patterns in sessile drops actuated by SAW with hydrodynamic simulation and were able to show how this relates to the acoustic field. They found that the acoustic field that drives streaming is dominated by a small number of caustics despite the presence of a chaotic field (this chaotic field was quantified earlier by Shilton in the context of flow in microfluidic wells [157]). In the case of a sessile drop on LN they use scaling to reduce the problem to dimensionless numbers for surface attenuation and bulk attenuation that may be used to predict flow patterns in new situations.

One of the major advantages of sessile drop microfluidics is the extremely small sample volumes that are possible. Recently, Shilton *et al.* [158] were able to shrink the size of sessile drops while maintaining control of the flow for mixing, and Miansari *et al.* [75] were able to crudely manipulate 10 fℓ droplets in a nanoslit using SAW.

Generally, these devices are operated below a critical input power necessary to translate the sessile drop across the substrate. This critical power depends on the contact line pinning of the drop, in turn dependent upon the wetting properties of the fluid/surface combination; for example, Shilton *et al.* [154] report the critical power for their arrangement to be 700 mW. Once identified for a given system, this critical power level represents the upper practical limit for inducing mixing, flow, or internal manipulation within the droplet.

Particle, Colloidal, and Cell Manipulation in Sessile Drops

The manipulation of micro-scale objects in fluid by SAW relies on both the acoustic streaming-induced flow described in the previous section and the acoustic radiation force and other forces introduced in section 1.4.1. Acoustic streaming depends upon the properties of the acoustic wave generated by the source and by the geometry and fluid properties of the drop. The size, density relative to the fluid,

and compressibility of the particles determine the effectiveness of acoustic radiation forces upon them.

Concentration, separation, or isolation of target particles are typical needs in biochemical analysis. For dilute samples, an effective collection procedure for the targeted particles can significantly reduce the amount of fluid handling [159]. Particle concentration helps to minimize measurement noise and improve detection sensitivity. Acoustic forces can be used to non-invasively position, concentrate, or fractionate particles. In something of a scientific curiosity, standing waves were first identified by the concentration of suspended particles at acoustic pressure nodal or antinodal planes in a fluid by Kundt and Lehmann in 1874 [160]. However, the process was slow, with concentration requiring at least several minutes. Recently, researchers have used SAW devices to accelerate and otherwise improve concentration, separation, and centrifugation.

The position of the particles in sessile drops vary with the drag force and acoustic radiation force applied to the particles. Destgeer *et al.* investigated four regimes of particle position [161]. A droplet with $R > \alpha^{-1}$ has reduced potential for symmetrical vortices. Droplet size and SAW attenuation length also determine whether the acoustic radiation field produces standing waves or traveling waves in the case of counter-propagating IDTs. If $R > \alpha^{-1}$, then TSAW is generated from

each side of the drop. If $R < \alpha^{-1}$, then standing waves are set up in the portion of the drop where overlap occurs.

As described in Section 1.4.2, Li produced azimuthal flow in a sessile drop. This type of flow allows particles to be rapidly concentrated at the center of the drop due to shear-induced migration. It is important to note that concentration was only observed in a range of applied power between 150–450 mW while dispersion was observed on either side of this range. This intermediate range of SAW power represents a Goldylocks state below which streaming does not overwhelm particle concentration and above which the particles are transported [123]. Li showed that bio-particles remained viable and were concentrated to within 10% of the drops volume under asymmetric SAW actuation. These results show promise for use in conjunction with the bio-sensors discussed in Section 1.4.2 in order to reduce the sensitivity requirements among other applications.

Wilson *et al.* introduced a method using phononic superstrates to achieve programmable complex fluid manipulation on-chip [162]. The phononic structures can produce filter and waveguide effects by scattering and reflecting the SAW without fabricating multiple IDTs on the substrate. They chose a square array of circular holes made in a silicon wafer via dry-etch photolithography and demonstrated centrifugation of 10 μm polystyrene beads and blood cells in a droplet using either a

filter-based design or a waveguide-based design. This technique may be useful in certain specialized applications where a single SAW device could be used for multiple types of manipulation depending on the superstrate, which could be switched out as desired. Later on, Riaud *et al.* [163] claimed an improved result from a set of 32 IDTs patterned in a circle and driven by a programmable circuit in order to effectively drive planar waves. They demonstrated droplet division, merging, and atomization with the platform. Moreover, they later demonstrated particle manipulation and positioning through careful control of the signals input into the IDTs [119].

As mentioned earlier FIDTs can improve fluid actuation in SAW devices. Shilton found that a concentric circular-arc SPUDT was capable of concentrating particles in microliter drops in under 1 second, which is an order of magnitude faster than the straight SPUDT [115].

Destgeer *et al.* [164] have claimed that the conclusions made by Rezk *et al.* about their poloidal flow, Lamb wave device are incorrectly based entirely on acoustic streaming flow without due consideration of the acoustic radiation force. The experiments by Rezk included only one droplet size (1.5 mm) and single particle size (5 μm), whereas those by Destgeer included a range of particle sizes and droplet volumes, while both researchers varied frequency. Rezk claimed that shear-induced

migration caused concentration within the poloidal vortex (*see* Fig. 1.16). Destgeer found that particles were only concentrated when a parameter representing the balance of radiation force to drag force, $\kappa = \pi d_p f_{LW}/c_f$, was greater than unity (*see* Fig. 1.15(a)). Here d_p is the particle diameter, f_{LW} is the frequency of the Lamb waves, and c_f is the speed of sound in the fluid. They were able to accurately predict which combinations of particle size and frequency would result in concentrated rings (*see* Fig. 1.15(b)). However, Destgeer *et al.* [164] failed to take shear migration into account, important in forming such a ring. It may be that poloidal flow is a necessary, but not sufficient condition for concentration in a ring shape, which requires radiation force. The studies agreed that increasing the frequency, and thus reducing the attenuation length in the substrate, moved the concentrated ring towards the perimeter of the drop. Regardless of the precise mechanism, these studies show that particles can be reliably concentrated to a narrow ring at a tunable radius in a sessile drop without the need for microfabricated IDTs.

Translation

The primary application for sessile drop translation is planar microfluidic lab-on-a-chip platforms. Transport in microfluidics is conventionally achieved by pumping in continuously filled channels, but it can also be achieved with sessile

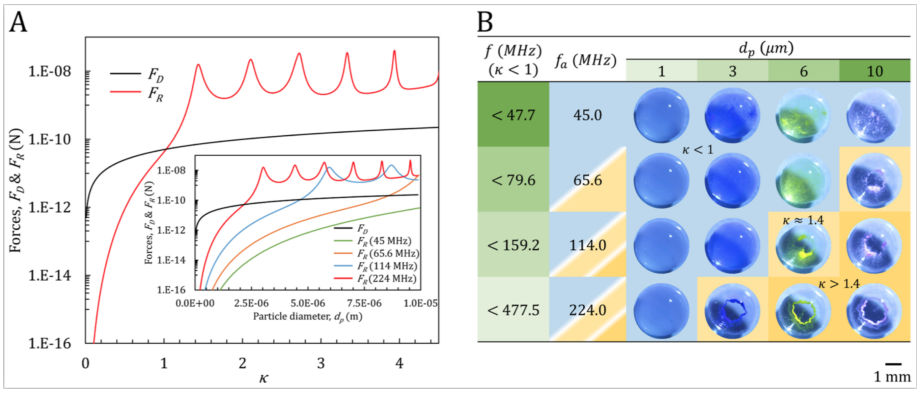

Figure 1.15: A) Force vs κ, where F_D is the drag force and F_R is the radiation force. Notice that F_R overtakes F_D at $\kappa = 1$. The inset shows the similar Force vs drop size relationship for various frequencies. B) Each image corresponds to a frequency, drop size pair and the values of κ for each pair are indicated to show that ring formation occurs for $\kappa > 1$, where radiation force dominates drag. Reprinted (adapted) with permission from G. Destgeer, B. Ha, J. Park and H. J. Sung, *Analytical Chemistry*, 2016, **88**, 3976–3981. Copyright 2016 American Chemical Society.

drops using SAW. With this approach, drops are isolated from their surroundings and require smaller volumes, though evaporation can become an issue [165]. The SAW input power must exceed a threshold that arises due to contact line pinning and contact angle hysteresis, which must be overcome in order to translate the drop. These concepts are well explained in a review of surface science by Gao *et al.* [166].

Wixforth *et al.* [167] first demonstrated drop translation using a combination of TSAW and patterning of the surface wettability. Renaudin *et al.* then explored the effects of surface wettability treatments on the power necessary to translate a 2 μL drop [168]. It is important to point out that they used X-cut LN rather than the more common 128° YX LN, which have different coupling coefficients. On bare LN, which

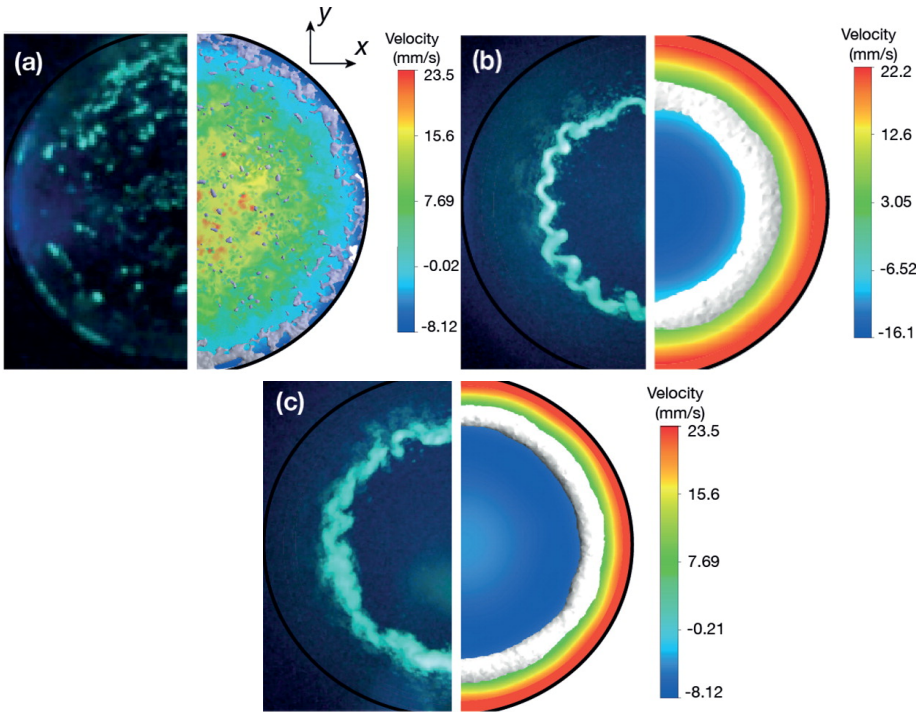

Figure 1.16: Experimental images (left) compared to finite element analysis predictions of fluid velocity (right) for a sessile drop actuated by Lamb waves. a) At 25 MHz no vortex is formed. b) At 157 MHz a clear vortex is formed and the particles collect at the lowest shear area. c) At 225 MHz the vortex and particle ring shift towards the perimeter due to a shortened attenuation length. Adapted with permission from A. R. Rezk, L. Y. Yeo and J. R. Friend, *Langmuir*, 2014, **30**, 11243–11247. Copyright 2014 American Chemical Society.

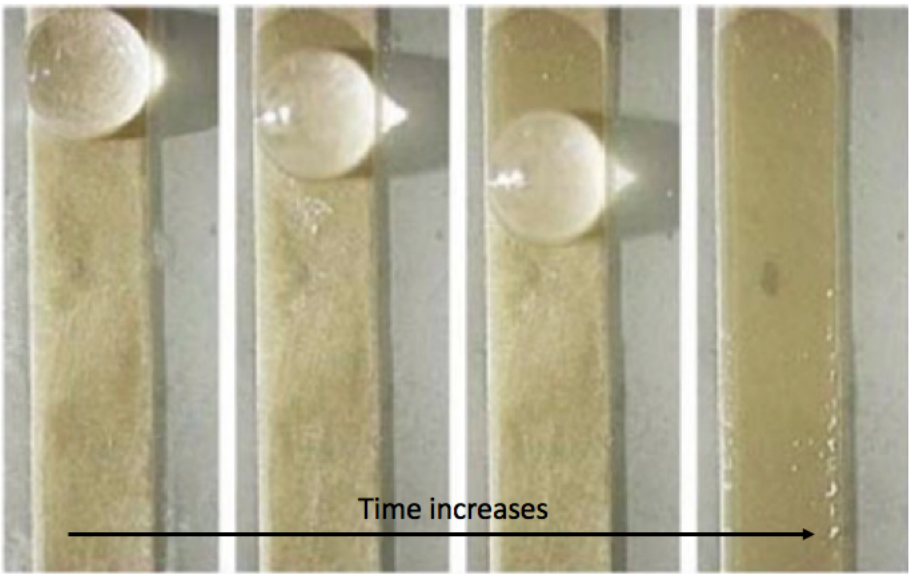

Figure 1.17: A water droplet being translated on a 10 μm thick hydrophilic Teflon path atop a LN substrate via a TSAW. Adapted with permission [122] from The Royal Society of Chemistry.

is hydrophilic, the drop required 1.6 W and after a hydrophobic treatment it required only 0.56 W. They found that predictable movement required a surface patterned path, but bare LN paths lead to inefficient movement and clearly, hydrophobic paths would lose drops to the surrounding area. In 2007, Tan approached the problem in a slightly different way using elevated teflon strips (10 μm thin) on bare LN [122] (*see* Fig. 1.17). This technique regained the translation efficiency while avoiding the predictable movement problems encountered by Renaudin *et al.* by using a slightly raised surface to isolate the intended path rather than surface treatment.

Because the acoustic and hydrodynamic response time-scales are radically

different, input signal modulation can be used to improve translation efficiency. Both Renaudin *et al.* [168] and Tan *et al.* [122] employed duty cycles in their signals. Renaudin *et al.* found that, at a certain pulse duration, the displacement per pulse was constant with respect to increases in drop volume so that greater efficiency is possible with short pulse width modulation. Baudoin *et al.* [169] presented a modulation of the SAW by Rayleigh-Lamb inertial-capillary frequencies that reduces the power required for translation by a factor of two. Modulation may also be useful for mixing, jetting, and atomization.

In 2010, Brunet *et al.* [170] numerically and experimentally explored the effects of surface displacement amplitude, drop volume, and viscosity on drop translation. The drop experienced internal flow, asymmetric deformation at the Rayleigh angle, vertical, free-surface oscillations and translation. They observed, as expected, that a minimum amplitude was required for translation, but this minimum did not seem to depend at all on drop volume. In the same set of experiments, varying the amplitude at a fixed volume revealed an asymptotic drop velocity maximum whose value depended on the choice of volume.

There was also a velocity maximum as the volume was varied at fixed amplitude, but this maximum occurred at the same volume regardless of which amplitude was chosen. We can understand this by noting that attenuation of SAW in the sub-

strate indicates how much energy is absorbed by the drop. Maximum velocity occurs when the drop/surface interface is at least as long as α^{-1}. Drops larger than this do not absorb more energy, but gain excess mass and thus move slower.

This study highlights the importance of considering both radiation pressure and streaming. Radiation pressure becomes important when the acoustic beam reaches the drop's free surface before being attenuated. Thus, the size of the drop relative to β^{-1} determines in part the effect of radiation pressure. Brunet observed vertical oscillations in the drops at frequencies and amplitudes (referring to the fluid oscillation not the solid displacement) that correspond to inertial-capillary vibration modes (similar to Rayleigh-Lamb as exploited by Baudoin above). In their interpretation, the free-surface deforms upward due to radiation pressure, but this deformation simultaneously reduces the effect of radiation pressure so that capillary forces pull the drop back down and the cycle repeats. Viscosity had the obvious effect of decreasing the translation speed, but it also reduced oscillations. Since viscosity increases attenuation it reduces radiation pressure and increases streaming. Clearly radiation pressure is critical for translation and for deformation of the free surface.

A drop can also spread as a thin film towards a SAW source as shown by Rezk *et al.* [171] (and recently explored by Morozov *et al.* [172]). This phenomena was observed (regardless of fluid type) when the contact angle was small enough

(requiring surface treatment in some cases) to produce a region at the edge of the drop where Rayleigh streaming dominated over Eckart streaming. They derived a constant velocity film front by neglecting Eckart streaming and applying appropriate boundary conditions for the region near the contact line. Their derivation matched with experiment across various frequencies, viscosities, and substrate velocities without employing an empirical fitting parameter as shown in Fig. 1.18. The data is separated by streaming Reynolds number $\mathrm{Re}_s = \rho_f U \lambda_{\mathrm{SAW}}/4\pi\mu$, where ρ_f is the fluid density and U is the particle velocity of the surface. This thin film phenomena was utilized by Collins *et al.* for atomization, which will be covered in Section 1.4.2.

Additional functionality is required if planar SAW microfluidics are to live up to their promise as a lab-on-a-chip platform. The ability to stop, merge, and split drops as well as increased speed are valuable for future devices.

In 2012, Travagliati *et al.* [173] introduced a new tool to effectively detect when a drop has reached its desired location. They drove a drop via SAW towards a cavity with a certain resonance. When the drop entered the cavity, the resonance of the cavity shifted, causing the SAW to be reflected and thus halting the drop.

In the same year, Ai *et al.* [174] applied the concept of focused SAW to translation. They showed that a circular FIDT was able to translate a drop placed just outside its focal distance approximately 5 times faster than a straight IDT under

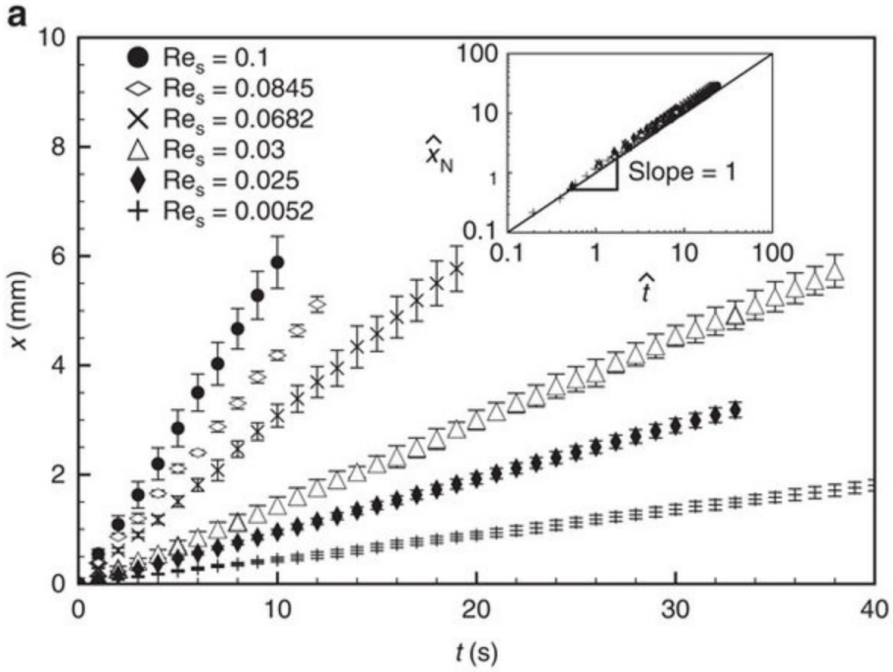

Figure 1.18: Experimental results of film front displacement, X, versus time, t, indicating constant velocity for various values of Re_s. The inset shows the same data with X and t normalized based on the derived film evolution equation showing agreement between theory and experiment. Adapted by permission from Macmillan Publishers, Ltd., [171] copyright 2012.

the same power, frequency, and drop size. Though not in strict contradiction, this calls into question the maximum volume-dependent velocity of drops as amplitude is increased described by Riaud *et al.* [156]. Within the focal distance the speed was still 3 times faster and all drops, regardless of location, moved toward the focal point. They suggested that this phenomena may be useful in merging drops.

Indeed, Collignon *et al.* [175] achieved merging by this phenomena, but splitting required a more complex mechanism. A two-part signal (*see* Fig. 1.19(a)) was produced that first initiated internal rotation and then elongated the drop towards a necking event. Rotational flow due to the first part was critical to suppress jetting behavior allowing sufficient injection of momentum without ejecting the drop. From there a balance of capillary force and drainage due to necking causes the drop to split as seen in Fig. 1.19(c). Collignon *et al.* performed the task with a range of fluids and obtained a non-dimensional number to predict the capillary bridge effect that ultimately splits the drop; the Ohnesorge number, $\mathrm{Oh} = \mu/\sqrt{\rho_f \gamma R_0}$ describes the balance of inertial and viscous stresses, where R_0 is the radius of curvature of the neck. In Fig. 1.19(b) we see that splitting occurs in a narrow band at a critical Oh value. We will return to this concept of capillary bridge hydrodynamics in the next section describing the application of jetting to extensional rheometry.

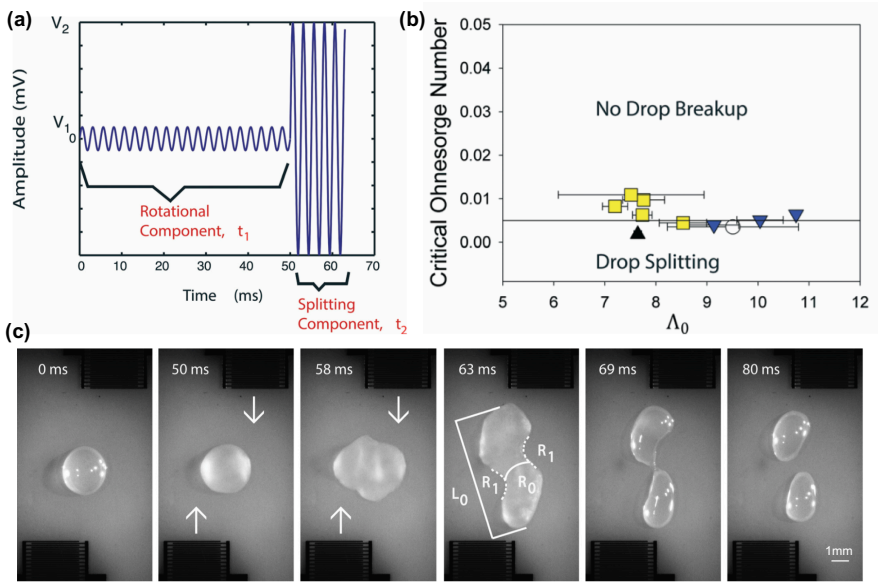

Figure 1.19: (a) The waveform of a single pulse used to split a sessile drop via counter-propagating offset SAW. The low-amplitude phase, applied over a period t_1, provides the initial energy for stretching the drop while avoiding jetting. The second, high-amplitude phase is applied over a much shorter duration t_2 comparable to the inertial time scale to rapidly elongate the drop. (b) The relationship between Oh and a dimensionless aspect ratio (Λ_0), showing the collapse of data points representing successful splitting events to a critical value of Oh. (c) A sequence of photographs depicting a successful splitting event with counter-propagating SAW indicated by arrows. Reproduced [175] with permission from The Royal Society of Chemistry.

Jetting

In general, jetting occurs at a fluid-fluid interface when inertial pressure overcomes surface tension, which tends to maintain the interfacial shape. The well-known Weber number, We is a good metric for this balance; We $= \rho_f u^2 L_c/\gamma$, where L_c is the characteristic length, u is the fluid velocity, and γ is the surface tension. Viscosity, which intuitively should factor into this balance, is not present in We, but is

indirectly expressed via the fluid velocity. More viscous fluids will derive less inertia from a given stimulus. Fluid velocities high enough to overcome surface tension, which increases for smaller fluid geometry, typically require a nozzle so that sufficient inertia can be generated. SAW is capable of producing very large surface accelerations, which translate into fluid velocity for a drop placed directly on the surface, thus eliminating the need for a nozzle.

The interaction between acoustic waves, elastic solids, and liquid drops to produce jets and satellite droplets is very complex [176]. Tan *et al.* attempted to elucidate the phenomenon by focusing SAW from two counter-propagating, FIDTs into various sized drops sitting upon Teflon coated LN [177]. This setup provided a stable drop location and high intensity, which promote jetting over other sessile drop phenomena such as internal flow and translation. Standing wave actuation produced an axisymmetric jet, which was assumed cylindrical. Vertical inertia generated by the focused SAW lead to elongation of the drop and eventually to a break-up event once a threshold input power was exceeded. Below this size dependent threshold, only vibration of the drop was observed (similar to that observed by Bussonniere *et al.* [178]) and above the threshold a Rayleigh-Plateau instability resulted in multiple droplets per jet.

They showed that the various jetting regimes corresponded to a modified

jetting We as seen in Fig. 1.20, where u was replaced by the jet velocity (U_j) and L_c was replaced by the jet radius. They were also able to predict experimental values of U_j for various fluids, graphed in Fig. 1.21, by modifying the momentum balance derived by Eggers *et al.* [176] for the case of acoustic streaming. It is critical to note that jetting only seems to occur during a pulse of SAW energy, either at the onset of the signal or during a pulsed signal. This was convincingly shown by Wang *et al.* [179] in a detailed, high speed video study of a sessile drop.

Atomization

Atomization has received abundant attention in recent years due both to its interesting physics and many important applications. In SAW devices, it tends to occur at higher power inputs than do the phenomena discussed so far. Atomization produces a continuous flow of many small droplets in a tight size distribution and much of the research is undertaken to optimize and predict the relevant parameters. The underlying mechanism of SAW atomization is still not completely clear, but several studies on the effects of viscosity, input frequency, fluid geometry, and acoustic amplitude have been recently completed. There have also been advances made in the engineering of devices necessary to reliably produce SAW atomization at lower input powers.

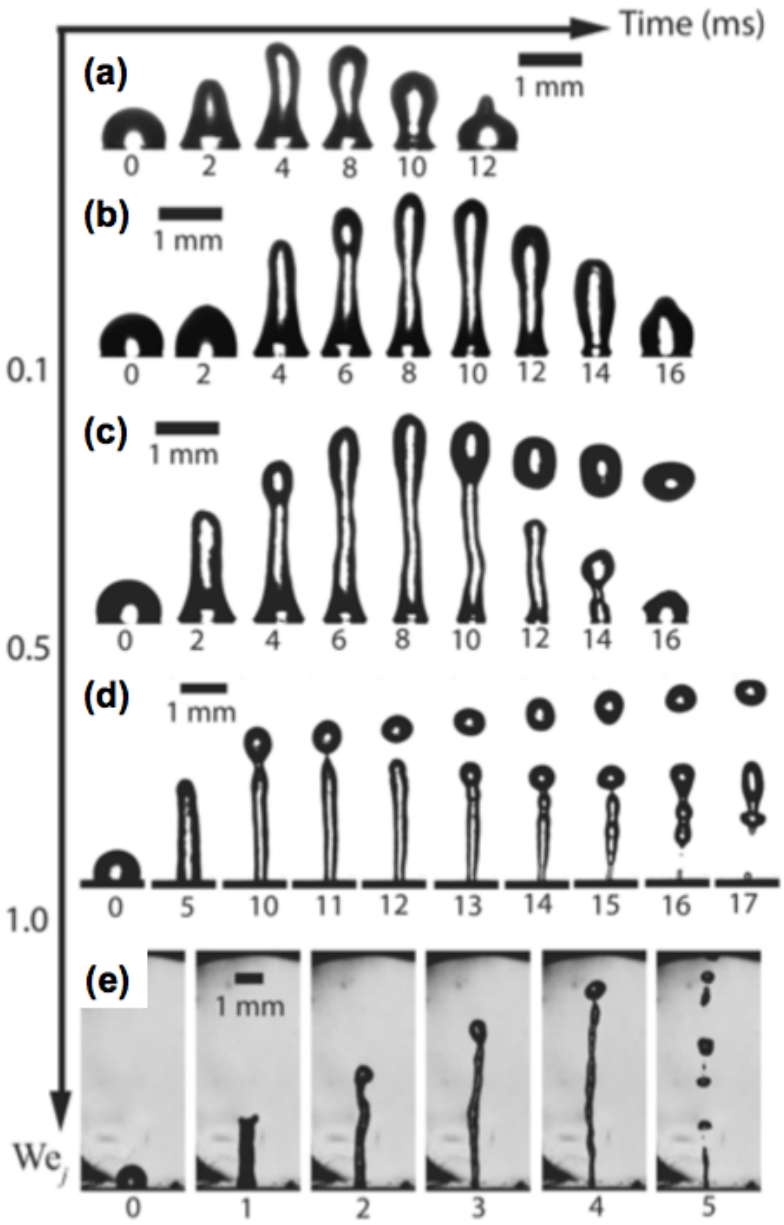

Figure 1.20: Jetting behavior according to We_j (on the vertical axis) from an investigation by Tan in 2009. Regimes involving (a) & (b) drop elongation, (c) pinch-off of a single droplet, and (d) & (e) jet breakup to form multiple droplets are depicted. Reprinted figure with permission [177]. Copyright (2009) by the American Physical Society.

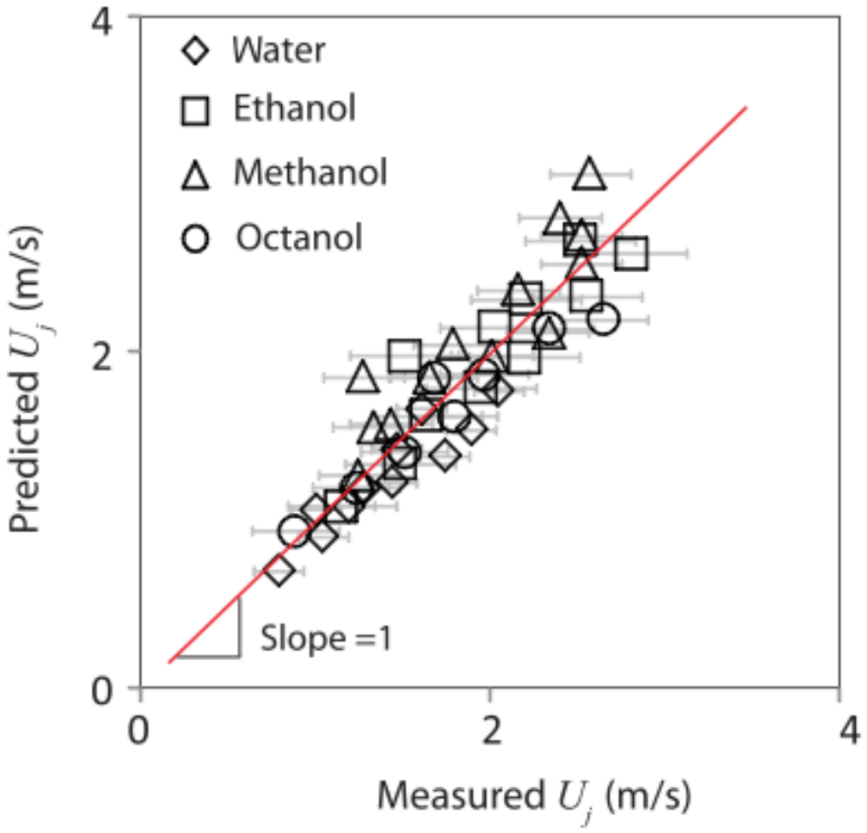

Figure 1.21: Comparison of the jet velocities, U_j, predicted by a momentum balance for acoustic streaming with measured values for various liquids. Proximity to the red line with unit slope indicates good agreement between measurement and prediction. Reprinted figure with permission [177]. Copyright (2009) by the American Physical Society.

It was posited early on that the mechanism of droplet production was somehow linked to capillary waves on the free surface of the fluid. In 1962, Lang used a piezoelectric transducer to induce acoustic waves in thin films and bulk, contained fluids [180]. He was able to show a link between capillary wavelength, λ_c and droplet size by varying the applied piezoelectric excitation frequency, f. In Kelvin's equation $\lambda_c^3 = 2\pi\gamma/\rho_f f_c$, λ_c is dependent on the capillary wave frequency, f_c. Lang assumed that f_c was equal to $f/2$ based on work by Faraday and others [181, 182, 183] and found that the capillary waves followed this modified Kelvin's equation and that the median drop diameter was a constant factor, 0.34, of λ_c when f was between 10–800 kHz. It is important to note that these experiments were not done using SAW and sessile drops and that the capillary wave observation was done at a different acoustic amplitude than the droplet production and sizing.

Kurosawa *et al.* created the first SAW atomization devices much later [184, 185] but used the same modification of Kelvin's equation to predict the resulting droplet size—they used $f/2$ in place of f_c and allowed for an empirical fitting constant. However, the fitting constant they found was 3.8 rather than 0.34. They suggested that the difference was due to the large surface vibration amplitudes in their study compared to those in Lang *et al.* but another important consideration is that they used 10–40 MHz acoustic waves as opposed to 10–800 kHz. Many ideas

later investigated more rigorously were mentioned by Kurosawa *et al.* They noticed that atomization occurred more readily from a thin film than from a drop, the atomization rate increased linearly with input power above an initial threshold and then reached a maximum, and the resulting droplet size distribution had multiple peaks.

Bio-sensors

In the last thirty years, SAW devices have been widely used to develop fast and sensitive bio-sensors for detecting pathogens, cells, and bio-molecules. Similar to devices used for communication, SAW sensors are comprised of a pair of IDTs. One generates a SAW while the other identifies changes in the SAW signal produced in the intervening space. The target under investigation is immobilized between output and input IDTs and this area is called the interaction region. Differences in the frequency, velocity, phase, and amplitude between the input and output SAW reveal the density and mechanical properties of the target.

The primary metric of bio-sensor performance is sensitivity so the large attenuation that occurs when Rayleigh SAW encounter a fluid initially precluded SAW bio-sensors. Other modes that are more compatible with a fluid environment, which is often required for biological samples, have been explored. Among them are: shear horizontal surface waves (SH-SAW), surface transverse waves (STW), and love waves

(LW). This topic and other early work in biosensing has already been well covered in reviews by Länge and Rapp [186] and by Rocha-Gaso *et al.* [187]. Here we will introduce some representative applications that is related to SAW bio-sensors.

Pathogens and cells can be bonded to the interaction region directly for detection. Howe and Harding studied *Escherichia coli* (*E. coli*) and *Legionella* by attaching specimens directly onto the surface of a SAW device [188]. The bacteria were exposed to an antibody at pH 4.0, which is close to their isoelectric point. After that, antibodies for *E. coli* or a combination of antibodies for both *E. coli* and *Legoinella* were added and bound to the bacteria on the surface. Significant differences in frequency were observed confirming the ability to detect (*E. coli*) and *Legoinella* with sensitivity of 10^6 cells per milliliter. Compared to other bacterial detection techniques, the use of SAW is both sensitive and fast–the process can be completed within 3 hours. Other than love wave adopted in Howe and Harding's work, SH-SAW is also used by Berkenpas to detect bacteria bonded to the surface of SAW device [189]. Both measurement setup with pathogens immersed in flow and 'dip-and-dry' method are used in the experiments.

Baca *et al.* [190] reported a method to rapidly detect the Ebola virus in 2015. Antibodies were functionalized on the surface of a SAW biosensor with Ebola antibodies in the test lane and a control group of antibodies in the preference lane.

The phase signal was recorded and compared between these lanes. A phase shift was observed caused by bioagents immobilized on the antibody.

Other than detection of mass increase caused by bonding between cells and specific antibodies on the surface, mechanical properties are also used as biomarkers in SAW bio-sensors for cell detection and analysis. In 2016, Senveli *et al.* [191] found that stiffness measured at high frequency was a potential biomarker for tumor cells. They reported a method for sensing tumor cells via microcavity coupled SAW devices. Cells were trapped in microcavities fabricated on the substrate of the SAW device. Based on the difference of ultrasound velocity between cells and substrate, the phase changes of SAW were measured thus revealing the elastic modulus of the cells. They were able to differentiate between certain types of tumor cells based on these measurements of elastic modulus. This technique and others like it may be beneficial for cancer diagnosis and possibly for future rapid cancer screening assays.

In addition to the organisms themselves, bio-molecules such as protein, sugar and DNA from target cells and pathogens can also be trapped on the surface of the sensors and detected. Take DNA detection as an example, many of the DNA detection approaches need DNA segments to be amplified (PCR for example) which requires long time while SAW bio-sensors provide a possible way to detect DNA target with high sensitivity. In 2007, Sakong *et al.* [192] developed a SH-SAW-based

sensor system with micro-fluidic channels to detect oligonucleotide DNA. DNA with a thiol group was used as a probe and immobilized on a gold coated interaction region. A frequency shift was observed when the target DNA was continuously flowed over the probe DNA layer. They showed that this method has sensitivity up to 135 pg/(mℓ·Hz). In 2015 Cai *et al.* [193] proposed a method detecting DNA using third-order harmonic mode (6.4 GHz) of SAW device fabricated on LN substrate. The high-order mode which achieves atomic resolution makes it possible to sense a single DNA base with SAW bio-sensor.

Biosensor signals can also be amplified by bonding bio-molecules to larger particles. Lee *et al.* [194] presented a SH-SAW immunosensor that was able to simultaneously detect multiple cardiac makers (cardiac troponin (cTnI), creatine kinase (CK)-MB, and myoglobin) with high sensitivity in human serum. Antibodies were conjugated with gold nanoparticles (AuNPs) in advance to enhance the signal and then used to capture analytes. Finally the antibodies were immobilized on the sensing area between two IDTs. The SAW signal was observed to change with the concentration of conjugated antibodies that were bounded to the surface. Minimum detectable concentrations of cardiac markers were reported as 20 pg/mL, 1.1 ng/mL, and 16.0 ng/mL for cTnI, CK-MB, and myoglobin, respectively with a 200 MHz device. The author also verified that higher mass sensitivity could be achieved by

increasing the operating frequency of the SAW device.

1.4.3 Fluid Manipulation in Closed Channels

We have discussed fluid manipulation in sessile drops, but, at the time of this writing, microfluidic processes necessary for lab-on-chip applications are more commonly accomplished in channels. This is likely due to the relative ease of fabrication of microfluidic chips based on channels and the lack of evaporation. Continuous flow in a microchannel can provide rapid and high-throughput flow manipulation and analysis of a variety of samples. Closed channels also reduce contamination from the surrounding environment during the analysis.

PDMS is widely used to form microfluidic channels. However, there are two major, well-known issues with this material in the context of acoustic waves: heating [195] and attenuation [196], though each can be controlled and mitigated. In what follows, some researchers choose to accept these drawbacks due to the ease of fabrication, but alternatives like glass or milling directly into LN are available.

Fluid mixing

Mixing is essential for chemical reactions and the promise of miniaturized bio-chemical processes requires chemical reactions. However, at the scales of channel

based microfluidics and nanofluidics, extremely low Reynolds numbers make the flow laminar and difficult to effectively mix. In the absence of turbulence, diffusion-based mixing cannot meet the requirements for most chemical mixing in microfluidic applications. In acoustofluidic systems, the nonlinear average effects of acoustics such as acoustic streaming are able to create a net streaming flow in the fluid, and thus will cause rapid and effective mixing. In light of this advantage, applications of rapid and active mixing have recently been developed and demonstrated in acoustofluidic research.

Following the progress made by the rest of the Wixforth group in drop translation, Sritharan *et al.* [197] also demonstrated SAW-induced mixing in a simple Y-shaped microfluidic chip with two inlets for dissimilar fluids, which were mixed in the third channel. An acoustic wave generated by a SAW device was coupled through the bottom of the chip and was diffracted based on the chip material (silicon, glass, polymer, etc). This is a prime example of an extra capability provided by acoustofluidics beyond those available to conventional microfluidics, powered by external pumps. In very similar devices, Tseng *et al.* [198] compared the mixing efficiency between channels oriented parallel to wave propagation (parallel-type) and those oriented perpendicular to wave propagation (transverse-type). They showed that the parallel-type mixer was more effective and that higher voltages were as-

sociated with better mixing. Jo *et al.* [199] showed that, in the specific case of transverse-type micro-mixers, SSAW was more efficient for mixing than TSAW. Furthermore, Luong *et al.* [200] reported that, as in sessile drop translation and particle concentration, FIDTs offered greater efficiency than straight IDTs.

The effect of the channel geometry on acoustic mixing has also been investigated. In parallel-type microchannel mixers, Tan *et al.* [201] noted that a uniform channel flow became a mixing flow when the channel width was larger than the wavelength of the sound in the fluid. This finding suggests the possibility of dynamically choosing between flow and mixing in a single device by controlling the input frequency of the SAW device. Conversely, Miansari *et al.* [75] presented active mixing via SAW in nanoslits (nanoscale channel height but width $> 100\ \mu$m). Mixing tended to occur with vortices aligned in the plane of the transducer rather than the typical vortices perpendicular to this plane. The authors suggest that sound waves cannot travel in the fluid due to it's nanoscale height and thus the typical acoustic streaming that causes mixing does not occur. More work is needed to understand nanoscale confinement in the context of fluid/acoustic wave interaction. We will present other aspects of this paper and others dealing with nanofluidics later in this review.

Acoustic mixing not only occurs in channels and sessile drops, but Rezk *et al.* [202] also presented a uniform mixing method in a simple paper-based microfluidic

device using SAW, offering a low-cost and disposable alternative to microchannel mixing. This technique could be especially relevant to diagnostics and other biological testing.

Other modes of acoustic vibration besides SAW have been used for mixing. Piezoelectric elements can produce a large variety of fluid motions in channels and chambers because they can be driven in several different vibrational modes. Among them, the thickness-mode is widely used for active mixing due to large amplitude substrate displacements in this mode. Thickness-mode devices have been used at a range of frequencies in the literature. Rife *et al.* presented mixing in an isolated PMMA chamber (a thin square box) via 50 MHz actuation of two $BaTiO_3$ transducers, but suggested improvements in mixing through larger frequencies and more or larger transducers [203]. Yang *et al.* investigated a very similar glass mixing chamber, but included inlet and outlet ports and chose PZT transducers [204]. Their device proved the concept, but was slow (2 seconds to reach stable mixing), high power (operated at 50-90V), and unsuitable for many applications due to the use of PZT (driving frequencies of 15-100kHz caused fluid heating and cavitation, which are each harmful to many bio-medically relevant fluids). Yaralioglu *et al.* applied a similar idea to perpendicular mixing in a PDMS microchannel using zinc oxide transducers at 450 MHz [205] (*see* Fig. 1.22). They were able to produce turbulent flow

across a 300 μm channel at up to 60 μL/min and while using a much lower voltage than Yang, 1.2 V (30 mW of power). They experienced minimal heating partly due to low power actuation and partly due to the continuous flow carrying away heat. Up to this point the location of the mixing was determined by the transducers, but Oberti *et al.* [206] used a large transducer at a much lower frequency (100 Hz) to vibrate the entire device while selecting the location of mixing via a T-junction. The authors did a careful and detailed analysis and determined that the sharp edges of the T-junction caused vortices in the flow that lead to mixing. Phan *et al.* also utilized geometric features in a channel to change the boundary conditions of the flow in order to produce turbulent flow [207]. They fabricated a microscale silicon nitride membrane with a hole etched through it, which was bonded to the bottom of a Y-channel, that generated strong streaming vortices for fast and homogeneous mixing. At the opposite end of the frequency spectrum, 1.54 GHz was utilized by Cui *et al.* [208] to achieve rapid (within 1 ms) and homogeneous mixing in a y-channel without geometric features (*see* Fig. 1.23).

Fluid pumping

One of the key problems in lab-on-a-chip devices is the ability to provide effective fluid flow against a resistance in a chip-sized device. We now examine

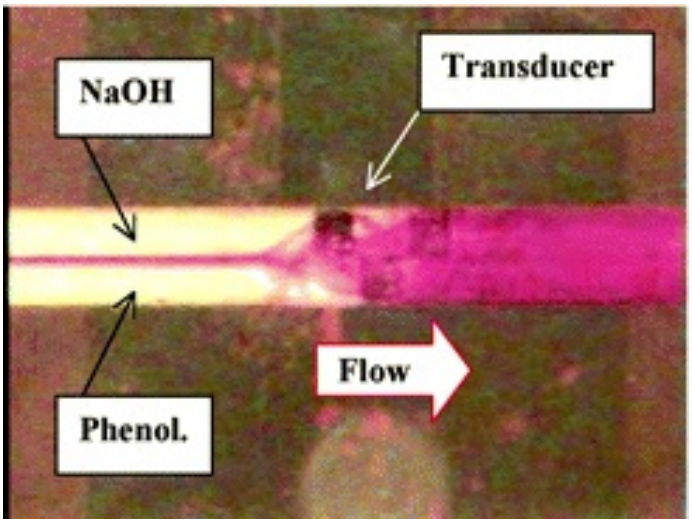

Figure 1.22: Laminar flow before the transducer (left side) and mixing flow after the transducer (right side) with an embedded piezoelectric transducer. A strong acoustic streaming effect is produced for more active and rapid mixing. Reprinted with permission from Yaralioglu *et al.* [205]. Copyright (2004) American Chemical Society.

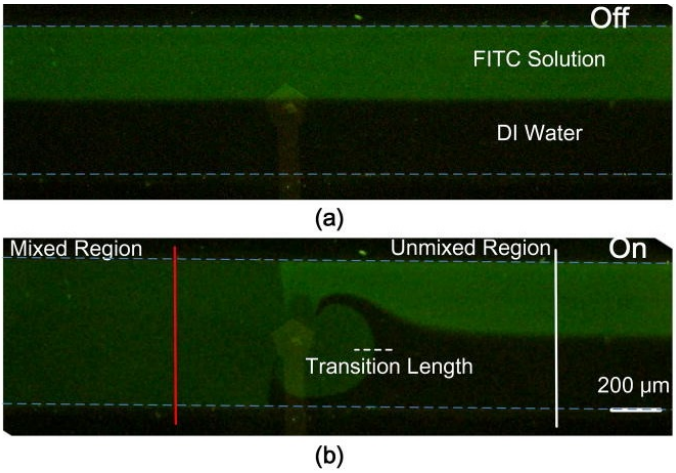

Figure 1.23: (a) Laminar flow and no mixing effect in the absence of acoustic waves. (b) Fast and uniform mixing of water and fluorescent dye in the presence of high frequency SAW within 1 ms. Reprint permits from Cui (2016) [208].

several approaches to this problem using acoustic waves.

Acoustic counterflow occurs when fluid in a channel is drawn opposite the direction of SAW propagation due to atomization at the fluid/air interface and coalescence upstream [209] (*see* Fig. 1.24). Masini *et al.* showed that fluid can be turned at right angles and split at an intersection in a 2D array of PDMS channels by this method [210]. Recently Shilton *et al.* performed mechanistic investigations of this technique [211]. The authors showed that the input power required for atomization in a channel did not increase over the frequency range 50–750 MHz. They also observed optimal SAW transmission through the channel when its width, W, was greater than $10\lambda_{\mathrm{SAW}}$. This allowed them to produce optimal counter-flow in very small channels by increasing the SAW excitation frequency. They found that

flow vortices in the channel scaled with the size of the channel if the frequency was adjusted to match $W = 10\lambda_{\mathrm{SAW}}$ (unsurprising since β^{-1} decreases with increasing f). Similar to Shilton's work on sessile drops in 2014, these findings could allow further miniaturization of SAW microfluidic devices. As an interesting side note: we have seen that viscosity also plays a role in acoustic attenuation (the cause of streaming vortices) and an earlier study [212] showed that channel vortices were reduced in length with increasing viscosity, which again demonstrates the similar effects of viscosity and acoustic actuation frequency.

Acoustic counter flow cannot be used for closed channel systems where no free air/liquid interface exists. However, conventional pumping (rather than counter-flow) is difficult using SAW since the maximum amplitude of a travelling SAW on a LN substrate is $\sim$10 nm, which produces negligible peristaltic effect in a microscale channel. Instead fluid flow is due to acoustic streaming that tends to promote vortices, which in turn lead to circulation rather than unidirectional flow across the channels entire cross section. A possible solution to this problem was presented by Tan, *et al.* [201, 213] They changed the width of the channel relative to the wavelength of sound in the fluid and observed uniform pumping of fluid flow when $W < \lambda_f$. This first demonstration of SAW-based uniform pumping was accomplished in a short, isolated channel segment with no inlet or outlet. Subsequently, Schmid *et al.* [214] demon-

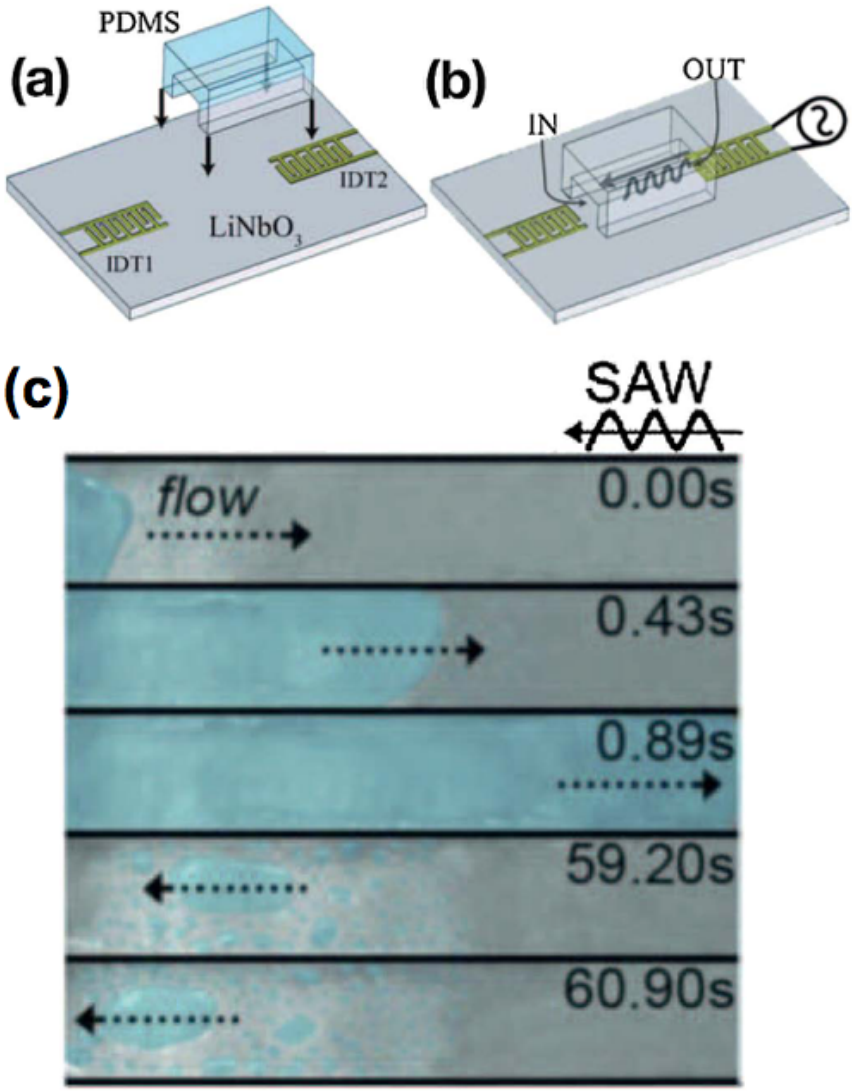

Figure 1.24: A PDMS channel was bonded onto a LN substrate with two straight IDTs at two ends of the channel, as shown in (a), (b). The liquid performed counterflow relative to SAW propagation due to atomization at liquid-air interface and coalescence upstream, as shown in (c).

strated a continuous, closed-loop SAW-driven PDMS microchannel pump. Lossy interaction between SAW and PDMS was avoided by elevating the PDMS on water and glass coupling layers. They used a high frequency device (142 MHz) and a wide channel (1 by 0.75 mm) so that λ_f was much greater than W, which would seem to contradict Tan's conclusions. This inconsistency has not been explained and further work is required. A different type of SAW-driven pump device using an open-circuit channel constructed from glass (bonded directly to LN) was presented around the same time by Langelier *et al.* [126] ($W > \lambda_f$ again in this device). The elimination of extra coupling layers from the system greatly increased the pumping efficiency due to increased SAW transmission. It remains unclear how acoustic streaming creates unidirectional flow overall in these channels despite the presence of vortices in the path of the SAW.

In addition to mixing, the nanoslit demonstrated by Miansari *et al.* [75] was shown to perform SAW-driven pumping at a remarkably large 1 MPa of pressure. The capillary filling rate of the hydrophilic LN nanoslit was increased by 2–5 times when SAW radiation was applied in the same direction as capillary filling, while the nanoslit could be drained against 1 MPa capillary pressure when SAW radiation was applied in the opposite direction (*see* Figures 1.25 & 1.26). Miansari was also able to pump an isolated droplet back and forth within the nanoslit using the same

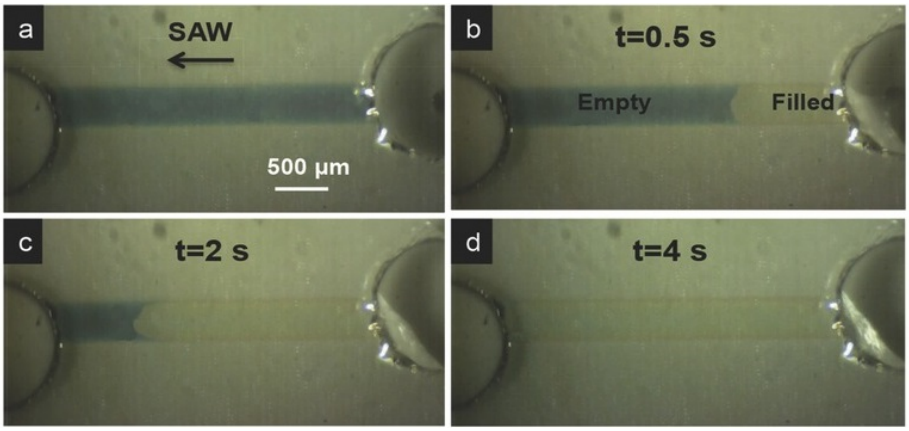

Figure 1.25: LN nanoslit filling with water induced by SAW propagation from the right end of the nanoslit. The capillary filling rate of the hydrophilic LN nanoslit can be increased by 2–5 times when SAW is applied in the same direction. The magnitude of SAW is in the same order as the channel height so that it has a unique pumping mechanism different from SAW-induced pumping in microchannel, which needs to be further investigated. Reprint permits from Miansari (2016) [75].

mechanisms. The reduction of channel dimensions to the nanoscale may remove previously unknown limitations of microchannel pumping.

1.4.4 Particle Manipulation in Closed Channels

SAW-based particle, droplet, and cell manipulation has been a popular topic of investigation in recent years, prompting several reviews on the subject [12, 215, 216, 217, 14]. Here, we will review the latest SAW-based manipulation results in four main areas: concentration and focusing, separation and sorting, patterning and manipulation, and droplet production and splitting. We will then cover the use of glass capillary tubes as an alternative to other ways of forming channels.

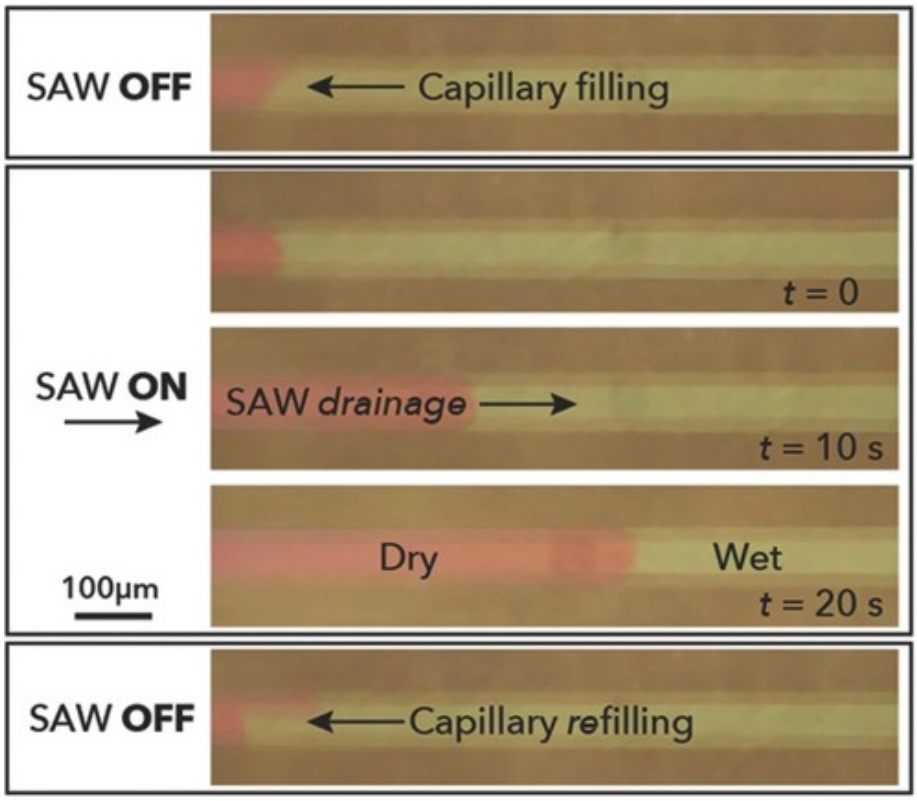

Figure 1.26: Water drainage in LN nanoslit induced by SAW. SAW drained the nanoslit against 1 MPa capillary pressure when SAW was applied in the opposite direction of capillary filling. It showed powerful SAW-induced pumping effect in a nanoscale channel. Reprint permits from Miansari (2016) [75].

Concentration and Focusing

Particles and cells that have been focused within a flow cross section can then be easily detected by various methods. This process, cytometry, is a major capability required in biological assays and future lab-on-a-chip devices. Many focusing techniques have been investigated, including hydrodynamic, electrokinetic, and dielectrophoresis (DEP) methods. However, the SAW method is simple, highly

efficient, contact-free, and can be applied to focus a wide variety of microparticles. Furthermore, the transparency of LN makes it feasible to integrate with most optical techniques.

Shi *et al.* [218] demonstrated particle focusing in a microchannel by depositing two IDTs on each side of the channel. The channel width and the wavelength of SAW were specified so that a SSAW formed across the channel width with a single pressure node located at the channel center, collecting particles at this node (*see* Fig. 1.27). Zeng *et al.* [219] then integrated Bragg reflectors (BR) with the focusing device to enhance SSAW formation. Air cavities were also introduced on both sides of the microchannel and SSAW propagation area in order to reduce absorption by the PDMS walls. Jo *et al.* [220] utilized these focusing capabilities to perform density-based particle separation.

To perform SSAW-based on-chip flow cytometry, 3D focusing capabilities are desired in order to maintain constant focal depth during cell detection. Shi *et al.* [221] discovered that the acoustic radiation force in the z-direction (perpendicular to the device plane) is also non-uniform. Through theoretical and numerical calculations, they showed that this non-uniformity could be used to force particles toward the plane of maximum acoustic kinetic energy which had a constant height with respect to the substrate. Experimental results agreed with these calculations and they were

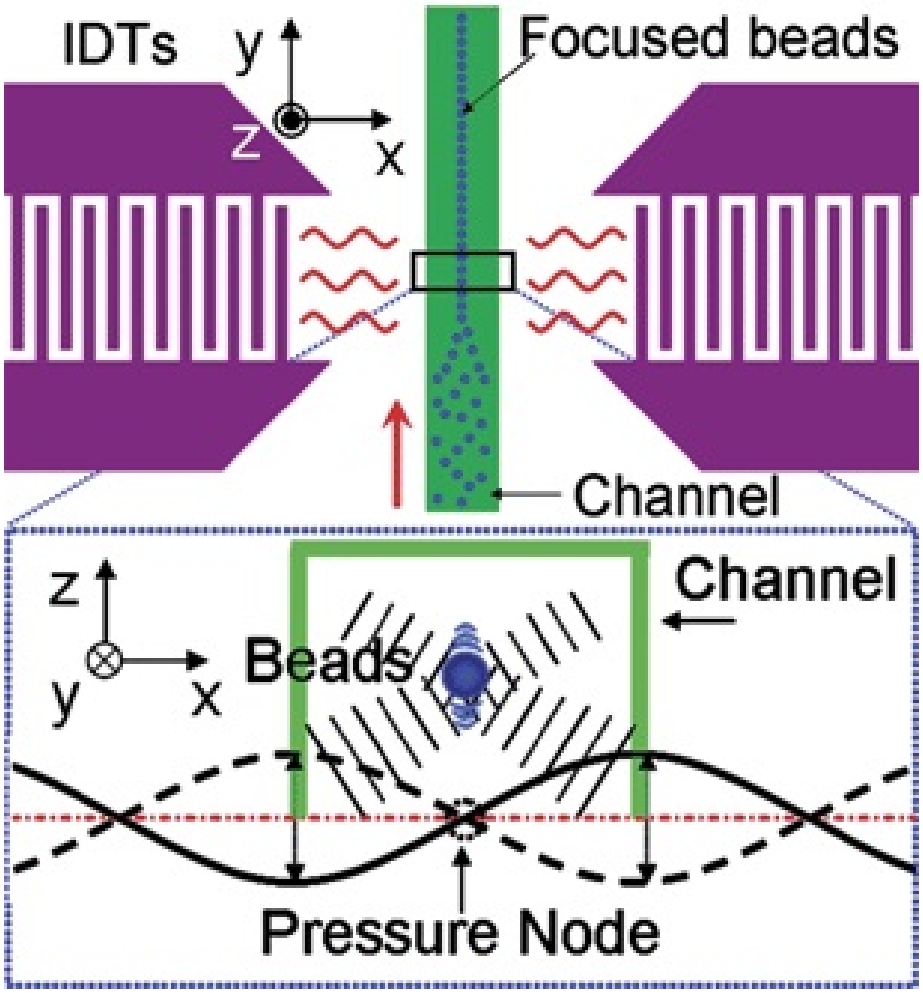

Figure 1.27: Schematic and working mechanism of the SSAW-based focusing device. The IDTs were on the opposite side of the channel. The width of the channel was matched with the wavelength of SAW to generate single pressure node at the center of the channel. The acoustic radiation force led beads into pressure nodes to perform particles focusing. Reproduced [218] with permission from The Royal Society of Chemistry.

able to perform SSAW-based 3D continuous particle focusing in a microchannel.

TSAW can also be used for particle focusing, as demonstrated by Tan *et al.* [213]. A single IDT generates a SAW that is subsequently reflected from the opposite channel wall that generates a standing acoustic node within the channel if conditions are engineered correctly. Relatively weak SAW were used in Tan's work to focus particles in an initially homogeneous suspension into equally spaced nodal lines parallel to the channel with a separation of one-half the wavelength (*see* Fig. 1.28). The dependence on wavelength allowed particles to be focused to different locations based on the applied frequency (using a slanted IDT). Witte *et al.* produced a similar device, but added a glass superstrate [222]. A slanted IDT allowed for small differences between superstrates to be compensated for by tuning the resonant frequency. This kind of technique will allow cytometry within disposable inserts, which could allow for quick, clean processing of many samples in sequence on a single device.

Tan *et al.* presented a unique way of performing cytometric functions using TSAW streaming and non-nodal radiation [223]. A double-aperture FIDT enabled asymmetric actuation so that particles could be directed to the left or right as they are propelled along the channel. They also milled the channel cross section into a trapezoidal shape that greatly reduced the formation of standing waves (similar to

the effect of an anechoic chamber) so that particles would not be trapped along nodal lines.

Separation and Sorting

The goal of particle separation and sorting is to lead specific particles from their original streamlines to targeted streamlines which finally flow into a sorted outlet. Related SAW techniques can be divided into two general categories: TSAW-based and SSAW-based. Franke *et al.* [224] first presented continuous droplet sorting in a PDMS microchannel using TSAW. Droplets flowed passively into one channel, but were pushed into the path of a second channel by acoustic streaming when actuated. However, this technique cannot inherently differentiate between particles and thus can only temporally sort. Destgeer *et al.* [225] were able to continuously isolate particles of a single size from an assortment of particles by utilizing the acoustic radiation force of TSAW. As mentioned earlier, detachable superstrates are potentially useful for applications where biological samples are processed. Ma *et al.* [226] developed a device similar to Destgeer *et al.*, but with a PDMS superstrate that contained the microfluidic channels. They also developed a platform for separating particles of similar sizes but with different densities using TSAW of carefully selected frequency [227].

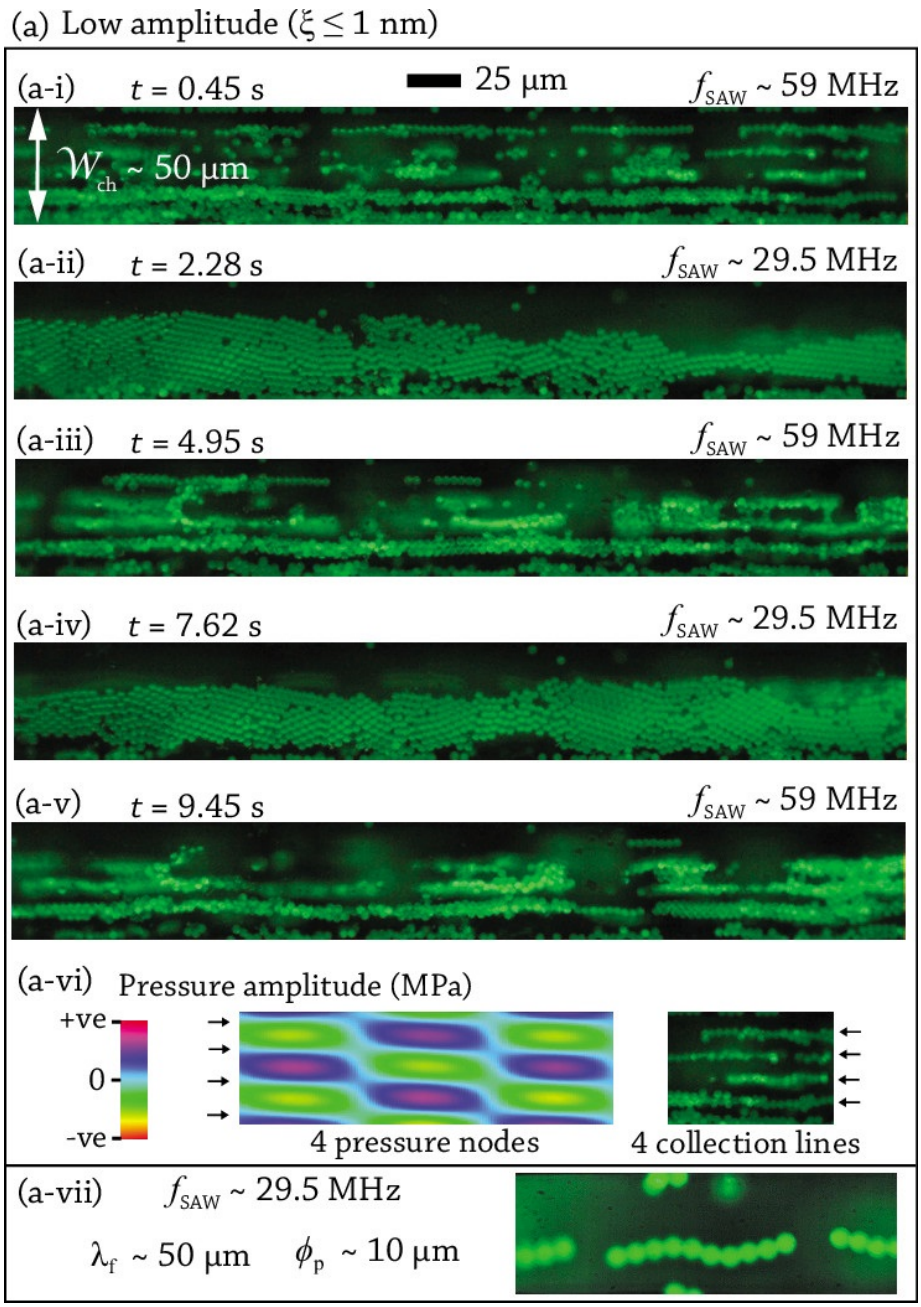

Figure 1.28: Time lapse images of TSAW focusing in a microchannel at amplitudes below 1 nm. Specific lines of focus could be selected by applied frequency and were quickly and easily switched, in this case between 29.5 MHz and 59 MHz. Reprint permits. Tan (2010) [213].

TSAW methods displace particles from their original laminar flow path, but SSAW methods sort particles into one or more nodal paths regardless of their original path. Also, recall that the acoustic radiation forces due to TSAW and SSAW differ strongly in their dependence on particle size (*see* Eqns. 1.6 and 1.5). Size-based [228, 229, 230, 231] and density-based [220] particle separation have been demonstrated. Numerical studies on SSAW in microchannels has further explained the mechanism of particle separation. A 2D model helped reveal the effect of boundary vibrations and channel properties on particle aggregation near PDMS channel walls [232].

Wu *et al.* [233] further scaled down the particle separation technique to submicron scale. Tilted-angle SSAW was utilized to separate 500 nm and 110 nm particles, showing a finer resolution for particle separation than the standard SSAW configuration. Next, Kishor *et al.* [234] demonstrated integration of tilted-angle SSAW with a photoacoustic detection technique into an integrated microfluidic platform capable of size-based separation, concentration, and quantitative detection of microparticles. Such integrated platforms show promise for future lab-on-a-chip systems that utilize the functionality described in this review.

The ability to separate microscale particles has also been shown using SFITs. Destgeer *et al.* [225] was able to separate particles into three size groups by placing SFITs with two distinct frequency ranges on either side of a microchannel. Thus,

TSAW could be generated at desired frequencies and locations. Recently, Park *et al.* [235] demonstrated bidirectional, multichannel droplet sorting using SFITs. They also added a new functionality: dynamic formation of temperature gradients in the channel.

In a more biologically relevant proof of concept, Nam *et al.* [236] demonstrated a device to separate blood cells from platelets using SSAW. Pressure nodes were set up near the two side walls and blood cells experienced larger acoustic radiation forces, since they are larger than platelets, and moved to the sides of the channel while platelets remained at the center. The authors reported platelet purity up to 98% using this method. They were also able to separate beads of polymer encapsulated cells based on their density.

Using focused SAW of higher frequency (up to 636 MHz), Collins and Ma [237, 238] recently demonstrated size-selective particle concentration—as small as 300 nm—via acoustic streaming. In one arrangement, streaming and radiation concentrate particles to one edge of a flow (*see* Fig. 1.29). Note that size selective concentration in sessile drops has been demonstrated down to 200 nm [164]. Concentration generally refers to separating many particles at once into two or more groups, while sorting considers one particle at a time.

Depending on the position and design of the acoustic source, both SSAW

[239, 218] and TSAW [240] devices can be used for cell sorting, as the acoustic actuation area in the fluid can be well controlled. A high-throughput acoustic cell sorter using focused SAW was introduced by Ren *et al.* [241] An FIDT allowed them to generate SSAW with higher energy intensity and a narrower beam width resulting in a larger actuation force and a higher sorting resolution (*see* Fig. 1.30). According to their data, the FIDT exerted 4–9 times larger acoustic radiation force than did the straight IDT, indicating that to attain the same sorting effect an FIDT would require only 10–20% of the input power of a straight IDT. Collins *et al.* [242] demonstrated a very similar system only they used TSAW rather than SSAW and used a higher frequency, 386 MHz, to achieved even finer resolution particle sorting (similar to Fig. 1.30), but with only one FIDT). They shrunk the actuation area to a few tens of micrometers with highly focused SAW that produced large acoustic gradients. With pulse durations of $\sim$100 μs, they were able to nudge particles as small as 2 μm from their path without altering the path of the next particle in sequence.

Patterning and Manipulation

The ability to arrange cells and microparticles into desired patterns is important for many biological applications, for example in tissue engineering [243]. Patterning of particles in one and two dimensions using SAW has been recently

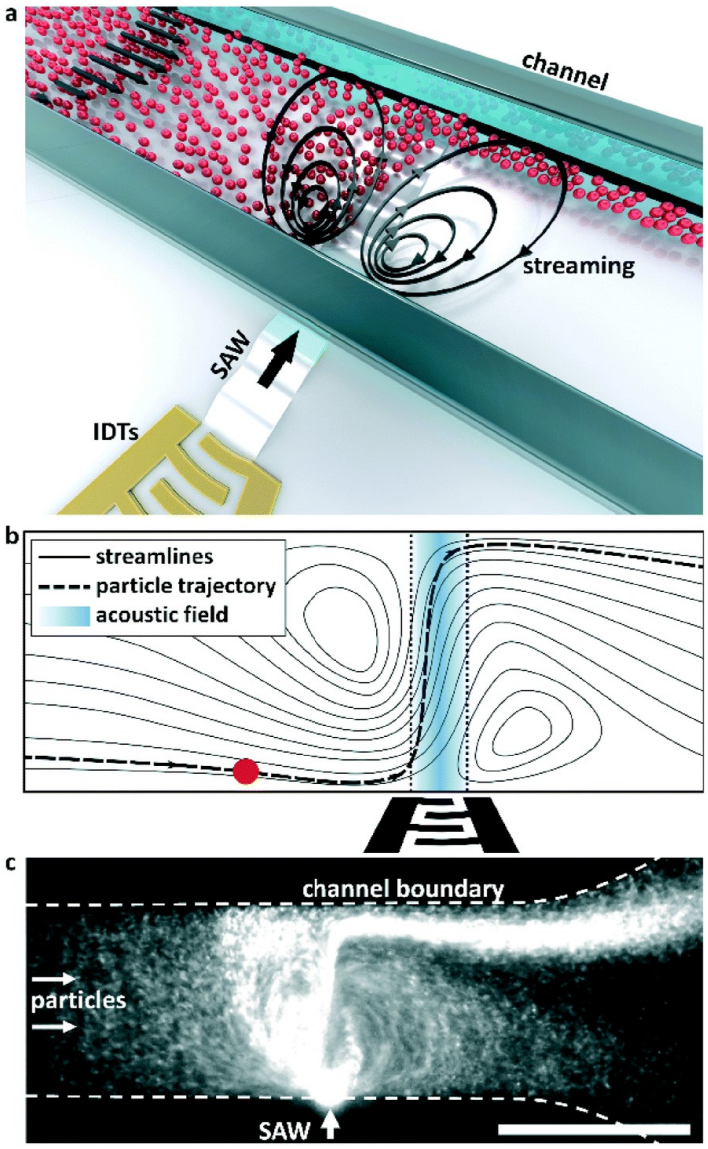

Figure 1.29: Principle of SAW based nanoparticle focusing of using SAW. (a) A conceptual diagram: the combined streaming field and acoustic radiation forces resulting from the coupling of substrate vibrations produced by an IDT on a piezoelectric substrate results in focused particle displacements. (b) A particle (red) is displaced relative to the fluid streamlines by the acoustic radiation force as it passes through a focused SAW beam. The streaming serves to direct the particle laterally to the acoustic beam and maximize its exposure to the acoustic gradients in its periphery. (c) A continuous influx of 300 nm particles is focused in a low velocity flow. Adapted [238] with permission from The Royal Society of Chemistry.

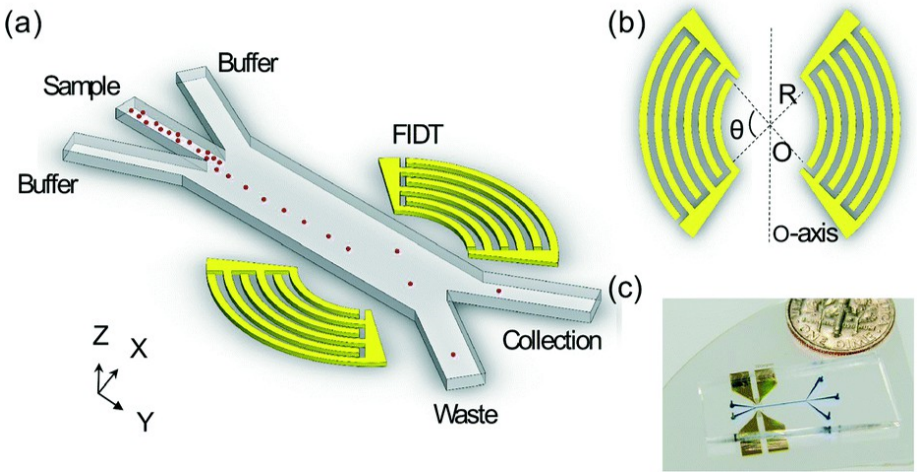

Figure 1.30: (a) Schematic of the SSAW-based sorter excited by FIDT. (b) The concentric geometry of the FIDTs. O is the focal point and the two sets of FIDTs is O-axis symmetric. (c) An optical image of the high-throughput SSAW sorter. Adapted [241] with permission from The Royal Society of Chemistry.

demonstrated. Wood *et al.* [244] first performed 1D patterning (also known as alignment) of particles using SSAW in microfluidic systems. As a next step, they performed 2D patterning using two pairs of counter propagating IDTs in orthogonal directions [245]. They used a liquid coupling film similar to that used by Schmid [240], which cannot support continuous operation due to a lack of inlet and outlet ports. Shi *et al.* [246] enabled continuous 1D and 2D patterning by bonding PDMS directly to the substrate to form a closed channel. Building on this concept, O'Rorke *et al.* [247] achieved translation of a patterned array of particles by modulating the frequency of the SAW. The pattern could be translated laterally by up to one wavelength ($\sim$118 μm in this case—a standard, straight $\sim$30 MHz device) by changing the frequency in small increments across the bandwidth of the IDT.

In the last five years, other forms of patterning using SAW have been presented. Ding *et al.* [248] performed tunable 1D and 2D patterning of microparticles using slanted-finger IDTs (SFITs), which offer a much larger resonant frequency bandwidth than the standard IDTs used for translation. They showed that, by tuning the frequency applied to the SFITs, they could vary the line spacing of a 2D pattern, for example, from 141 μm to 250 μm. Another novel patterning capability was added by Collins *et al.* [249] who produced patterning in only a desired section rather than over the entire area between two transducers. They engineered

nanosecond pulse signals whose duration was less than the time-of-flight between transducers so that standing waves were only set up in a central region of tunable width. Yet another degree of freedom was demonstrated by Tian *et al.* [250] who could control both the spatial patterning and the shape of microdroplets themselves, which compose the pattern.

Particle patterning into defined nodal positions is useful, but in addition, some applications require the movement of particles to arbitrary locations. This has been accomplished with a technique known as acoustic tweezers, an old concept [251, 252] receiving renewed interest. Compared to optical tweezers, acoustic tweezers require lower power density, are bio-compatible, and are amenable to miniaturization. Nodal position can be tuned by either phase shift [253] or frequency modulation [254, 255] (*see* Fig. 1.31). More recently, Devendran *et al.* [65] used an acoustic field combining both traveling and standing wave components along with a swept excitation frequency to collect and isolate particles of different sizes in a static fluid volume. The varied tools created through more and more complex acoustic field control are bound to be useful in other fields where small particles need to be manipulated. One such example is the work by Chen *et al.* [256] who used acoustic tweezers to trap cells in a micro-channel for cell enrichment. The cells accumulated at SSAW nodes as more and more fluid was passed through the channel. They reported an increase

in concentration of originally dilute red blood cell samples (10^5, 10^4 and 10^3 cells per mL) by a factor of 100–1000.

We point the interested reader to a more detailed review of dynamic ultrasonic field control presented by Drinkwater [257]. It includes in-plane manipulators, beam manipulators, and planar array manipulators used for transportation and rotation of individual particles as well as biosensing and microscale assembly in channel-less microfluidic devices.

Droplet Production and Splitting

SAW actuation has become a promising tool for droplet generation, droplet splitting, and droplet manipulation because it is inherently robust and contamination-free. The general idea is to apply acoustic streaming or acoustic radiation force induced by SAW near a fluid-fluid interface in order to produce drops of a dispersed phase within a continuous phase (*see* for example the bottom left of Fig. **??**).

Schmid *et al.* [258] integrated an IDT at the junction of flow-focusing channels as seen in Fig. 1.32. The magnitude of SAW power—rather than channel geometry or flow speed—was used to regulate droplet size. This method relies on increased pressure at the lower inlet due to acoustic streaming. Collins *et al.* [6] used an FIDT to demonstrate droplet generation from a T-junction in order to encapsulate

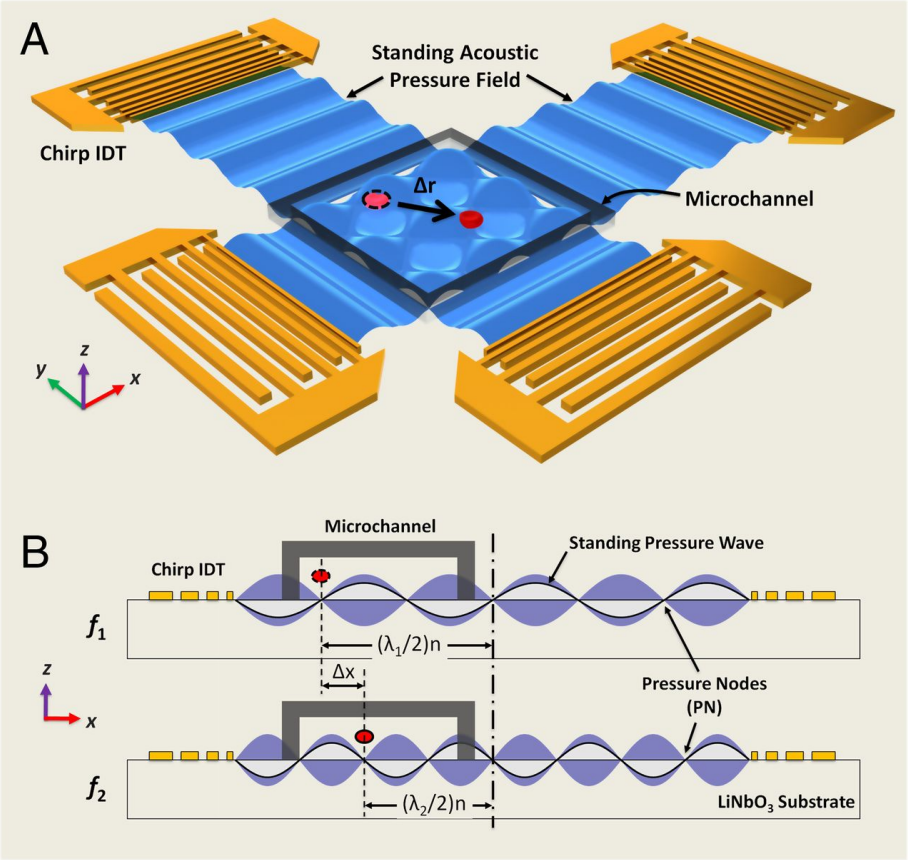

Figure 1.31: Two-dimensional particle manipulation with frequency-control using chirped IDTs. A microchannel was bonded near one side of chirped IDTs. Particles in the pressure nodes were forced to move by changing the location of pressure nodes, which were dependent on the frequencies of SAW [254].

concentrated particle suspensions. A low-power SAW was activated to move and concentrate particles at the interface, then a high-power pulse was used to deform the interface and generate a water-in-oil droplet with encapsulated particles. Based on a similar device configuration, Brenker *et al.* [259] experimentally and numerically explored the working mechanism of the FIDT-induced T-junction droplet generator. They identified three distinct droplet production regimes depending on the relative speeds of the continuous and dispersed fluid flows.

SAW-induced drop splitting in microchannels has also been demonstrated recently. Sesen *et al.* [260] performed water-in-oil plug steering and real-time on-demand plug splitting using an FIDT-integrated Y-junction microfluidic device. Two FIDTs (one on each side) were pointed directly at the junction from the direction perpendicular to the inlet channel. Precise acoustic radiation pressure on the oil/water interface allowed the plug to be steered entirely into one outlet or the other or to be split into desired proportions (without actuation the plug would naturally split in half). Jung *et al.* [261] used SFITs instead of FIDTs to direct acoustic radiation pressure to a specific region for droplet splitting based on the input frequency. Sesen *et al.* [262] applied pulsed acoustic streaming in a branched channel to suck a portion of fluid into it thus splitting droplets as they passed (*see* Fig. 1.33).

Sesen *et al.* [263] also reported on-demand droplet merging using focused

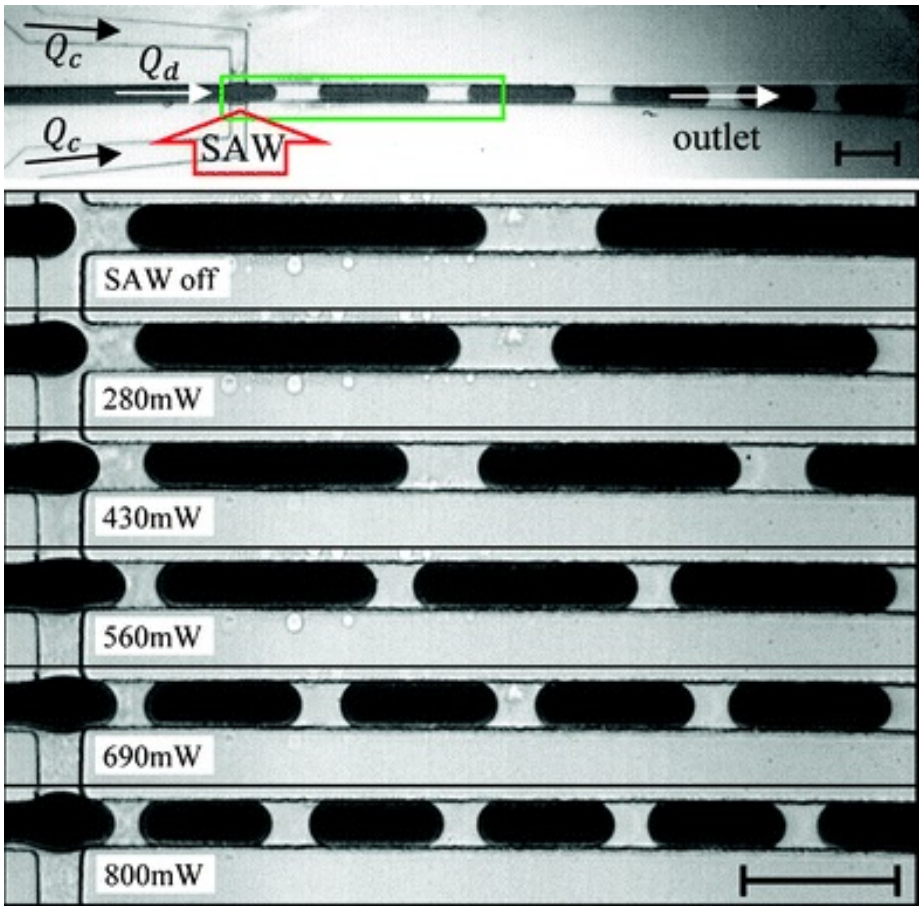

Figure 1.32: SAW was applied at the flow-focusing droplet/plug generation region and regulated the plug size by different SAW power. Stronger SAW power reduced pinch off time due to increased interface pressure, which in turn reduced the size of plugs. Reproduced [258] with permission from The Royal Society of Chemistry.

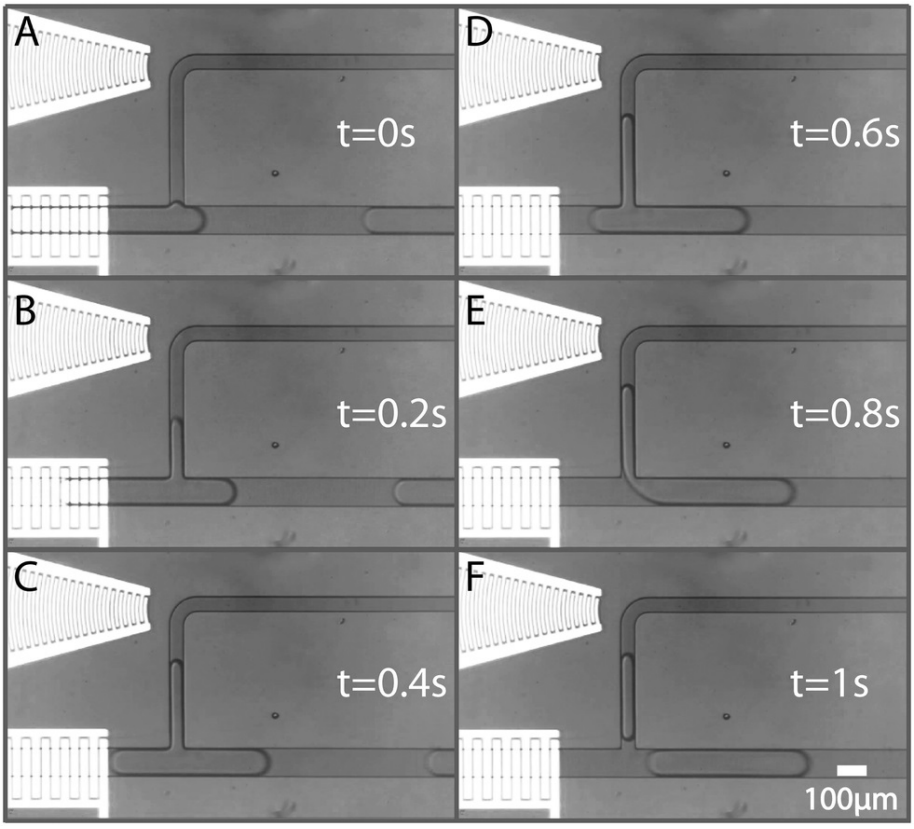

Figure 1.33: Droplet splitting in closed branched microchannel induced by SAW. FIDT-induced acoustic streaming produced a pressure offset between the main channel and the branched channel, and performed as a micropipette in the closed channel. Reproduced [262] with permission from The Royal Society of Chemistry.

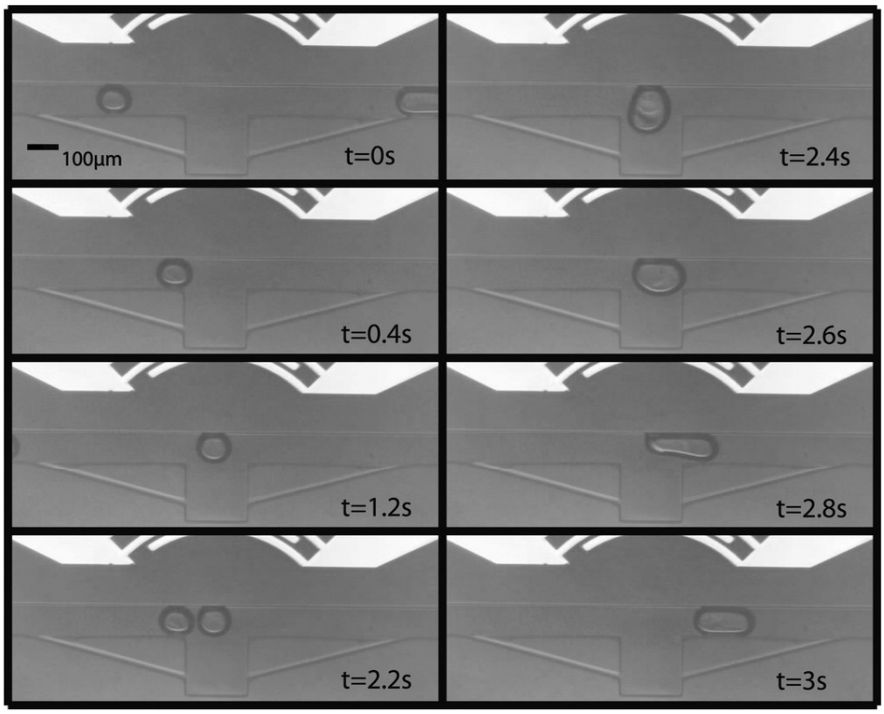

Figure 1.34: Time lapse images of the droplet merging experiment. The first droplet is immobilized across the FIDTs while the next droplet comes and merges with the stationary one. The merged droplet travels downstream because the acoustic energy in the system is not enough to hold a bigger volume droplet. The FIDTs is placed at the right-side while the oil flow is from left to right. Reproduced [263] with permission from The Royal Society of Chemistry.

SAW. Acoustic radiation forces generated from an FIDT were used to stop the progress of a selected droplet such that successive droplets merged until a certain volume was reached (*see* Fig. 1.34).

Jung *et al.* [264] demonstrated on-demand droplet capture and release at specific microwells using SFITs. At different frequencies, different parts of the SFITs resonated corresponding to the designed wavelength at that location. Thus the

location of a particular microwell could be selected and droplets could be pushed into or out of it as desired.

Particle Manipulation in Capillary Tubes

We have already covered the phenomena where by nodes and anti-nodes form in acoustic resonant cavities which we have called channels. Capillary tubes can also be used as resonant cavities. They can be bonded to a piezoelectric substrate often more easily than a channel can be fabricated in the substrate or in some superstrate. Being widely used in other industries capillary tubes are easily obtained in many sizes and shapes as ready to use parts that both have well known properties and are disposable.

A review by Lenshof etal. presents a good summary of the work done in this area in the section called "Capillaries" [265]. They cover the focusing and trapping of particles and the use of these techniques in bio-chemical assays. Another good example, not found in the above review, is the work of Grundy *et al.* [266]. They applied this technology to rapid diagnostics and were able to reduce, for example, the agglutination time of bacteria from 4 hours to 5 minutes by encapsulating samples within droplets within a capillary tube. Work by Araz *et al.* [267] is also valuable due to the simplicity of the design in which particles are separated based on size

and/or density along the length of the capillary due to bending modes produce by actuation of a C-shaped PZT plate.

We also wish to highlight two works that have been published since the review by Lenshof. Gralinski *et al.* [268] have performed numerical simulations of particle trapping in capillaries with circular cross sections. They vary several design parameters and discuss the advantages of a design containing 4 PZT transducers for particle focusing in the center. A follow up paper [269] presents experimental results and also includes patterning along the length of the capillary tube. Recently, Mao *et al.* [270] published work on coupling SAW into a capillary tube bonded to a LN substrate. They showed that in this case not only are nodes established due to acoustic radiation, but also acoustic streaming establishes a single vortex which allowed them to focus particles in the nanometer size range. We cover this work further in the following section.

1.5 Nanofluidics

When we zoom into the nanometer scale, several interesting and fundamental physical and chemical phenomena become accessible, including nonlinear electrokinetic flow and ion focusing [271, 272], nanocapillarity [273], mass transport in nanoscale spaces [274, 275], and electrical double layer (EDL) overlap effects

[276, 277, 278]. DNA stretching [279], detection of single DNA molecules [280], water purification [281], and many other practical applications have been demonstrated using these effects.

Several review papers have been published about nanoscale fluid transport [282, 283, 275, 284] and flow in CNTs [285, 286, 287] in the last ten years. Extremely high aspect ratio, nanoscale inner diameter, and molecularly smooth hydrophobic graphitic walls make CNTs an ideal applicable material and platform for investigating nanofluidics. Numerical molecular dynamics simulations of nanopumping through CNTs has been presented by Insepov *et al.* [288], Longhurst *et al.* [289], and Rinne *et al.* [290], showing that the nanopumping phenomena can be driven by temperature, AC electric fields, and the friction between gas particles and nanotube walls induced by SAW.

In addition to CNTs, inorganic nanotubes have been synthesized for use as a novel platform for nanofluidics [291]. Their advantages included a controllable inner diameter from 1 to 100 nm, facile functionalization of the inner and outer surfaces, and tunable compositions and aspect ratio. These features effectively provide the ability to mediate the ionic and electrostatic environment, both spatially and temporally. These forces are dominant at the femtoliter scale, which makes inorganic nanotube synthesis a powerful tool for femtoliter biological and chemical analyses.

Acoustic *nano*fluidics exhibits significant differences from acoustic *micro*fluidics and has not yet been as well developed [292]. However, early results are promising. Insepov *et al.* [288] used molecular dynamics simulation to predict a new nanopumping effect where SAW at the surface of a CNT cause gas flow within. The SAW-induced peristaltic motion along the CNT surface was predicted to pump the gas at 30 km/s. At these small scales, light can be used to create sound. Lin *et al.* [293] showed optical generation and spatial manipulation of nanoacoustic waves with nanoscale spot sizes. Pezeri *et al.* [294] was able to optically generate GHz-frequency shear acoustic waves in liquid glycerol. Van *et al.* [295] generalized nonlinear ultrafast acoustics at the nanoscale, reviewing both main properties of nonlinear ultrafast acoustic propagation and recent results. These initial investigations have set the stage for further practical applications.

The fabrication of nanoslits and nanochannels [284], fluidic devices with nanometer scale in one or two dimensions, respectively, has been demonstrated [296, 297, 298] and applied to a number of applications such as DNA stretching [279, 299, 300] and single DNA molecule dynamics [301, 302], due to their flexibility of channel shape and surface properties. More specifically for acoustic nanofluidics, room-temperature bonding of LN to silicon wafers was demonstrated by Takagi *et al.* [303] and has been widely used to achieve enclosed nanochannels for the acoustic propagation of

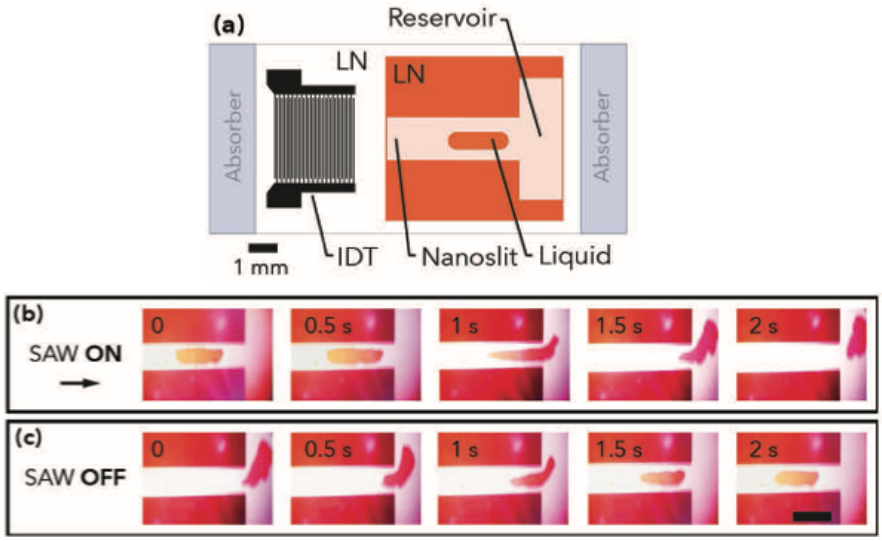

Figure 1.35: Manipulation of a liquid drop within the nanoslit based on SAW-driven acoustic streaming and capillary forces. When SAW was on, the SAW-driven acoustic streaming overcame the capillary force in the T-shape channel and pushed the liquid drop into the reservoir. When SAW was off, the capillary force led the liquid drop into the targeted nanoslit. Reprint permis. Miansari (2016) [75].

fluid.

Recently, Miansari *et al.* [75] developed a novel room temperature LN/LN bonding technique and demonstrated a SAW-induced nanoslit platform for pumping nanoscale flows at up to 1 MPa (*see* Fig. 1.25), manipulating 10 fL drops (*see* Fig. 1.35), and separating nanoscale particles by size. The mechanisms responsible for these results need to be further investigated and explained in the future.

1.6 Acknowledgments

This chapter, in part, is a reprint of materials appearing in Lab on Chip 2018. Connacher, William, Zhang, Naiqing; Huang, An; Mei, Jiyang; Zhang, Shuai; Gopesh, Tilvawala; Friend, James. "Micro/Nano Acoustofluidics: Materials, Phenomena, Design, Devices, and Applications" Lab on a Chip 18.14 (2018): 1952-1996. The dissertation author was one of the investigators and authors of this paper.

Chapter 2

Waveguides

2.1 Why waveguides?

As discussed in Section 1.2, SAW devices are usually designed so that waves propagated along the direction correspond to different rotated cuts of the material. However, materials most commonly used in acoustofluidics are anisotropic in nature due to their crystal structure. The 128° YX LN, for example, can generate SAWs of the same frequency and amplitude only in one direction. Any veering from the primary propagation direction is affected by *beam steering* (explained later), SAW velocity or frequency, and the SAW's electromechanical coupling coefficients. Kurosawa *et al.* [184] demonstrated in using SAW along both the X and Y axes of a 128°

YX LN wafer that the vibration displacement and velocity were 250% higher along the X axis compared to the Y axis.

Though efforts had been made to overcome the anisotropic nature of the piezoelectric substrates, as Guo *et al.* [64] and Devendran *et al.* [65] illustrated perpendicular IDT pairs at 45° to the X-axis to create an orthogonal standing wave at the same frequency, the issue of beam steering remains: beam steering is lateral transport of the acoustic wave at an angle to the intended propagation direction, usually toward a specific crystallographic axis of the substrate, such as the X-axis in 128° YX LN for SAW propagating at some angle with respect to this axis. The superior electromechanical coupling present along the X-axis and the unmatched wave velocities along the X- and Y-axis are responsible for the phenomena in this case. Consequently, the design, performance characteristics and ultimately efficiency of high frequency SAW devices made using LN substrates are typically limited to the X axis direction for acoustic wave propagation.

Another problem with SAWs on LN is *lateral diffraction*, a major constraint in current SAW devices inevitably resulting in energy dissipation along certain directions. As shown in Section 1.3, SAW propagates as largely parallel wavefronts in the near-field region (Fresnel region); while in the far-field region (Fraunhofer region) it is broadly diffracted. Though one may seek to minimize its effects by the choice of

a low diffraction propagation direction, there are situations in which fluid or particle manipulation at disparate locations in a micro device may be expected. The difficulties in controlling the direction of wave propagation make these applications inefficient as well [304].

However, these limitations may all be overcome by the use of waveguides for such surface waves, where the term waveguide implies a geometrical structure which confines the lateral extent of SAWs. Wave diffraction, which is one of the most important difficulties associated with wide surface wave propagation, is thereby automatically prevented as the field cross section associated with the waveguide remains constant as the wave travels. As long as the radius of the bend is not too small, the propagating wave will remain bounded to the guiding structure.

Waveguides have been widely utilized in the applications of long delay lines [305] and structural health monitoring [306, 307], while in the context of acoustofluidics is absent for two reasons. In some applications, losses due to waveguides can be significant, although sometimes wide-beam surface waves on the material can be even lossier. The other reason could be the question of whether or not waveguides are worth their design and fabrication difficulty to meet current device requirements. Nevertheless, current SAW devices generally perform single functions: mixing [202, 198], sorting [239, 240], concentration [218, 223], pumping [214, 126]

and so on. When it inevitably comes to more sophisticated and multifunctional design, waveguides can be called upon, due to the ability of waveguides to confine and control the wave propagation.

2.2 Types of waveguides

There are mainly three types of waveguides [304]:

1. Overlay waveguides: a thin film of another material is deposited on the substrate,

2. Topographic waveguides: a locally defined structure from the substrate surface itself,

3. Waveguides that produces a local change of the properties of the substrate instead of its geometry.

Flat overlay waveguides may be the most well known, as they have been thoroughly analyzed and experimentally utilized [308]. The central region in each case is considered the relatively low-velocity (slow) wave region, so that the SAW field will be laterally confined in the central region: any SAW exiting the slow region will be forced to speed up, thus caused to turn back into the slow region and away from the fast region. In the strip waveguide (*see* Fig. 2.1(a)), the strip itself is a material

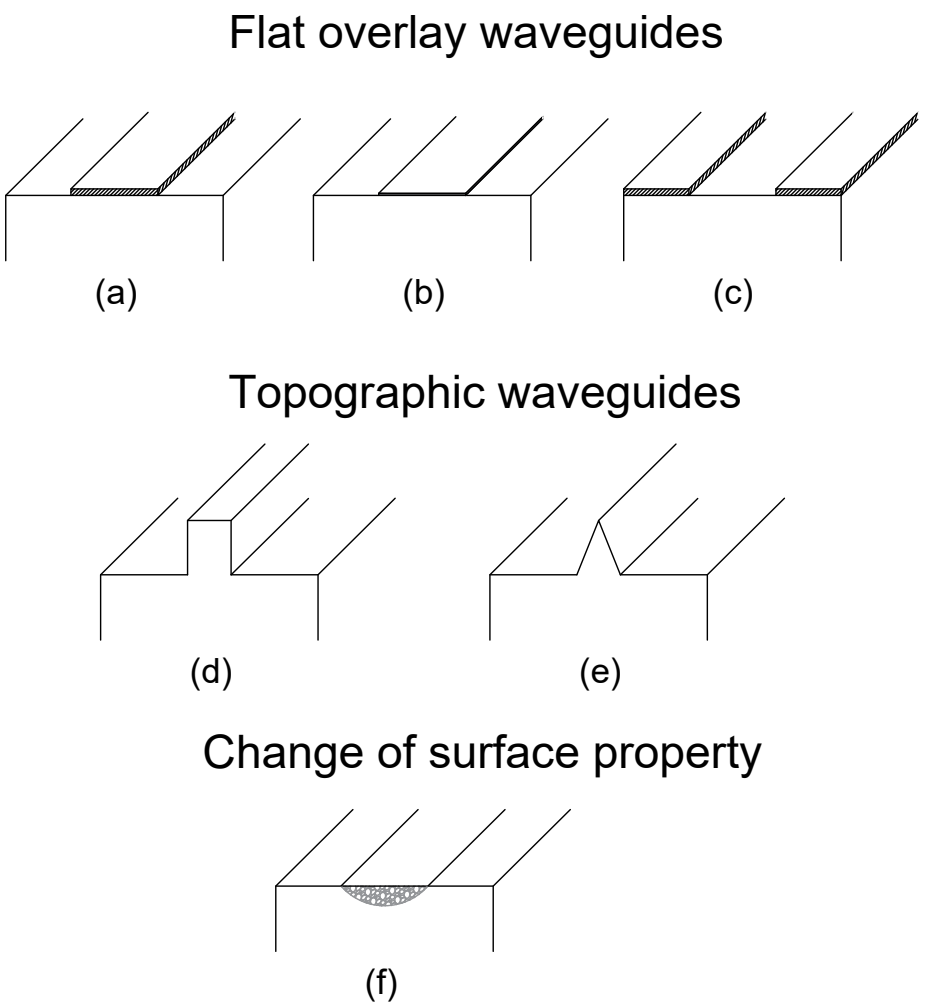

Figure 2.1: Various types of waveguides for SAW. Flat overlay waveguides: (a) strip, (b) shorting-strip, (c) slot. Topographic waveguides: (d) rectangular ridge, (e) wedge. Change of surface property: (f) in-diffused or ion-implanted, (Figure redrawn from the paper of Oliner *et al.* [304])

in which SAW travels slower than in the substrate. The shorting-strip waveguide (*see* Fig. 2.1(b)) is made of a conducting layer upon and in contact with the piezoelectric substrate. The conducting thin film short-circuits the electric field associated with

the piezoelectric SAW, producing a slight decrease of the wave velocity under the strip. It is also known as the $\Delta v/v$ waveguide, as the velocity is reduced by the shorting strip in an amount directly dependent upon the electromechanical coupling, itself proportional to the $\Delta v/v$ ratio. In the slot waveguide structure (*see* Fig. 2.1(c)), the overlay strips on the sides are "faster" than the substrate, making the central region "slower". More details on thin-film waveguides will be discussed in Section 2.3.

Topographic waveguides guide the waves by reducing the straining forces acting on the material [309]. It is also pointed out in the literature that such guiding structures have no counterpart in electromagnetic waveguides. The rectangular ridge waveguide (*see* Fig. 2.1(d)) includes two dominant modes: symmetric and antisymmetric. The symmetric mode possesses no dispersion and is also called the pseudo-Rayleigh mode as its displacement field resembles a slice out of a Rayleigh SAW [310, 311]. By contrast, the better-known antisymmetric mode exhibits strong dispersion [312, 313, 314, 315]. The wedge waveguide (*see* Fig. 2.1(e)) has no dispersion for waves possessing a frequency over a certain critical value [313]. These waveguides will be considered in greater detail in Section 2.4.

The structure in Fig. 2.1(f) generally remains geometrically flat, as the properties of the substrate are altered—in the dotted region shown in the figure—by atomic in-diffusion or ion-implantation to produce measurable changes in the SAW

Table 2.1: Summary of the properties of different types of waveguides

Type of waveguide	Field Confinement	Amount of Slowing	Dispersion	Loss	Versatility
Strip	moderate	moderate	moderate	medium	moderate
Shorting-strip	weak	small	low	medium	low to moderate
Slot	weak to moderate	small to moderate	low	low to medium	moderate
In-diffused	weak	small	low	low	low to moderate
Topographic ridge, symmetric mode	strong to very strong	moderate to large	high	low	high
Topographic ridge, antisymmetric mode	very strong	small	very low	low	high
Topographic wedge	very strong	moderate to very large	very low to nil	low	high

velocity. For example. Schmidt [316] demonstrated the diffusion of certain metals into LN produced a velocity increase of about one to two percent, while there was no apparent increase in loss due to the in-diffusion process. Such low-loss modification of the substrate is helpful for some applications in acoustofluidics where high power SAW is typically necessary. The in-diffused and ion-implanted waveguides will be discussed further in Section 2.5.

Each of the waveguide configurations above possesses unique properties, and the main features, advantages, and disadvantages of each are summarized in Table 2.1 [304].

Over the past few years, waveguiding layers have also found use as biosensors [317, 318]. The typical structure consists of input IDTs and output IDTs both on a piezoelectric substrate. The input IDTs generates SAW propagating towards the output. With a thin dielectric material overlaid on the device, the acoustic energy is therefore confined in this guiding layer. Perturbations to the SAW during its propagation through the guiding layer, such as a change in the resonant frequency,

electromechanical coupling, or wave attenuation, may be identified at the output IDTs. The presence of the thin layer, at approximately one wavelength thick, greatly increases the sensitivity of the sensor [319, 187]. However, we focus on actuation rather than sensing, as so the ample literature in the field is set outside the scope of this review article.

2.3 Thin film waveguides

The concept of the thin film waveguide was first introduced by Seide *et al.* [320]. They suggested that thin metal films of finite width deposited on an isotropic substrate can be used to guide elastic surface waves in the substrate. This kind of guiding structure in the use of SAW applications reduced the wave propagating velocity in the corresponding area either by its own property of being "slow" or short circuiting the electric field of the substrate, so that waves on the surface tended to be confined in the low-velocity region and propagate accordingly, as shown in Fig. 2.2. The guiding mechanism of thin film waveguides is analogous to the total reflection of an electromagnetic wave (*e.g.*, light) when a dielectric thin film is placed on the substrate. The "slow" region, relative to the "fast" region, corresponds in the optical case to a strip with a higher index of refraction.

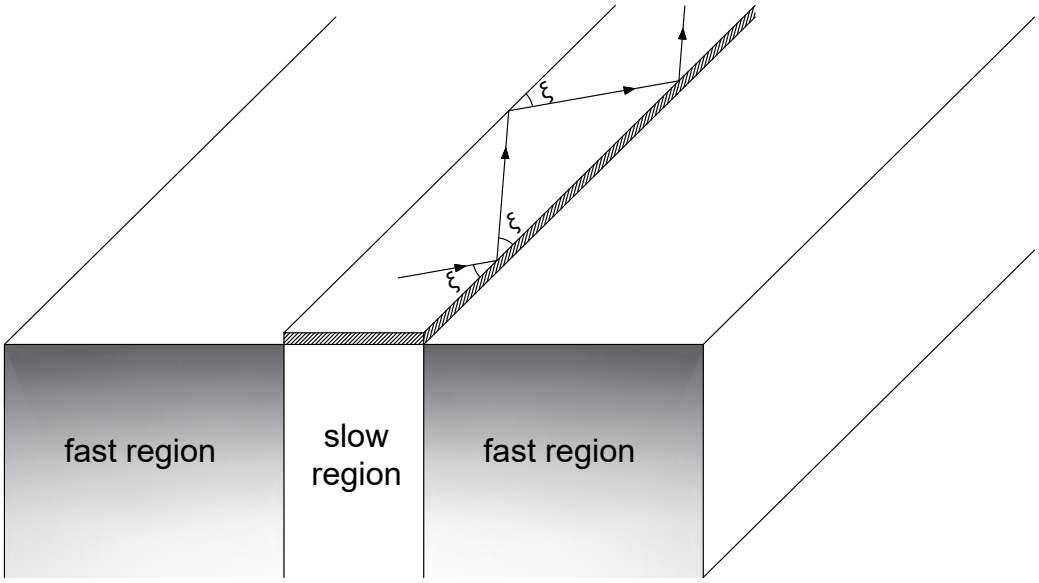

Figure 2.2: Model of thin film waveguide showing wave zigzagging back and forth in the "slow central region". (Figure redrawn from the the paper of Schmidt *et al.* [321])

2.3.1 Strip waveguides

The strip waveguide involves a "slow" material (strip) and a "fast" (substrate). The wave is inclined to travel in the region where the wave velocity is lower than that in the other material. The strip is usually wide and flat, with a width-to-thickness aspect ratio ranging from 5 to 50, and the slowing effect is obtained through *mass loading* of the substrate, enabling the choice of non-conductive materials for the strip. Conductive strip materials can also be used, but this tends to be associated with a different form of waveguide that principally functions by short-circuiting the

piezoelectric substrate below, covered in Section 2.3.2.

One of the analytical methods in theoretically investigating the guiding performance of these waveguides is microwave network analysis [322, 323]. Tiersten [324] proposed the pioneering theoretical investigation of structures which depended upon a velocity differential for guidance. The structure of a strip waveguide is replotted in Fig. 2.3(a). An equivalent network is derived from the approach, allowing us to view the propagation of the guided mode of the modified Rayleigh wave in the strip region which bounces back and forth from the strip sides, as depicted in Fig. 2.3(b). The modified Rayleigh wave is shown as the central transmission line, and the outer transmission lines represent the Rayleigh waves on the free surface. The transverse field behavior for the dominant mode is summarized in Fig. 2.3(c). The transverse decay along the substrate surface (x direction), simply decreases exponentially. The acoustic field substantially stretches out generally for the waveguides so that the wave is weakly bounded, which discourages sharp bends on the surface.

The *dispersion behavior*, variation of propagation velocity with frequency, is distinct for those waveguides described in Section 2.2. The dispersion properties of the strip waveguide are shown in Fig. 2.4, where the aspect ratio is defined as $G = w/t$ (w is the half width and t is the thickness of the metal strip on the substrate). It can easily be inferred that the free surface Rayleigh wave is faster than that in the

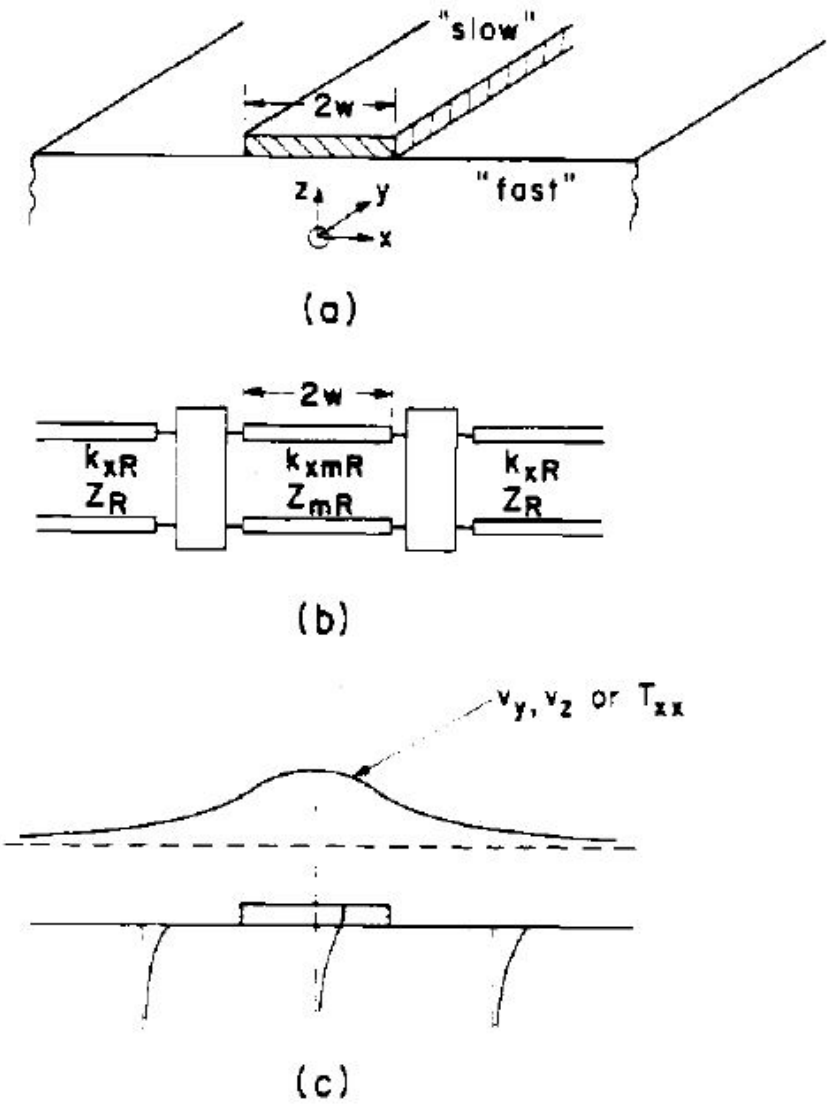

Figure 2.3: The (a) geometry of a strip waveguide, consisting of an overlay of "slow" material on a "fast" substrate. (b) The transverse equivalent network for the dominant mode; k_{xR} and k_{xmR} are the transverse wavenumbers in the x direction. (c) The transverse acoustic field behavior; v_x and v_y are particle velocity components and T_{xx} is a stress tensor component. (Figure permission acquired from the paper of Oliner *et al.* [304])

guiding structure. And for waveguides with a higher aspect ratio, the guided wave is slower. Furthermore, the field spreads out at low frequencies, which indicates that none of the field is in the guiding layer with energy propagation in the substrate as a Rayleigh wave. The velocity remains approximately the same as the Rayleigh wave on the substrate. When the frequency is increased, the wave velocity decreases as more of the field is confined into the "slow region". Finally, when the frequency is very high, nearly all the wave displacement field is confined to the slow region of the strip and the velocity decreases to the velocity of the Rayleigh wave in the strip material alone. The dispersion relation for the dominant guided mode is given by the lowest resonance value found from the dispersion equation [325]:

$$\tan\left(\sqrt{k_{mR}^2 - \beta^2}w\right) = \sqrt{\frac{\beta^2 - k_R^2}{k_{mR}^2 - \beta^2}}, \tag{2.1}$$

where β is the propagation wavenumber of the guided mode, and k_R and k_{mR} are the wavenumbers of the Rayleigh wave and the modified Rayleigh wave, respectively. The corresponding phase velocities of each wavenumber are $v_p = \omega/\beta$, $v_R = \omega/k_R$ and $v_{mR} = \omega/k_{mR}$. In addition, Freund *et al.* [326] adopted an alternative method to obtain the dispersion relations for the waveguides, in which one side of the guiding structure was considered to be infinite so that there was only one discontinuity in the boundary conditions. Solving the three-dimensional elasticity problem enabled

the investigation of the reflection and transmission of surface waves at this discontinuity. The three unknown and nonzero displacement vectors could be solved by either Laplace transform methods or the Wiener-Hopf technique [327]. The results could thus be applied to geometrical characterization of dispersion relations for the propagation of the unattenuated guided surface waves.

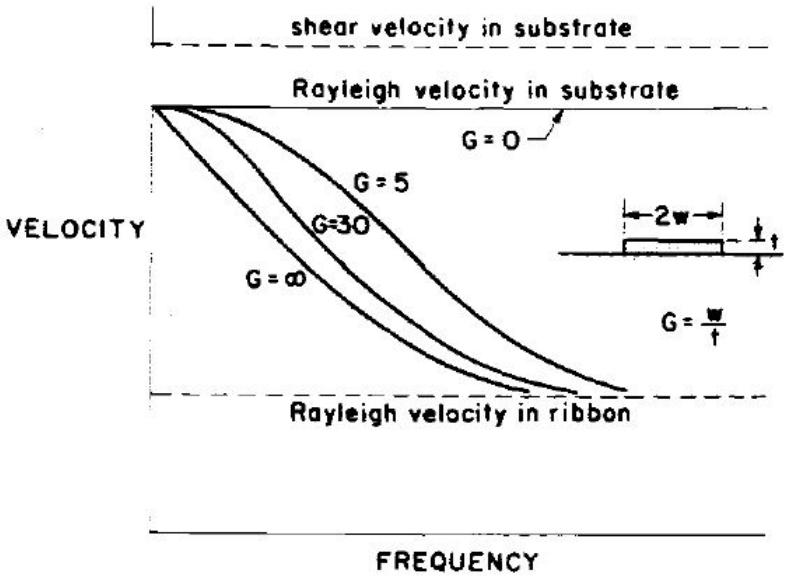

Figure 2.4: Dispersion characteristics for the dominant mode on the strip waveguide, for various aspect ratios. (Figure permission acquired from the paper of Oliner *et al.* [304])

So far the discussion has only included straight waveguides. Overcoming the anisotropy of the substrate in order to more completely control the SAW propagation is a key purpose of waveguides, and so the effects of turning waveguides is important. According to Tiersten *et al.* [328], the planar scalar wave approximation

procedure with large radius-to-guide-width ratios a/b (*see* Fig. 2.5) were extensively studied. They obtained the dispersion curves by solving Bessel's differential equations employing approximate bound modes in the partially bound wave functions and concluded that a critical a/b ratio exists which depended upon the deposited and substrate materials. Beyond this critical a/b ratio, the waveguide would fail to retain the wave and energy would be lost from it.

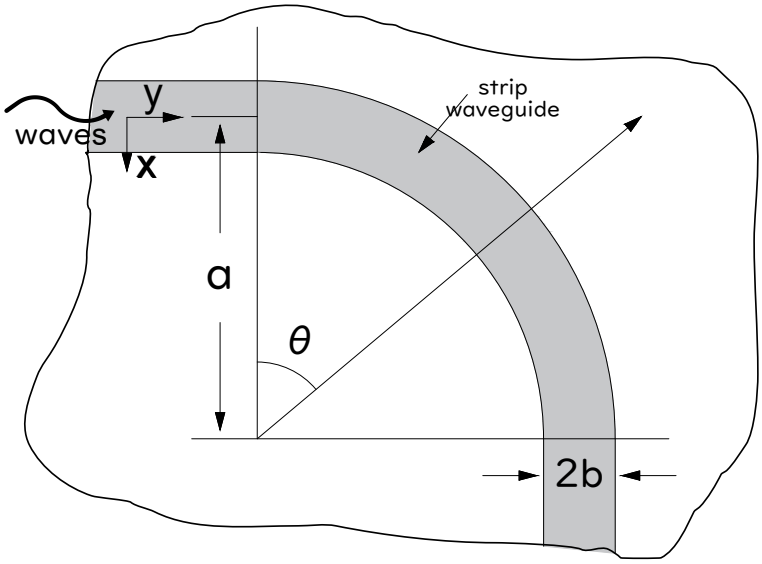

Figure 2.5: Circular guide connecting two straight guides normal to each other. (Figure redrawn from the paper of Tiersten *et al.* [328])

In the work cited so far, the substrate was assumed to be isotropic to facilitate analysis, but this precludes piezoelectricity and therefore the generation of the SAW in the substrate. However, in the specific case of single-crystal LN, modifications

necessary in the analysis due to the anisotropy have been carried out by Schmidt *et al.* [321]. Based on a few simplifying assumptions about the propagation of SAWs, they analyzed the dispersion relation by assuming a single scalar potential in the wave equation. They considered the wave, which propagated along the guiding layer, in terms of modified Rayleigh wave rays that were completely reflected from the side walls of the strip. Since in anisotropic substrates such as LN that the velocity of Rayleigh waves symmetrically vary about the waveguide axis, the propagation wavenumber of the guided mode β', corresponding to the propagating angle ξ with respect to the guide axis, may be simply corrected by using

$$\beta' = k_{mR}(\xi, t)\cos\xi, \tag{2.2}$$

where $k_{mR}(\xi, t)$ is the wavenumber of the modified Rayleigh wave along the ξ direction in the region of the deposited thin film with thickness t. The waves were assumed to propagate in a zigzagging path with the reflection angle ξ, as shown in Fig. 2.2. The transverse decay constants may be expressed as

$$k'_{mR} = \sqrt{k^2_{mR}(\xi, t) - \beta'^2} \tag{2.3}$$

for the slow region and

$$k'_R = \sqrt{\beta'^2 - k_R^2} \tag{2.4}$$

for the fast region. The dispersion relation may thus be modified and written as

$$\frac{1}{2} w \sqrt{k_{mR}^2(\xi, t) - \beta'^2} = i\frac{\pi}{2} + \tan^{-1} \sqrt{\frac{\beta'^2 - k_R^2}{k_{mR}^2(\xi, t) - \beta'^2}}, \tag{2.5}$$

$$\frac{1}{2} w \sqrt{k_{mR}'^2(\xi, t) - \beta'^2} = i\frac{\pi}{2} + \tan^{-1} \sqrt{\frac{\beta'^2 - k_R'^2}{k_{mR}'^2(\xi, t) - \beta'^2}} \tag{2.6}$$

in which i indexes the propagation mode. Later they further applied a parabolic approximation [329] and finally expressed the wavenumber as

$$k_{mR}(\xi) = k_{mR}(\xi = 0)\left(1 + \alpha\xi^2\right) \tag{2.7}$$

$$k'_{mR}(\xi) = k'_R(\xi = 0)\left(1 + \alpha\xi^2\right) \tag{2.8}$$

where α is the parabolic anisotropy factor of the substrate. The value of k'_{mR} from Eq. (2.8) may then be substituted into Eq. (2.4) wherever k_{mR} appears to approximate the effects of the anisotropic media. As they concluded, this modification was valid for small angles of deviation from the guided axis, as typically found in high aspect ratio thin films.

2.3.2 Shorting-strip waveguides

The shorting-strip waveguide was first described by Engan [330]. The structure includes a very thin strip of metal on a piezoelectric substrate. Rather than a mass loading effect from the strip as used in strip waveguides, here the electric field associated with the piezoelectric surface wave will be short circuited by the metal strip, permitting free flow of current as the SAW passes through, reducing the net stiffness of the material and likewise the wave propagation velocity in the substrate under the strip. Unlike strip waveguides, the metal can be much thinner as all that is required is the ability to carry sufficient current to maintain the short-circuit condition. Due to how it reduces the velocity via the short circuit, this kind of waveguide is also called a $\Delta v/v$ waveguide, an unfortunate definition since all waveguides operate on the $\Delta v/v$ effect. The dispersion relation is similar to Eq. (2.1), but the approximate correction described in Eq. (2.8) is necessary because the mechanism of wave confinement under the shorting strip requires piezoelectric coupling that only appears in an anisotropic substrate. The reduction of velocity (Δv) produced by short circuiting the substrate under the strip is typically small, so the guiding action provided by the strip is weak. However, as the guided wave propagates, the transverse width of most shorting-strip waveguides is constant and if the wave is able to be initially confined it should remain confined.

Hughes [331] simply assumed the open-to-short circuit wave velocity difference Δv to be the dominant factor in guiding SAW within the shorting strip. His theoretical work—adopting an isotropic mode which incorporated the velocity difference—adequately predicted the major features of this kind of guiding structure: strong guidance and low dispersion for many common piezoelectric materials (*e.g.*, LN). However, failing to take the effects of the film stiffness and inertia into account, his results did not agree well with experimental results [332], as he used wavenumbers along the guide axis rather than the actual SAW path ξ that zigzagged along and back and forth across the shorting strip. Sinha *et al.* [333] later included the influence of the stiffness, inertia, and electrical shorting of the deposited film and worked out the depth dependence of the full straight-crested surface wave solution from the three-dimensional equations of linear piezoelectricity [334], so that the associated dispersion relation could also be obtained. One of the results they achieved involved the dispersion curves, with different values of aspect ratio G, for guided SAWs propagating in both x and z directions on Y-cut LN, where thin gold films were deposited. It revealed that the dispersion curve possessed an unusual hump for the X-propagating SAW on LN (*see* Fig. 2.6), indicating two ranges of nondispersive propagation. They further attributed this to the strong mode coupling of the two straight-crested surface waves in the propagating direction, the extended Rayleigh

wave and the fundamental quasi-Love wave. They approximated the wave propagation with a single scalar surface wave function, which described only one mode, precluding the application of the analysis to the fully mode coupled case.

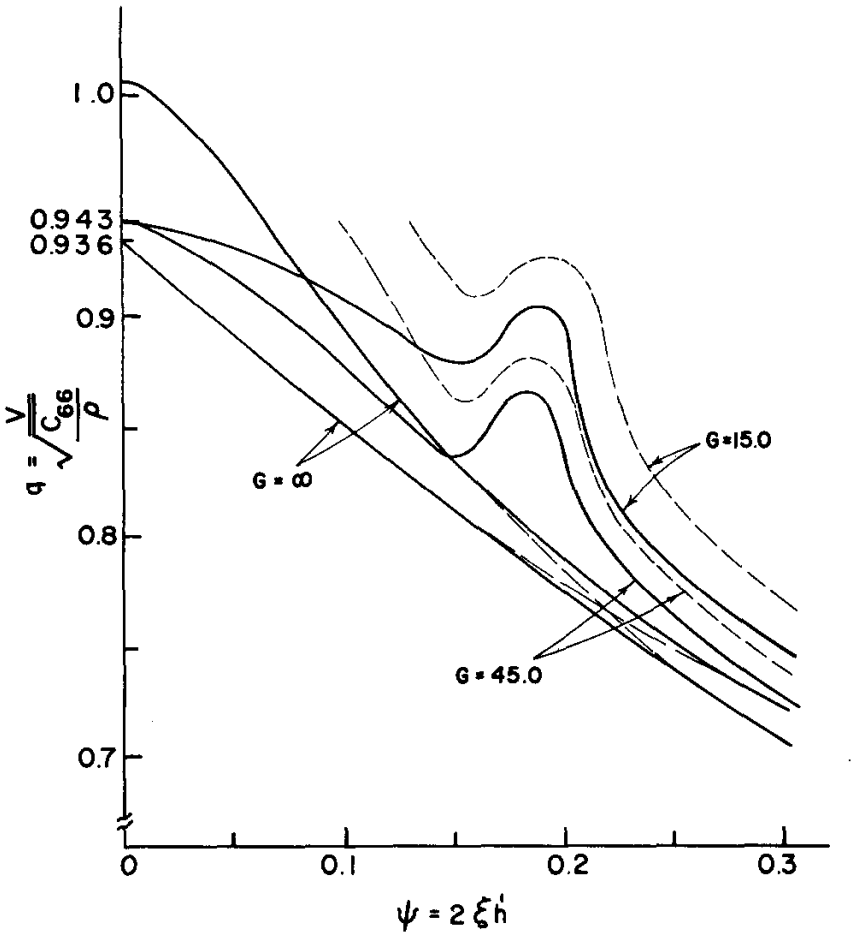

Figure 2.6: Dimensionless phase velocity dispersion curves for essentially Rayleigh-type surface waves guided by strips of gold plated on a Y-cut LN substrate for X-propagation for various width-to-thickness ratios. The solid curves represent the lowest symmetric mode and the dotted, the lowest antisymmetric mode with respect to the width of the plating. (Figure permission acquired from the paper of Sinha *et al.* [333])

The relative velocity reduction for an aluminum strip on YZ LN, with respect to the shorted surface wavenumber, was reported by Schmidt *et al.* [321] (*see* Fig. 2.7), where v_p and v_g denoted phase velocity and group velocity, respectively, and α stood for anisotropy factor of the substrate. The dimensionless velocity reduction could be very small, about one to two percent. The substrate anisotropy obviously made a nontrivial contribution to the dispersion of the waveguide, if one compared the solid and dashed lines. Their measured data—the black dots and triangles—sufficiently supported the calculated relation. Furthermore, as the anisotropy factor $\alpha = 0.25$ closely approximated the shorted velocity of LN, the zigzagging ray direction ξ was computed to be about 7°, which suggested that the SAW would be confined in the "slow" region and would propagate back and forth at this angle (*see* Fig. 2.2).

Since both mass-loading and piezoelectric shorting can be present at the same time, it is important to note the result in Fig. 2.7 omits the dispersive effects of mass loading of the 30 nm thick aluminum strip. Schmidt *et al.* [321] considered this effect as well with an 180 μm wide and 50 nm thick aluminum strip on a YZ LN substrate (*see* Fig. 2.8), in which v_s, v_p, v_g, α and δ_s represent the wave velocity in the slow region, the phase velocity, the group velocity, the anisotropy factor, and the mass loading coefficient, respectively. When the mass loading effect was taken into

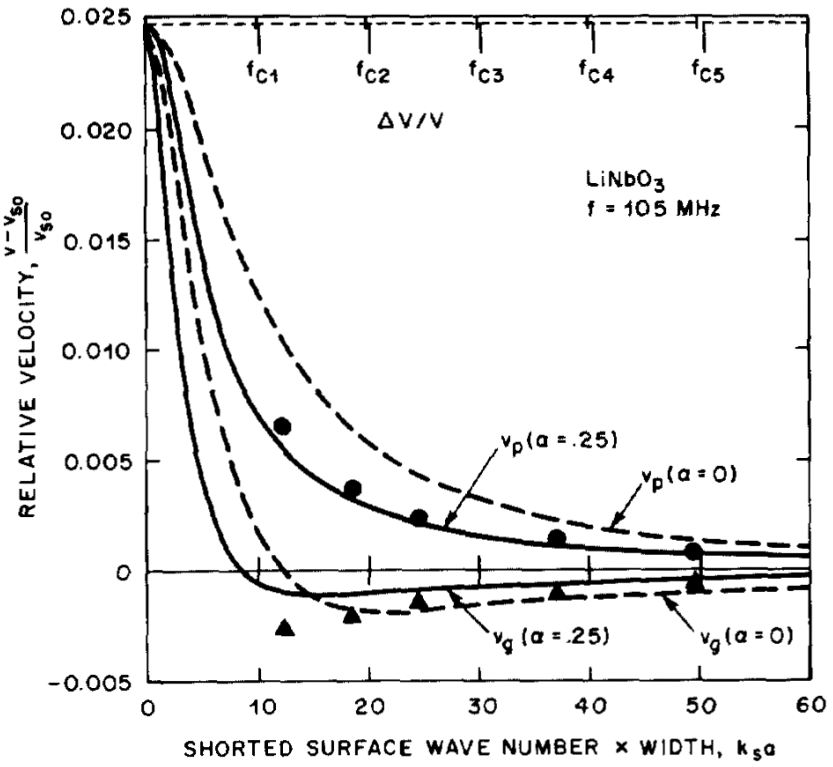

Figure 2.7: Theoretical dispersion curves of $\Delta v/v$ waveguide on $LiNbO_3$,with anisotropy included ($\alpha = 0.25$) and without anisotropy ($\alpha = 0$); phase velocity (black dots), group velocity (black triangles). Measurements at fixed frequency for guides of varying width. (Figure permission acquired from the paper of Schmidt *et al.* [321])

account, the solid curves for phase velocity and group velocity were plotted using the approximation method mentioned above, which had a downward sloping curve, rather different than when only the shorting effect of the guiding strip (dashed lines) was considered. From their finding, it is reasonable to omit the mass loading effect on the wave propagation when the metal film is very thin and the SAW is at a relatively

low frequency. But most importantly, they showed that the positive dispersion curve from the short-circuiting behavior of the shorting strip waveguide could be balanced with the mass loading of the metal in the waveguide to eliminate the dispersion—in their case, from 45 MHz to about 120 MHz.

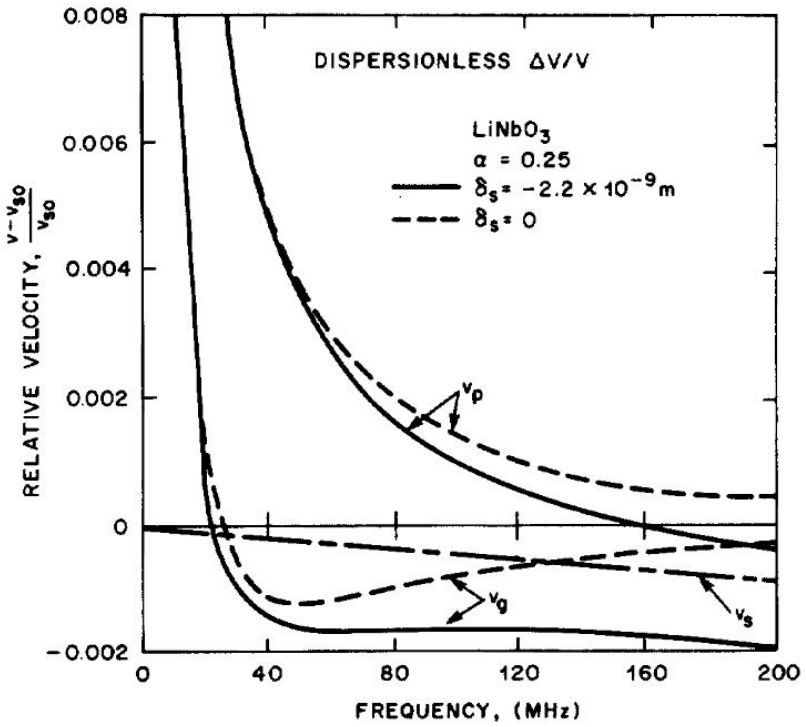

Figure 2.8: Dispersion curves for the aluminum shorting-strip waveguide, taking into account the mass loading and short-circuit effects of the metal waveguide material, showing group velocity dispersion compensation. Dashed curves represent the shorting effect only. Solid curves include slight mass loading dispersion compensation (represented by the v_s curve). (Figure permission acquired from the paper of Schmidt *et al.* [321])

2.4 Topographic waveguides

Absent using a second material, surface waveguiding can be realized by a sufficient localized geometric shaping of the substrate surface, which is distinct from the overlay waveguiding structure discussed in the previous subsection. Rather than seek to guide waves by controlling the spatial distribution of the wave speed, the waves are instead guided by reducing the restraining forces acting on the substrate through the presence of local geometry—a ridge of material, for example—and entrapping the wave into the local geometry. This form of waveguide tends to bound the wave rather well, reducing loss to the surrounding structure in comparison to other waveguide geometries. These waveguides furthermore have no real analogy in electromagnetics. There are two important topographic waveguide shapes: ridge and wedge structures. The two typical but distinct wave propagation modes in such waveguides will next be considered.

2.4.1 Antisymmetric flexural mode

A typical ridge waveguide has a width W and height H and is bound at its base to the substrate and is free along the top edge as shown in Fig. 2.1(d). When W is sufficiently small, it is convenient to treat the fields in the ridge region as different plate modes of propagation. In the antisymmetric flexural (ASF) ridge mode—the

odd mode—particle displacement transverse to the long axis of the ridge and the wave propagation direction is significant. The low stiffness of the ridge in this type of lateral motion causes the velocity of waves formed from it to be well below the Rayleigh velocity. The term "flexural" indicates the motion in the ridge region rocks back and forth as the wave travels down it (*see* Fig. 2.11 (a–c) and Fig. 2.12(a)). Mason *et al.* [335] have shown the dispersion results for the ASF in the form of a normalized phase velocity as a function of $(\omega W/v_R)$ with their experimental data. As shown in Fig. 2.9, the lowest curve is the analytical solution to the lowest ASF mode for an infinite plate (*i.e.*, $H/W \rightarrow \infty$) [336]. Comparing the experimental results for ridge guides of different H/W values, it is reasonable to conclude that, at high frequencies, the ASF phase velocity asymptotically converges to the velocity of the Lamb plate mode (lowest ASF mode) [335]; while at low frequencies, the phase velocity increases rapidly towards infinity as a low-frequency cutoff. An infinite phase velocity corresponding to a finite frequency apparently indicates an infinite guiding wavelength, therefore the ridge must vibrate monolithically along its entire length as a cantilever at this cutoff. In this cantilever resonance, the energy leaks from the guide to a bulk mode that freely propagates underneath. Experiments have revealed that, in the range $0.75 < H/W < 3$, the rectangular ridge guide is estimated to be one quarter of an ASF Lamb mode high.

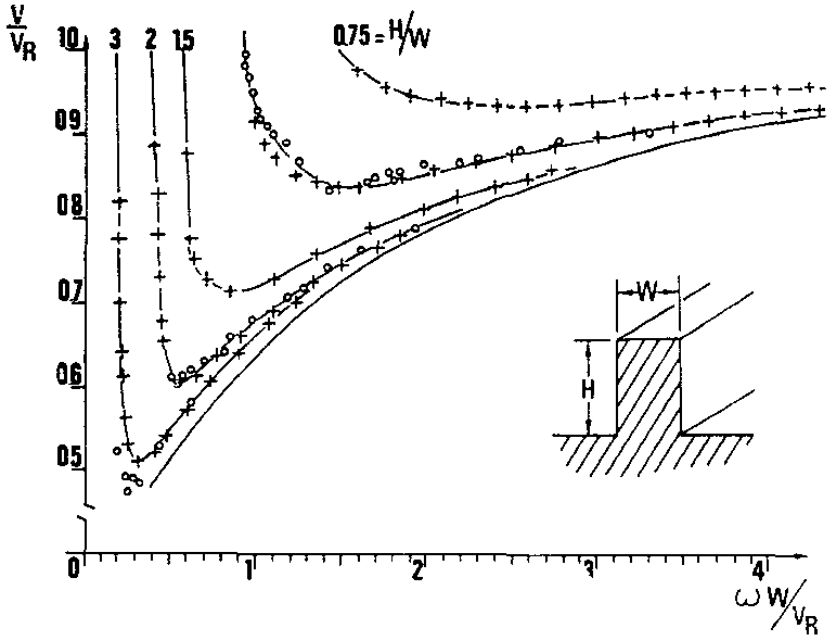

Figure 2.9: The rectangular ridge waveguide (inset), with measured dispersion characteristics of the fundamental ASF mode. The parameter is H/W. Circles denote laser probe results, crosses the results of ring resonator experiments. The dispersion characteristics of the fundamental ASF Lamb wave is also shown. (Figure permission acquired from the paper of Lagasse *et al.* [337])

In a less rigorous approximation, it is reasonable to regard the ASF modes as traveling and non-destructive interference patterns of the fundamental mode that is specularly reflected by the impedance discontinuities at the ends of the ridge guide. With this in mind, the phase condition

$$2k_s H \cos\theta - \phi_1 - \phi_2 = 2m\pi \tag{2.9}$$

must be satisfied, where k_s is the wavenumber of substrate, and ϕ_1 and ϕ_2 are the phase changes of the ASF waves at the free (top) end of the ridge and at the ridge's base at the substrate, respectively. The phase changes can be constrained as π or 0 upon the assumption that the discontinuities are equivalent to open- and short-circuits. As a result, the terms ϕ_1 and ϕ_2 can be simplified and produce a mode number change from $2m$ to $2m-1$. Introducing the wavenumber of guide $k_g = k_s \sin\theta$, the dispersion relation can be derived by integrating the ridge mode product of phase and group velocities and applying the quarter-wavelength cutoff condition:

$$k_g^2 \approx k_s^2 - \left(\frac{n\pi}{2H}\right)^2, \tag{2.10}$$

where n is an odd integer denoting the order of the ASF mode. Dispersion characteristics for the ASF ridge mode can be plotted with Eq. (2.10). The calculated results were compared with the experimental data by Lagasse [313]. This simple model predicted the dispersion characteristics quite well for tall ridge structures ($H/W \geq 3$). The error was reported to be only 3% for $H/W = 3$. However, when the guide is shrunk to $H/W = 1.0$, the discrepancy increases to 15%, which can be explained as the energy propagating in the substrate becomes more significant, according to this theory.

Later, in the work of Oliner *et al.* [323] and Li *et al.* [338], a more accurate

transverse resonance formulation was established by treating the substrate to be coupled to shear-horizontal (SH) bulk waves instead of simply a free surface. This approach produced a corrected dispersion relationship of

$$\left(k_s^2 - k_g^2\right)^{1/2} = \left(\frac{k_s}{k_g}\right)^2 \left(k_s^2 - k_b^2\right)^{1/2} \cot\left[\left(k_s^2 - k_g^2\right)^{1/2} H\right], \tag{2.11}$$

where k_b was the bulk shear wavenumber. Comparing this new result with experiments (*see* Fig. 2.10) shows a substantial improvement over the past models.

Lagasse [313] has also proposed to apply finite-element analysis in determining the characteristics of the ridge mode waveguides, by dividing the cross section of the guiding structure into sufficiently small—usually triangular [339, 340]—elements. Both the anticipated gradients of the field quantities and the geometry of the guide determine the number of elements. These elements can then be defined by simple polynomial shape functions to produce a linear algebraic representation for the complete system with—fortunately—linear solutions at first order [341]. A matrix eigenvalue equation is generated with application of the finite-element method to the variational principle-derived representation,

$$[S][U] = \omega_0^2[T][U], \tag{2.12}$$

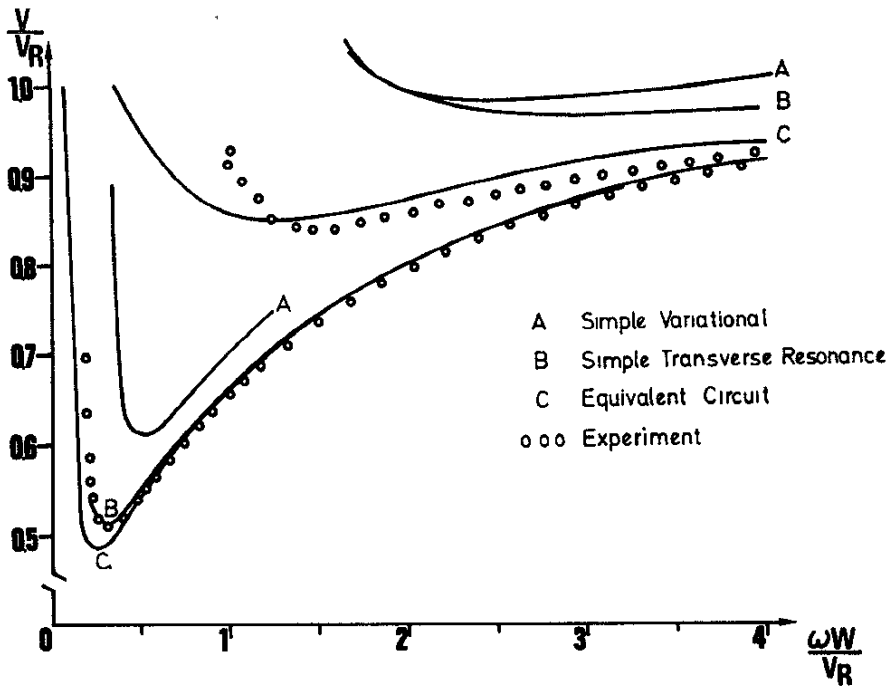

Figure 2.10: Fundamental ASF mode approximation theories compared with experiment for tall ($H/W = 3$) and short ($H/W = 1$) duralumin guides. The upper right curves are for tall ridges and the lower left curves are for short ridges. Curve A: Simple variational model. Curve B: Simple transverse resonance model. Curve C: Equivalent circuit model. Dots are the experimental data. (Figure permission acquired from the paper of Lagasse *et al.* [337])

where $[S]$, $[U]$ and $[T]$ are the stiffness tensor, field displacement tensor, and mass tensor, respectively, and ω_0 is the mode eigenfrequency. By applying appropriate boundary and symmetry conditions, Fig. 2.11(a–c) depicts the three ASF particle deformation patterns of a tall ridge guide, in which the particle motion is normal to the direction of propagation. When it comes to the case of piezoelectric substrates, one interesting fact worth noting is that considering piezoelectricity will not

reduce the dimensionality of the linear algebra representation of the system. Armstrong et al., in a private communication, had shown that the finite-element method worked accurately in obtaining an estimation of $\Delta v/v$, even for a materials with weak piezoelectricity. Their calculation of the CdS and lead zirconate titanate (PZT)–4A confirmed this accuracy, producing only 0.2 percent error in a comparison with the exact analytical value of $\Delta v/v$.

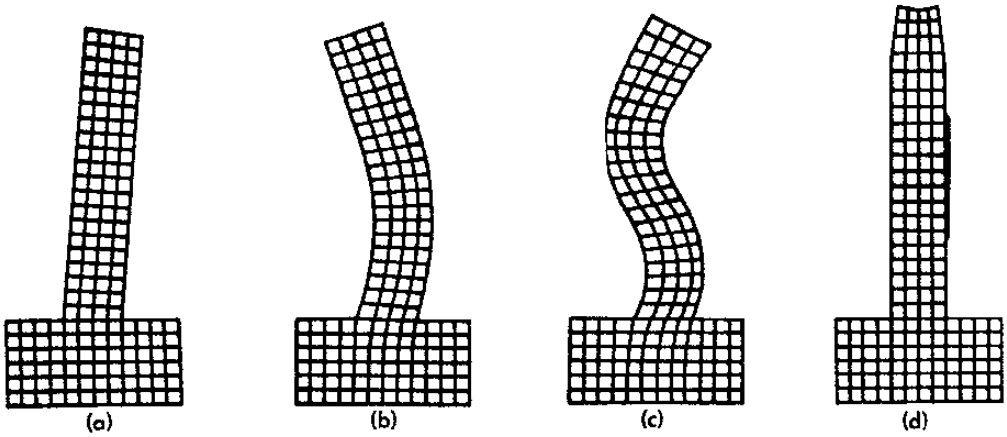

Figure 2.11: Displacement patterns of four tightly bound modes that exist in a high aspect ratio ($H/W = 5$) rectangular single-material ridge waveguide. (a)(b)(c) ASF mode, (d) symmetric mode. (Figure permission acquired from the paper of Lagasse *et al.* [337])

2.4.2 Symmetric pseudo-Rayleigh mode

Unlike the ASF mode, which has strong dispersion, the symmetric mode is almost dispersionless over a very wide frequency range, especially for ridges with high

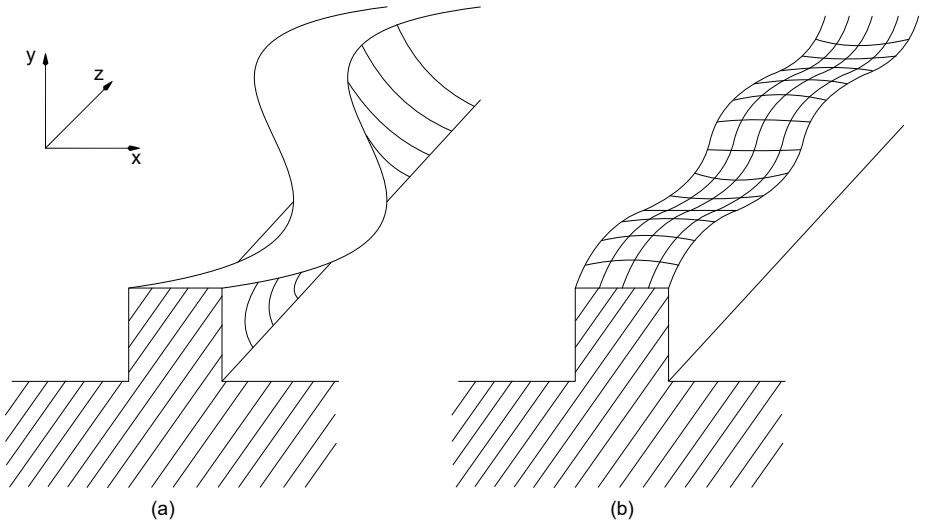

Figure 2.12: Sketch of propagation modes in the ridge guides. (a) ASF mode (particle displacement predominantly in x and z directions), (b) pseudo-Rayleigh mode (particle displacement predominantly in y and z directions). (Replotted using the data from the paper of Mason *et al.* [335])

aspect ratio. The acoustic field in the waveguide distinctly resembles a Rayleigh wave, and that is why it is also named the pseudo-Rayleigh mode. As shown in Fig. 2.11(d) and Fig. 2.12(b), the constituent waves displace vertically in the tall ridge rather than horizontally.

In this mode, the lowest symmetric Lamb mode and the lowest SH mode couple together at the top of the guide so that the p and s bulk waves combine to form a Rayleigh wave at a free planar surface. The dispersion relation was investigated by Markman *et al.* [342] and Li *et al.* [343], using a transverse equivalent network

approximation

$$\left(k_{sh}^2 - 2k_g^2\right)^2 \frac{\sqrt{k_g^2 - k_l^2} + \sqrt{k_g^2 - k_c^2}\tanh\sqrt{k_g^2 - k_l^2}H}{\sqrt{k_g^2 - k_c^2} + \sqrt{k_g^2 - k_l^2}\tanh\sqrt{k_g^2 - k_l^2}H} = 4k_g^2\sqrt{k_g^2 - k_{sh}^2}\sqrt{k_g^2 - k_l^2}, \tag{2.13}$$

where k_{sh}, k_c and k_l were the shear, compressional wave, and lowest symmetric Lamb wave wavenumbers, respectively. Experimental data is also shown in Fig. 2.13, using values from Yen *et al.* [310]. It has been pointed out [304] that the dispersion relation in Eq. (2.13) can only be valid for frequencies below $k_R W = 2$ (k_R is the Rayleigh wavenumber). Additional transverse propagation modes would need to be considered when attempting to determine the motions in the waveguide above this frequency, and Eq. (2.13) would need to be adjusted accordingly.

It is known that at zero frequency, all energy is kept in the substrate and the dispersion curve infinitely approaches the Rayleigh wave velocity. At very low frequency, the effect of the substrate exists as the field decay is still small. When frequency is above a certain threshold, which seems to be rather low, the particle motion associated with the wave is mostly confined within the guide, similar to symmetric waveguide modes propagating along the ridge. Over a very wide frequency range, the symmetric pseudo-Rayleigh mode in the waveguide has almost no dispersion, thus making it useful in long delay line applications and potentially in acoustofluidics.

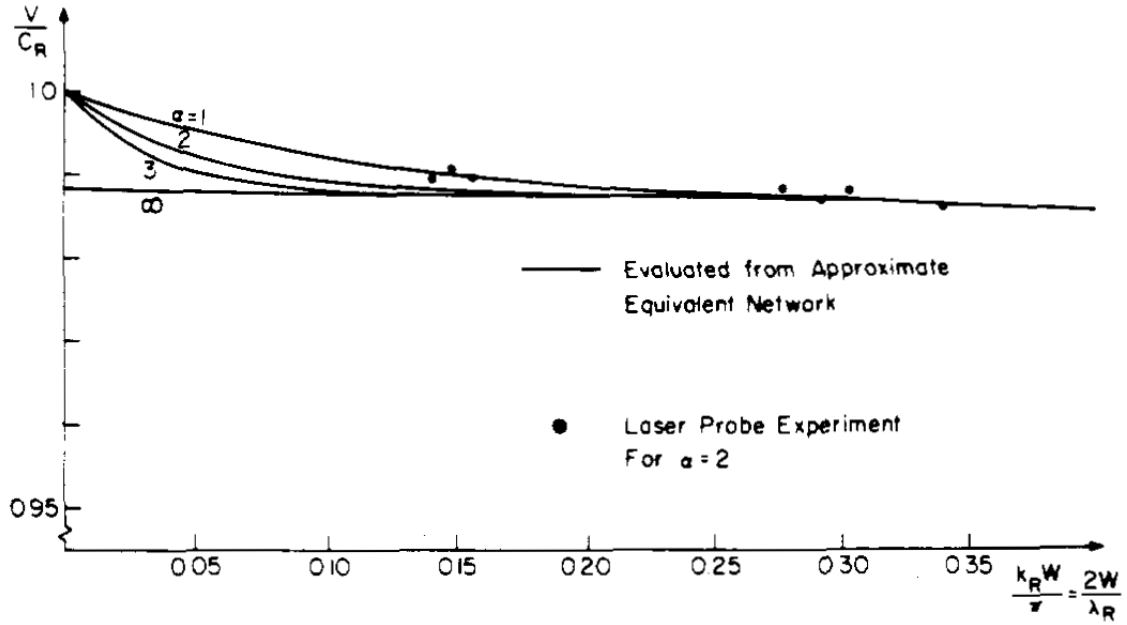

Figure 2.13: Dispersion characteristics for the dominant symmetric pseudo-Rayleigh mode on the topographic rectangular ridge waveguide, using an expanded ordinate scale to show the effect at low frequencies of different aspect ratios. (Figure permission acquired from the paper of Oliner [304])

2.4.3 Wedge

In 1972, Lagasse [313] further studied the fundamental ASF modes of the dispersion characteristics in two trapezoidal ridge guides (*see* Fig. 2.14): a truncated knife edge and a dovetail ridge, in which $H = W$. The dispersion characteristic becomes flattened as the top of the guide narrows. The waveguides can become nearly dispersion-free if the slope angle keeps increasing and eventually forms a knife edge. According to analysis [344], the dispersion curve for an ideal wedge (substrate is infinitely far away) is a straight line; *i.e.*, the velocity does not change with respect

to frequency. This can be understood as such tall knife-edge structures have no characteristic dimension. For a more realistic case—where the height of the wedge is not infinitely large—a portion of the energy dissipates into the substrate and the wave velocity increases at low frequencies. At greater frequencies, the wave velocity stays constant and the energy is essentially confined in the guiding structure, as the structure acts as an infinite wedge.

Although it was difficult to obtain an analytical solution for the wedge guides, Lagasse et al. had applied the finite-element method, as discussed in subsection 2.4.1, towards the wedge performance in the 1970s. Their efforts in calculating the dispersion characteristics involved various conditions: for higher modes [314, 344], for different top angles θ [337, 344], for anisotropic substrates [314] and for the effects of a truncated or rounded wedge shape [345].

Rendering one of their results, though more than one mode can take place simultaneously depending on the wedge angle, Fig. 2.15 presents the particle displacement for the lowest order mode. One can easily tell that the particle motion is predominantly transverse to the propagation direction and this mode is tightly bounded to the tip of the wedge. A good numerical approximation of the displacement decay regarding the depth from the apex is presented in Fig. 2.16, where $|u_1|$ is the displacement amplitude and x_2 is the depth. One typical result states the

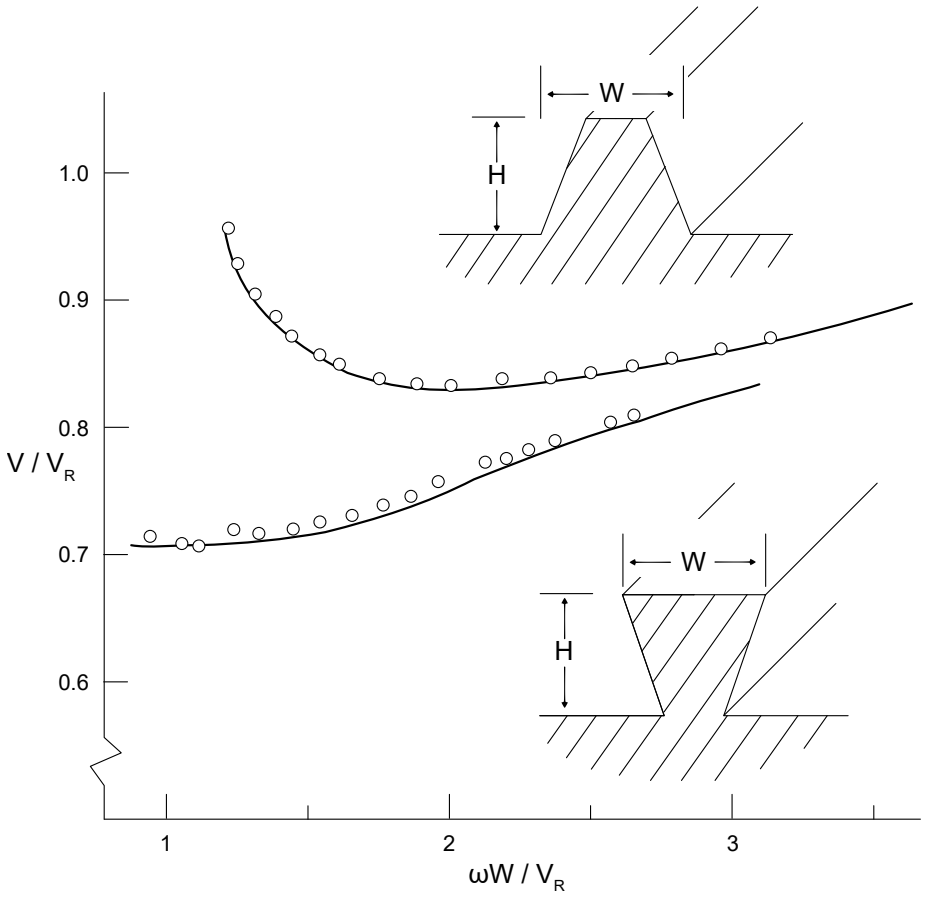

Figure 2.14: Theory compared with experiment for the fundamental ASF mode in trapezoidal duralumin ridges. $H/W = 1$. Sides deviate from substrate normal by 15°. (Replotted using the data from the paper of Lagasse *et al.* [313])

amplitude drops to 10% of the maximum amplitude at depth $x_2 = 0.9\lambda_R \tan\theta/2$, where λ_R is the Rayleigh wavelength. And the penetration depth of the mode will rapidly decrease as the top angle gets smaller. Further investigation has pushed the deformation amplitude decay rate to about $\exp(-2x_2/\lambda_R)$.

Besides the finite-element calculation, the dispersion relation was also empir-

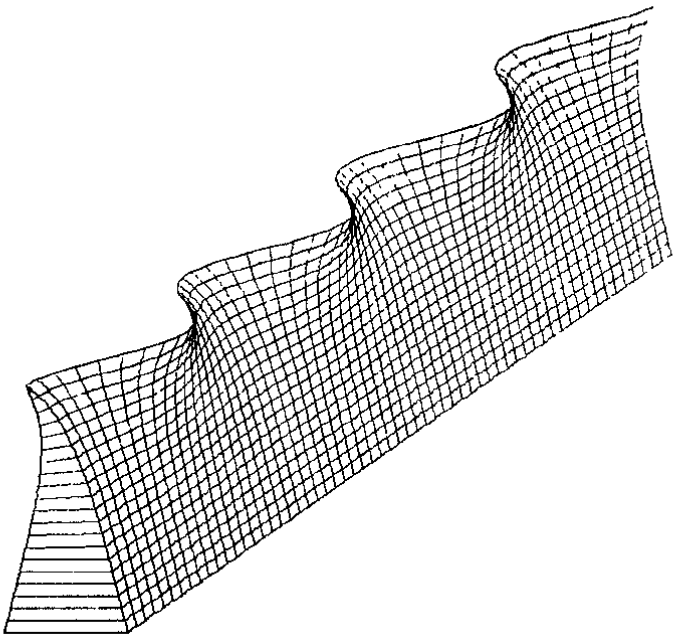

Figure 2.15: Computer-generated perspective view of propagation in the lowest order mode on a narrow apex wedge. Wave motion is predominantly antisymmetric flexural. (Figure permission acquired from the paper of Lagasse *et al.* [337])

ically solved [337]. The guided velocity was found to have a strong dependence upon the apex angle θ,

$$v \approx v_R \sin(m\theta), m\theta < 90^\circ, \tag{2.14}$$

where v_R was the half-space Rayleigh wave velocity and m was an integer denoting the mode order. The equation indicates that an potentially dispersion free mode can be achieved for small apex angles. In a 15° wedge, for instance, a guided wave with velocity only quarter of v_R can be supported. Mason *et al.* [346] has concluded,

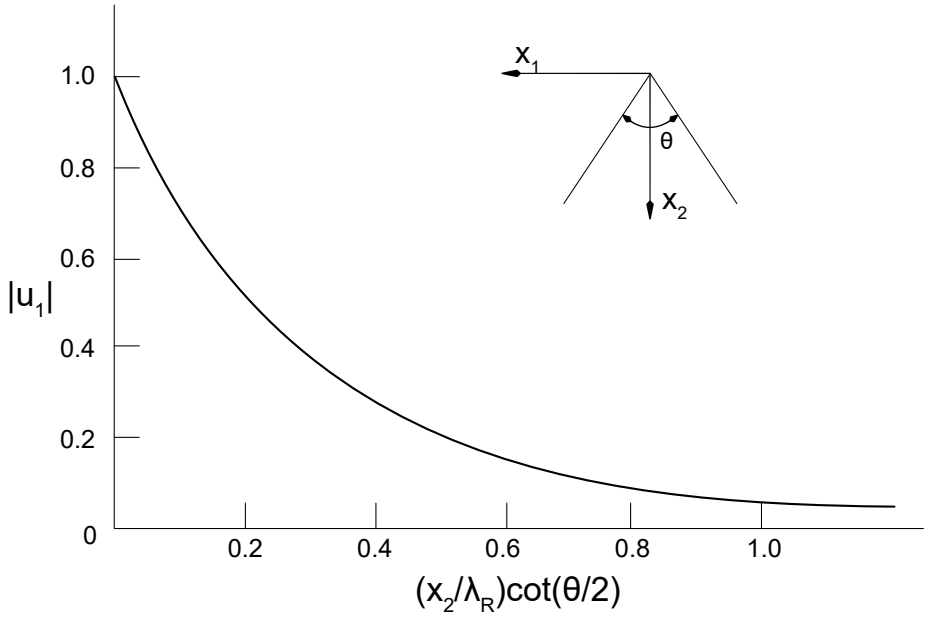

Figure 2.16: Displacement amplitude as a function of depth. (Replotted using the data from the paper of Lagasse [313])

and verified by experiments, the advantages of narrow-angle wedge waveguides, high acoustic field density, very low dispersion, and low velocity made them a perfect candidate for nonlinear interactions devices.

Although the acoustic waves propagating at the tip of an ideal infinite wedge waveguide is dispersionless, the weak dispersion still attributes to a number of factors. As a result, in later years, wedge waves can be used in non-destructive testing [347, 348], as modifying the geometry of the wedge can apparently change the dispersion relation. And sometimes the dispersion is intentionally introduced to produce nonlinear effects as needed [349, 350, 351, 352].

Sokolova *et al.* [353] applied perturbation theory on the early work of Lagasse *et al.* [345] to investigate the dependence of frequency or phase velocity on the wavenumber (inverse wavelength). They found that when one or two surfaces of the wedge were coated by a thin film (*see* Fig. 2.17(a)), the dispersion law turned to be

$$\omega^2 = (v_p k)^2(1 - 2kd \times F_1) \tag{2.15}$$

where ω, v_p and k were the angular frequency, phase velocity, and wavenumber, respectively, and d was the thickness of the thin film coating. The dimensionless constant F_1 depended on the acoustic mismatch of the two materials, such as density and elastic modulus, and the angle of the wedge. Besides, when a small part of the cross section of the wedge close to the tip was changed, for example, truncation (*see* Fig. 2.17(b)), rounding of the tip, or replacement by another material, the dispersion relation became

$$\omega^2 = (v_p k)^2(1 - 2kA_1 \times F_2), \tag{2.16}$$

where A_1 was the cross-section that was removed or replaced, and coefficient F_2 depended upon the acoustic mismatch between the filling material and the wedge. The finite element analysis (FEA) simulation of Hladky [354] confirmed that the modification of the tip strongly induced a dispersion of wedge wave velocity at small

angles.

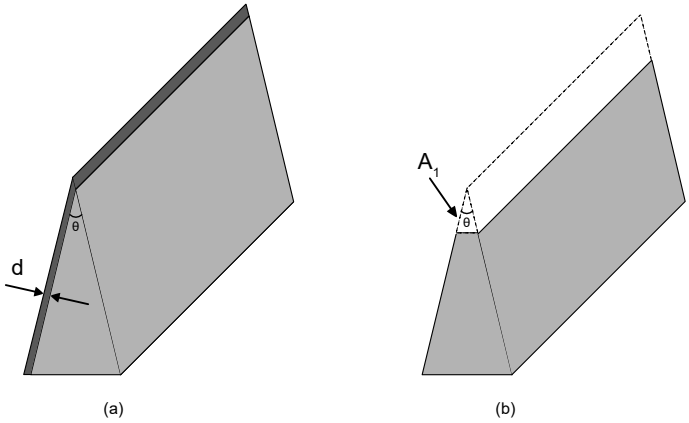

Figure 2.17: Influence of wedge wave dispersion by (a) coating of one of the surfaces, (b) truncation of the tip of the wedge. (Figure redrawn from the paper of Sokolova *et al.* [353])

In more recent years, research has analyzed a type of highly localized plasmon—channel plasmon polaritons (CPP)—-in metallic grooves, which showed superior features in subwavelength guiding with strong localization and low dispersion [355, 356, 357]. The structure could be regarded as a reverse of the wedge waveguide, where a "V" shape was cut into the substrate. In the context of acoustic waves, Liu *et al.* [358] simulated the dispersion relation by the compact two-dimensional finite-difference time-domain method, and concluded that when the V-groove was immersed in water, most of the elastic energy would be confined in the fluid domain at the bottom. They also calculated the cutoff angle of the groove, 90°, specifically for poly(methyl methacrylate) (PMMA), otherwise the groove waves would leak into

the two flat surfaces. This new type of waveguide could also be promising in piezoelectric materials.

2.5 Direct change of surface property on lithium niobate

The biggest problem with overlaid—shorting and mass-loading—waveguides is the fact that a layered substrate is lossier than an unlayered one. As a result, apart from the mass-loading and shorting-strip waveguiding structures, there is another route to waveguide structure fabrication that adds negligible loss but still allows the SAW velocity to be significantly changed: directly changing the material properties of the LN itself in the substrate.

As it has long been proved that diffusion of metals or their oxides into LN could locally increase the optical refractive index of the crystal [359], SAW waveguide can be fabricated by creating an in-diffused region (fast region) and an non-in-diffused region (slow region). Schmidt [316] and Weller *et al.* [360] proposed that the surface wave velocity could be increased by metal in-diffusion without additional acoustic loss. A thin layer of metal (Ti, Ni, Cr) of thickness τ was evaporated onto the LN surface in order to create a region of increased velocity via metal diffusion, for

which the effective depth obeyed the diffusion equation, $b = (4Dt)^{1/2}$, where D was the diffusion constant. A typical condition could be: $\tau = 100$ nm, $t = 30$ h, and $T = 1000$ °C. The diffused depth was reported to be 3 μm when Ti was involved, resulting in an increase of velocity at about 1% for SAWs at 412 MHz. And they also pointed out that the loss for waves traveling on both diffused and undiffused region were on the order of 0.1 dB. Their results indicated similar conclusion as that of Schmidt, and further bolstered the advantages of such waveguides: low loss, non-shorted surface, and potential dispersion control by tuning the diffusion parameters.

Other than metal diffusion, a novel means involving ion implantation, which successfully decreased the SAW velocity in LN, was proposed by Hartmann *et al.* [363, 361]. Ion implantation was commonly utilized for fabricating semiconductor components, and the most straightforward advantage was that it did not require high temperature as metal diffused. Two doses of helium ions at 100 keV, with ion beam density at 2.5×10^{15}, 6×10^{15} and 10^{16} ions/cm^2, have been used in their study. As the ion bombardment would induce a velocity decrease for LN, they attributed this reduction to the change of effective electromechanical coupling coefficient. Also as shown in Fig. 2.18, the acoustic power distribution was investigated with a laser probe for 150 MHz SAWs, which produced a Gaussian profile. And through their data and calculation using Knowles' scalar potential [364], for an 81.2 μm wide ion-

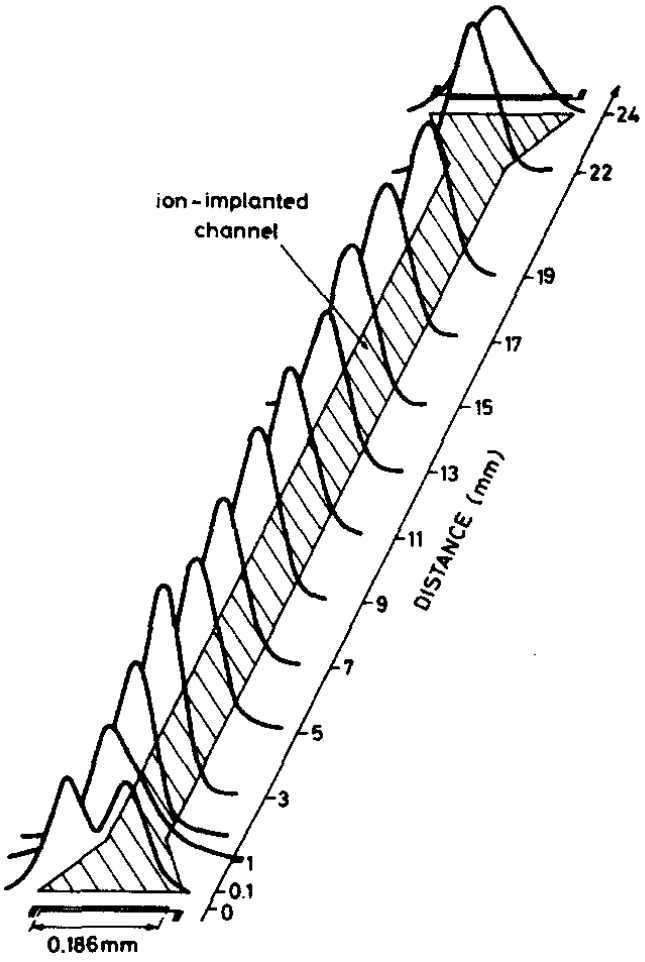

Figure 2.18: Acoustic power profiles along an ion-implanted 150 MHz SAW guide on YZ LN. The ion dose is equal to 6×10^{15} ions/cm^2 at 100 keV. The ion-implanted channel is 81.2 μm wide. (Figure permission acquired from the paper of Hartemann *et al.* [361])

implanted channel, 90% of the acoustic power was confined in a region of width 120 μm.

In the 1980s, new ideas on producing high-index optical waveguides were

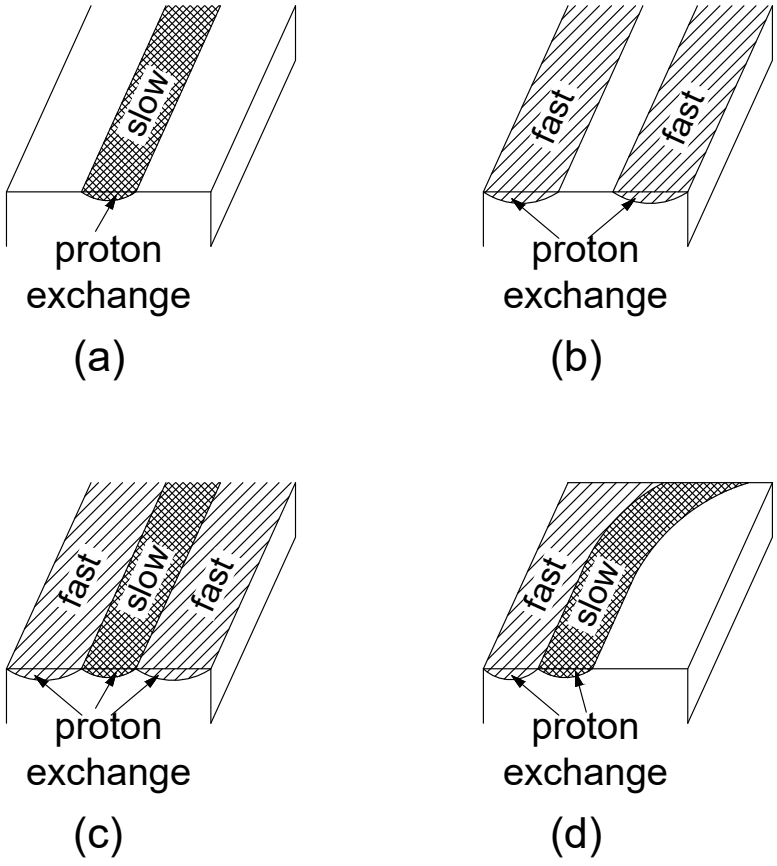

Figure 2.19: Possible proton exchanged SAW waveguiding structures on YX and YZ LN (a) "stripe-type guide"; (b) "slot-type guide"; (c) combined "stripe- and slot-type" guide; (d) curved asymmetric guide. (Figure adapted from the paper of Hinkov [362])

devised with the exchange of Li^+ ion by protons in LN [365]. Proton exchange caused the density of LN to reduce, resulted from the lighter protons which substituted the heavier Li^+ ions and a small increase in the volume of the material from an expansion of the structure [366]. This technique led to a large decrease (up to 20%) of phase

as well as group velocity on the LN surface, because of the drastic reduction of the corresponding elastic constants. It could be used to construct acoustic waveguides (*see* Fig. 2.19) due to the strong field confinement and relative low loss [362], and superior to ion implantation as a low-cost alternative.

2.6 Conclusions

This review at first briefly described the devices and materials used to generate SAWs, later pointing out the two main problems that prevent the use of SAW on a piezoelectric substrate in microfluidics, nanofluidics, and acoustofluidics applications: beam steering and lateral diffraction. A possible solution is proposed in the form of waveguides that can not only overcome these difficulties but also confine the wave in the "slow" region and thus manipulate the direction of wave propagation on the surface. As in the context of wave confinement, devices that are able to generate relatively narrow beam SAW (FIDT) are introduced in detail. In the discussion of flat overlay waveguides, comparing with mass-loading waveguides, shorting-strip waveguides show the ability of reducing the velocity by a short-circuiting effect, producing a method for waveguiding regardless of the anisotropy of the piezoelectric substrate, especially LN. Topographic waveguides, different from thin film waveguides, are essentially single material structures with locally defined geometries. In

rectangular ridge waveguides, the ASF mode shows both strong confinement and dispersion, while the pseudo-Rayleigh mode is almost dispersionless. The wedge shaped waveguide is able to efficiently confine the waves and energy at the wedge tip with minimal dispersion. Another type of guiding technique, altering the substrate's material properties, was also discussed. To sum up, thin film waveguides have been proven to possess the advantages of low loss propagation and ability to readily follow any waveguide bends, such as acoustic wave steering and splitting using different waveguide structures, which could be useful in enhancing the devices performance. Furthermore, by incorporating waveguides, it is promising to allow wave propagation in arbitrary direction and drive acoustic energy to independent locations to achieve fluid or particle manipulation at disparate positions, which can be widely applied in the field of acoustofluidics.

2.7 Acknowledgments

This work was in significant part generously supported by a research grant from the W.M. Keck Foundation, the National Institutes of Health Interdisciplinary Anesthesiology Research Training Program T32–GM121318–01, a grant from the Office of Naval Research (12368098), and a grant from the Department of Energy (DE–EE0008363). The authors are grateful to Prof. Kenjiro Takemura for advice

and comments regarding this work.

This chapter, in full, is a reprint of material appearing in Mechanical Engineering Reviews 2020. Jiyang Mei, and James Friend. "A review: controlling the propagation of surface acoustic waves via waveguides for potential use in acoustofluidics." Mechanical Engineering Reviews 7, no. 1 (2020): 19-00402. The dissertation author was the primary investigator and author of this paper.

Chapter 3

Fabrication of Surface Acoustic Wave devices On Lithium Niobate

3.1 Introduction

Relying on the well-known inverse piezoelectric effect, where the atomic dipoles create strain corresponding to the application of an electric field, piezoelectric crystals such as lithium niobate $LiNbO_3$ (LN), lithium tantalite $LiTaO_3$ (LT), can be used as electromechanical transducers to generate SAW for microscale applications [239, 126, 202, 240, 214, 218]. By enabling the generation of displacements up to 1 nm at 10-1000 MHz, SAW-driven vibration overcomes the typical obstacles of traditional

ultrasound: small acceleration, large wavelengths, and large device size. Research to manipulate fluids and suspended particles has recently accelerated, with a large number of recent and accessible reviews [11, 12, 14, 367].

Fabrication of SAW-integrated microfluidic devices requires fabrication of the electrodes—the interdigital transducer (IDT) [368]—on the piezoelectric substrate to generate the SAW. The comb-shape fingers create compression and tension in the substrate when connected to an alternating electric input. The fabrication of SAW devices has been presented in many publications, whether using lift-off ultraviolet photolithography alongside metal sputter or wet etching processes [367]. However, the lack of knowledge and skills in fabricating these devices is a key barrier to entry into acoustofluidics by many research groups, even today. For the lift-off technique [369, 370], a sacrificial layer (photoresist) with an inverse pattern is created on a surface, so that when the target material (metal) is deposited on the whole wafer, it can reach the substrate in the desired regions, followed by a "lift-off" step to remove the remaining photoresist. By contrast, in the wet etching process [371, 98, 372, 373], the metal is first deposited on the wafer and then photoresist is created with a direct pattern on the metal, to protect the desired region from "etching" away by a metal etchant.

In a most commonly used design, the straight IDT, the wavelength of the

resonant frequency of the SAW device is defined by the periodicity of the finger pairs, where the finger width and the spacing between fingers are both $\lambda_{\mathrm{SAW}}/4$ [99]. In order to balance the electric current transmission efficiency and the mass loading effect on the substrate, the thickness of the metal deposited on the piezoelectric material is optimized to be about 1% of the SAW wavelength [91]. Localized heating from Ohmic losses [374], potentially inducing premature finger failure, can occur if insufficient metal is deposited. On the other hand, an excessively thick metal film can cause a reduction in the resonant frequency of the IDT due to a mass loading effect and can possibly create unintentional acoustic cavities from the IDTs, isolating the acoustic waves they generate from the surrounding substrate. As a result, the photoresist and UV exposure parameters chosen vary in the lift-off technique, depending upon different designs of SAW devices, especially frequency. Here, we describe in detail the lift-off process to fabricate a 100 MHz SAW-generating device on a double-sided polished 0.5 mm-thick 128° Y-rotated cut LN wafer, as well as the wet etching process to fabricate the 100 MHz device of identical design. Our approach offers a microfluidic system enabling investigation of a variety of physical problems and biological applications.

3.2 Protocol

3.2.1 SAW device fabrication via the lift-off method

1. Perform wafer solvent cleaning in a Class 100 clean room facility by immersing the 4" (101.6 mm) LN wafer into acetone, followed by isopropyl alcohol (IPA), then deionized water (DI water), each in a sonication bath for 5 min. Pick up the wafer and blow the surface dry with nitrogen (N_2) gas flow to remove the remaining DI water from the wafer.

   CAUTION: Perform the acetone and IPA immersions in a fume hood. Avoid inhalation and skin contact with IPA. Avoid skin and eye contact with acetone. Do not swallow.

   NOTE: Do not allow any fluid to evaporate upon the wafer; if any dust or debris on the surface, start this step over.

2. Place the wafer onto a hotplate at 100 °C to prebake for 3 min.

   NOTE: Because of the pyroelectric property of LN, it will generate static charges and associated stress within the wafer during heating and cooling. It is recommended to put the wafer onto a piece of aluminum (Al) foil after removing it from the hot plate to release the static charges and thus avoid breaking it.

3. Place the wafer onto a spin coater. Using a dropper, cover about 75% of the wafer's surface with negative photoresist (NR9-1500PY). Program a speed of 500 rpm with an acceleration of 3000 rpm/sec for 5 sec and then a speed of 3500 rpm with an acceleration of 3000 rpm/sec for 40 sec, to produce a layer of photoresist around 1.3 μm.

   CAUTION: Perform spin coating in a fume hood. Inhalation of photoresist fumes can cause headaches.

   NOTE: The thickness may vary depending on the condition of the photoresist and the spin coater used, even with the same spin settings. The photoresist may be spun beyond the edge and onto the wafer's obverse edge; this must be removed by using an acetone-doused swab. Left present, the photoresist will stick the wafer to the hotplate during the soft bake.

4. To soft bake, place the wafer onto a hotplate at 100 °C, ramp the temperature up to 150 °C, hold it at 150 °C for 1 min. Then move the wafer from the hotplate, and let the wafer cool in the air to room temperature (RT).

   NOTE: Due to the pyroelectric effect, if the temperature of the LN wafer is suddenly changed, for example, by directly transferring the LN wafer onto the hotplate at 150 °C or Al foil at RT, the thermal shock within the wafer will likely shatter it. The presence of nonuniform metal on the surface, such as elec-

trodes, significantly enhances this risk. In applications where the transparency of the LN is not important, consider using so-called "black" LN or more accurately reduced LN, which is dark brown and translucent but has negligible pyroelectricity.

5. Transfer the wafer to the mask aligner (MLA150) for ultraviolet exposure. Expose the photoresist with an energy dose of 400 mJ/cm^2 at 375 nm. The required dose may vary depending on the mask design and the age and condition of the photoresist.

   NOTE: The wave propagation direction induced by IDTs should be along the X-propagating direction in order to effectively generate SAW. In other words, this implies the "fingers" of the IDT should be perpendicular to the X-axis direction. Typical LN wafer manufacturers place the primary (larger) wafer flat (straight edge alongside of wafer) perpendicular to the X-axis, so your IDT fingers should be parallel to this flat. Some manufacturers introduce a second (smaller) wafer flat to help indicate the Y- and Z-axis directions, but this detail is unimportant for SAW generation. Manufacturers often request specifications for the surface finish of the wafer; if you require a transparent wafer, request double-sided optically polished wafers. However, keep in mind that LN is birefringent, so any object illuminated with standard laboratory

light and seen through the material will produce not one but two images. Overcoming this problem is discussed later. Single-side polished LN is a better choice for SAW generation if you do not need to see through the wafer, because spurious acoustic waves are diffused by the rough back surface.

6. Place the wafer onto a hotplate at 100 °C for 3 min for a post-exposure bake. Then transfer it onto Al foil and allow it to cool to RT.

   NOTE: The patterns should be visible after the post-exposure bake. If not, consider stripping the photoresist and restarting the process over from step 1 above.

7. Develop the wafer by placing it in a beaker filled with pure RD6 developer for 15 sec. Gently shake the beaker during development. Immerse the wafer into DI water for 1 min, and then rinse the wafer under DI water flow. Finally, use dry N_2 flow to remove the remaining DI water from the wafer. Never let any fluid evaporate on the wafer surface.

   CAUTION: Develop the wafer in a fume hood. Avoid breathing in vapors or contacting the developer with eyes and skin.

   NOTE: The photolithography is complete after this step. The protocol can be paused here.

8. Hard bake the wafer on a hotplate at 100 °C for 3 min. Then transfer it onto Al foil and allow it to cool to RT.

   NOTE: This step is to remove any moisture from the wafer and photoresist to prevent later outgassing during sputtering.

9. For electrode sputter deposition, place the wafer into a sputter deposition system. Vacuum the chamber to 5×10^{-6} mTorr. Use argon flow at 2.5 mTorr, sputter chromium (Cr) with a power of 200 W for 5 nm as an adhesion layer, followed by sputtering Al with a power of 300 W for 400 nm to form the conductive electrodes.

   NOTE: Deposition time should be calculated from the expected thickness and the deposition rate. Titanium (Ti) can be used instead of Cr, though the removal process is more difficult as Ti is tougher. Gold (Au) is also commonly deposited as conductive electrodes. For higher frequency SAW devices, Al should replace Au to avoid the mass loading effects of the AU IDT fingers which reduce the local SAW response frequency under the IDT, forming an acoustic cavity from which the SAW can only escape with significant loss.

10. For the lift-off process, transfer the wafer into a beaker and immerse in acetone. Sonicate at medium intensity for 5 min. Rinse with DI water and dry the wafer

with N_2 flow.

CAUTION: Use acetone in a fume hood. Avoid inhalation and skin or eye contact with acetone. Do not swallow.

NOTE: The protocol can be paused here.

11. Use a dicing saw to dice the entire wafer into small pieces of chips as SAW devices for further applications.

    NOTE: The process is complete. The protocol can be paused here.

    NOTE: Instead of a saw, a diamond-tipped wafer scribe (or even a glass cutter) can be used to dice the LN wafer with some practice, though due to the anisotropy of LN it is important to scribe and break the wafer first along scribe lines perpendicular to the X-axis, followed by those lines along the X-axis.

3.2.2 SAW device fabrication via the wet etching method

1. Perform wafer solvent cleaning in a Class 100 clean room facility by immersing the 4" (101.6 mm) LN wafer in acetone, followed by IPA, then DI water, each in a sonication bath for 5 min. Pick up the wafer and dry the surface using N_2 to remove the remaining DI water from the wafer.

   CAUTION: Use acetone and IPA in a fume hood. Avoid inhalation and skin

contact with IPA. Avoid acetone contact with skin and eyes. Do not swallow.

2. Place the wafer onto a hotplate at 100 °C for thermal treatment for 3 min. Then transfer it onto Al foil to cool down to RT.

3. Place the wafer into a sputter deposition system. Vacuum the chamber to 5×10^{-6} mTorr. Use argon flow at 2.5 mTorr, sputter Cr with a power of 200 W for 5 nm as an adhesion layer, followed by sputtering Au with a power of 300 W for 400 nm to form the conductive electrodes.

   NOTE: The protocol can be paused here.

4. Place the wafer onto a spin coater. Using a dropper, cover about 75% of the wafer's surface with positive photoresist (AZ1512). Program a speed of 500 rpm with an acceleration of 3000 rpm/sec for 10 sec and then a speed of 4000 rpm with an acceleration of 3000 rpm/sec for 30 sec, ultimately producing a layer of photoresist around 1.2 μm.

   CAUTION: Perform spin coating in a fume hood. Inhalation of photoresist fumes can cause headaches.

5. To soft bake, place the wafer onto a hotplate at 100 °C for 1 min. Then transfer it onto Al foil and allow it to cool to RT.

6. Transfer the wafer to the mask aligner (MLA150) for ultraviolet exposure. Expose the photoresist with an energy dose of 150 mJ/cm^2 at 375 nm. The dose required may vary depending on the mask design and the age and condition of the photoresist.

7. Place the wafer into a beaker filled with pure AZ300MIF developer for 30 sec. Gently shake the beaker during development. Immerse the wafer into DI water for 1 min, then rinse the wafer under DI water flow. Finally, use dry N_2 flow to remove the remaining DI water from the wafer. Never let any fluid evaporate on the wafer surface.

   CAUTION: Avoid contacting AZ300MIF with skin or eyes. Do not swallow.

8. Immerse the wafer into a beaker filled with Au etchant for 90 sec, gently shaking the beaker. After rinse the wafer under DI water flow, dry with N2 flow to remove the remaining DI water from the wafer. Never let any fluid evaporate on the wafer surface.

   CAUTION: Gold etchant can be hazardous to the eyes and skin, and will cause respiratory irritation. This step requires more personal protective equipment (PPE), such as safety glass, black neoprene gloves, apron, etc.

9. Immerse the wafer into a beaker filled with Cr etchant for 20 sec, gently shaking

the beaker. After rinse the wafer under DI water flow, dry with N_2 flow to remove the remaining DI water from the wafer. Never let any fluid evaporate on the wafer surface.

CAUTION: Chromium etchant can cause eye, skin and respiratory irritation. This step also requires more PPE.

10. Clean the (sample) wafer, by putting it into acetone, followed by IPA, and DI water in a sonication bath for 5 min each. Pick up the wafer and dry with N_2 gas flow over the surface of the wafer to remove the remaining DI water from the wafer.

    CAUTION: Use acetone in a fume hood. Avoid inhalation and skin contact acetone with skin and eyes. Do not swallow.

    NOTE: This step is to remove the undesired photoresist on the wafer. The protocol can be paused here.

11. Use a dicing saw to dice the entire wafer into discrete SAW devices for further use.

    NOTE: The process is complete. The protocol can be paused here.

3.3 Experimental setup and testing

1. Observe the SAW device under bright-field optical microscopy.

   NOTE: Observe the SAW device under bright-field optical microscopy.

2. For SAW actuation, attach absorbers at both ends along the propagation direction of the SAW device to prevent reflected acoustic waves from the edges.

3. Use a signal generator to apply a sinusoidal electric field to the IDT at its resonant frequency of around 100 MHz. An amplifier should be connected to amplify the signal.

4. Use an oscilloscope to measure the actual voltage, current, and power applied onto the device. The amplitude and frequency response of the SAW are measured by a laser Doppler vibrometer (LDV); the SAW-actuated droplet motion is recorded using a high-speed camera attached to the microscope.

3.4 Representative results

The IDT to be measured is designed to have a resonant frequency at 100 MHz, as the the finger width and the spacing between them are 10 μm, producing a wavelength of 40 μm. Figure 3.1 shows the IDTs fabricated using this method.

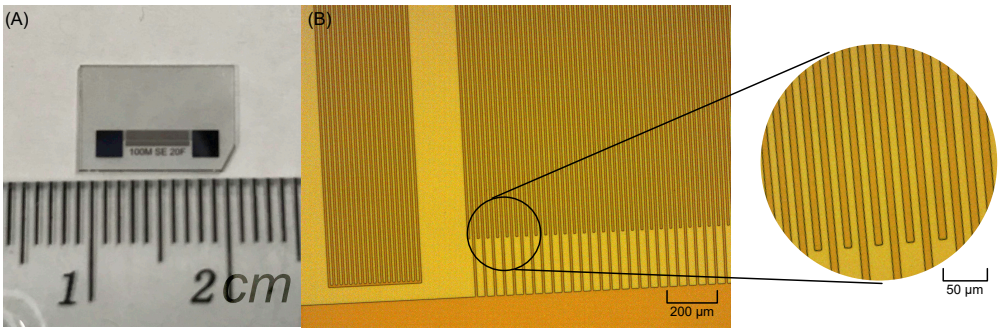

Figure 3.1: **Images of fabricated devices.** (A) A gold-electrode IDT with 7 mm aperture on an LN substrate for 100 MHz SAW generation and propagation. (B) The fingers of the IDT. Scale bar: 200 μm. (The gratings on the left are reflectors to prevent energy loss.) The inset illustrates the fingers at a greater magnification. Scale bar: 50 μm.

Using an oscillating electrical signal matched to the resonant frequency of the IDT, SAW can be generated across the surface of the piezoelectric material. The LDV measures the vibration via the Doppler effect on the surface, and through signal processing, information such as amplitude, velocity, acceleration, and phase could be acquired and displayed using the software. We illustrate the frequency response under a frequency sweep from 90 to 105 MHz, with an input power of 140 mW, a peak-to-peak voltage of 70 V, and peak-to-peak current of 720 mA. As Figure 3.2B indicates, the amplitude of the SAW is 19.444 pm at a resonant frequency of 96.5844 MHz. The slight reduction in frequency from the 100 MHz design is attributed to the mass loading of the metal IDT electrodes. Figure 3.2A illustrates the LDV-measured vibration of the SAW on the surface, shown to be propagating from the IDTs. The standing wave ratio (SWR) is calculated to be 2.06, determined by using the ratio of maximum amplitude to minimum amplitude (SWR = 1 for a pure traveling wave while SWR = ∞ for a pure standing wave), suggesting a good traveling wave has been obtained here.

We also demonstrated the motion of a sessile droplet actuated by the SAW device, under a single frequency signal input (80.6 mW) at its resonance (96.5844 MHz). A 0.2 μL droplet is pipetted on LN about 1 mm away from the IDT (*see* Figure 3.3A). When the SAW propagates and encounters the water droplet upon the

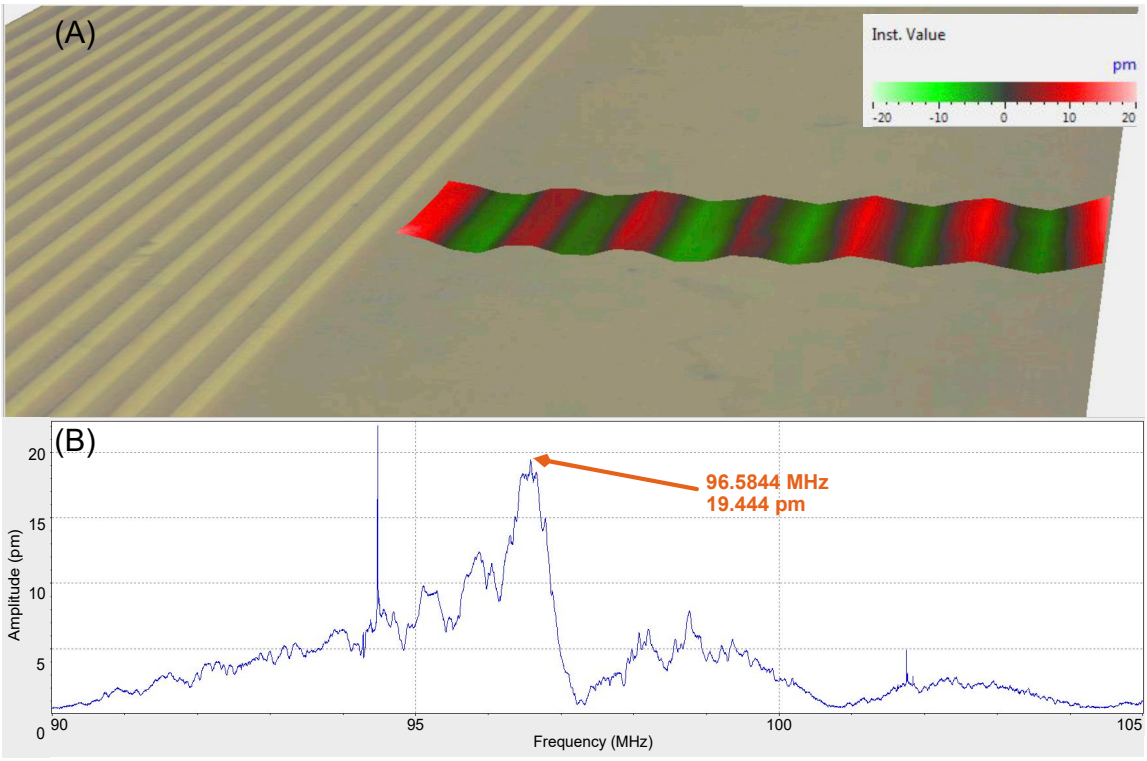

Figure 3.2: **LDV measurement of the SAW device.** (A) A snapshot of the traveling wave generated by the IDT. The SAW present upon the LN substrate as it propagates from the IDT. The phase has been determined by scanning the LDV head to measure in multiple locations, with the phase referenced against the input electrical signal. (B) A frequency response (amplitude vs. frequency) of the SAW device from 90 MHz to 105 MHz includes its resonance at 96.5844 MHz with 19.444 pm amplitude at the input level of 140 mW from the LDV.

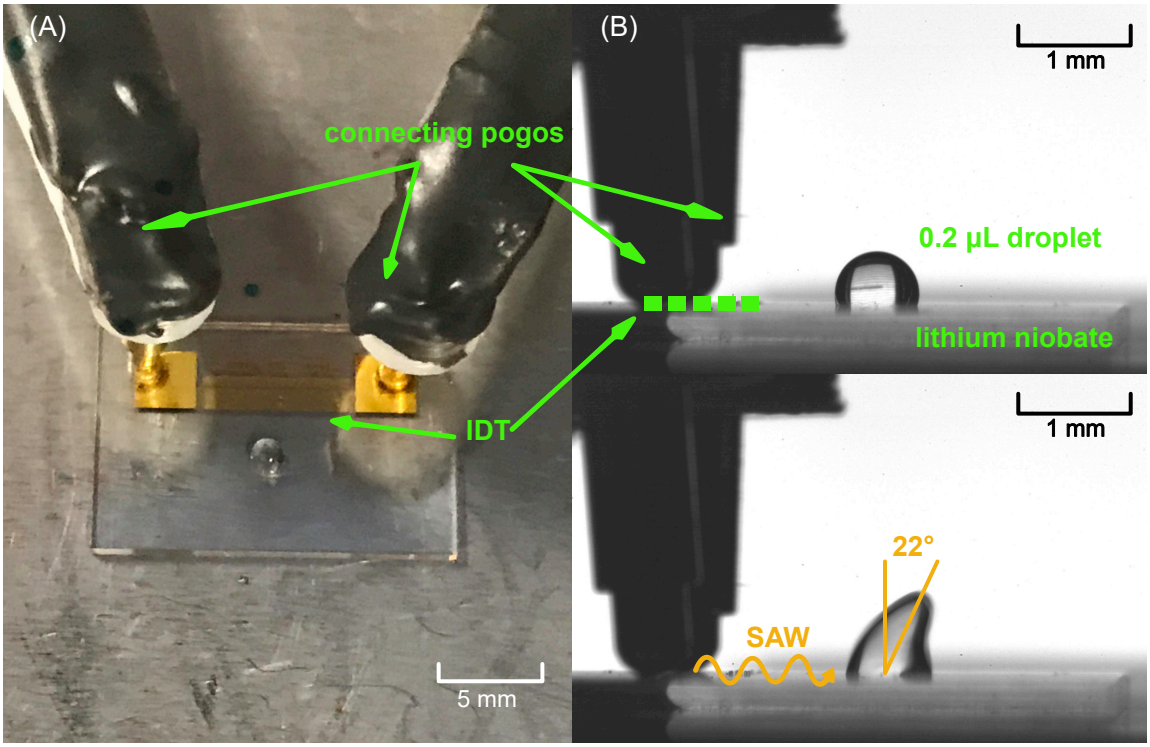

Figure 3.3: **SAW-induced droplet jetting.** (A) The experimental setup for SAW-induced sessile drop actuation on LN. Scale bar: 5 mm. (B) SAW is propagating from the left to right in the images. The droplet jetting, at approximately the Rayleigh angle (22 °) occurs at 80.6 mW power input. Scale bar: 1 mm.

surface, it "leaks" into the liquid at the Rayleigh angle, because of the impedance difference from LN to water, and calculated as the ratio of sound speed in these two media,

$$\theta_R = \sin^{-1}\left(\frac{v_{\text{water}}}{v_{\text{SAW,LN}}}\right) = \sin^{-1}\left(\frac{1498\ \text{m/s}}{3992\ \text{m/s}}\right) \approx 22^\circ \tag{3.1}$$

The jetting angle shown in Figure 3.3B confirmed the presence of SAW.

3.5 Discussion

SAW devices fabricated from either method are capable of generating useful traveling waves on the surface, and these methods underpin more complex processes to produce other designs. The resonant frequency is usually a little lower than the designed value, due to the mass loading effect of the metal deposited on top. However, there are still some points worth discussing to avoid problems.

3.5.1 Lift-off method

The choice of photoresist is important. It is possible to use a positive photoresist for the fabrication, which, nevertheless, will be more difficult. Because the unexposed photoresist is dissolved, the part left on the substrate will form a trapezoidal shape, especially with underexposure, as exaggerated in Figure 3.4A. The metal sputtered on the top of such a photoresist will prevent the solvent from penetrating and result in difficulties in removing it during the lift-off step. On the other hand, UV-exposed regions of a negative photoresist are removed, and, as shown in Figure 3.4B, an inverted trapezoidal is typically formed with overhang that makes lift-off step much easier.

Apart from the lift-off problem of positive photoresist, the fingers will eventually be slightly narrower than designed, *i.e.*, the spacing between them will be

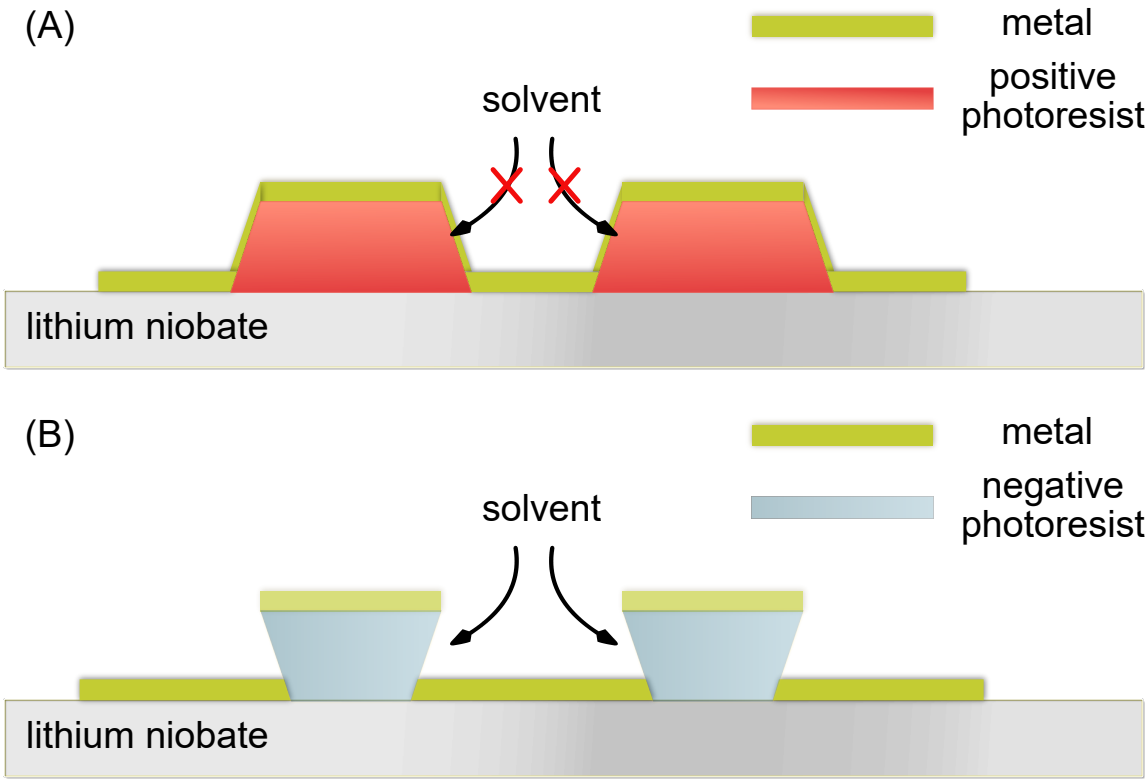

Figure 3.4: **Scheme for photoresist left on the substrate.** (A) When positive photoresist is used, it has an undesirable trapezoidal shape after development. Depositing metal on such a surface makes the subsequent lift-off process difficult and prone to failure. (B) However, using a negative photoresist produces an inverted trapezoidal shape with overhang, making it far easier to dissolve the underlying photoresist and remove the metal during lift-off.

slightly larger, due to the trapezoidal shape. With negative photoresist, the spacing is smaller. These effects slightly change the resonant frequency from the design intent.

When using negative photoresist, the UV exposure dose is crucially important. Due to the variety of equipment, photoresists, and reagents available today, the exposure time required in your fabrication process will very likely vary. Observation of the fabricated device result can guide you in trying to determine what went wrong. Over-exposure will cause the fingers to be narrower and the spacing wider than designed. Under-exposure may leave some of the photoresist after development, in which case the metal in the desired area will peel off together with the thin layer of the remaining photoresist after lift-off. Sometimes people tend to use a single polished LN wafer, as mentioned above, which is opalescent. The time and dose required for UV exposure with such a wafer will be increased, since the light is diffused at the back.

3.5.2 Wet etching method

The key step for this method is to ensure the photoresist is completely dissolved from the area where metal needs to be etched away, otherwise the etchant will be blocked and the lithography will fail.

As the metal etching is isotropic, it occurs both through and across the metal layer, making the fingers narrower than designed. Negative photoresist is therefore a better choice in this technique to reduce the undesired feature loss.

3.5.3 Limitation

Both methods are limited to fabricating feature sizes to greater than a few micrometers. According to our experience in our facilities, the limit can be pushed to as small as 2-3 μm. If submicron features are required, other fabrication techniques may be called upon.

3.6 Acknowledgments

The authors are grateful to the University of California and the NANO3 facility at UC San Diego for provision of funds and facilities in support of this work. This work was performed in part at the San Diego Nanotechnology Infrastructure (SDNI) of UCSD, a member of the National Nanotechnology Coordinated Infrastructure, which is supported by the National Science Foundation (Grant ECCS–1542148). The work presented here was generously supported by a research grant from the W.M. Keck Foundation. The authors are also grateful for the support of this work by the Office of Naval Research (via Grant 12368098).

This chapter, in full, is a reprint of material appearing in Journal of Visualized Experiments 2020. Jiyang Mei, Naiqing Zhang, and James Friend. "Fabrication of surface acoustic wave devices on lithium niobate." JoVE (Journal of Visualized Experiments) 160 (2020): e61013. The dissertation author was the primary investigator and author of this paper.

Chapter 4

Non-contact three-dimensional cell cluster formation on demand in open dishware using focused SAW through a couplant layer

4.1 Introduction

Cell cultures, regenerative medicine, and tissue engineering rely on efficient production of cell agglomerates to replicate human body processes and functions

for biological and clinical applications [375, 376]. In 1907, Harrison established cell culturing to probe the origin of nerve fibers. His technique and subsequent improvements enabled the continuous observation of tissue growth and differentiation of targeted cells outside the body [377]. Cells are traditionally seeded and grown on a flat substrate, such as a flask or a petri dish, in which cell culture media and antibiotics are added to ensure cell health in a single layer at 37 °C [378]. Though monolayer cell cultures are used to probe signaling pathways, recent studies have demonstrated that these cultures behave much differently than tissue in *in vivo* physiological conditions [379]. Consequently, information obtained from two-dimensional (2D) cultures may be misleading in real tissues, particularly for intercelluar functions, *e.g.*, proteins in the matrix [380], structural architecture [381], and cell-to-cell interactions [382].

Three-dimensional (3D) cell cultures have been shown to overcome these limitations, better mimicking the *in vivo* complex microenvironment and intercelluar behaviors of animal tissues [383, 384]. Moreover, these 3D systems have been used in biology and tissue engineering [385], drug screening [386], and tumor metastasis [387], tumor angiogenesis [388], toxicology [389], and cell proliferation studies [390].

As agglomerated 3D cell cultures, organoids and spheroids simulate a live cell's *in vivo* environmental conditions far better than two-dimensional cell cultures [391], which makes them useful for tracking physiological changes [392, 393]. Spheroids,

an older construct, are 3D spherical clusters of cells with a necrotic core, formed mostly from cancer cell lines or tumor biopsies where the importance of cell-cell interactions and the morphology and behavior of cells in real tissue are important [394]. Organoids, organ-like structures produced from small fragments of tissue in an extracellular scaffolding environment, were initially regarded as an extension of three-dimensional (3D) cultures. They are able to exhibit functionality similar to the organs from which they are derived [395, 396]. Placed between single cell-based evaluations and animal testing, multicellular constructs like these more closely match the oxygen, nutrient, and waste gradients observed in avascular tumors, beneficial for anti-tumor therapy [397] and cancer drug development [381]. For example, self-organizing organotypic organoids established from stomach [398], kidney [399], liver [400, 401], intestine [402], and breast cancer biopsies [403] contribute to better, more physiologically relevant models of healthy and cancerous human tissue. And, very recently, brain organoids of Neanderthals have been devised to study how modern human brains evolved from this closely related, extinct species to make *homo sapiens* unique among the archaic hominids [404].

However, it is difficult to fabricate uniform and high-quality 3D cell agglomerates to eventually form spheroids or organoids for screening and testing. Existing methods include hanging droplets [386, 405], matrices [406] and scaffolds [407],

self-formation on non-adherent surfaces [408], magnetic-assisted assembly [409], the forced-floating method [410], and dielectrophoresis [411]. These techniques individually suffer from multiple disadvantages. For instance, some are low throughput and tedious, while others require careful labeling of individual cell clusters. A majority of these methods depend upon complicated or specific equipment, like prepared magnetic particle-containing hydrogels or a dielectrophoretic chamber. Most importantly, none of these methods rapidly form the structures.

Acoustofluidic devices have become rather broadly accepted to manipulate biological matter without contact at the submillimeter scale, as comprehensively reviewed in the past [367, 11], serving to engineer tissues [412], sort cells [413, 414, 415], diagnose clinical conditions [416], probe intercellular signaling [417], deliver drugs [418], and analyze single cells [419]. These microfluidic devices have also been further applied to cell culturing, especially for 3D tissue constructs [420, 421, 422]. Bulk acoustic waves (BAW) in particular have been reported to help in forming agglomerates, but it is difficult to maintain uniform results due to the complicated design of the resonator structure [133]. Later studies have shown that biological specimens can be translated and focused under a pressure gradient created by surface acoustic waves (SAW), which is known to manipulate cells [64, 423] without changing their characteristics [424]. Acoustic streaming is also commonly used to concentrate

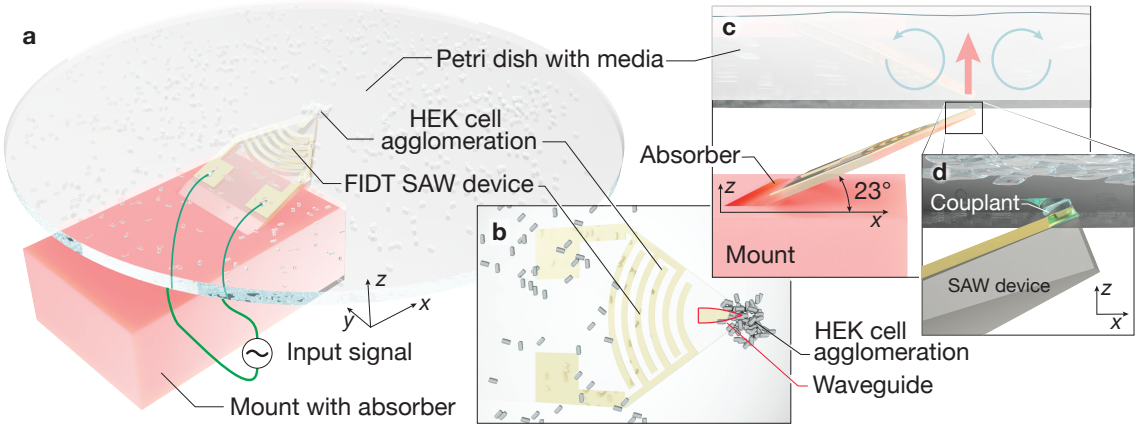

Figure 4.1: **The cell agglomeration device.** The (a) lithium niobate (LN) substrate is held in place by a mount with an absorber to prevent spurious and reflected acoustic waves at the Rayleigh angle of 23°. This structure is mounted below a petri dish laden with media and HEK cells. Focusing surface acoustic waves generated by an input signal into a (b) focusing interdigital transducer (FIDT) on a lithium niobate substrate propagate into the superstrate (petri dish) through an Au focusing waveguide (thickness exaggerated, outlined in red) and into ¡ 0.2 μL Tween 20 as a couplant. The (b) view is from above and along the $-z$ axis through the media, cells, and petri dish. The mount is omitted for clarity. Acoustic energy is passed (c) vertically through the (d) couplant (along the z axis), through the petri dish, and into the cell-laden media (thick arrow). Acoustic streaming is generated in the media, in turn leading to a (c) local recirculation region (thin arrows) around the coupling position. This, in turn, leads to (a,b) cell agglomeration above the SAW device's 40 μm wide tip. (Cells and Au thickness are not to scale for clarity.)

cells and apply drag forces via the surrounding flow [414]. Despite all this effort, a need remains for a reliable, contact-free, flexible, label-free, and biocompatible approach to rapidly form 3D cell clusters.

Here we propose an on-demand method for rapidly and controllably creating cell clusters in an open petri dish using SAW through a thin couplant layer. In

our system, illustrated in Fig. 4.1, the SAW is generated from curved interdigital transducers (IDTs) that laterally focus it to a width of about two wavelengths on the substrate. By introducing a fluid atop the SAW-carrying substrate, this acoustic energy is converted—or *leaked*—into the fluid as longitudinally-propagating acoustic waves at the Rayleigh angle. By mounting the SAW device at this same angle, it is possible to vertically propagate the acoustic waves through the couplant fluid until they come into contact with a petri dish. Lamb waves [425] are produced from modal conversion in the dish substrate, in turn causing longitudinal acoustic waves to be formed in the cell-laden fluid within the petri dish. These acoustic waves propagate at a different Rayleigh angle, as the speed of the Lamb wave in the petri dish is not the same as the speed of the SAW across the lithium niobate (LN) substrate. Acoustic streaming induced by these propagating longitudinal acoustic waves generates local regions of fluid recirculation sufficient to accumulate cells into small clusters. Using this method, we demonstrate local multi-layer cell agglomeration within a well-free container. We further demonstrate the ability to *simultaneously* form several adjacent clusters in a cell culture dish with a set of SAW devices, and then to combine these clusters to form much larger 3D cell agglomerations than have been seen in past work. In what follows, we explain the details of this technique, illustrate its use, and combine imaging and analysis to illustrate how this technique may be used

to easily produce 3D cell cultures on demand.

4.2 Methods

4.2.1 SAW device fabrication

A resonant frequency of 100 MHz for the SAW device was selected based on a desire to have a rapidly attenuating acoustic wave [99] in the cell-laden media after it is converted from SAW to sound, a Lamb wave, and to sound again as it passes through and into the petri dish [125]. This helps reduce reflection of the acoustic wave in the media, and, with the reduction in the wavelength as the frequency is increased, it also helps to facilitate easier manipulation of the individual cells to form an agglomeration. A circularly-focused IDT (FIDT) was deposited on a piezoelectric substrate (LN, 127.68° y-rotated, x-propagating, single crystal, double-side optically polished lithium niobate, PMOptics, Burlington, MA USA) with unweighted and equally spaced fingers to produce a wavelength of 40 μm ($\lambda = v/f$, where λ, v, and f are the wavelength, velocity, and frequency, respectively, of the SAW on the substrate). Details of the fabrication process are provided elsewhere [426], and a brief summary specific to these devices is given here. Standard ultraviolet (UV, 375 nm) photolithography was used for the fabrication of the device, using a nega-

tive photoresist (NR9–1500PY, Futurrex, NJ USA) and associated developer (RD6, Futurrex, NJ USA). This was followed by sputter deposition (Denton 18, Denton Vacuum, NJ USA) of 400 nm Au atop 5 nm Cr, with the latter as an adhesive layer. A triangle-shaped guiding layer with tip width at 40 μm was deposited at the same thickness using the same method to serve as a waveguide for the SAW and reduce lateral diffraction losses [427]. The SAW device was mounted on a 3D-printed platform at the Rayleigh angle (22°).

4.2.2 Cell culture

Human embryonic kidney cells (HEK293 cells, CRL–1573, ATCC (American Type Culture Collection), Manassas, VA USA) were cultured using standard procedure in Dulbecco's Modified Eagle Medium (DMEM, MilliporeSigma, Burlington, MA USA) supplemented with 10% fetal bovine serum (FBS, MilliporeSigma, Burlington, MA USA) and 20 mM glutamine in a 37 °C and 4.4% carbon dioxide (CO_2) incubator (Model 370 Steri-Cycle CO_2 Incubator, ThermoFisher Scientific, Waltham, MA USA). Cells beyond passage thirty were discarded in favor of a lower passage aliquot. Cells were trypsinated in the native container and triturated before being moved into an ultra-low attachment 35 mm petri dish (MS-90350Z, S-bio, Hudson, NH USA) for subsequent cluster formation.

4.2.3 Actuation and measurements

The SAW was powered using a sinusoidal signal input using a signal generator (WF1967 multifunction generator, NF Corporation, Yokohama, Japan) and amplifier (5U1000, AR Instrumentation, Souderton, PA USA). The voltage and current were monitored to allow for the power to be calculated by the oscilloscope (InfiniVision 2000 X-Series, Keysight Technologies, Santa Rosa, CA USA). A small droplet ($\leq$ 0.2 μL) of wetting, surfactant-laden couplant liquid, (Tween 20, #9005-64-5, Cole-Parmer, Vernon Hills, IL USA), was introduced between the mounted lithium niobate substrate and ultra-low attachment petri dish superstrate. The fluid choice essentially eliminated fluid loss to evaporation and ensured wetting of both surfaces. The surface vibration was measured by a laser Doppler vibrometer (UHF–120SV, Polytec, Irvine CA USA and Waldbronn, Germany). All images and videos were acquired by a digital single lens reflex camera (D5300, Nikon, Minato, Tokyo, Japan) attached to a long-working distance microscope (K2-DistaMax, Infinity Photo Optical, Centennial, CO USA) with a 5X objective lens (Mitutoyo M Plan Apo 5X LWD Objective, Edmund Optics Inc., Barrington, NJ USA).

4.2.4 Simulation of fluid flow due to SAW

We simulated the acoustic field due to surface acoustic waves propagating into the medium using finite element analysis (COMSOL Multiphysics 5.5, Comsol Inc., Los Angeles, CA USA) following an approach similar to the one used by Nama *et al.* [428]. This involved using a perturbation approach that resulted in first and second-order equations for the acoustic radiation force and acoustic streaming behavior, respectively, which were successively solved. The second-order results were time-averaged to determine the acoustic streaming-driven fluid velocity. The resulting flow field due to streaming shows an upwelling region at the center, surrounded by a toroidal vortex with inflows along the bottom. This is similar to the experimentally observed flowfield using particle imaging velocimetry (PIV), as shown in Fig. 4.2. The simulation domain was modeled to replicate the geometry of the petri dish with fluid with the 100-MHz transducer at the bottom of the cavity. The left, right and top boundaries of the domain were defined to be walls, to correspond to the geometry of the petri dish. The magnitude of displacement of the transducer face was measured via laser Doppler vibrometry (LDV) to be about 1 nm in amplitude in these experiments, a velocity boundary condition was used for the transducer surface instead. The mesh size was defined to be one-sixth the viscous penetration depth ($\delta_v/6$; consult the Supplementary Information for a sample of the mesh) at

the frequency of operation close to the walls. The fluid in the domain was assumed to have the properties of water.

4.2.5 Visualization of fluid flow using μPIV

In order to visualize and experimentally simulate the trajectories of particles suspended in the SAW-driven recirculation within the petri dish, micro-particle image velocimetry (μPIV) was used. Polystyrene fluorescent particles (ϕ = 43.2 μm, #18242-2, Polysciences Inc., Warrington, PA USA) were introduced into a 35 mm petri dish filled with water, mimicking cells in medium in the dish. The particles were illuminated at 455 nm (M455L3, ThorLabs, Newton, NJ USA). When the SAW was turned on and the recirculation established, the videos were acquired by a high-speed camera (Fastcam Mini UX100, Photron, San Diego, CA USA) at fifty frames per second via epifluorescence filtering centered at 455 nm and a long working distance microscope with a 5X objective lens described above, after which each frame of the videos was extracted to form image sequences (ImageJ 1.53g, National Institutes of Health, Gaithersburg, MD USA). The motion of the particles was then analyzed and calculated by PIVlab [429], revealing the velocity vectors and streamlines.

4.2.6 Cluster characterization

Calcium migration

Ultrasound-formed clusters were analyzed using calcium imaging via an inverted microscope (IN480TC-HD18-HDM, AmScope, Irvine, CA USA). Prior to ultrasound cluster formation, a HEK293 cell line expressing GCaMP6f was generated using a GCaMP6f lentivirus (PLV-10181-50, Cellomics Technology, Halethorpe, MD USA) followed by fluorescence-activated cell sorting (FACS) to maintain 100% GCaMP6f positive cells. Clusters generated by ultrasound were left to rest in a 37°C incubator for 22 hours and then moved to a 60 mm petri dish for imaging. To quantify the intensity and illustrate how the Ca^{2+} concentration evolved across the imaged cells, a circular shape was picked as the region of interest (ROI) where the signaling (green) started to emerge. To measure the progressive signal propagation radially outwards, a series of concentric donut-shaped ROIs was identified and quantified. The pixel intensity was determined (ImageJ) for each region over the time frame and normalized to its own baseline fluorescence, which in this case was the first twenty frames of the video, so that corresponding brightness curves started at one and could be compared, in intensity and time-course.

Immunohistochemistry and imaging

Ultrasound-generated HEK293 cell clusters were fixed in 4% paraformaldehyde in phosphate buffered saline (PBS) for 20 minutes. Immunohistological stainings for tight- and gap-junctions were performed with ZO1 (abcam216880; 1:500, Abcam, Cambridge, UK) and connexin 43 (abcam11370; 1:500, Abcam, Cambridge, UK), respectively, followed by mounting of the clusters between a slide and a coverslip before imaging on a confocal microscope (LSM 800, Zeiss, Oberkochen, Germany) with a 20x objective scanning along the z-axis to visualize cross sections. Junction markers were imaged at 561 nm.

4.3 Results and discussion

4.3.1 Working mechanism

To actuate a small area, focused SAW was generated from the focused interdigital transducer (FIDT) on the lithium niobate substrate (*see* Fig. 4.1(a)). The fabrication and experimental details are described in the *Methods*. A thin 400-nm layer of gold was patterned in a triangular shape as a waveguide to overcome wave steering due to the anisotropic nature of the lithium niobate substrate and further confine the acoustic energy to the tip [427]. The tip of the waveguide was set to have

a 40 μm width to match the wavelength of the SAW as the minimum possible width of the confined SAW in the LN substrate. From formation within the IDT, SAW was propagated on the substrate until it encountered the couplant liquid (Tween 20) placed at the waveguide tip. Upon propagating under the liquid, the SAW diffracted at the Rayleigh angle into the couplant liquid to produce sound. The Rayleigh angle is determined by the speed of sound in the two media, with v_{SAW} as the speed of the Rayleigh SAW in LN and v_{fluid} the longitudinal speed of sound in the coupling fluid, $\theta_R = \sin^{-1}\left(v_{\mathrm{fluid}}/v_{\mathrm{SAW}}\right) = 22^{\circ}$. As the SAW device was tilted at this angle, the longitudinal sound waves were transmitted vertically toward the superstrate, where they were converted to Lamb waves in the superstrate material. The superstrate was a petri dish in our study that contained cell-laden media (*see* Fig. 4.1(b)). Viewed from the top, the vibration induced in the petri dish propagates concentrically outward from the coupling location as shown in Fig. 4.2(a). The wavelength of this propagating wave, about 100 μm, is longer than the SAW in the LN device source, because the velocity of the Lamb wave in the petri dish is higher. The propagating leaky Lamb waves produced longitudinal sound waves in the fluid medium, leading to acoustic streaming sufficient to induce recirculation in the medium.

The power of the SAW, and therefore the velocity of the recirculation, was controlled such that the cells would be translated to the center by the drag force,

but would not be pushed up and carried away by the recirculation, along the lines of past work using other devices [414]. This produced a monolayer of cells adjacent the petri dish's bottom surface. The hydrodynamic drag from the flow at low Reynolds number can be derived from Stokes' equation as $F_d = 6\pi\eta r v$, where η is the dynamic viscosity of the medium; r is the radius of the particle; and v is the flow velocity. Later, we show that as the size of the "particle" grows through agglomeration of cells, it becomes possible to lift and fold these monolayer agglomerates to form large multilayer groupings of cells.

4.3.2 Cell agglomeration

We first considered the ability to rapidly agglomerate cells using the device. As described in Subsection 4.2.2, HEK293 cells were diluted to a density of 1.25×10^5 cells/mL and 1.2 mL of the suspension was transferred to the low-attachment petri dish. A recirculation vortex formed in the fluid contained by the petri dish during exposure to acoustic energy from our device. The flow carried unattached cells present in this vortex to the center of the actuation area, gradually forming a flat, monolayer to few-layer cluster. Power sufficient to initially move the cells was about 15 mW, although this is insufficient to draw the cells into the vortical flow. The velocity of the cells may be intrinsically adjusted by altering the power

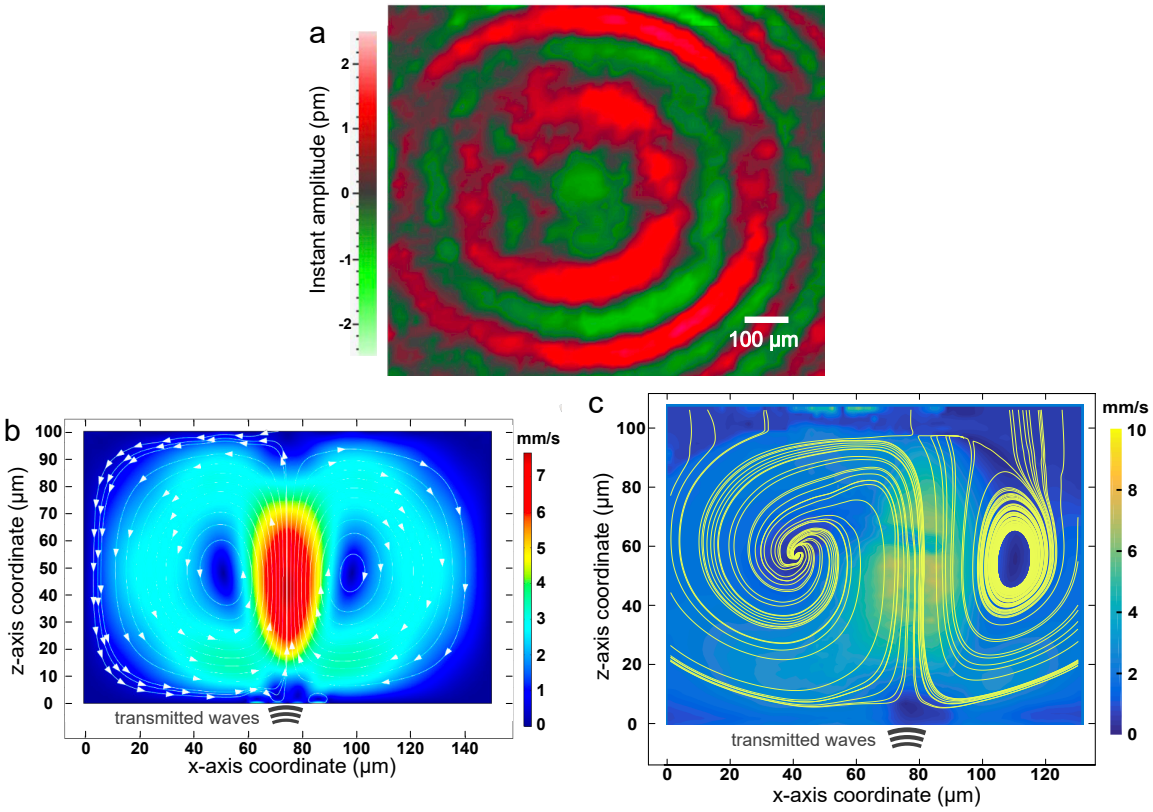

Figure 4.2: **Generation of local vortical flow by leaky Lamb waves from the coupling point.** (a) LDV measurements display the Lamb wave propagating along the petri dish, from roughly at the center, the source of acoustic energy from coupling with the SAW device from below. The Lamb wave concentrically spreads out from the center of transmission, where red and green colors denote the instantaneous peaks and valleys of the vibration. Scale bar: 100 μm. Side views of the recirculation in the fluid within the petri dish, as actuated by the transmitted acoustic waves from the SAW device through the couplant liquid, and onward through the glass of the petri dish into the fluid within, using (b) finite element analysis, and (c) experimental μPIV, where the background color represents the velocity magnitude and the yellow lines display the streamlines. The petri dish's top surface is at $z = 0$, and the couplant is centered at $x = 78$ μm along the x axis. The x, y, and z directions are identified in Fig. 4.1(a).

input. However, when the power was increased above 92 mW, individual cells were lifted into the recirculation and lost instead of adhering to the nascent agglomerate, greatly slowing the agglomerate's growth. Compared with the hours to days required for agglomeration to form using other methods, our technique accumulated the cells together within minutes. Whatever the method, incubation is required for a few hours so that the cells are bound together by an actin network. In our method, this is fortunately accomplished without needing to apply SAW after forming the initial agglomerate.

Cells roughly agglomerate from a dispersed condition into a circular, flat monolayer to few-layer shape in 2 min with a diameter of about 280 μm, as shown in Fig. 4.3(a). The agglomeration grows with time to 310 μm at 4 min and 360 μm at 6 min. It is important to note that the dark, chevron-shaped spots in Fig. 4.3 were introduced to identify the point at which the couplant fluid touches the petri dish. The observed cell cluster area was measured and plotted in Fig. 4.3(b) for operation at 92 mW input into the SAW device. The error bars represent the standard deviation of the data, repeated five times per data point, with the average used as the main data point. Data were acquired from three parallel agglomeration experiments using the same batch of cells under the same power (92 mW).

The agglomeration's growth slows over time, to essentially a constant at about

500 s or 8 min. Nearly all the cells have been extracted from the recirculating vortex by this time, and only rarely do cells from outside the vortex enter into it. Further, the size of the agglomerate with respect to time under the same input power at different cell density levels is also presented in Fig. 4.3(b), showing a similar trend. This indicates that the method works for different cell concentrations, though the final cluster size strongly depends on the concentration. In fact, the initial change in the cluster size with respect to time corresponds to the square of the cell concentration to less than 5% error. This is indicative of *orthokinetic coagulation*, a term coined long ago by von Smoluchowski [430] to represent shear-based particle agglomeration [431].

4.3.3 Cluster translation

A natural extension from forming flat, monolayer to few-layer clusters of cells is to manipulate them. For example, moving them around in the petri dish without a pipette. The ability to form multilayer to wholly spherical agglomerations of cells would be even better. Moreover, if one wishes to increase the size of a cluster beyond what a given vortex recirculation cell can provide, it is reasonable to suppose the SAW device, the vortex cell it is generating, and the cluster entrapped within the cell could all be moved around to collect more cells and enlarge the cluster. Alternatively,

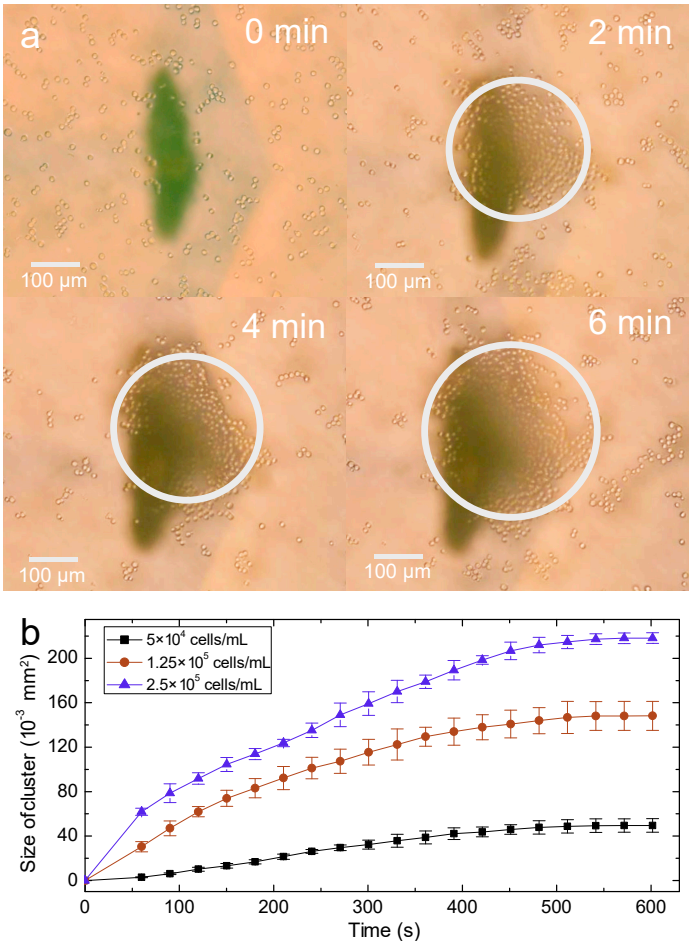

Figure 4.3: **Cell agglomeration via coupled SAW-Lamb waves.** Initially, cells are homogeneously distributed in the media at a concentration of 1.25×10^5 cells/mL with no SAW. Upon activating 92 mW SAW in this arrangement, cells are gradually accumulated above the coupling point where the acoustic wave is transmitted from below, indicated in the images above with a dark right-handed chevron shape. The white circles outline the grouping of cells that gradually grow over time until they reach an almost steady state. This is more clearly shown by b) a plot of the cluster's area with respect to time at various cell concentrations, 5×10^4 cells/mL (black squares), 1.25×10^5 cells/mL (red circles), 2.5×10^5 cells/mL (blue triangles). After eight minutes, the cluster size reached a steady state in this experiment. The error bars denote the standard deviation from five measurements of the cluster size. A video of the phenomenon is provided in the Supplementary Information. Scale bar: 100 μm

one could create several clusters and merge them afterwards.

Similar to the process of agglomeration, where the cells are "dragged" by the flow into a quiescent point at the center of the vertical flow, translation of an entire monolayer agglomeration is also possible when the flow is sufficient. In our experiments, a cluster about 350 μm in size was translated over a 560 μm distance in 90 s at a speed of 5.77 μm/s using a power of 91.48 mW (*see* Fig. 4.4 and a video of the phenomenon in the Supplementary Information). In these results, the SAW device and microscope were held in a fixed position while the petri dish was moved. The cell agglomeration remained fixed in place with the SAW transducer's tip while the petri dish was moved.

Unsurprisingly, the transport speed is reduced as the size of the object is increased. For example, a larger, elliptical, and thin cluster about 1029 μm $\times$ 750 μm in size was moved at about 2.35 μm/s. In doing so, it also shows how this cluster may be translated to come into contact with another, smaller 647 μm cluster. By placing the center of the induced flow vortex at a point between these two clusters, it was possible to merge them together to form a 1410 μm $\times$ 810 μm sized monolayer cluster. In this way it becomes possible to form rather large monolayer clusters of cells. To date, we have assembled monolayer clusters up to about 1510 μm $\times$ 1100 μm in size with this procedure. This size—and the size of the agglomerates we report

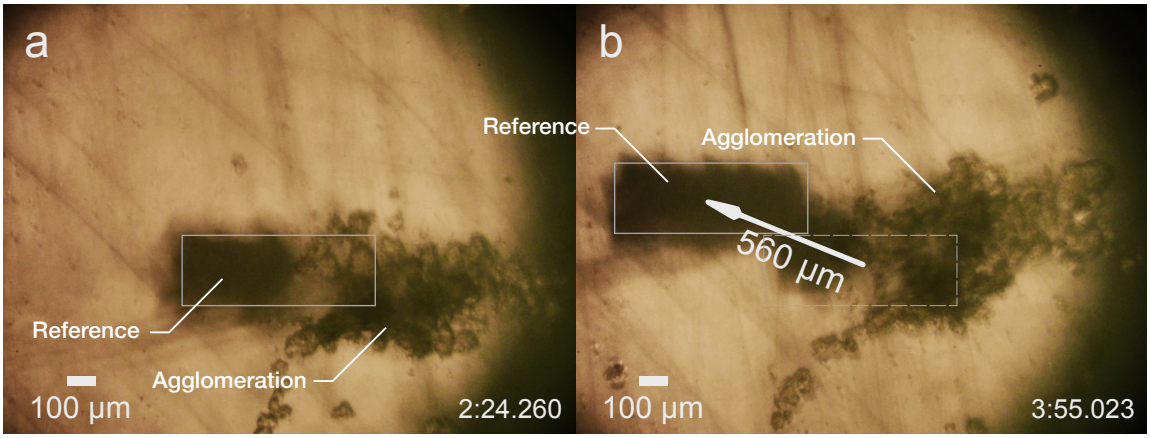

Figure 4.4: **Translation of cell agglomerations in the petri dish.** After agglomeration and waiting (with the transducer off) for about five minutes, the cell cluster may be transported along with the tip of the transducer underneath the petri dish. The (boxed) reference mark as shown is attached to the petri dish. By leaving the transducer coupling tip and the observation microscope fixed in place, and translating the dish up and to the left by 560 μm (for example) over a period of 90 s—from (a) 2 min 24.260 s to (b) 3 min 55.023 s—the agglomeration was moved downward and to the right by this distance relative to the petri dish. Scale bar: 100 μm

later—is significantly larger than the majority of the existing work reported using conventional methods mentioned in Section 4.1, which are, at most, a few hundred micrometers in diameter [394, 432, 414]. This may be potentially beneficial as larger 3D cultures can be expected to behave more like *in vivo* tissue.

4.3.4 Three-dimensional cellular agglomeration formation via origami-like manipulation

As previously mentioned, monolayer (2D) clusters have distinct drawbacks in emulating real tissue in comparison to 3D multilayer cell structures. To form these desirable multilayer agglomerations, the power must be increased so that the cells may be lifted from the petri dish's surface and folded. It is possible to lift an edge of the thin cell agglomeration from the petri dish and lay it across the remaining layer of cells, all without breaking the intercellular connectivity defined in the original layer. This is analogous to origami folding used to produce micro to nanoscale devices from planar media [433].

Figure 4.5 illustrates an example of this folding procedure with our device. After forming the monolayer agglomeration as previously described, waiting about five minutes is sufficient to allow the agglomeration to be handled via pipetting and hand tools without its separation. Complete intercellular binding occurs only after several hours of incubation; the functional agglomerates we describe later were formed after 22 h incubation.

To have a sufficiently large number of cells in the agglomeration for a cluster, we adopted the following procedure after waiting for five minutes to allow for limited intercellular binding after SAW agglomeration. We exposed the left edge of the

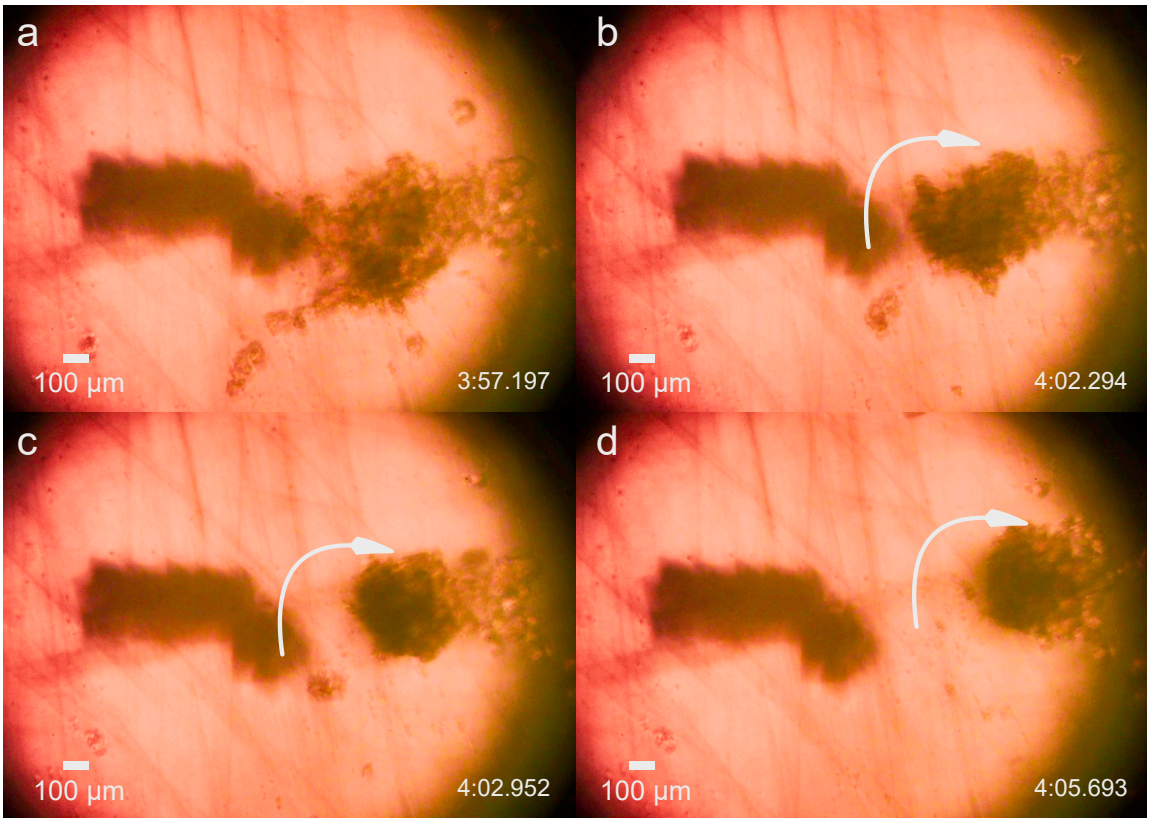

Figure 4.5: **Cell agglomerate folding and rolling.** After waiting for 5 min to weakly bind the existing cells together, increasing the input power to 350 mW causes the cluster to (a,b) roll upon itself from the left edge, folding atop the remainder of the cells and forming (c,d) a roughly spherical cell agglomeration in 8 s. Scale bar: 100 μm

agglomeration to vortex flow generated from 350 mW input to the SAW device. The left side of the monolayer agglomeration folded up, over, and down upon the right side while the cells remained bound to each other. In this way, monolayer clusters can be folded from an arbitrary direction, defined by the location of the acoustic device's coupling point with respect to the agglomeration's edge. This folding process progresses to tumbling of the cell agglomeration, forming a compact and roughly spherical ball of cells.

At this point, one wonders how well the intercellular communication has developed among these agglomerated cells after their folding and subsequent 22-hour incubation. This is explored in the next subsection.

4.3.5 Characterization of 3D cell agglomerations

Fluorescent imaging is vital to discern the quality of intercellular binding and communication to determine whether they exhibit cell-cell communication behavior or not. Clusters made with our device, first in a monolayer format and then folded to form a multilayer bound cluster, were carefully transferred with a pipette to an ordinary well plate for further observation. In order to ensure sufficient time for cells to bind together, they were incubated at 37 °C and 4.4% CO_2 for 22 hours before imaging; details are in the *Methods*.

Calcium migration

Calcium (Ca^{2+}); (green in the images in Fig. 4.6—*see* Methods 4.2.6) is commonly used to identify communication among cells, as it plays a significant role in signal transduction through the cell membranes. Because the cells are nonuniformly distributed, calcium imaging is likewise nonuniform. However, intercelluar transmission of Ca^{2+} signaling may be easily distinguished in the sequence of images and associated brightness in Fig. 4.6 and as a video in the Supplementary Information. The calcium signal emerged at the center (blue) in Fig. 4.6(a) and concentrically spread out (blue-orange-magenta-yellow) in about 16 s, showing a gradual progression and weakening of the signal from the source as time elapsed in Fig. 4.6(b).

Marking cell junctions

Cell morphology and intercellular contact are essential for defining and modulating cellular functions for *in vitro* cell cultures. Immunohistochemistry is widely used in basic research to identify the presence of certain proteins, and to understand the distribution and localization of biomarkers in different parts of a biological tissue. In order to better understand and explain the calcium propagation illustrated in Fig. 4.6, we evaluated the establishment of tight and gap junctions among adja-

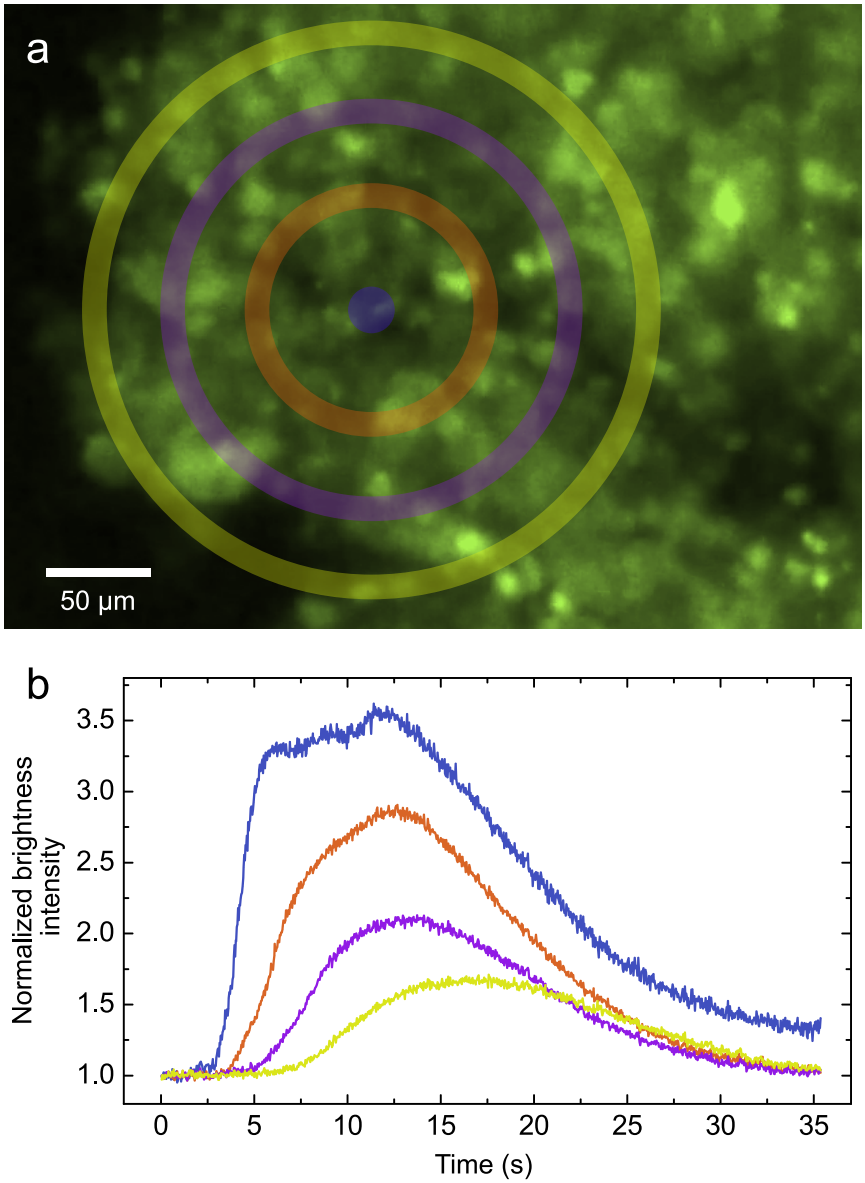

Figure 4.6: **Calcium ion signaling in a cell agglomerate after 22 h incubation.** The calcium (in green) transmission in a 3D cell agglomerate in the order from center to periphery (blue-orange-magenta-yellow). (a) The concentric regions of interest denoted on a photo of the cluster acquired from fluorescent microscopy. (b) The normalized brightness intensity mapping across of the corresponding regions. The Ca^{2+} signaling seen here and in the video in the Supplementary Information indicates the cells are functioning as a collective group. Scale bar: 50 μm

cent cells in the SAW-formed clusters by staining ZO1 and connexin43 (*see* Methods 4.2.6). Images from confocal microscopy show the stained tight junctions and gap junctions, both in red. The ubiquitous presence of the tight junctions in Fig. 4.7(a) suggests the cells are bound together, as this is one of the functions of tight junctions. Fig. 4.7(b) indicates the gap junctions (marked by yellow arrows), which support the passage of various molecules, ions and electrical impulses between cells, potentially contributing to the previously discussed calcium propagation in Fig. 4.6. The presence of tight junctions and gap junctions along the cell membranes suggests the cells have formed tissue-like connections, revealing intercellular interaction behaviors from these agglomerated cells. The possibility exists to form organoids if the method is applied to stem cells.

4.3.6 Forming multiple cell clusters in a single petri dish

A key advantage of this method is the ability to make 3D-structured clusters on demand. The efficiency of agglomerate construction can also be increased by creating arrays of clusters in the same container, without—for example—having to resort to individual wells in a well plate. As shown in Fig. 4.8(a), a 3D-printed platform was designed so that three SAW devices could be inserted and actuated at the same time to simultaneously form three clusters.

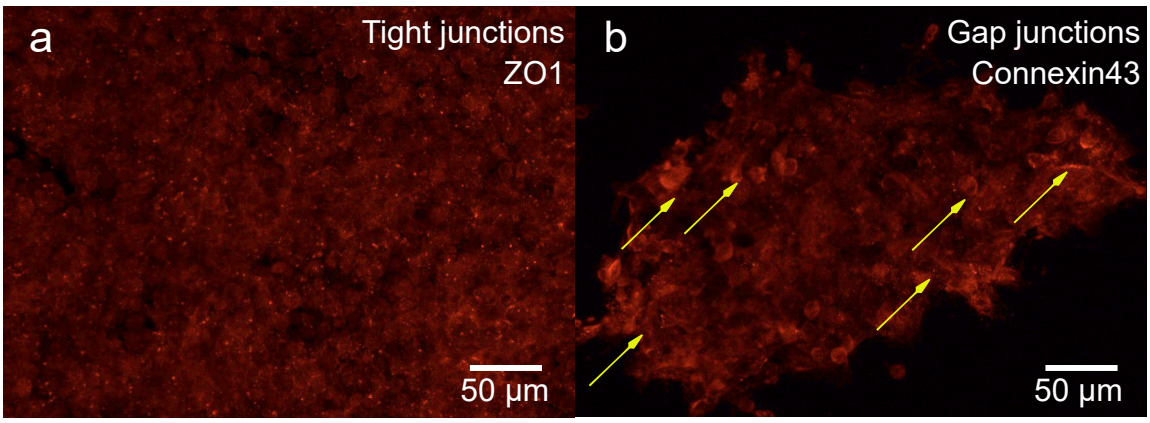

Figure 4.7: **Indication of tight and gap junctions in the cell agglomeration.** Confocal images of multiprotein junctional complexes (in red) in acoustically-formed 3D clusters. (a) Tight junctions in the cluster support intracellular bonding, maintaining the aggregated structure. (b) Gap junctions (stronger signals marked by yellow arrows) permit intercellular communication, including Ca^{2+} propagation in the cluster as shown in Fig. 4.6. Scale bar: 50 μm

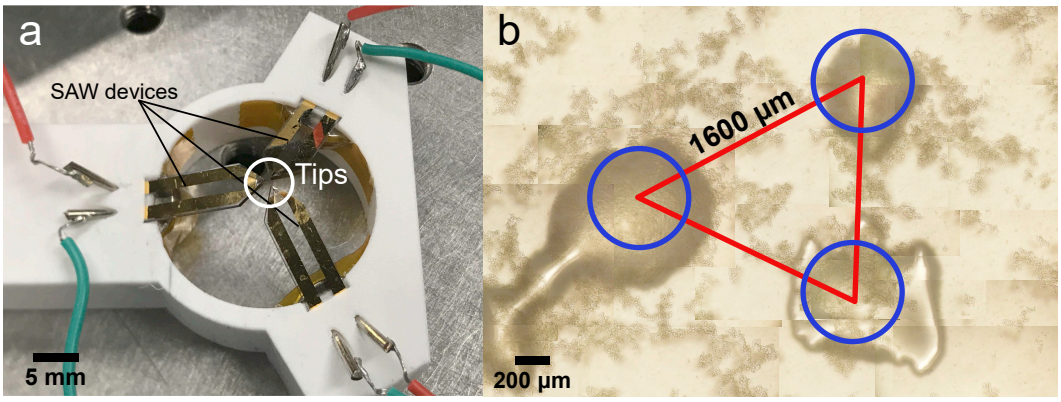

Figure 4.8: **Simultaneous formation of multiple agglomerates.** (a) The platform holding three mounted SAW devices could transmit waves to the superstrate at three distinct locations. (b) Three clusters, at sizes of about 500 μm, were simultaneously made in the petri dish.

The tips of the devices were adjusted to be on the same plane with a 1.8 mm lateral separation from tip to tip. The petri dish was set level above these three tips, with a gap of 350 μm. Each tip was loaded with about 0.15 μL of couplant to span this gap and to transmit the acoustic energy into the cell-laden medium through the bottom of the petri dish. In this way, the cells may be driven to accumulate at each of the three points due to localized recirculation as described in subsection 4.3.2. In Fig. 4.8(b), the distances between each of the three cell agglomerations was about 1.6 mm. As the size of each agglomeration grows, it may become necessary to increase the separation distance to prevent them from merging. For example, with three 500-μm agglomerations, 1.6 mm is entirely sufficient. However, if each agglomeration grows beyond about 1 mm in size, they begin to interact and will merge.

A question then arises as to how close these three regions may be placed before it becomes impossible to collect cells to form agglomerations at each point. Here, with a cell concentration of 1.25×10^5 cells/mL and 100-MHz SAW, the smallest separation possible is 711 μm, regardless of the cluster size. The SAW power used to obtain this result was 20.83 mW; other input powers required greater separation distances for individual clusters. This implies that, if the agglomerates are hexagonally close packed, [434], and each agglomerate is sufficient by itself to use as a 3D cluster after

folding it into a multilayer structure, it should be possible to form over ten thousand agglomerates in a 35-mm diameter petri dish like the one we used. Conservatively, at least a thousand agglomerates should be possible in a single petri dish.

Of course, the key limitation is not space, but time, in that the time required to achieve this with three SAW devices—almost exactly two weeks—would be vastly greater than the viable life of the cells. However, if the idea were developed beyond the research context with a greater number of SAW devices, either monolithic (on the same substrate), stacked, or both, then the time to form so many clusters becomes more reasonable: a thousand such devices would be able to produce ten thousand agglomerates in about an hour. Likewise one can imagine a flow-through device to accomplish the same outcome, but only by trading the complexity of so many SAW devices with the complexity of cluster handling in specialized microfluidic dishware. This is likely to be difficult during the time spent waiting for the cells to adhere to each other after agglomeration—and hopefully not the walls of the microchannels in the device.

4.4 Conclusions

Three-dimensional cell cultures are useful tissue analogs for biomedical research applications. To date, creating agglomerates is tedious with individual clus-

Table 4.1: Changing the power controls the essential functions of the SAW-driven cell agglomeration and manipulation device in this study, from agglomeration to translation and folding of agglomerated cells.

Function	Input V_{pp} (V)	Input power (mW)
Agglomerate	3.01	14.32
	4.6	32.29
	6.01	56.40
	7.56	91.64
Translate	9.04	130.7
	10.83	227.6
Fold	15.06	357.4
	22.53	894.7

ters formed in pendant droplets or wells, a physical separation that requires skill in handling and use. Through the use of coupled SAW with modal conversion into a Lamb wave [425], which transmits the acoustic energy through a simple petri dish, cells suspended in media in the petri dish may be agglomerated. In our case, we employed human embryonic kidney (HEK293) cells to form the agglomerations. After formation of the agglomerated cells, they remain bound together. To improve their suitability as clusters, we used our device once again to combine several of the individual agglomerates together and folded that result into an irregular but bound structure shown to transmit Ca^{2+} signaling and gap and tight junctions among the cells. Table 4.1 indicates the input power required to perform agglomeration, translation, and folding. At power levels less than tabulated here, there is little to no cell motion. Beyond these power levels, recirculation is sufficient to prevent formation of any cell clusters, instead causing the cells to rapidly circulate above the contact

point of the SAW device.

This work illustrates a potential method that, when developed further, could help the reader conveniently produce large numbers of organoids. It illustrates the potential of acoustofluidics in streamlining laboratory procedures through a simple chip device, even with standard laboratory dishware.

4.5 Acknowledgments

The authors are grateful to the University of California, the Qualcomm Institute, and the NANO3 facility at UC San Diego for provision of funds and facilities in support of this work. This work was performed in part at the San Diego Nanotechnology Infrastructure (SDNI) of UCSD, a member of the National Nanotechnology Coordinated Infrastructure, which is supported by the National Science Foundation (Grant ECCS–1542148). The work presented here was generously supported by a research grant to J. Friend from the W.M. Keck Foundation. S. Chalasani is grateful to the NIH in support of this work via grant R01MH111534; S. Chalasani and J. Friend are grateful to the NIH in support of this work via grant R01NS115591.

This chapter, in full, is a reprint of material that is in review 2022. Jiyang Mei, Aditya Vasan, Uri Magaram, Kenjiro Takemura, Sreekanth Chalasani, and James Friend. "Non-contact three-dimensional cell cluster formation on demand in

open dishware using focused surface acoustic waves through a couplant layer." The dissertation author was the primary investigator and author of this paper.

Bibliography

[1] George M Whitesides. The origins and the future of microfluidics. *Nature*, 442(7101):368, 2006.

[2] Eric K Sackmann, Anna L Fulton, and David J Beebe. The present and future role of microfluidics in biomedical research. *Nature*, 507(7491):181, 2014.

[3] Holger Becker. Hype, hope and hubris: the quest for the killer application in microfluidics. *Lab on a Chip*, 9(15):2119–2122, 2009.

[4] Holger Becker and Claudia Gärtner. Microfluidics-enabled diagnostic systems: Markets, challenges, and examples. *Microchip Diagnostics: Methods and Protocols*, pages 3–21, 2017.

[5] Chia-Yen Lee, Wen-Teng Wang, Chan-Chiung Liu, and Lung-Ming Fu. Passive mixers in microfluidic systems: A review. *Chemical Engineering Journal*, 288:146–160, 2016.

[6] David J Collins, Tuncay Alan, Kristian Helmerson, and Adrian Neild. Surface acoustic waves for on-demand production of picoliter droplets and particle encapsulation. *Lab on a Chip*, 13(16):3225–3231, 2013.

[7] Leigh Van Valen. A new evolutionary law. *Evol Theory*, 1:1–30, 1973.

[8] Ernst Florens Friedrich Chladni. *Discoveries on the theory of sound*. Weidmanns, Erben und Reich, 1787.

[9] Michael Faraday. On the forms and states assumed by fluids in contact with vibrating elastic surfaces. *Philosophical Transactions of the Royal Society London*, 121(319):1831, 1831.

[10] August Kundt. On a new kind of acoustic dust figures and on the application of the same for determining sound velocity in solid bodies and gases. *Annals of Physics*, 203(4):497–523, 1866.

[11] James Friend and Leslie Y. Yeo. Microscale acoustofluidics: Microfluidics driven via acoustics and ultrasonics. *Reviews of Modern Physics*, 83(2):647–704, 2011.

[12] Xiaoyun Ding, Peng Li, Sz-Chin Steven Lin, Zackary S Stratton, Nitesh Nama, Feng Guo, Daniel Slotcavage, Xiaole Mao, Jinjie Shi, Francesco Costanzo, and Tony Jun Huang. Surface acoustic wave microfluidics. *Lab on a Chip*, 13(18):3626–3649, 2013.

[13] Leslie Y Yeo and James R Friend. Surface acoustic wave microfluidics. *Annual Review of Fluid Mechanics*, 46:379–406, 2014.

[14] Ghulam Destgeer and Hyung Jin Sung. Recent advances in microfluidic actuation and micro-object manipulation via surface acoustic waves. *Lab on a Chip*, 15(13):2722–2738, 2015.

[15] Carl Eckart. Vortices and streams caused by sound waves. *Physical Review*, 73(1):68, 1948.

[16] Lord Rayleigh. On waves propagated along the plane surface of an elastic solid. *Proceedings of the London Mathematical Society*, 1(1):4–11, 1885.

[17] RM White and FW Voltmer. Direct piezoelectric coupling to surface elastic waves. *Applied Physics Letters*, 7(12):314–316, 1965.

[18] Bernard Jaffe. *Piezoelectric ceramics*, volume 3. Elsevier, 2012.

[19] Hansu Birol, Dragan Damjanovic, and Nava Setter. Preparation and characterization of $(K_{0.5}Na_{0.5})NbO_3$ ceramics. *Journal of the European Ceramic Society*, 26(6):861–866, 2006.

[20] Xiang Yang Kong and Zhong Lin Wang. Spontaneous polarization-induced nanohelixes, nanosprings, and nanorings of piezoelectric nanobelts. *Nano Letters*, 3(12):1625–1631, 2003.

[21] Andrew J. Lovinger. Ferroelectric polymers. *Science*, 220(4602):1115–1121, 1983.

[22] S. M. Nakhmanson, M. Buongiorno Nardelli, and J. Bernholc. Collective polarization effects in β-polyvinylidene fluoride and its copolymers with tri- and tetrafluoroethylene. *Phys. Rev. B*, 72:115210, Sep 2005.

[23] Jacques Curie and Pierre Curie. Contractions and expansions produced by voltages in hemihedral crystals with inclined faces. *Comptes Rendus*, 93:1137–1140, 1881.

[24] Xiao-hong Du, Jiehui Zheng, Uma Belegundu, and Kenji Uchino. Crystal orientation dependence of piezoelectric properties of lead zirconate titanate near the morphotropic phase boundary. *Applied Physics Letters*, 72(19):2421–2423, 1998.

[25] Shifeng Huang, Jun Chang, Lingchao Lu, Futian Liu, Zhengmao Ye, and Xin Cheng. Preparation and polarization of 0–3 cement based piezoelectric composites. *Materials Research Bulletin*, 41(2):291–297, 2006.

[26] Metin Ozgul, Koichi Takemura, Susan Trolier-McKinstry, and Clive A Randall. Polarization fatigue in $Pb(Zn_{1/3}Nb_{2/3})O_3$–$PbTiO_3$ ferroelectric single crystals. *Journal of Applied Physics*, 89(9):5100–5106, 2001.

[27] Warren P Mason. Piezoelectricity, its history and applications. *The Journal of the Acoustical Society of America*, 70(6):1561–1566, 1981.

[28] Ian Donald. Sonar: the story of an experiment. *Ultrasound in Medicine & Biology*, 1(2):109–117, 1974.

[29] Amir Manbachi and Richard SC Cobbold. Development and application of piezoelectric materials for ultrasound generation and detection. *Ultrasound*, 19(4):187–196, 2011.

[30] William B Robertson. The ultrasonic cleaner in the laboratory. *J. Chem. Educ*, 44(8):460, 1967.

[31] LD Rozenberg. Efficiency of ultrasonic cleaning. In *Physical Principles of Ultrasonic Technology*, pages 270–318. Springer, 1973.

[32] Naim Dam. Non-contact ultrasonic micromeasurement system, March 9 1999. US Patent 5,880,364.

[33] Dezhong Yang. Ultrasonic range finder, February 12 2008. US Patent 7,330,398.

[34] Salem Saadon and Othman Sidek. A review of vibration based MEMS piezoelectric energy harvesters. *Energy Conversion and Management*, 52(1):500–504, 2011.

[35] M Kuribayashi Kurosawa, Osamu Kodaira, Yuki Tsuchitoi, and Toshiro Higuchi. Transducer for high speed and large thrust ultrasonic linear motor using two sandwich-type vibrators. *IEEE Transactions on Ultrasonics, Ferroelectrics, and Frequency Control*, 45(5):1188–1195, 1998.

[36] B Watson, J Friend, and L Yeo. Piezoelectric ultrasonic micro/milli-scale actuators. *Sensors and Actuators A: Physical*, 152(2):219–233, 2009.

[37] James Friend, Kentaro Nakamura, and Sadayuki Ueha. A piezoelectric micromotor using in-plane shearing of PZT elements. *IEEE/ASME Transactions on Mechatronics*, 9(3):467–473, 2004.

[38] Shigetaka Tonami, Atsuhiro Nishikata, and Yasutaka Shimizu. Characteristics of leaky surface acoustic waves propagating on $LiNbO_3$ and $LiTaO_3$ substrates. *Japanese Journal of Applied Physics*, 34(5S):2664, 1995.

[39] Yuri V Gulyaev. Review of shear surface acoustic waves in solids. *IEEE Transactions on Ultrasonics, Ferroelectrics, and Frequency Control*, 45(4):935–938, 1998.

[40] Fabrice Martin. Propagation characteristics of harmonic surface skimming bulk waves on ST quartz. *Electronics Letters*, 38(16):941–942, 2002.

[41] Vesseline L Strashilov and Ventsislav M Yantchev. Surface transverse waves: properties, devices, and analysis. *IEEE Transactions on Ultrasonics, Ferroelectrics, and Frequency Control*, 52(5):812–821, 2005.

[42] Sean Collignon, Ofer Manor, and James Friend. Improving and predicting fluid atomization via hysteresis-free thickness vibration of lithium niobate. *Advanced Functional Materials*, 28(8):1704359, 2018.

[43] B Jaffe, RS Roth, and S Marzullo. Piezoelectric properties of lead zirconate-lead titanate solid-solution ceramics. *Journal of Applied Physics*, 25(6):809–810, 1954.

[44] Iñigo Bretos, Ricardo Jiménez, Javier Garcïa-López, Lorena Pardo, and M. Lourdes Calzada. Photochemical solution deposition of lead-based ferroelectric films: Avoiding the pbo-excess addition at last. *Chemistry of Materials*, 20(18):5731–5733, 2008.

[45] Product ID Label, Packaging Label, and R oHS Compliance Engineer. Directive 2002/95/ec of the european parliament and of the council of 27 january 2003 on the restriction of the use of certain hazardous substances in electrical and electronic equipment. 2005.

[46] Yasuyoshi Saito, Hisaaki Takao, Toshihiko Tani, Tatsuhiko Nonoyama, Kazumasa Takatori, Takahiko Homma, Toshiatsu Nagaya, and Masaya Nakamura. Lead-free piezoceramics. *Nature*, 432(7013):84–87, 11 2004.

[47] Kenji Uchino and Seiji Hirose. Loss mechanisms in piezoelectrics: how to measure different losses separately. *IEEE Transactions on Ultrasonics, Ferroelectrics, and Frequency Control*, 48(1):307–321, 2001.

[48] Shigeru Jyomura, Kazuyuki Nagatsuma, and Hiroshi Takeuchi. SAW propagation loss mechanism in piezoelectric ceramics. *Journal of Applied Physics*, 52(7):4472–4478, 1981.

[49] Robert N Thurston, Allan D Pierce, and Emmanuel P Papadakis. *Reference for Modern Instrumentation, Techniques, and Technology: Ultrasonic Instruments and Devices I: Ultrasonic Instruments and Devices I*, volume 23. Academic Press, 1998.

[50] RC Williamson. Case studies of successful surface-acoustic-wave devices. In *Ultrasonics Symposium, 1977*, pages 460–468. IEEE, 1977.

[51] CS Hartmann. Systems impact of modern rayleigh wave technology. In *Rayleigh-Wave Theory and Application*, pages 238–253. Springer, 1985.

[52] I. M. Mason and E. A. Ash. Acoustic surface-wave beam diffraction on anisotropic substrates. *Journal of Applied Physics*, 42(13):5343–5351, 1971.

[53] A Takayanagi, K Yamanouchi, and K Shibayama. Piezoelectric leaky surface wave in LiNbO3. *Applied Physics Letters*, 17(5):225–227, 1970.

[54] AJ Slobodnik and ED Conway. New high-frequency high-coupling low-beam-steering cut for acoustic surface waves on $LiNbO_3$. *Electronics Letters*, 6(6):171–173, 1970.

[55] Kimio Shibayama, Kazuhiko Yamanouchi, Hiroaki Sato, and Toshiyasu Meguro. Optimum cut for rotated Y-cut $LiNbO_3$ crystal used as the substrate of acoustic-surface-wave filters. *Proceedings of the IEEE*, 64(5):595–597, 1976.

[56] Colin K Campbell. Applications of surface acoustic and shallow bulk acoustic wave devices. *Proceedings of the IEEE*, 77(10):1453–1484, 1989.

[57] D Ciplys and R Rimeika. Measurements of electromechanical coupling coefficient for surface acoustic waves in proton-exchanged lithium niobate. *Ultrasound*, 33(3):14–20, 2014.

[58] V Soluch and Magdalena Lysakowska. Surface acoustic waves on X-cut $LiNbO_3$. *IEEE Transactions on Ultrasonics, Ferroelectrics, and Frequency Control*, 52(1):145–147, 2005.

[59] Fred S Hickernell. Surface acoustic wave technology macrosuccess through microseisms. *Physical Acoustics*, 24:135–207, 1999.

[60] Colin K Campbell. Longitudinal-mode leaky SAW resonator filters on 64/spl deg/YX lithium niobate. *IEEE Transactions on Ultrasonics, Ferroelectrics, and Frequency Control*, 42(5):883–888, 1995.

[61] J Hechner and W Soluch. Pseudo surface acoustic wave dual delay line on 41 YX $LiNbO_3$ for liquid sensors. *Sensors and Actuators B: Chemical*, 111:436–440, 2005.

[62] Antoine Riaud, Jean-Louis Thomas, Eric Charron, Adrien Bussonnière, Olivier Bou Matar, and Michael Baudoin. Anisotropic swirling surface acoustic waves from inverse filtering for on-chip generation of acoustic vortices. *Physical Review Applied*, 4(3):034004, 2015.

[63] M. Kurosawa, M. Takahashi, and T. Higuchi. Ultrasonic linear motor using surface acoustic waves. *IEEE Transactions on Ultrasonics, Ferroelectrics, and Frequency Control*, 43(5):901–906, 1996.

[64] Feng Guo, Peng Li, Jarrod B French, Zhangming Mao, Hong Zhao, Sixing Li, Nitesh Nama, James R Fick, Stephen J Benkovic, and Tony Jun Huang. Controlling cell–cell interactions using surface acoustic waves. *Proceedings of the National Academy of Sciences*, 112(1):43–48, 2015.

[65] Citsabehsan Devendran, Nipuna R Gunasekara, David J Collins, and Adrian Neild. Batch process particle separation using surface acoustic waves (SAW): integration of travelling and standing SAW. *Royal Society of Chemistry Advances*, 6(7):5856–5864, 2016.

[66] Massimiliano Gasparetti, Gian M Revel, and Enrico P Tomasini. Theoretical modeling and experimental evaluation of an in-plane laser Doppler vibrometer in different working conditions. In *Third International Conference on Vibration Measurements by Laser Techniques: Advances and Applications*, pages 317–327. International Society for Optics and Photonics, 1998.

[67] P Castellini, M Martarelli, and EP Tomasini. Laser Doppler Vibrometry: Development of advanced solutions answering to technology's needs. *Mechanical Systems and Signal Processing*, 20(6):1265–1285, 2006.

[68] SJ Rothberg, MS Allen, P Castellini, D Di Maio, JJJ Dirckx, DJ Ewins, Ben J Halkon, P Muyshondt, N Paone, T Ryan, H Steger, EP Tomasini, S Vanlanduit, and JF Vignola. An international review of laser Doppler vibrometry: Making light work of vibration measurement. *Optics and Lasers in Engineering*, 2016.

[69] Paolo Castellini and Claudio Santolini. Vibration measurements on blades of naval propeller rotating in water. In *Second International Conference on Vibration Measurements by Laser Techniques: Advances and Applications*, pages 186–194. International Society for Optics and Photonics, 1996.

[70] AJ Barker, PE Jaeger, and David E Oliver. Non-contacting vibration measurement: role in design and industrial applications. *Stress and Vibration: Recent Developments in Industrial Measurement and Analysis*, 1084:293–299, 1989.

[71] LY Zhu, KF Hallamasek, and DB Bogy. Measurement of head/disk spacing with a laser interferometer. *IEEE Transactions on Magnetics*, 24(6):2739–2741, 1988.

[72] James M Sabatier and Ning Xiang. Laser-Doppler-based acoustic-to-seismic detection of buried mines. In *AeroSense'99*, pages 215–222. International Society for Optics and Photonics, 1999.

[73] RG White. Acoustic and vibration transducers and measurement techniques. *Journal of Physics E: Scientific Instruments*, 18(9):790, 1985.

[74] Romain Herdier, David Jenkins, Elhadj Dogheche, Denis Rèmiens, and Miroslav Sulc. Laser Doppler vibrometry for evaluating the piezoelectric coefficient d 33 on thin film. *Review of Scientific Instruments*, 77(9):093905, 2006.

[75] Morteza Miansari and James R Friend. Acoustic nanofluidics via room-temperature lithium niobate bonding: A platform for actuation and manipulation of nanoconfined fluids and particles. *Advanced Functional Materials*, 26(43):7861–7872, 2016.

[76] John E Sader and James R Friend. Note: Calibration of atomic force microscope cantilevers using only their resonant frequency and quality factor. *Review of Scientific Instruments*, 85(11):116101, 2014.

[77] James Friend and Leslie Yeo. Using laser Doppler vibrometry to measure capillary surface waves on fluid-fluid interfaces. *Biomicrofluidics*, 4(2):026501, 2010.

[78] Joris Vanherzeele, Mark Brouns, Paolo Castellini, Patrick Guillaume, Milena Martarelli, Daniele Ragni, Enrico Primo Tomasini, and Steve Vanlanduit. Flow characterization using a laser Doppler vibrometer. *Optics and Lasers in Engineering*, 45(1):19–26, 2007.

[79] Jeremy Blamey, Leslie Y Yeo, and James R Friend. Microscale capillary wave turbulence excited by high frequency vibration. *Langmuir*, 29(11):3835–3845, 2013.

[80] Takehiro Tachizaki, Toshihiro Muroya, Osamu Matsuda, Yoshihiro Sugawara, David H Hurley, and Oliver B Wright. Scanning ultrafast sagnac interferometry for imaging two-dimensional surface wave propagation. *Review of Scientific Instruments*, 77(4):043713, 2006.

[81] Georg Siegmund. Sources of measurement error in laser Doppler vibrometers and proposal for unified specifications. In *Proc. SPIE*, volume 7098, pages 70980Y–1, 2008.

[82] Leonid Yarovoi and Georg Siegmund. The effect of three-wave interference in laser Doppler vibrometry. *Measurement Science and Technology*, 15(10):2150, 2004.

[83] Ben J Halkon and SJ Rothberg. Vibration measurements using continuous scanning laser Doppler vibrometry: theoretical velocity sensitivity analysis with applications. *Measurement Science and Technology*, 14(3):382, 2003.

[84] Julien Poittevin, François Gautier, Charles Pézerat, and Pascal Picart. High-speed holographic metrology: principle, limitations, and application to vibroacoustics of structures. *Optical Engineering*, 55(12):121717–121717, 2016.

[85] Mathieu Leclercq, Pascal Picart, Guillaume Penelet, and Vincent Tournat. Investigation of 3D surface acoustic waves in granular media with 3-color digital holography. *Journal of Applied Physics*, 121(4):045112, 2017.

[86] T Cacace, M Paturzo, P Memmolo, M Vassalli, P Ferraro, M Fraldi, and G Mensitieri. Digital holography as 3D tracking tool for assessing acoustophoretic particle manipulation. *Optics Express*, 25(15):17746–17752, 2017.

[87] Cheng-kai Luo, Prasad S Gudem, and James F Buckwalter. A 0.2–3.6-GHz 10-dBm B1dB 29-dBm IIP3 tunable filter for transmit leakage suppression in SAW-less 3G/4G FDD receivers. *IEEE Transactions on Microwave Theory and Techniques*, 63(10):3514–3524, 2015.

[88] Colin Campbell. *Surface acoustic wave devices for mobile and wireless communications*. Academic Press, 1998.

[89] Gudem Prasad Luo, Cheng-kai and James Buckwalter. A 0.4-6-GHz 17-dBm B1dB 36-dBm IIP3 channel-selecting low-noise amplifier for SAW-less 3G/4G FDD diversity receivers. *IEEE Transactions on Microwave Theory and Techniques*, 64(4):1110–1121, 2016.

[90] H Nakahata, S Fujii, K Higaki, A Hachigo, H Kitabayashi, S Shikata, and N Fujimori. Diamond-based surface acoustic wave devices. *Semiconductor science and technology*, 18(3):S96, 2003.

[91] David Morgan. *Surface Acoustic Wave Filters: With Applications to Electronic Communications and Signal Processing*. Academic Press, 2010.

[92] T Nishihara, T Yokoyama, T Miyashita, and Y Satoh. High performance and miniature thin film bulk acoustic wave filters for 5 GHz. In *Ultrasonics Symposium, Proceedings*, volume 1, pages 969–972. IEEE, 2002.

[93] Amgad R Rezk, James R Friend, and Leslie Y Yeo. Simple, low cost MHz-order acoustomicrofluidics using aluminium foil electrodes. *Lab on a Chip*, 14(11):1802–5, 2014.

[94] Jeonghun Nam and Chae Seung Lim. A conductive liquid-based surface acoustic wave device. *Lab on a Chip*, 16(19):3750–3755, 2016.

[95] Andreas Winkler, Paul Bergelt, Lars Hillemann, and Siegfried Menzel. Influence of Viscosity in Fluid Atomization with Surface Acoustic Waves. *Open Journal of Acoustics*, 6:23–33, 2016.

[96] A. Winkler, S. Harazim, D.J. Collins, R. Brünig, H. Schmidt, and S.B. Menzel. Compact SAW aerosol generator. *Biomedical Microdevices*, 19(1):9, 2017.

[97] Richie J Shilton, Virgilio Mattoli, Marco Travagliati, Matteo Agostini, Andrea Desii, Fabio Beltram, and Marco Cecchini. Rapid and controllable digital microfluidic heating by surface acoustic waves. *Advanced Functional Materials*, 25(37):5895–5901, 2015.

[98] Marc J Madou. *Fundamentals of microfabrication: the science of miniaturization*. CRC press, 2002.

[99] Michael B Dentry, Leslie Y Yeo, and James R Friend. Frequency effects on the scale and behavior of acoustic streaming. *Physical Review E*, 89(1):013203, 2014.

[100] M. Pekarcikova, M. Hofmann, S. Menzel, H. Schrnidt, T. Gemming, and K. Wetzig. Investigation of high power effects on Ti/Al and Ta-Si-N/Cu/Ta-Si-N electrodes for SAW devices. *IEEE Transactions on Ultrasonics, Ferroelectrics, and Frequency Control*, 52(5):911–917, May 2005.

[101] Hank Wohltjen. Mechanism of operation and design considerations for surface acoustic wave device vapour sensors. *Sensors and Actuators*, 5(4):307–325, 1984.

[102] Zhichao Ma, Adrian JT Teo, Say Hwa Tan, Ye Ai, and Nam-Trung Nguyen. Self-aligned interdigitated transducers for acoustofluidics. *Micromachines*, 7(12):216, 2016.

[103] David Morgan. *Surface Acoustic Wave Filters*. Academic Press, 2007.

[104] JB Green and GS Kino. SAW convolvers using focused interdigital transducers. *IEEE Transactions on Sonics Ultrasonics*, 30:43–50, 1983.

[105] Y Nakagawa. A new SAW convolver using multichannel waveguide. In *IEEE 1991 Ultrasonics Symposium Proceedings*, pages 255–258. IEEE, 1991.

[106] TJ Marynowski. Focusing transducer for SAW beamwidth compression on YZ lithium niobate. In *1982 Ultrasonics Symposium*, pages 160–165. IEEE, 1982.

[107] JB Green, GS Kino, and BT Khuri-Yakub. Focused surface wave transducers on anisotropic substrates: a theory developed for the waveguided storage correlator. In *1980 Ultrasonics Symposium*, pages 69–73. IEEE, 1980.

[108] Jaroslava Z Wilcox and Robert E Brooks. Time-fourier transform by a focusing array of phased surface acoustic wave transducers. *Journal of Applied Physics*, 58(3):1148–1159, 1985.

[109] MM de Lima Jr, R Hey, JAH Stotz, and PV Santos. Acoustic manipulation of electron–hole pairs in gaas at room temperature. *Applied Physics Letters*, 84(14):2569–2571, 2004.

[110] Muhammed S Kharusi and Gerald W Farnell. On diffraction and focusing in anisotropic crystals. *Proceedings of the IEEE*, 60(8):945–956, 1972.

[111] MG Cohen. Optical study of ultrasonic diffraction and focusing in anisotropic media. *Journal of Applied Physics*, 38(10):3821–3828, 1967.

[112] Song Ru Fang, SY Zhang, and ZHENG FENG Lu. SAW focusing by circular-arc interdigital transducers on YZ-$LiNbO_3$. *IEEE Transactions on Ultrasonics, Ferroelectrics, and Frequency Control*, 36(2):178–184, 1989.

[113] Tsung-Tsong Wu, He-Tai Tang, and Yung-Yu Chen. Frequency response of a focused SAW device based on concentric wave surfaces: simulation and experiment. *Journal of Physics D: Applied Physics*, 38(16):2986, 2005.

[114] Tsung-Tsong Wu, He-Tai Tang, Yung-Yu Chen, and Pei-Ling Liu. Analysis and design of focused interdigital transducers. *IEEE Transactions on Ultrasonics, Ferroelectrics, and Frequency Control*, 52(8):1384–1392, 2005.

[115] Richard Shilton, Ming K Tan, Leslie Y Yeo, and James R Friend. Particle concentration and mixing in microdrops driven by focused surface acoustic waves. *Journal of Applied Physics*, 104(1):014910, 2008.

[116] Vincent Laude, Davy Gérard, Naima Khelfaoui, Carlos F Jerez-Hanckes, Sarah Benchabane, and Abdelkrim Khelif. Subwavelength focusing of surface acoustic waves generated by an annular interdigital transducer. *Applied Physics Letters*, 92(9):094104, 2008.

[117] Antoine Riaud, Michael Baudoin, Jean-Louis Thomas, and Olivier Bou Matar. SAW synthesis with IDTs array and the inverse filter: toward a versatile saw

toolbox for microfluidics and biological applications. *IEEE Transactions on Ultrasonics, Ferroelectrics, and Frequency Control*, 63(10):1601–1607, 2016.

[118] Mickaël Tanter, Jean-Louis Thomas, and Mathias Fink. Time reversal and the inverse filter. *The Journal of the Acoustical Society of America*, 108(1):223–234, 2000.

[119] Antoine Riaud, Michael Baudoin, Olivier Bou Matar, Loic Becerra, and Jean-Louis Thomas. Selective manipulation of microscopic particles with precursor swirling rayleigh waves. *Physical Review Applied*, 7(2):024007, 2017.

[120] Ming K Tan, James R Friend, and Leslie Y Yeo. Direct visualization of surface acoustic waves along substrates using smoke particles. *Applied Physics Letters*, 91(22):224101, 2007.

[121] RW Rambach, J Taiber, CML Scheck, C Meyer, J Reboud, JM Cooper, and T Franke. Visualization of surface acoustic waves in thin liquid films. *Scientific Reports*, 6, 2016.

[122] Ming K. Tan, James R. Friend, and Leslie Y. Yeo. Microparticle collection and concentration via a miniature surface acoustic wave device. *Lab on a Chip*, 7(5):618, 2007.

[123] Haiyan Li, James R Friend, and Leslie Y Yeo. Surface acoustic wave concentration of particle and bioparticle suspensions. *Biomedical Microdevices*, 9(5):647–656, 2007.

[124] RM Arzt, E Salzmann, and K Dransfeld. Elastic surface waves in quartz at 316 MHz. *Applied Physics Letters*, 10(5):165–167, 1967.

[125] Ryan P. Hodgson, Ming Tan, Leslie Yeo, and James Friend. Transmitting high power RF acoustic radiation via fluid couplants into superstrates for microfluidics. *Applied Physics Letters*, 94(2):024102, 2009.

[126] Sean M Langelier, Leslie Y Yeo, and James Friend. UV epoxy bonding for enhanced SAW transmission and microscale acoustofluidic integration. *Lab on a Chip*, 12(16):2970–2976, 2012.

[127] James Lighthill. Acoustic streaming. *Journal of Sound and Vibration*, 61(3):391–418, 1978.

[128] Showko Shiokawa, Yoshikazu Matsui, and Toyosaka Moriizumi. Experimental study on liquid streaming by SAW. *Japanese Journal of Applied Physics*, 28(S1):126, 1989.

[129] Hermann Schlichting. Berechnung ebener periodischer grenzschichtströmungen. *Phys. Z*, 33(1932):327–335, 1932.

[130] Amgad R Rezk, Ofer Manor, Leslie Y Yeo, and James R Friend. Double flow reversal in thin liquid films driven by megahertz-order surface vibration. In *Proc. R. Soc. A*, volume 470, page 20130765. The Royal Society, 2014.

[131] Louis Vessot King. On the acoustic radiation pressure on spheres. *Proceedings of the Royal Society of London. Series A-Mathematical and Physical Sciences*, 147(861):212–240, 1934.

[132] K Yosioka and Y Kawasima. Acoustic radiation pressure on a compressible sphere. *Acta Acustica United With Acustica*, 5(3):167–173, 1955.

[133] Henrik Bruus. Acoustofluidics 7: The acoustic radiation force on small particles. *Lab on a Chip*, 12(6):1014–1021, 2012.

[134] François Nadal and Eric Lauga. Asymmetric steady streaming as a mechanism for acoustic propulsion of rigid bodies. *Physics of Fluids*, 26(8):082001, 2014.

[135] Philip L. Marston. Phase-shift expansions for approximate radiation forces on solid spheres in inviscid-acoustic standing waves. *The Journal of the Acoustical Society of America*, 142(6):3358–3361, 2017.

[136] Boa-Teh Chu and Robert E Apfel. Acoustic radiation pressure produced by a beam of sound. *The Journal of the Acoustical Society of America*, 72(6):1673–1687, 1982.

[137] Lawrence A Crum. Bjerknes forces on bubbles in a stationary sound field. *The Journal of the Acoustical Society of America*, 57(6):1363–1370, 1975.

[138] MAH Weiser, RE Apfel, and EA Neppiras. Interparticle forces on red cells in a standing wave field. *Acta Acustica united with Acustica*, 56(2):114–119, 1984.

[139] Björn Hammarström, Thomas Laurell, and Johan Nilsson. Seed particle-enabled acoustic trapping of bacteria and nanoparticles in continuous flow systems. *Lab on a Chip*, 12(21):4296–4304, 2012.

[140] Priscilla Rogers and Adrian Neild. Selective particle trapping using an oscillating microbubble. *Lab on a Chip*, 11(21):3710–3715, 2011.

[141] Ann Huang, Morteza Miansari, and James Friend. Driving morphological changes in magnetic nanoparticle structures through the application of acoustic waves and magnetic fields. In *APS Meeting Abstracts*, 2017.

[142] Gibum Kwon, Divya Panchanathan, Seyed Reza Mahmoudi, Mohammed A Gondal, Gareth H McKinley, and Kripa K Varanasi. Visible light guided manipulation of liquid wettability on photoresponsive surfaces. *Nature Communications*, 8, 2017.

[143] Yen-Heng Lin and Gwo-Bin Lee. Optically induced flow cytometry for continuous microparticle counting and sorting. *Biosensors and Bioelectronics*, 24(4):572–578, 2008.

[144] Song-Bin Huang, Min-Hsien Wu, Yen-Heng Lin, Chia-Hsun Hsieh, Chih-Liang Yang, Hung-Chih Lin, Ching-Ping Tseng, and Gwo-Bin Lee. High-purity and label-free isolation of circulating tumor cells (CTCs) in a microfluidic platform by using optically-induced-dielectrophoretic (ODEP) force. *Lab on a Chip*, 13(7):1371–1383, 2013.

[145] Stefan Haeberle and Roland Zengerle. Microfluidic platforms for lab-on-a-chip applications. *Lab on a Chip*, 7(9):1094–1110, 2007.

[146] Achim Wixforth, Christoph Strobl, Ch Gauer, A Toegl, J Scriba, and Z v Guttenberg. Acoustic manipulation of small droplets. *Analytical and bioanalytical chemistry*, 379(7-8):982–991, 2004.

[147] Rohan Raghavan, James R. Friend, and Leslie Y Yeo. Particle concentration via acoustically driven microcentrifugation: microPIV flow visualization and numerical modelling studies. *Microfluidics and Nanofluidics*, 8:73–84, 2010.

[148] W. L. M. Nyborg. *Physical Acoustics*, volume 2, chapter Acoustic Streaming, pages 265–331. Academic Press, 1965.

[149] Showko Shiokawa, Yoshikazu Matsui, and Toshihiko Ueda. Study on SAW streaming and its application to fluid devices. *Japanese Journal of Applied Physics*, 29(S1):137, 1990.

[150] M Alghane, BX Chen, Yong Qing Fu, Yifan Li, JK Luo, and AJ Walton. Experimental and numerical investigation of acoustic streaming excited by using a surface acoustic wave device on a 128° YX-$LiNbO_3$ substrate. *Journal of Micromechanics and Microengineering*, 21(1):015005, 2010.

[151] J Vanneste and O Bühler. Streaming by leaky surface acoustic waves. *Proceedings of the Royal Society A: Mathematical, Physical and Engineering Sciences*, 467(2130):1779–1800, 2011.

[152] Amgad R Rezk, Leslie Y Yeo, and James R Friend. Poloidal flow and toroidal particle ring formation in a sessile drop driven by megahertz order vibration. *Langmuir*, 30(37):11243–11247, 2014.

[153] Antoine Riaud, Michael Baudoin, Jean-Louis Thomas, and Olivier Bou Matar. Cyclones and attractive streaming generated by acoustical vortices. *Physical Review*, 90(013008):8, 2014.

[154] Richard Shilton, Ming Tan, Leslie Yeo, and James Friend. Concentration and mixing of particles in microdrops driven by focused surface acoustic waves. *Proceedings - IEEE Ultrasonics Symposium*, pages 930–933, 2008.

[155] Antoine Riaud, Michael Baudoin, Olivier Bou Matar, Loic Becerra, and Jean-Louis Thomas. Selective manipulation of microscopic particles with precursor swirling rayleigh waves. *Physical Review Applied*, 7(2), 2017.

[156] A Riaud, M Baudoin, O Bou Matar, J-L Thomas, and P Brunet. On the influence of viscosity and caustics on acoustic streaming in sessile droplets: an experimental and a numerical study with a cost-effective method. *Journal of Fluid Mechanics*, 821:384–420, 2017.

[157] Richie J Shilton, Leslie Y Yeo, and James R Friend. Quantification of surface acoustic wave induced chaotic mixing-flows in microfluidic wells. *Sensors and Actuators B: Chemical*, 160(1):1565–1572, 2011.

[158] Richie J Shilton, Marco Travagliati, Fabio Beltram, and Marco Cecchini. Nanoliter-droplet acoustic streaming via ultra high frequency surface acoustic waves. *Advanced Materials*, 26(29):4941–4946, 2014.

[159] C-M Ho. Fluidics-the link between micro and nano sciences and technologies. In *Micro Electro Mechanical Systems, 2001. MEMS 2001. The 14th IEEE International Conference on*, pages 375–384. IEEE, 2001.

[160] August Kundt and O Lehmann. Ueber longitudinale schwingungen und klangfiguren in cylindrischen flüssigkeitssäulen. *Annalen der Physik*, 229(9):1–12, 1874.

[161] Ghulam Destgeer, Hyunjun Cho, Byung Hang Ha, Jin Ho Jung, Jinsoo Park, and Hyung Jin Sung. Acoustofluidic particle manipulation inside a sessile droplet: four distinct regimes of particle concentration. *Lab on a Chip*, 16(4):660–667, 2016.

[162] Rab Wilson, Julien Reboud, Yannyk Bourquin, Steven L Neale, Yi Zhang, and Jonathan M Cooper. Phononic crystal structures for acoustically driven microfluidic manipulations. *Lab on a Chip*, 11(2):323–328, 2011.

[163] Antoine Riaud, Michael Baudoin, Jean-Louis Thomas, and Olivier Bou Matar. SAW synthesis with IDTs array and the inverse filter: Toward a versatile saw toolbox for microfluidics and biological applications. *IEEE Transactions on Ultrasonics, Ferroelectrics, and Frequency Control*, 63(10):1601–1607, 2016.

[164] Ghulam Destgeer, Byunghang Ha, Jinsoo Park, and Hyung Jin Sung. Lamb wave-based acoustic radiation force-driven particle ring formation inside a sessile droplet. *Analytical Chemistry*, 88(7):3976–3981, 2016.

[165] Zeno Guttenberg, Helena Müller, Heiko Habermüller, Andreas Geisbauer, Jürgen Pipper, Jana Felbel, Mark Kielpinski, Jürgen Scriba, and Achim Wixforth. Planar chip device for PCR and hybridization with surface acoustic wave pump. *Lab on a Chip*, 5(3):308–317, 2005.

[166] Lichao Gao and Thomas J McCarthy. Wetting 101 °. *Langmuir*, 25(24):14105–14115, 2009.

[167] Achim Wixforth. Acoustically driven planar microfluidics. *Superlattices and Microstructures*, 33(5):389–396, 2003.

[168] A. Renaudin, P. Tabourier, V. Zhang, J. C. Camart, and C. Druon. SAW nanopump for handling droplets in view of biological applications. *Sensors and Actuators, B: Chemical*, 113(1):389–397, 2006.

[169] Michael Baudoin, Philippe Brunet, Olivier Bou Matar, and Etienne Herth. Low power sessile droplets actuation via modulated surface acoustic waves. *Applied Physics Letters*, 100(15):154102, 2012.

[170] P. Brunet, M. Baudoin, O. Bou Matar, and F. Zoueshtiagh. Droplet displacements and oscillations induced by ultrasonic surface acoustic waves: A quantitative study. *Physical Review E - Statistical, Nonlinear, and Soft Matter Physics*, 81(3):1–8, 2010.

[171] Amgad R Rezk, Ofer Manor, James R Friend, and Leslie Y Yeo. Unique fingering instabilities and soliton-like wave propagation in thin acoustowetting films. *Nature Communications*, 3:1167, 2012.

[172] Matvey Morozov and Ofer Manor. An extended Landau – Levich model for the dragging of a thin liquid film with a propagating surface acoustic wave. *Journal of Fluid Mechanics*, 810:307–322, 2017.

[173] Marco Travagliati, Giorgio De Simoni, Maria Lazzarini, and Vincenzo Piazza. Interaction-free, automatic, on-chip fluid routing by surface acoustic waves. *Lab on a Chip*, 12:2621–2624, 2012.

[174] Ye Ai and Babetta L Marrone. Droplet translocation by focused surface acoustic waves. *Microfluidics and Nanofluidics*, 13:715–722, 2012.

[175] Sean Collignon, James Friend, and Leslie Yeo. Planar microfluidic drop splitting and merging. *Lab on a Chip*, 15(8):1942–1951, 2015.

[176] Jens Eggers. Nonlinear dynamics and breakup of free-surface flows. *Reviews of Modern Physics*, 69(3):865, 1997.

[177] Ming K Tan, James R Friend, and Leslie Y Yeo. Interfacial jetting phenomena induced by focused surface vibrations. *Physical Review Letters*, 103(2), 2009.

[178] A Bussonniere, Michael Baudoin, Philippe Brunet, and O Bou Matar. Dynamics of sessile and pendant drops excited by surface acoustic waves: Gravity effects and correlation between oscillatory and translational motions. *Physical Review E*, 93(5):053106, 2016.

[179] Junxiong Wang, Hong Hu, Aipeng Ye, Jian Chen, and Peng Zhang. Experimental investigation of surface acoustic wave atomization. *Sensors and Actuators, A: Physical*, 238:1–7, 2016.

[180] Robert J Lang. Ultrasonic Atomization of Liquids. *The Journal of the Acoustical Society of America*, 34:6–8, 1962.

[181] W Eisenmenger. Dynamic properties of the surface tension of water and aqueous solutions of surface active agents with standing capillary waves in the frequency range from 10 kc/s to 1.5 mc/s. *Acta Acustica united with Acustica*, 9(4):327–340, 1959.

[182] T Brooke Benjamin and F Ursell. The stability of the plane free surface of a liquid in vertical periodic motion. In *Proceedings of the Royal Society of London A: Mathematical, Physical and Engineering Sciences*, volume 225, pages 505–515. The Royal Society, 1954.

[183] Michael Faraday. On a peculiar class of acoustical figures; and on certain forms assumed by groups of particles upon vibrating elastic surfaces. *Philosophical transactions of the Royal Society of London*, 121:299–340, 1831.

[184] M Kurosawa, T Watanabe, A Hutami, and T Higuchi. Surface Acoustic Wave Atomizer with Pumping Effect. *IEEE*, pages 25–30, 1995.

[185] Minoru Kurosawa, Akira Futami, and Toshiro Higuchi. Characteristics of liquids atomization using surface acoustic wave. In *Solid State Sensors and Actuators, 1997. TRANSDUCERS'97 Chicago., 1997 International Conference on*, volume 2, pages 801–804. IEEE, 1997.

[186] Kerstin Länge, Bastian E Rapp, and Michael Rapp. Surface acoustic wave biosensors: a review. *Analytical and Bioanalytical Chemistry*, 391(5):1509–1519, 2008.

[187] María-Isabel Rocha-Gaso, Carmen March-Iborra, Ángel Montoya-Baides, and Antonio Arnau-Vives. Surface generated acoustic wave biosensors for the detection of pathogens: A review. *Sensors*, 9(7):5740–5769, 2009.

[188] Effie Howe and Geoffrey Harding. A comparison of protocols for the optimisation of detection of bacteria using a surface acoustic wave (SAW) biosensor. *Biosensors and Bioelectronics*, 15(11):641–649, 2000.

[189] E Berkenpas, Paul Millard, and M Pereira Da Cunha. Detection of escherichia coli o157: H7 with langasite pure shear horizontal surface acoustic wave sensors. *Biosensors and Bioelectronics*, 21(12):2255–2262, 2006.

[190] Justin T Baca, Virginia Severns, Debbie Lovato, Darren W Branch, and Richard S Larson. Rapid detection of ebola virus with a reagent-free, point-of-care biosensor. *Sensors*, 15(4):8605–8614, 2015.

[191] Sukru U Senveli, Zheng Ao, Siddarth Rawal, Ram H Datar, Richard J Cote, and Onur Tigli. A surface acoustic wave biosensor for interrogation of single tumour cells in microcavities. *Lab on a Chip*, 16(1):163–171, 2016.

[192] Jungyul Sakong, Heesu Roh, and Yongrae Roh. Surface acoustic wave DNA sensor with micro-fluidic channels. *Japanese Journal of Applied Physics*, 46(7S):4729, 2007.

[193] Hua-Lin Cai, Yi Yang, Xiao Chen, Mohammad Ali Mohammad, Tian-Xiang Ye, Cang-Ran Guo, Li-Ting Yi, Chang-Jian Zhou, Jing Liu, and Tian-Ling Ren. A third-order mode high frequency biosensor with atomic resolution. *Biosensors and Bioelectronics*, 71:261–268, 2015.

[194] Joonhyung Lee, Youn-Suk Choi, Yeolho Lee, Hun Joo Lee, Jung Nam Lee, Sang Kyu Kim, Kyung Yeon Han, Eun Chol Cho, Jae Chan Park, and Soo Suk Lee. Sensitive and simultaneous detection of cardiac markers in human serum using surface acoustic wave immunosensor. *Analytical Chemistry*, 83(22):8629–8635, 2011.

[195] Byung Hang Ha, Kang Soo Lee, Ghulam Destgeer, Jinsoo Park, Jin Seung Choung, Jin Ho Jung, Jennifer Hyunjong Shin, and Hyung Jin Sung. Acoustothermal heating of polydimethylsiloxane microfluidic system. *Scientific Reports*, 5, 2015.

[196] Myeong Chan Jo and Rasim Guldiken. Effects of polydimethylsiloxane (PDMS) microchannels on surface acoustic wave-based microfluidic devices. *Microelectronic Engineering*, 113:98–104, 2014.

[197] K Sritharan, CJ Strobl, MF Schneider, A Wixforth, and Zeno von Guttenberg. Acoustic mixing at low Reynolds numbers. *Applied Physics Letters*, 88(5):054102, 2006.

[198] Wei-Kuo Tseng, Jr-Lung Lin, Wang-Chou Sung, Shu-Hui Chen, and Gwo-Bin Lee. Active micro-mixers using surface acoustic waves on Y-cut 128 $LiNbO_3$. *Journal of Micromechanics and Microengineering*, 16(3):539, 2006.

[199] Myeong Chan Jo and Rasim Guldiken. Dual surface acoustic wave-based active mixing in a microfluidic channel. *Sensors and Actuators A: Physical*, 196:1–7, 2013.

[200] Trung-Dung Luong, Vinh-Nguyen Phan, and Nam-Trung Nguyen. High-throughput micromixers based on acoustic streaming induced by surface acoustic wave. *Microfluidics and Nanofluidics*, 10(3):619–625, 2011.

[201] MK Tan, LY Yeo, and JR Friend. Rapid fluid flow and mixing induced in microchannels using surface acoustic waves. *EPL (Europhysics Letters)*, 87(4):47003, 2009.

[202] Amgad R Rezk, Aisha Qi, James R Friend, Wai Ho Li, and Leslie Y Yeo. Uniform mixing in paper-based microfluidic systems using surface acoustic waves. *Lab on a Chip*, 12(4):773–779, 2012.

[203] JC Rife, MI Bell, JS Horwitz, MN Kabler, RCY Auyeung, and WJ Kim. Miniature valveless ultrasonic pumps and mixers. *Sensors and Actuators A: Physical*, 86(1):135–140, 2000.

[204] Zhen Yang, Sohei Matsumoto, Hiroshi Goto, Mikio Matsumoto, and Ryutaro Maeda. Ultrasonic micromixer for microfluidic systems. *Sensors and Actuators A: Physical*, 93(3):266–272, 2001.

[205] Goksen G Yaralioglu, Ira O Wygant, Theodore C Marentis, and Butrus T Khuri-Yakub. Ultrasonic mixing in microfluidic channels using integrated transducers. *Analytical Chemistry*, 76(13):3694–3698, 2004.

[206] Stefano Oberti, Adrian Neild, and Tuck Wah Ng. Microfluidic mixing under low frequency vibration. *Lab on a Chip*, 9(10):1435–1438, 2009.

[207] Hoang Van Phan, M Bulut Coşkun, Muhsincan Şeşen, Gregory Pandraud, Adrian Neild, and Tuncay Alan. Vibrating membrane with discontinuities for rapid and efficient microfluidic mixing. *Lab on a Chip*, 15(21):4206–4216, 2015.

[208] Weiwei Cui, Hao Zhang, Hongxiang Zhang, Yang Yang, Meihang He, Hemi Qu, Wei Pang, Daihua Zhang, and Xuexin Duan. Localized ultrahigh frequency acoustic fields induced micro-vortices for submilliseconds microfluidic mixing. *Applied Physics Letters*, 109(25):253503, 2016.

[209] Marco Cecchini, Salvatore Girardo, Dario Pisignano, Roberto Cingolani, and Fabio Beltram. Acoustic-counterflow microfluidics by surface acoustic waves. *Applied Physics Letters*, 92(10):104103, 2008.

[210] Luca Masini, Marco Cecchini, Salvatore Girardo, Roberto Cingolani, Dario Pisignano, and Fabio Beltram. Surface-acoustic-wave counterflow micropumps for on-chip liquid motion control in two-dimensional microchannel arrays. *Lab on a Chip*, 10(15):1997–2000, 2010.

[211] Richie J Shilton, Marco Travagliati, Fabio Beltram, and Marco Cecchini. Microfluidic pumping through miniaturized channels driven by ultra-high frequency surface acoustic waves. *Applied Physics Letters*, 105(7):074106, 2014.

[212] Shihoko Ito, Mitsunori Sugimoto, Yoshikazu Matsui, and Jun Kondoh. Study of surface acoustic wave streaming phenomenon based on temperature measurement and observation of streaming in liquids. *Japanese Journal of Applied Physics*, 46(7S):4718, 2007.

[213] Ming K Tan, Leslie Y Yeo, and James R Friend. Unique flow transitions and particle collection switching phenomena in a microchannel induced by surface acoustic waves. *Applied Physics Letters*, 97(23):234106, 2010.

[214] Lothar Schmid, Achim Wixforth, David A Weitz, and Thomas Franke. Novel surface acoustic wave (SAW)-driven closed PDMS flow chamber. *Microfluidics and Nanofluidics*, 12(1-4):229–235, 2012.

[215] Zhuochen Wang and Jiang Zhe. Recent advances in particle and droplet manipulation for lab-on-a-chip devices based on surface acoustic waves. *Lab on a Chip*, 11(7):1280–1285, 2011.

[216] Alireza Barani, Hossein Paktinat, Mohsen Janmaleki, Aminollah Mohammadi, Peiman Mosaddegh, Alireza Fadaei-Tehrani, and Amir Sanati-Nezhad. Microfluidic integrated acoustic waving for manipulation of cells and molecules. *Biosensors and Bioelectronics*, 85:714–725, 2016.

[217] Michael Gedge and Martyn Hill. Acoustofluidics 17: Theory and applications of surface acoustic wave devices for particle manipulation. *Lab on a Chip*, 12(17):2998–3007, 2012.

[218] Jinjie Shi, Xiaole Mao, Daniel Ahmed, Ashley Colletti, and Tony Jun Huang. Focusing microparticles in a microfluidic channel with standing surface acoustic waves (SSAW). *Lab on a Chip*, 8(2):221–223, 2008.

[219] Q Zeng, HWL Chan, XZ Zhao, and Y Chen. Enhanced particle focusing in microfluidic channels with standing surface acoustic waves. *Microelectronic Engineering*, 87(5):1204–1206, 2010.

[220] Myeong Chan Jo and Rasim Guldiken. Active density-based separation using standing surface acoustic waves. *Sensors and Actuators A: Physical*, 187:22–28, 2012.

[221] Jinjie Shi, Shahrzad Yazdi, Sz-Chin Steven Lin, Xiaoyun Ding, I-Kao Chiang, Kendra Sharp, and Tony Jun Huang. Three-dimensional continuous particle focusing in a microfluidic channel via standing surface acoustic waves (SSAW). *Lab on a Chip*, 11(14):2319–2324, 2011.

[222] C Witte, J Reboud, R Wilson, JM Cooper, and SL Neale. Microfluidic resonant cavities enable acoustophoresis on a disposable superstrate. *Lab on a Chip*, 14(21):4277–4283, 2014.

[223] Ming K Tan, Ricky Tjeung, Hannah Ervin, Leslie Y Yeo, and James Friend. Double aperture focusing transducer for controlling microparticle motions in trapezoidal microchannels with surface acoustic waves. *Applied Physics Letters*, 95(13):134101, 2009.

[224] Thomas Franke, Adam R Abate, David A Weitz, and Achim Wixforth. Surface acoustic wave (SAW) directed droplet flow in microfluidics for PDMS devices. *Lab on a Chip*, 9(18):2625–2627, 2009.

[225] Ghulam Destgeer, Kyung Heon Lee, Jin Ho Jung, Anas Alazzam, and Hyung Jin Sung. Continuous separation of particles in a PDMS microfluidic channel via travelling surface acoustic waves (TSAW). *Lab on a Chip*, 13(21):4210–4216, 2013.

[226] Zhichao Ma, David J Collins, and Ye Ai. Detachable acoustofluidic system for particle separation via a traveling surface acoustic wave. *Analytical Chemistry*, 88(10):5316–5323, 2016.

[227] Zhichao Ma, David J Collins, Jinhong Guo, and Ye Ai. Mechanical properties based particle separation via traveling surface acoustic wave. *Analytical Chemistry*, 88(23):11844–11851, 2016.

[228] Sergey Kapishnikov, Vasiliy Kantsler, and Victor Steinberg. Continuous particle size separation and size sorting using ultrasound in a microchannel. *Journal of Statistical Mechanics: Theory and Experiment*, 2006(01):P01012, 2006.

[229] Jinjie Shi, Hua Huang, Zak Stratton, Yiping Huang, and Tony Jun Huang. Continuous particle separation in a microfluidic channel via standing surface acoustic waves (SSAW). *Lab on a Chip*, 9(23):317–326, 2011.

[230] Jeonghun Nam, Yongjin Lee, and Sehyun Shin. Size-dependent microparticles separation through standing surface acoustic waves. *Microfluidics and Nanofluidics*, 11(3):317–326, 2011.

[231] Ghulam Destgeer, Byung Hang Ha, Jinsoo Park, Jin Ho Jung, Anas Alazzam, and Hyung Jin Sung. Microchannel anechoic corner for size-selective separation and medium exchange via traveling surface acoustic waves. *Analytical Chemistry*, 87(9):4627–4632, 2015.

[232] Zhangming Mao, Yuliang Xie, Feng Guo, Liqiang Ren, Po-Hsun Huang, Yuchao Chen, Joseph Rufo, Francesco Costanzo, and Tony Jun Huang. Experimental and numerical studies on standing surface acoustic wave microfluidics. *Lab on a Chip*, 16(3):515–524, 2016.

[233] Mengxi Wu, Zhangming Mao, Kejie Chen, Hunter Bachman, Yuchao Chen, Joseph Rufo, Liqiang Ren, Peng Li, Lin Wang, and Tony Jun Huang. Acoustic separation of nanoparticles in continuous flow. *Advanced Functional Materials*, 27(14), 2017.

[234] Rahul Kishor, Zhichao Ma, Sivaramapanicker Sreejith, Yen Peng Seah, Haiyun Wang, Ye Ai, Zhenfeng Wang, Teik-Thye Lim, and Yuanjin Zheng. Real time size-dependent particle segregation and quantitative detection in a surface acoustic wave-photoacoustic integrated microfluidic system. *Sensors and Actuators B: Chemical*, 2017.

[235] Jinsoo Park, Jin Ho Jung, Ghulam Destgeer, Husnain Ahmed, Kwangseok Park, and Hyung Jin Sung. Acoustothermal tweezer for droplet sorting in a disposable microfluidic chip. *Lab on a Chip*, 17(6):1031–1040, 2017.

[236] Jeonghun Nam, Hyunjung Lim, Dookon Kim, and Sehyun Shin. Separation of platelets from whole blood using standing surface acoustic waves in a microchannel. *Lab on a Chip*, 11(19):3361–3364, 2011.

[237] David J Collins, Zhichao Ma, and Ye Ai. Highly localized acoustic streaming and size-selective submicrometer particle concentration using high frequency microscale focused acoustic fields. *Analytical Chemistry*, 88(10):5513–5522, 2016.

[238] David J Collins, Zhichao Ma, Jongyoon Han, and Ye Ai. Continuous microvortex-based nanoparticle manipulation via focused surface acoustic waves. *Lab on a Chip*, 17(1):91–103, 2017.

[239] Xiaoyun Ding, Sz-Chin Steven Lin, Michael Ian Lapsley, Sixing Li, Xiang Guo, Chung Yu Chan, I-Kao Chiang, Lin Wang, J Philip McCoy, and Tony Jun Huang. Standing surface acoustic wave (SSAW) based multichannel cell sorting. *Lab on a Chip*, 12(21):4228–4231, 2012.

[240] Lothar Schmid, David A Weitz, and Thomas Franke. Sorting drops and cells with acoustics: acoustic microfluidic fluorescence-activated cell sorter. *Lab on a Chip*, 14(19):3710–3718, 2014.

[241] Liqiang Ren, Yuchao Chen, Peng Li, Zhangming Mao, Po-Hsun Huang, Joseph Rufo, Feng Guo, Lin Wang, J Philip McCoy, Stewart J Levine, and Tony Jun Huang. A high-throughput acoustic cell sorter. *Lab on a Chip*, 15(19):3870–3879, 2015.

[242] David J Collins, Adrian Neild, and Ye Ai. Highly focused high-frequency travelling surface acoustic waves (SAW) for rapid single-particle sorting. *Lab on a Chip*, 16(3):471–479, 2016.

[243] James P Lata, Feng Guo, Jinshan Guo, Po-Hsun Huang, Jian Yang, and Tony Jun Huang. Surface acoustic waves grant superior spatial control of cells embedded in hydrogel fibers. *Advanced Materials*, 28(39):8632–8638, 2016.

[244] CD Wood, SD Evans, JE Cunningham, R O'Rorke, C Wälti, and AG Davies. Alignment of particles in microfluidic systems using standing surface acoustic waves. *Applied Physics Letters*, 92(4):044104, 2008.

[245] CD Wood, JE Cunningham, R O'Rorke, C Wälti, EH Linfield, AG Davies, and SD Evans. Formation and manipulation of two-dimensional arrays of micron-scale particles in microfluidic systems by surface acoustic waves. *Applied Physics Letters*, 94(5):054101, 2009.

[246] Jinjie Shi, Daniel Ahmed, Xiaole Mao, Sz-Chin Steven Lin, Aitan Lawit, and Tony Jun Huang. Acoustic tweezers: patterning cells and microparticles using standing surface acoustic waves (SSAW). *Lab on a Chip*, 9(20):2890–2895, 2009.

[247] RD O'Rorke, CD Wood, C Wälti, SD Evans, AG Davies, and JE Cunningham. Acousto-microfluidics: transporting microbubble and microparticle arrays in acoustic traps using surface acoustic waves. *Journal of Applied Physics*, 111(9):094911, 2012.

[248] Xiaoyun Ding, Jinjie Shi, Sz-Chin Steven Lin, Shahrzad Yazdi, Brian Kiraly, and Tony Jun Huang. Tunable patterning of microparticles and cells using standing surface acoustic waves. *Lab on a Chip*, 12(14):2491–2497, 2012.

[249] David J Collins, Citsabehsan Devendran, Zhichao Ma, Jia Wei Ng, Adrian Neild, and Ye Ai. Acoustic tweezers via sub–time-of-flight regime surface acoustic waves. *Science Advances*, 2(7):e1600089, 2016.

[250] Liangfei Tian, Nicolas Martin, Philip G Bassindale, Avinash J Patil, Mei Li, Adrian Barnes, Bruce W Drinkwater, and Stephen Mann. Spontaneous assembly of chemically encoded two-dimensional coacervate droplet arrays by acoustic wave patterning. *Nature Communications*, 7, 2016.

[251] Junhui Hu and Armand Kertoputro Santoso. A/spl pi/-shaped ultrasonic tweezers concept for manipulation of small particles. *IEEE Transactions on Ultrasonics, Ferroelectrics, and Frequency Control*, 51(11):1499–1507, 2004.

[252] Junhui Hu, Jianbo Yang, and Jun Xu. Ultrasonic trapping of small particles by sharp edges vibrating in a flexural mode. *Applied Physics Letters*, 85(24):6042–6044, 2004.

[253] Nathan D Orloff, Jaclyn R Dennis, Marco Cecchini, Ethan Schonbrun, Eduard Rocas, Yu Wang, David Novotny, Raymond W Simmonds, John Moreland, Ichiro Takeuchi, and James C Booth. Manipulating particle trajectories with phase-control in surface acoustic wave microfluidics. *Biomicrofluidics*, 5(4):044107, 2011.

[254] Xiaoyun Ding, Sz-Chin Steven Lin, Brian Kiraly, Hongjun Yue, Sixing Li, I-Kao Chiang, Jinjie Shi, Stephen J Benkovic, and Tony Jun Huang. On-chip manipulation of single microparticles, cells, and organisms using surface acoustic waves. *Proceedings of the National Academy of Sciences*, 109(28):11105–11109, 2012.

[255] SBQ Tran, Philippe Marmottant, and Pierre Thibault. Fast acoustic tweezers for the two-dimensional manipulation of individual particles in microfluidic channels. *Applied Physics Letters*, 101(11):114103, 2012.

[256] Yuchao Chen, Sixing Li, Yeyi Gu, Peng Li, Xiaoyun Ding, Lin Wang, J Philip McCoy, Stewart J Levine, and Tony Jun Huang. Continuous enrichment of low-abundance cell samples using standing surface acoustic waves (SSAW). *Lab on a Chip*, 14(5):924–930, 2014.

[257] Bruce W Drinkwater. Dynamic-field devices for the ultrasonic manipulation of microparticles. *Lab on a Chip*, 16(13):2360–2375, 2016.

[258] Lothar Schmid and Thomas Franke. SAW-controlled drop size for flow focusing. *Lab on a Chip*, 13(9):1691–1694, 2013.

[259] Jason C Brenker, David J Collins, Hoang Van Phan, Tuncay Alan, and Adrian Neild. On-chip droplet production regimes using surface acoustic waves. *Lab on a Chip*, 16(9):1675–1683, 2016.

[260] Muhsincan Sesen, Tuncay Alan, and Adrian Neild. Microfluidic plug steering using surface acoustic waves. *Lab on a Chip*, 15(14):3030–3038, 2015.

[261] Jin Ho Jung, Ghulam Destgeer, Byunghang Ha, Jinsoo Park, and Hyung Jin Sung. On-demand droplet splitting using surface acoustic waves. *Lab on a Chip*, 16(17):3235–3243, 2016.

[262] Muhsincan Sesen, Citsabehsan Devendran, Sean Malikides, Tuncay Alan, and Adrian Neild. Surface acoustic wave enabled pipette on a chip. *Lab on a Chip*, 2017.

[263] Muhsincan Sesen, Tuncay Alan, and Adrian Neild. Microfluidic on-demand droplet merging using surface acoustic waves. *Lab on a Chip*, 14(17):3325–3333, 2014.

[264] Jin Ho Jung, Ghulam Destgeer, Jinsoo Park, Husnain Ahmed, Kwangseok Park, and Hyung Jin Sung. On-demand droplet capture and release using microwell-assisted surface acoustic waves. *Analytical Chemistry*, 89(4):2211–2215, 2017.

[265] Andreas Lenshof, Mikael Evander, Thomas Laurell, and Johan Nilsson. Acoustofluidics 5: Building microfluidic acoustic resonators. *Lab on a Chip*, 12(4):684–695, 2012.

[266] MA Grundy, WE Bolek, WT Coakley, and E Benes. Rapid agglutination testing in an ultrasonic standing wave. *Journal of Immunological Methods*, 165(1):47–57, 1993.

[267] Muhammet K Araz, Chung-Hoon Lee, and Amit Lal. Ultrasonic separation in microfluidic capillaries. In *Ultrasonics, 2003 IEEE Symposium on*, volume 2, pages 1111–1114. IEEE, 2003.

[268] Ian Gralinski, Tuncay Alan, and Adrian Neild. Non-contact acoustic trapping in circular cross-section glass capillaries: a numerical study. *The Journal of the Acoustical Society of America*, 132(5):2978–2987, 2012.

[269] Ian Gralinski, Samuel Raymond, Tuncay Alan, and Adrian Neild. Continuous flow ultrasonic particle trapping in a glass capillary. *Journal of Applied Physics*, 115(5):054505, 2014.

[270] Zhangming Mao, Peng Li, Mengxi Wu, Hunter Bachman, Nicolas Mesyngier, Xiasheng Guo, Sheng Liu, Francesco Costanzo, and Tony Jun Huang. Enriching nanoparticles via acoustofluidics. *ACS Nano*, 11(1):603–612, 2017.

[271] Aigars Piruska, Maojun Gong, Jonathan V Sweedler, and Paul W Bohn. Nanofluidics in chemical analysis. *Chemical Society Reviews*, 39(3):1060–1072, 2010.

[272] Thomas A Zangle, Ali Mani, and Juan G Santiago. Theory and experiments of concentration polarization and ion focusing at microchannel and nanochannel interfaces. *Chemical Society Reviews*, 39(3):1014–1035, 2010.

[273] Joost W van Honschoten, Nataliya Brunets, and Niels R Tas. Capillarity at the nanoscale. *Chemical Society Reviews*, 39(3):1096–1114, 2010.

[274] Eric B Kalman, Ivan Vlassiouk, and Zuzanna S Siwy. Nanofluidic bipolar transistors. *Advanced Materials*, 20(2):293–297, 2008.

[275] Reto B Schoch, Jongyoon Han, and Philippe Renaud. Transport phenomena in nanofluidics. *Reviews of Modern Physics*, 80(3):839, 2008.

[276] Sung Jae Kim, Leon D Li, and Jongyoon Han. Amplified electrokinetic response by concentration polarization near nanofluidic channel. *Langmuir*, 25(13):7759–7765, 2009.

[277] Qiaosheng Pu, Jongsin Yun, Henryk Temkin, and Shaorong Liu. Ion-enrichment and ion-depletion effect of nanochannel structures. *Nano Letters*, 4(6):1099–1103, 2004.

[278] Sung Jae Kim, Ying-Chih Wang, Jeong Hoon Lee, Hongchul Jang, and Jongyoon Han. Concentration polarization and nonlinear electrokinetic flow near a nanofluidic channel. *Physical Review Letters*, 99(4):044501, 2007.

[279] L Jay Guo, Xing Cheng, and Chia-Fu Chou. Fabrication of size-controllable nanofluidic channels by nanoimprinting and its application for DNA stretching. *Nano Letters*, 4(1):69–73, 2004.

[280] Mathieu Foquet, Jonas Korlach, Warren Zipfel, Watt W Webb, and Harold G Craighead. DNA fragment sizing by single molecule detection in submicrometer-sized closed fluidic channels. *Analytical Chemistry*, 74(6):1415–1422, 2002.

[281] Sung Jae Kim, Sung Hee Ko, Kwan Hyoung Kang, and Jongyoon Han. Direct seawater desalination by ion concentration polarization. *Nature Nanotechnology*, 5(4):297–301, 2010.

[282] Lydéric Bocquet and Elisabeth Charlaix. Nanofluidics, from bulk to interfaces. *Chemical Society Reviews*, 39(3):1073–1095, 2010.

[283] W vd Sparreboom, A Van Den Berg, and JCT Eijkel. Principles and applications of nanofluidic transport. *Nature Nanotechnology*, 4(11):713–720, 2009.

[284] Kumuditha M Weerakoon-Ratnayake, Colleen E O'Neil, Franklin I Uba, and Steven A Soper. Thermoplastic nanofluidic devices for biomedical applications. *Lab on a Chip*, 17(3):362–381, 2017.

[285] M Whitby and N Quirke. Fluid flow in carbon nanotubes and nanopipes. *Nature Nanotechnology*, 2(2):87–94, 2007.

[286] Aleksandr Noy, Hyung Gyu Park, Francesco Fornasiero, Jason K Holt, Costas P Grigoropoulos, and Olgica Bakajin. Nanofluidics in carbon nanotubes. *Nano Today*, 2(6):22–29, 2007.

[287] Davide Mattia and Yury Gogotsi. Static and dynamic behavior of liquids inside carbon nanotubes. *Microfluidics and Nanofluidics*, 5(3):289–305, 2008.

[288] Zeke Insepov, Dieter Wolf, and Ahmed Hassanein. Nanopumping using carbon nanotubes. *Nano Letters*, 6(9):1893–1895, 2006.

[289] MJ Longhurst and N Quirke. Temperature-driven pumping of fluid through single-walled carbon nanotubes. *Nano Letters*, 7(11):3324–3328, 2007.

[290] Klaus F Rinne, Stephan Gekle, Douwe Jan Bonthuis, and Roland R Netz. Nanoscale pumping of water by ac electric fields. *Nano Letters*, 12(4):1780–1783, 2012.

[291] Joshua Goldberger, Rong Fan, and Peidong Yang. Inorganic nanotubes: a novel platform for nanofluidics. *Accounts of Chemical Research*, 39(4):239–248, 2006.

[292] Joshua Edel, Aleksandar Ivanov, and MinJun Kim. *Nanofluidics*, volume 41. Royal Society of Chemistry, 2016.

[293] Kung-Hsuan Lin, Chih-Ming Lai, Chang-Chi Pan, Jen-Inn Chyi, Jin-Wei Shi, Shih-Ze Sun, Chieh-Feng Chang, and Chi-Kuang Sun. Spatial manipulation of nanoacoustic waves with nanoscale spot sizes. *Nature Nanotechnology*, 2(11):704–708, 2007.

[294] T Pezeril, C Klieber, S Andrieu, and KA Nelson. Optical generation of gigahertz-frequency shear acoustic waves in liquid glycerol. *Physical Review Letters*, 102(10):107402, 2009.

[295] PJS van Capel, Emmanuel Péronne, and JI Dijkhuis. Nonlinear ultrafast acoustics at the nano scale. *Ultrasonics*, 56:36–51, 2015.

[296] Franklin I Uba, Bo Hu, Kumuditha Weerakoon-Ratnayake, Nyote Oliver-Calixte, and Steven A Soper. High process yield rates of thermoplastic nanofluidic devices using a hybrid thermal assembly technique. *Lab on a Chip*, 15(4):1038–1049, 2015.

[297] D Mijatovic, JCT Eijkel, and A Van Den Berg. Technologies for nanofluidic systems: top-down vs. bottom-up; a review. *Lab on a Chip*, 5(5):492–500, 2005.

[298] Jiahao Wu, Rattikan Chantiwas, Alborz Amirsadeghi, Steven A Soper, and Sunggook Park. Complete plastic nanofluidic devices for DNA analysis via direct imprinting with polymer stamps. *Lab on a Chip*, 11(17):2984–2989, 2011.

[299] Jonas O Tegenfeldt, Christelle Prinz, Han Cao, Steven Chou, Walter W Reisner, Robert Riehn, Yan Mei Wang, Edward C Cox, James C Sturm, Pascal Silberzan, and Robert H Austin. The dynamics of genomic-length DNA molecules in 100-nm channels. *Proceedings of the National Academy of Sciences of the United States of America*, 101(30):10979–10983, 2004.

[300] Lasse H Thamdrup, Anna Klukowska, and Anders Kristensen. Stretching DNA in polymer nanochannels fabricated by thermal imprint in PMMA. *Nanotechnology*, 19(12):125301, 2008.

[301] Walter Reisner, Keith J Morton, Robert Riehn, Yan Mei Wang, Zhaoning Yu, Michael Rosen, James C Sturm, Stephen Y Chou, Erwin Frey, and Robert H Austin. Statics and dynamics of single DNA molecules confined in nanochannels. *Physical Review Letters*, 94(19):196101, 2005.

[302] Pawel Utko, Fredrik Persson, Anders Kristensen, and Niels B Larsen. Injection molded nanofluidic chips: fabrication method and functional tests using single-molecule DNA experiments. *Lab on a Chip*, 11(2):303–308, 2011.

[303] Hideki Takagi, Ryutaro Maeda, Naoe Hosoda, and Tadatomo Suga. Room-temperature bonding of lithium niobate and silicon wafers by argon-beam surface activation. *Applied Physics Letters*, 74(16):2387–2389, 1999.

[304] Arthur A Oliner. Waveguides for acoustic surface waves: A review. *Proceedings of the IEEE*, 64(5):615–627, 1976.

[305] PL Adams and HJ Shaw. Surface acoustic waveguide for long time delay. In *1972 IEEE Ultrasonics Symposium*, 1972.

[306] Ajay Raghavan and Carlos ES Cesnik. Review of guided-wave structural health monitoring. *Shock and Vibration Digest*, 39(2):91–116, 2007.

[307] MHS Siqueira, CEN Gatts, RR Da Silva, and JMA Rebello. The use of ultrasonic guided waves and wavelets analysis in pipe inspection. *Ultrasonics*, 41(10):785–797, 2004.

[308] KH Yen and AA Oliner. The strip acoustic surface waveguide: comparison between measurement and theory. *Applied Physics Letters*, 28(7):368–370, 1976.

[309] Eric A Ash, RM De La Rue, and RF Humphryes. Microsound surface waveguides. *IEEE Transactions on Microwave Theory and Techniques*, 17(11):882–892, 1969.

[310] KH Yen, HL Bertoni, AA Oliner, and S Markman. Mode coupling at a plate edge with application to acoustic ridge waveguides. In *Symposium on Optical and Acoustical Micro-Electronics*, pages 297–309, 1975.

[311] John J McCoy and RD Mindlin. Extensional waves along the edge of an elastic plate. *Journal of Applied Mechanics*, 30(1):75–78, 1963.

[312] PE Lagasse. Analysis of silicon ridge waveguides for acoustic surface waves. In *Microwave Conference, 1973. 3rd European*, volume 2, pages 1–4. IEEE, 1973.

[313] PE Lagasse and IM Mason. Analysis of propagation in ridge guides for acoustic surface waves. *Electronics Letters*, 8(4):82–84, 1972.

[314] PE Lagasse. Finite element analysis of piezoelectric elastic waveguides. *IEEE Transactions on Sonics and Ultrasonics*, 20(4):354–359, 1973.

[315] PE Lagasse. Higher-order finite-element analysis of topographic guides supporting elastic surface waves. *The Journal of the Acoustical Society of America*, 53(4):1116–1122, 1973.

[316] RV Schmidt. Acoustic surface wave velocity perturbations in $LiNbO_3$ by diffusion of metals. *Applied Physics Letters*, 27(1):8–10, 1975.

[317] Zhangliang Xu and Yong J Yuan. Implementation of guiding layers of surface acoustic wave devices: a review. *Biosensors and Bioelectronics*, 99:500–512, 2018.

[318] E Gizeli, F Bender, A Rasmusson, K Saha, F Josse, and R Cernosek. Sensitivity of the acoustic waveguide biosensor to protein binding as a function of the waveguide properties. *Biosensors and Bioelectronics*, 18(11):1399–1406, 2003.

[319] KM Mohibul Kabir, Ylias M Sabri, Ahmad Esmaielzadeh Kandjani, Samuel J Ippolito, and Suresh K Bhargava. Development and comparative investigation of ag-sensitive layer based SAW and QCM sensors for mercury sensing applications. *Analyst*, 141(8):2463–2473, 2016.

[320] Harold Seidel and Donald L White. Ultrasonic surface waveguides, January 6 1970. US Patent 3,488,602.

[321] Ronald V Schmidt and LA Coldren. Thin film acoustic surface waveguides on anisotropic media. *IEEE Transactions on Sonics and Ultrasonics*, 22(2):115–122, 1975.

[322] RCM Li, AA Oliner, and HL Bertoni. Microwave network analyses of surface acoustic waveguides. I-flat overlay guides. *IEEE Transactions on Sonics Ultrasonics*, 24:66–78, 1977.

[323] AA Oliner, RCM Li, and HL Bertoni. Microwave network approach to guided acoustic surface wave structures. Technical report, Polytechnic Institute of Brooklyn Farmingdale New York Department of Electrophysics, 1971.

[324] HF Tiersten. Elastic surface waves guided by thin films. *Journal of Applied Physics*, 40(2):770–789, 1969.

[325] LR Adkins and AJ Hughes. Elastic surface waves guided by thin films: gold on fused quartz. *IEEE Transactions on Microwave Theory and Techniques*, 17(11):904–911, 1969.

[326] LB Freund. Guided surface waves on an elastic half space. *Journal of Applied Mechanics*, 38(4):899–905, 1971.

[327] LB Freund and JD Achenbach. Waves in a semi-infinite plate in smooth contact with a harmonically disturbed half-space. *International Journal of Solids and Structures*, 4(6):605–621, 1968.

[328] HF Tiersten and RC Davis. Elastic surface waves guided by curved thin films. *Journal of Applied Physics*, 44(5):2097–2112, 1973.

[329] Thomas L Szabo and AJ Slobodnik. The effect of diffraction on the design of acoustic surface wave devices. *IEEE Transactions on Sonics and Ultrasonics*, 20(3):240–251, 1973.

[330] H Engan. *Experiments with Elastic Surface Waves in Piezoelectric Ceramics*. Electronics Research Laboratory, Norwegian Institute of Technology, 1969.

[331] A James Hughes. Elastic surface wave guidance by $(\triangle v/v)$ effect guidance structures. *Journal of Applied Physics*, 43(6):2569–2586, 1972.

[332] LA Coldren and RV Schmidt. Acoustic surface wave $\triangle v/v$ waveguides on anisotropic substrates. *Applied Physics Letters*, 22(10):482–483, 1973.

[333] BK Sinha and HF Tiersten. Elastic and piezoelectric surface waves guided by thin films. *Journal of Applied Physics*, 44(11):4831–4854, 1973.

[334] Henry Frank Tiersten. *Linear Piezoelectric Plate Vibrations: Elements of the Linear Theory of Piezoelectricity and the Vibrations Piezoelectric Plates*. Springer, 2013.

[335] IM Mason, RM De La Rue, RV Schmidt, EA Ash, and PE Lagasse. Ridge guides for acoustic surface waves. *Electronics Letters*, 7(14):395–397, 1971.

[336] TR Meeker and AH Meitzler. Guided wave propagation in elongated cylinders and plates. *Physical Acoustics*, 1(Part A):111–167, 1964.

[337] Paul E Lagasse, Iain M Mason, and Eric A Ash. Acoustic surface waveguides—analysis and assessment. *IEEE Transactions on Microwave Theory and Techniques*, 21(4):225–236, 1973.

[338] RCM Li, HL Bertoni, AA Oliner, and S Markman. Simple equivalent network for the flexural mode of the ridge guide for acoustic surface waves. *Electronics Letters*, 8(8):211–212, 1972.

[339] P Silvester. A general high-order finite-element analysis program waveguide. *IEEE Transactions on Microwave Theory and Techniques*, 17(4):204–210, 1969.

[340] I Fried. Accuracy of finite element eigenproblems. *Journal of Sound and Vibration*, 18(2):289–295, 1971.

[341] R Burridge and FJ Sabina. Theoretical computations on ridge acoustic surface waves using the finite-element method. *Electronics Letters*, 7(24):720–722, 1971.

[342] S Markman, Robert CM Li, AA Oliner, and HL Bertoni. Microwave network analyses of surface acoustic waveguides. II-rectangular ridge guides. *IEEE Transactions on Sonics Ultrasonics*, 24:79–87, 1977.

[343] RCM Li, HL Bertoni, AA Oliner, and S Markman. Propagation characteristics of the pseudo-rayleigh mode of the ridge guide for acoustic surface waves. *Electronics Letters*, 8(9):220–221, 1972.

[344] PE Lagasse. Analysis of a dispersionfree guide for elastic waves. *Electronics Letters*, 8(15):372–373, 1972.

[345] PE Lagasse, M Cabus, and M Verplanken. The influence of truncation on dispersion of wedge guides. In *1974 Ultrasonics Symposium*, pages 121–124. IEEE, 1974.

[346] IM Mason, MD Motz, and J Chambers. Wedge waveguide parametric signal processing. In *1972 Ultrasonics Symposium*, pages 314–315. IEEE, 1972.

[347] Wen-Chih Wang and Che-Hua Yang. Antisymmetric flexural modes propagating along apex of piezoelectric wedges. *Japanese Journal of Applied Physics*, 46(9R):5939, 2007.

[348] IH Liu and CH Yang. An investigation on wedge waves and the interaction with a defect using a quantitative laser ultrasound visualization system. In *2010 IEEE International Ultrasonics Symposium*, pages 817–820. IEEE, 2010.

[349] VV Krylov and DF Parker. Harmonic generation and parametric mixing in wedge acoustic waves. *Wave Motion*, 15(2):185–200, 1992.

[350] Victor V Krylov, AP Mayer, and DF Parker. Nonlinear evolution of initially sine-like wedge acoustic waves. In *1993 Proceedings IEEE Ultrasonics Symposium*, pages 765–768. IEEE, 1993.

[351] Andreas P Mayer, Elena A Garova, and Vladimir G Mozhaev. Nonlinear surface and wedge acoustic waves in the presence of weak dispersion. *Proceedings of the Estonian Academy of Sciences, Physics and Mathematics*, 46:85–93, 1997.

[352] Andreas P Mayer, Alexey M Lomonosov, and Peter Hess. Nonlinear acoustic waves localized at crystal edges. In *2009 IEEE International Ultrasonics Symposium*, pages 1088–1091. IEEE, 2009.

[353] Elena S Sokolova, Alexander S Kovalev, Reinhold Timler, and Andreas P Mayer. On the dispersion of wedge acoustic waves. *Wave Motion*, 50(2):233–245, 2013.

[354] A-C Hladky-Hennion. Finite element analysis of the propagation of acoustic waves in waveguides. *Journal of Sound and Vibration*, 194(2):119–136, 1996.

[355] Sergey I Bozhevolnyi, Valentyn S Volkov, Eloise Devaux, Jean-Yves Laluet, and Thomas W Ebbesen. Channel plasmon subwavelength waveguide components including interferometers and ring resonators. *Nature*, 440(7083):508, 2006.

[356] Dmitri K Gramotnev and David FP Pile. Single-mode subwavelength waveguide with channel plasmon-polaritons in triangular grooves on a metal surface. *Applied Physics Letters*, 85(26):6323–6325, 2004.

[357] David FP Pile and Dmitri K Gramotnev. Channel plasmon–polariton in a triangular groove on a metal surface. *Optics Letters*, 29(10):1069–1071, 2004.

[358] Fengming Liu, Shasha Peng, Han Jia, Manzhu Ke, and Zhengyou Liu. Strongly localized acoustic surface waves propagating along a V-groove. *Applied Physics Letters*, 94(2):023505, 2009.

[359] RV Schmidt and IP Kaminow. Metal-diffused optical waveguides in $LiNbO_3$. *Applied Physics Letters*, 25(8):458–460, 1974.

[360] JF Weller, JD Crowley, and TG Giallorenzi. Surface acoustic waveguides on $LiNbO_3$ formed by titanium in-diffusion. *Applied Physics Letters*, 31(3):146–148, 1977.

[361] P Hartemann, P Cauvard, and D Desbois. Ion-implanted surface-acoustic-wave guides on lithium niobate. *Applied Physics Letters*, 32(5):266–268, 1978.

[362] V Hinkov. Proton exchanged waveguides for surface acoustic waves on $LiNbO_3$. *Journal of Applied Physics*, 62(9):3573–3578, 1987.

[363] P Hartemann. Acoustic-surface-wave velocity decrease produced by ion implantation in lithium niobate. *Applied Physics Letters*, 27(5):263–265, 1975.

[364] Raymond R Knowles and Neil D Opdyke. Paleomagnetic results from the mauch chunk formation: A test of the origin of curvature in the folded appalachians of pennsylvania. *Journal of Geophysical Research*, 73(20):6515–6526, 1968.

[365] Janet L Jackel, CE Rice, and JJ Veselka. Proton exchange for high-index waveguides in $LiNbO_3$. *Applied Physics Letters*, 41(7):607–608, 1982.

[366] JL Jackel and CE Rice. Topotactic $LiNbO_3$ to cubic perovskite structural transformation in $LiNbO_3$ and $LiTaO_3$. *Ferroelectrics*, 38(1):801–804, 1981.

[367] William Connacher, Naiqing Zhang, An Huang, Jiyang Mei, Shuai Zhang, Tilvawala Gopesh, and James Friend. Micro/nano acoustofluidics: materials, phenomena, design, devices, and applications. *Lab on a Chip*, 2018.

[368] RM White and FW Voltmer. Direct piezoelectric coupling to surface elastic waves. *Applied Physics Letters*, 7(12):314–316, 1965.

[369] Henry I Smith, Frank J Bachner, and N Efremow. A high-yield photolithographic technique for surface wave devices. *Journal of the Electrochemical Society*, 118(5):821, 1971.

[370] Henry I Smith. Fabrication techniques for surface-acoustic-wave and thin-film optical devices. *Proceedings of the IEEE*, 62(10):1361–1387, 1974.

[371] Nicolle Wilke, A Mulcahy, S-R Ye, and A Morrissey. Process optimization and characterization of silicon microneedles fabricated by wet etch technology. *Microelectronics Journal*, 36(7):650–656, 2005.

[372] Michael Köhler. *Etching in Microsystem Technology*. John Wiley & Sons, 2008.

[373] Ivor Brodie and Julius J Muray. *The physics of micro/nano-fabrication*. Springer Science & Business Media, 2013.

[374] Marcela Pekarcikova, Matthias Hofmann, Siegfried Menzel, H Schrnidt, Thomas Gemming, and Klaus Wetzig. Investigation of high power effects on Ti/Al and Ta-Si-N/Cu/Ta-Si-N electrodes for SAW devices. *IEEE Transactions on Ultrasonics, Ferroelectrics, and Frequency Control*, 52(5):911–917, 2005.

[375] Gang Bao and Subra Suresh. Cell and molecular mechanics of biological materials. *Nature Materials*, 2(11):715–725, 2003.

[376] François Berthiaume, Timothy J Maguire, and Martin L Yarmush. Tissue engineering and regenerative medicine: history, progress, and challenges. *Annual Review of Chemical and Biomolecular Engineering*, 2:403–430, 2011.

[377] Rose G Harrison, MJ Greenman, Franklin P Mall, and CM Jackson. Observations of the living developing nerve fiber. *The Anatomical Record*, 1(5):116–128, 1907.

[378] Alison Abbott. Biology's new dimension, 2003. Nature Publishing Group.

[379] G.B. West. *Scale: The Universal Laws of Growth, Innovation, Sustainability, and the Pace of Life in Organisms, Cities, Economies, and Companies*. Penguin Press, 2017.

[380] Christian Frantz, Kathleen M Stewart, and Valerie M Weaver. The extracellular matrix at a glance. *Journal of Cell Science*, 123(24):4195–4200, 2010.

[381] Francesco Pampaloni, Emmanuel G Reynaud, and Ernst HK Stelzer. The third dimension bridges the gap between cell culture and live tissue. *Nature Reviews Molecular Cell Biology*, 8(10):839–845, 2007.

[382] Jean Paul Thiery. Cell adhesion in development: a complex signaling network. *Current Opinion in Genetics & Development*, 13(4):365–371, 2003.

[383] Tyler Jacks and Robert A Weinberg. Taking the study of cancer cell survival to a new dimension. *Cell*, 111(7):923–925, 2002.

[384] Madeline A. Lancaster and Juergen A. Knoblich. Organogenesis in a dish: Modeling development and disease using organoid technologies. *Science*, 345(6194):1–9, 2014.

[385] Soojung Oh, Hyunryul Ryu, Dongha Tahk, Jihoon Ko, Yoojin Chung, Hae Kwang Lee, Tae Ryong Lee, and Noo Li Jeon. "open-top" microfluidic device for in vitro three-dimensional capillary beds. *Lab on a Chip*, 17(20):3405–3414, 2017.

[386] Yi-Chung Tung, Amy Y Hsiao, Steven G Allen, Yu-suke Torisawa, Mitchell Ho, and Shuichi Takayama. High-throughput 3D spheroid culture and drug testing using a 384 hanging drop array. *Analyst*, 136(3):473–478, 2011.

[387] Simone Bersini, Jessie S Jeon, Gabriele Dubini, Chiara Arrigoni, Seok Chung, Joseph L Charest, Matteo Moretti, and Roger D Kamm. A microfluidic 3D in vitro model for specificity of breast cancer metastasis to bone. *Biomaterials*, 35(8):2454–2461, 2014.

[388] Minhwan Chung, Jungho Ahn, Kyungmin Son, Sudong Kim, and Noo Li Jeon. Biomimetic model of tumor microenvironment on microfluidic platform. *Advanced Healthcare Materials*, 6(15):1700196, 2017.

[389] Sreenivasa C Ramaiahgari, Michiel W Den Braver, Bram Herpers, Valeska Terpstra, Jan NM Commandeur, Bob van de Water, and Leo S Price. A 3D in vitro model of differentiated HepG2 cell spheroids with improved liver-like properties for repeated dose high-throughput toxicity studies. *Archives of Toxicology*, 88(5):1083–1095, 2014.

[390] Biman B Mandal and Subhas C Kundu. Cell proliferation and migration in silk fibroin 3D scaffolds. *Biomaterials*, 30(15):2956–2965, 2009.

[391] Geoffrey B. West and James H. Brown. The origin of allometric scaling laws in biology from genomes to ecosystems: towards a quantitative unifying theory of biological structure and organization. *Journal of Experimental Biology*, 208(9):1575–1592, 2005.

[392] Eelco Fennema, Nicolas Rivron, Jeroen Rouwkema, Clemens van Blitterswijk, and Jan De Boer. Spheroid culture as a tool for creating 3D complex tissues. *Trends in Biotechnology*, 31(2):108–115, 2013.

[393] Matthias W Laschke and Michael D Menger. Life is 3D: boosting spheroid function for tissue engineering. *Trends in Biotechnology*, 35(2):133–144, 2017.

[394] Bin Chen, Yue Wu, Zheng Ao, Hongwei Cai, Asael Nunez, Yunhua Liu, John Foley, Kenneth Nephew, Xiongbin Lu, and Feng Guo. High-throughput

acoustofluidic fabrication of tumor spheroids. *Lab on a Chip*, 19(10):1755–1763, 2019.

[395] Aliya Fatehullah, Si Hui Tan, and Nick Barker. Organoids as an in vitro model of human development and disease. *Nature Cell Biology*, 18(3):246–254, 2016.

[396] Sunghee Estelle Park, Andrei Georgescu, and Dongeun Huh. Organoids-on-a-chip. *Science*, 364(6444):960–965, 2019.

[397] Maria Vinci, Sharon Gowan, Frances Boxall, Lisa Patterson, Miriam Zimmermann, William Court, Cara Lomas, Marta Mendiola, David Hardisson, and Suzanne A Eccles. Advances in establishment and analysis of three-dimensional tumor spheroid-based functional assays for target validation and drug evaluation. *BMC Biology*, 10(1):29, 2012.

[398] Sina Bartfeld, Tülay Bayram, Marc van de Wetering, Meritxell Huch, Harry Begthel, Pekka Kujala, Robert Vries, Peter J Peters, and Hans Clevers. In vitro expansion of human gastric epithelial stem cells and their responses to bacterial infection. *Gastroenterology*, 148(1):126–136, 2015.

[399] Minoru Takasato, PX Er, M Becroft, Jessica M Vanslambrouck, EG Stanley, Andrew George Elefanty, and Melissa H Little. Directing human embryonic stem cell differentiation towards a renal lineage generates a self-organizing kidney. *Nature Cell Biology*, 16(1):118–126, 2014.

[400] Takanori Takebe, Keisuke Sekine, Masahiro Enomura, Hiroyuki Koike, Masaki Kimura, Takunori Ogaeri, Ran-Ran Zhang, Yasuharu Ueno, Yun-Wen Zheng, Naoto Koike, Shinsuke Aoyama, yasuhise Adachi, and Hideki Taniguchi. Vascularized and functional human liver from an iPSC-derived organ bud transplant. *Nature*, 499(7459):481–484, 2013.

[401] Laura Broutier, Gianmarco Mastrogiovanni, Monique MA Verstegen, Hayley E Francies, Lena Morrill Gavarró, Charles R Bradshaw, George E Allen, Robert Arnes-Benito, Olga Sidorova, Marcia P Gaspersz, Nikitas Georgakopoulos, Bon-Kyoung Koo, Sabine Dietmann, Susan E Davies, Raaj K Proseedom, Ruby Lieshout, Jan N M IJzermans, Stephen J Wigmore, Kourosh Saeb-Pasey, Mathew J Garnett, Luc JW van der Laan, and Meritwell Huch. Human primary liver cancer–derived organoid cultures for disease modeling and drug screening. *Nature Medicine*, 23(12):1424, 2017.

[402] Jason R Spence, Christopher N Mayhew, Scott A Rankin, Matthew F Kuhar, Jefferson E Vallance, Kathryn Tolle, Elizabeth E Hoskins, Vladimir V Kalinichenko, Susanne I Wells, Aaron M Zorn, Noah F Shroyer, and James M Wells. Directed differentiation of human pluripotent stem cells into intestinal tissue in vitro. *Nature*, 470(7332):105–109, 2011.

[403] Norman Sachs, Joep de Ligt, Oded Kopper, Ewa Gogola, Gergana Bounova, Fleur Weeber, Anjali Vanita Balgobind, Karin Wind, Ana Gracanin, Harry Begthel, Jeroen Korving, Ruben van Boxtel, Alexandra Alves Duarte, Daphne Lelieveld, Arne van Hoeck, Robert Frans Ernst, Francis Blokzijl, Isaac Johannes Nijman, Marlous Hoogstraat, Marieke van de Ven, David Anthony Egan, Vittoria Zinzalla, Jurgen Moll, Sylvia Fernandez Boj, Emile Eugene Voest, Lodewyk Wessels, Paul Joannes van Diest, Sven Rottenberg, Robert Gerhardus Jacob Vries, Edwin Cuppen, and Hans Clevers. A living biobank of breast cancer organoids captures disease heterogeneity. *Cell*, 172(1-2):373–386, 2018.

[404] Cleber A Trujillo, Edward S Rice, Nathan K Schaefer, Isaac A Chaim, Emily C Wheeler, Assael A Madrigal, Justin Buchanan, Sebastian Preissl, Allen Wang, Priscilla D Negraes, Ryan A Szeto, Roberto H Herai, Alik Huseynov, Mariana S A Ferraz, Fernando S Borges, Alexandre H Kihara, Ashley Byrne, Maximillian Marin, Christopher Vollmers, Angela N Brooks, Jonathan D Lautz, Katerina Semendeferi, Beth Shapiro, Gene W Yeo, Stephen E P Smith, Richard E Green, and Alysson R Muotri. Reintroduction of the archaic variant of nova1 in cortical organoids alters neurodevelopment. *Science*, 371(6530):1–10, 2021.

[405] Nicholas Timmins, Stefanie Dietmair, and Lars Nielsen. Hanging-drop multicellular spheroids as a model of tumour angiogenesis. *Angiogenesis*, 7(2):97–103, 2004.

[406] Hynda K Kleinman and George R Martin. Matrigel: basement membrane matrix with biological activity. In *Seminars in Cancer Biology*, volume 15, pages 378–386. Elsevier, 2005.

[407] RH Dosh, A Essa, Nikki Jordan-Mahy, Chris Sammon, and CL le Maitre. Use of hydrogel scaffolds to develop an *in vitro* 3D culture model of human intestinal epithelium. *Acta Biomaterialia*, 62:128–143, 2017.

[408] Anthony P Napolitano, Peter Chai, Dylan M Dean, and Jeffrey R Morgan. Dynamics of the self-assembly of complex cellular aggregates on micromolded nonadhesive hydrogels. *Tissue Engineering*, 13(8):2087–2094, 2007.

[409] Glauco R Souza, Jennifer R Molina, Robert M Raphael, Michael G Ozawa, Daniel J Stark, Carly S Levin, Lawrence F Bronk, Jeyarama S Ananta, Jami Mandelin, Maria-Magdalena Georgescu, James A Bankson, Juri G Gelovani, T C Killian, Wadih Arap, and Renata Pasqualini. Three-dimensional tissue culture based on magnetic cell levitation. *Nature Nanotechnology*, 5(4):291–296, 2010.

[410] M Ingram, GB Techy, R Saroufeem, O Yazan, KS Narayan, TJ Goodwin, and GF Spaulding. Three-dimensional growth patterns of various human tumor cell lines in simulated microgravity of a NASA bioreactor. *In Vitro Cellular & Developmental Biology-Animal*, 33(6):459–466, 1997.

[411] Dirk R Albrecht, Gregory H Underhill, Travis B Wassermann, Robert L Sah, and Sangeeta N Bhatia. Probing the role of multicellular organization in three-dimensional microenvironments. *Nature Methods*, 3(5):369–375, 2006.

[412] Nak Won Choi, Mario Cabodi, Brittany Held, Jason P Gleghorn, Lawrence J Bonassar, and Abraham D Stroock. Microfluidic scaffolds for tissue engineering. *Nature Materials*, 6(11):908–915, 2007.

[413] Naiqing Zhang, Juan Hertz, Gopesh Tilvawala, Hemal Patel, and James Friend. Ultrafast microliter centrifuge platform for size-based separation using novel omnidirectional spiral surface acoustic wave for point-of-care diagnostics. *The FASEB Journal*, 34(S1):1–1, 2020.

[414] Yuta Kurashina, Kenjiro Takemura, and James Friend. Cell agglomeration in the wells of a 24-well plate using acoustic streaming. *Lab on a Chip*, 17(5):876–886, 2017.

[415] Chikahiro Imashiro, Makoto Hirano, Takashi Morikura, Yuki Fukuma, Kiyoshi Ohnuma, Yuta Kurashina, Shogo Miyata, and Kenjiro Takemura. Detachment of cell sheets from clinically ubiquitous cell culture vessels by ultrasonic vibration. *Scientific Reports*, 10(1):1–11, 2020.

[416] Mengying Zhou, Huipeng Ma, Hongli Lin, and Jianhua Qin. Induction of epithelial-to-mesenchymal transition in proximal tubular epithelial cells on microfluidic devices. *Biomaterials*, 35(5):1390–1401, 2014.

[417] Shannon Faley, Kevin Seale, Jacob Hughey, David K Schaffer, Scott VanCompernolle, Brett McKinney, Franz Baudenbacher, Derya Unutmaz, and John P

Wikswo. Microfluidic platform for real-time signaling analysis of multiple single T cells in parallel. *Lab on a Chip*, 8(10):1700–1712, 2008.

[418] Laura Mayol, Assunta Borzacchiello, Vincenzo Guarino, Carla Serri, Marco Biondi, and Luigi Ambrosio. Design of electrospayed non-spherical poly (l-lactide-co-glicolide) microdevices for sustained drug delivery. *Journal of Materials Science: Materials in Medicine*, 25(2):383–390, 2014.

[419] Sanjay M Prakadan, Alex K Shalek, and David A Weitz. Scaling by shrinking: empowering single-cell'omics' with microfluidic devices. *Nature Reviews Genetics*, 18(6):345–361, 2017.

[420] Guo You Huang, Li Hong Zhou, Qian Cheng Zhang, Yong Mei Chen, Wei Sun, Feng Xu, and Tian Jian Lu. Microfluidic hydrogels for tissue engineering. *Biofabrication*, 3(1):012001, 2011.

[421] Vincent van Duinen, Sebastiaan J Trietsch, Jos Joore, Paul Vulto, and Thomas Hankemeier. Microfluidic 3D cell culture: from tools to tissue models. *Current Opinion in Biotechnology*, 35:118–126, 2015.

[422] Dongeun Huh, Geraldine A Hamilton, and Donald E Ingber. From 3d cell culture to organs-on-chips. *Trends in Cell Biology*, 21(12):745–754, 2011.

[423] Feng Guo, Zhangming Mao, Yuchao Chen, Zhiwei Xie, James P Lata, Peng Li, Liqiang Ren, Jiayang Liu, Jian Yang, Ming Dao, Subra Suresh, and Tony Jun Huang. Three-dimensional manipulation of single cells using surface acoustic waves. *Proceedings of the National Academy of Sciences*, 113(6):1522–1527, 2016.

[424] Haiyan Li, Ayan Dasvarma, Leslie Yeo, James Friend, and Kathy Traianedes. Effect of surface acoustic waves on the viability, proliferation and differentiation of primary osteoblast-like cells. *Biomicrofluidics*, 3:034102, 2009.

[425] Ryan P Hodgson, Ming Tan, Leslie Yeo, and James Friend. Transmitting high power RF acoustic radiation via fluid couplants into superstrates for microfluidics. *Applied Physics Letters*, 94(2):024102, 2009.

[426] Jiyang Mei, Naiqing Zhang, and James Friend. Fabrication of surface acoustic wave devices on lithium niobate. *JoVE (Journal of Visualized Experiments)*, (160):e61013, 2020.

[427] Jiyang Mei and James Friend. A review: controlling the propagation of surface acoustic waves via waveguides for potential use in acoustofluidics. *Mechanical Engineering Reviews*, 7(1):19–00402, 2020.

[428] Nitesh Nama, Rune Barnkob, Zhangming Mao, Christian J Kähler, Francesco Costanzo, and Tony Jun Huang. Numerical study of acoustophoretic motion of particles in a pdms microchannel driven by surface acoustic waves. *Lab on a Chip*, 15(12):2700–2709, 2015.

[429] William Thielicke and Eize Stamhuis. Pivlab–towards user-friendly, affordable and accurate digital particle image velocimetry in matlab. *Journal of Open Research Software*, 2(1):e30, 2014.

[430] M von Smoluchowski. Mathematical theory of the kinetics of the coagulation of colloidal solutions. *Z. Phys. Chem*, 92(129):129–68, 1917.

[431] Richard Shilton, Ming K. Tan, Leslie Y. Yeo, and James R. Friend. Particle concentration and mixing in microdrops driven by focused surface acoustic waves. *Journal of Applied Physics*, 104:014910, 2008.

[432] Kejie Chen, Mengxi Wu, Feng Guo, Peng Li, Chung Yu Chan, Zhangming Mao, Sixing Li, Liqiang Ren, Rui Zhang, and Tony Jun Huang. Rapid formation of size-controllable multicellular spheroids via 3D acoustic tweezers. *Lab on a Chip*, 16(14):2636–2643, 2016.

[433] John Rogers, Yonggang Huang, Oliver G. Schmidt, and David H. Gracias. Origami MEMS and NEMS. *MRS Bulletin*, 41(2):123–129, 2016.

[434] J. Conway and N.J.A. Sloane. *Sphere Packings, Lattices and Groups*. Grundlehren der mathematischen Wissenschaften. Springer, New York, New York U.S., 1998.